

AD-A207 623

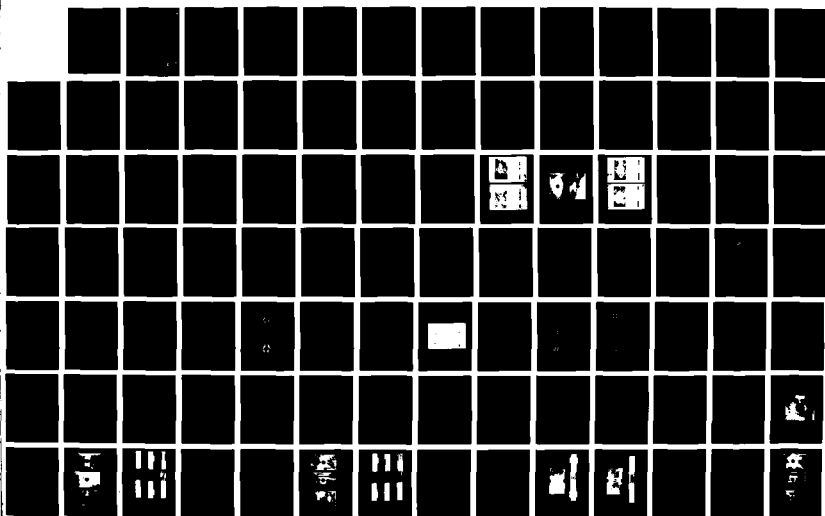
INVESTIGATION AND MODELING OF DAMAGE GROWTH IN  
COMPOSITE LAMINATES. (U) VIRGINIA POLYTECHNIC INST AND  
STATE UNIV BLACKSBURG MATERIALS.

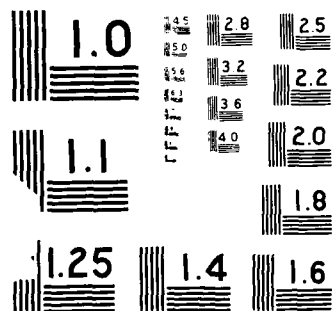
1/5

UNCLASSIFIED K L REIFSNIDER ET AL 25 SEP 88

F/G 11/4

NL





UNCLASSIFIED  
UNCL. FILED

SECURITY CLASSIFICATION OF THIS PAGE

①

## PORT DOCUMENTATION PAGE

AD-A207 623

2b. DECLASSIFICATION/DOWNGRADING		1d. RESTRICTIVE MARKINGS None									
4. PERFORMING ORGANIZATION REPORT NUMBER(S) Final Report		3. DISTRIBUTION/AVAILABILITY OF REPORT Unrestricted approved for public release, distribution unlimited									
6a. NAME OF PERFORMING ORGANIZATION Materials Response Group Virginia Tech		5b. OFFICE SYMBOL (If applicable)	7a. NAME OF MONITORING ORGANIZATION Aerospace Sciences AFOSR								
6c. ADDRESS (City, State and ZIP Code) Norris Hall Blacksburg, VA 24061-0219		7b. ADDRESS (City, State and ZIP Code) Building 410, Rm. A237 Bolling AFB Washington, DC 20332-6448									
8a. NAME OF FUNDING/SPONSORING ORGANIZATION AFOSR		8b. OFFICE SYMBOL (If applicable) NA	9. PROCUREMENT INSTRUMENT IDENTIFICATION NUMBER AFOSR-85-0087								
8c. ADDRESS (City, State and ZIP Code) Same as 7b.		10. SOURCE OF FUNDING NOS. <table border="1"><thead><tr><th>PROGRAM ELEMENT NO.</th><th>PROJECT NO.</th><th>TASK NO.</th><th>WORK UNIT NO.</th></tr></thead><tbody><tr><td>611024</td><td>2302</td><td>B2</td><td></td></tr></tbody></table>		PROGRAM ELEMENT NO.	PROJECT NO.	TASK NO.	WORK UNIT NO.	611024	2302	B2	
PROGRAM ELEMENT NO.	PROJECT NO.	TASK NO.	WORK UNIT NO.								
611024	2302	B2									
11. TITLE (Include Security Classification) Investigation and Modeling of Damage Growth in Composite Laminates											
12. PERSONAL AUTHOR(S) K.L. Reifsnider, W.W. Stinchcomb, C.E. Bakis, H.R. Yih, Doron Shalev											
13a. TYPE OF REPORT Final Report	13b. TIME COVERED FROM 1/1/88 TO 12/31/88	14. DATE OF REPORT (Yr., Mo., Day) September 25, 1988	15. PAGE COUNT 197								
16. SUPPLEMENTARY NOTATION											
17. COSATI CODES <table border="1"><thead><tr><th>FIELD</th><th>GROUP</th><th>SUB. GR.</th></tr></thead><tbody><tr><td></td><td></td><td></td></tr></tbody></table>		FIELD	GROUP	SUB. GR.				18. SUBJECT TERMS (Continue on reverse if necessary and identify by block number) Laminates, photoelastic, microstructure			
FIELD	GROUP	SUB. GR.									
19. ABSTRACT (Continue on reverse if necessary and identify by block number) Damage initiation and growth has been studied in several material systems and two notched geometries, revealing generic characteristics of damage development and its relationship to microstructure. Stress redistribution has been studied with photoelastic methods and simulated analytically. Adiabatic thermoelastic methods for strain field analysis under dynamic loading have been developed and the first micromechanical formulation of that problem has been achieved. A formulation of the singular stress problem in the boundary layer near a hole in composite laminates has been completed. And a brief study of the applicability of chaos theory to damage development representation was conducted. A critical element model of remaining strength and life of notched composite laminates has been constructed and validated.											
20. DISTRIBUTION/AVAILABILITY OF ABSTRACT UNCLASSIFIED/UNLIMITED <input checked="" type="checkbox"/> SAME AS RPT. <input checked="" type="checkbox"/> DTIC USERS <input checked="" type="checkbox"/>		21. ABSTRACT SECURITY CLASSIFICATION Unclassified E									
22a. NAME OF RESPONSIBLE INDIVIDUAL Lt. Colonel George K. Haritos		22b. TELEPHONE NUMBER (Include Area Code) 202/767-0463	22c. OFFICE SYMBOL AFOSR/NA								

ADDITIONAL TECHNICAL SCIENTIFIC RESEARCH (AFSC)  
DTIC TAB (Unannounced)  
This document report has been reviewed and is  
approved for public release in accordance with  
AFR 190-12.  
Distribution is unlimited.  
NEW J. KEEPER  
Chief, Technical Information Division

AFOSR-TR- 88-1253

Approved for public release;  
distribution unlimited.

# INVESTIGATION AND MODELING OF DAMAGE GROWTH IN COMPOSITE LAMINATES

Document Number AFOSR Contract No. 85.0087

25 September 1988

Accession For	
NTIS GRA&I	<input checked="checked" type="checkbox"/>
DTIC TAB	<input type="checkbox"/>
Unannounced	<input type="checkbox"/>
Justification	
By	
Distribution/	
Availability Codes	
Dist	Avail and/or Special
A-1	

K. REIFSNIDER, W. STINCHCOMB  
C. BAKIS, R. YIH

Materials Response Group

Virginia Tech

88 10 22



# Table of Contents

<b>Executive Summary</b> .....	<b>1</b>
1.1 Summary .....	1
 <b>Investigative Approach</b> .....	 <b>6</b>
2.1 Experiments .....	6
2.1.1 Mechanical Testing .....	6
2.1.2 Test Specimens .....	9
2.1.3 Stiffness Measurement .....	13
2.1.4 Ultrasonic C-Scan .....	14
2.1.5 X-Ray Radiography .....	15
2.1.6 Laminate Deploy .....	16
2.1.7 Adiabatic Thermography .....	17
2.1.7.1 Thermographic Apparatus .....	17
2.1.7.2 Mechanical Excitation .....	20
2.1.7.3 Specimen Preparation .....	22
2.1.7.4 SPATE Setup .....	22
2.1.7.5 Interpretation of Results .....	24
2.2 Analysis .....	29
2.2.1 Adiabatic Thermoelastic Effect .....	29
 <b>Basic Material Characterization</b> .....	 <b>57</b>
3.1 Monotonic Strength .....	57
3.2 Fatigue Life .....	60

3.3 Stiffness Measurements .....	63
<b>Fatigue Damage Mechanisms .....</b>	<b>70</b>
4.1 AS4/3501-6, Quasi-Isotropic Laminate .....	71
4.1.1 Center-Notched Specimens .....	71
4.1.1.1 High Load Level .....	71
4.1.1.2 Low Load Level .....	77
4.1.2 Double-Edge-Notched Specimens .....	81
4.2 AS4/3501-6, Orthotropic Laminate .....	84
4.2.1 Center-Notched Specimens .....	84
4.2.1.1 High Load Level .....	84
4.2.1.2 Low Load Level .....	88
4.2.2 Double-Edge-Notched Specimens .....	89
4.3 AS4/1808, Quasi-Isotropic Laminate .....	91
4.3.1 Center-Notched Specimens .....	91
4.3.1.1 High Load Level .....	91
4.3.1.2 Low Load Level .....	96
4.3.2 Double-Edge-Notched Specimens .....	104
4.3.2.1 High Load Level .....	104
4.3.2.2 Low Load Level .....	111
4.4 AS4/1808, Orthotropic Laminate .....	111
4.4.1 Center-Notched Specimens .....	111
4.4.1.1 High Load Level .....	111
4.4.1.2 Low Load Level .....	121
4.4.2 Double-Edge-Notched Specimens .....	131
4.5 Summary of Damage Mechanisms .....	131
4.5.1 Effect of Lamination Arrangement .....	131
4.5.2 Effect of Load Level .....	134

4.5.3	Effect of Material System	136
4.5.4	Effect of Notch Configuration	136
<b>Stress Redistribution Mechanisms</b>		<b>138</b>
<b>Residual Strength</b>		<b>165</b>
6.1	AS4/1808, Quasi-Isotropic Laminate	166
6.2	AS4/1808, Orthotropic Laminate	171
6.3	AS4/3501-6, Orthotropic Laminate	179
6.4	Summary of Residual Strength Data	182
<b>Modeling</b>		<b>184</b>
7.1	Model Development	184
7.1.1	Approach	184
7.1.2	Damage Analysis and Stress Redistribution	186
7.1.3	Modeling Features	189
<b>Conclusions</b>		<b>202</b>
8.1	Investigative Methods	202
8.2	Fatigue Response	203
8.2.1	Damage Development	203
8.2.2	Stress Redistribution	204
8.2.3	Residual Strength	205
8.2.4	Modeling of Remaining Strength	206
<b>References</b>		<b>208</b>

## List of Illustrations

Figure 1. Test specimen gripping arrangement .....	8
Figure 2. Test specimen configurations .....	10
Figure 3. Specimen axis and quadrant notations .....	12
Figure 4. Theoretical stress sensitivity of SPATE with various materials .....	18
Figure 5. SPATE signal in AS4/3502 laminates as a function of loading frequency .....	21
Figure 6. SPATE thermographs of 8-ply carbon epoxy laminates .....	25
Figure 7. Radiographs of 8-ply carbon epoxy laminates with fatigue damage .....	26
Figure 8. SPATE thermographs of 8-ply carbon epoxy laminates with fatigue damage ..	27
Figure 9. Dependence of adiabatic thermoelastic temperature change on in-plane stress components .....	33
Figure 10. Representative area of a fiber composite material .....	35
Figure 11. Effect of ply orientation on the temperature change in a unidirectional ply under constant axial stress or strain .....	42
Figure 12. Effect of ply orientation on the temperature change in an angle-ply laminate under constant axial stress or strain .....	43
Figure 13. Effect of ply orientation on the temperature change in a quasi-isotropic laminate under a constant global strain field .....	44
Figure 14. Effect of laminate Poisson's ratio on the temperature change in a 0-deg. ply under a constant longitudinal strain .....	45
Figure 15. Effect of fiber volume fraction on the adiabatic temperature change in a 0-deg. carbon epoxy lamina under constant longitudinal stress or strain .....	47
Figure 16. Predicted SPATE patterns in two center-notched carbon epoxy laminates ...	49
Figure 17. SPATE thermograph of a (0,90,45,-45) <sub>s</sub> carbon epoxy laminate with the resin-rich surface layer removed .....	52
Figure 18. Predicted SPATE patterns in a center-notched (0,90,45,-45) <sub>s</sub> carbon epoxy laminate with varied contributions of the constituents in the surface ply .....	54
Figure 19. Predicted SPATE patterns in a center-notched (0,90,45,-45) <sub>s</sub> carbon epoxy laminate with varied ply influences .....	55
Figure 20. Stress vs. life data for test specimens .....	61
Figure 21. Stiffness change in AS4/3501-6 specimens .....	65

Figure 22. Stiffness change in AS4/1808 specimens .....	66
Figure 23. Radiograph of a center-notched, AS4/3501-6, (0,45,90,-45) <sub>s4</sub> specimen after one high-level load cycle .....	72
Figure 24. Radiographs of center-notched, AS4/3501-6, (0,45,90,-45) <sub>s4</sub> specimens during high-load fatigue .....	74
Figure 25. Edge radiographs of center-notched, AS4/3501-6, (0,45,90,-45) <sub>s4</sub> specimens during high-load fatigue .....	75
Figure 26. Schematic of incremental, step-wise surface ply fractures influenced by matrix cracks in adjacent plies .....	76
Figure 27. Radiographs of center-notched, AS4/3501-6, (0,45,90,-45) <sub>s4</sub> specimens during low-load fatigue .....	78
Figure 28. Edge radiographs of center-notched, AS4/3501-6, (0,45,90,-45) <sub>s4</sub> specimens during low-load fatigue .....	79
Figure 29. Radiographs of a double-edge-notched, AS4/3501-6, (0,45,90,-45) <sub>s4</sub> specimen near high-load fatigue failure .....	82
Figure 30. Radiographs of a double-edge-notched, AS4/3501-6, (0,45,90,-45) <sub>s4</sub> specimen near low-load fatigue failure .....	83
Figure 31. Radiographs of center-notched, AS4/3501-6, (0,45,0,-45) <sub>s4</sub> specimens during high-load fatigue .....	86
Figure 32. Edge radiographs of center-notched, AS4/3501-6, (0,45,0,-45) <sub>s4</sub> specimens during high-load fatigue .....	87
Figure 33. Radiographs of a double-edge-notched, AS4/3501-6, (0,45,0,-45) <sub>s4</sub> specimen near high-load fatigue failure .....	90
Figure 34. Radiographs of center-notched, AS4/1808, (0,45,90,-45) <sub>s4</sub> specimens during high-load fatigue .....	93
Figure 35. Edge radiographs of center-notched, AS4/1808, (0,45,90,-45) <sub>s4</sub> specimens during high-load fatigue .....	94
Figure 36. A deplied, center-notched, AS4/1808, (0,45,90,-45) <sub>s4</sub> specimen at an early stage of damage development under the high load level .....	95
Figure 37. A deplied, center-notched, AS4/1808, (0,45,90,-45) <sub>s4</sub> specimen at a late stage of damage development under the high load level .....	97
Figure 38. Radiographs of center-notched, AS4/1808, (0,45,90,-45) <sub>s4</sub> specimens during low-load fatigue .....	100
Figure 39. Edge radiographs of center-notched, AS4/1808, (0,45,90,-45) <sub>s4</sub> specimens during low-load fatigue .....	101
Figure 40. A deplied, center-notched, AS4/1808, (0,45,90,-45) <sub>s4</sub> specimen at an early stage of damage development under the low load level .....	102

Figure 41. A deplied, center-notched, AS4/1808, (0,45,90,-45) <sub>s4</sub> specimen at a late stage of damage development under the low load level .....	105
Figure 42. Radiographs of double-edge-notched, AS4/1808, (0,45,90,-45) <sub>s4</sub> specimens during high-load fatigue .....	108
Figure 43. Edge radiographs of double-edge-notched, AS4/1808, (0,45,90,-45) <sub>s4</sub> specimens during high-load fatigue .....	109
Figure 44. Radiographs of double-edge-notched, AS4/1808, (0,45,90,-45) <sub>s4</sub> specimens after fatigue failure .....	110
Figure 45. Radiographs of a double-edge-notched, AS4/1808, (0,45,90,-45) <sub>s4</sub> specimen near low-load fatigue failure .....	112
Figure 46. Radiographs of center-notched, AS4/1808, (0,45,0,-45) <sub>s4</sub> specimens during high-load fatigue .....	114
Figure 47. Edge radiographs of center-notched, AS4/1808, (0,45,0,-45) <sub>s4</sub> specimens during high-load fatigue .....	115
Figure 48. A deplied, center-notched, AS4/1808, (0,45,0,-45) <sub>s4</sub> specimen at an early stage of damage development under the high load level .....	116
Figure 49. A deplied, center-notched, AS4/1808, (0,45,0,-45) <sub>s4</sub> specimen at a middle stage of damage development under the high load level .....	118
Figure 50. A deplied, center-notched, AS4/1808, (0,45,0,-45) <sub>s4</sub> specimen at a late stage of damage development under the high load level .....	119
Figure 51. Radiographs of center-notched, AS4/1808, (0,45,0,-45) <sub>s4</sub> specimens during low-load fatigue .....	122
Figure 52. Edge radiographs of center-notched, AS4/1808, (0,45,0,-45) <sub>s4</sub> specimens during low-load fatigue .....	123
Figure 53. A deplied, center-notched, AS4/1808, (0,45,0,-45) <sub>s4</sub> specimen at an early stage of damage development under the low load level .....	124
Figure 54. A deplied, center-notched, AS4/1808, (0,45,0,-45) <sub>s4</sub> specimen at a middle stage of damage development under the low load level .....	127
Figure 55. A deplied, center-notched, AS4/1808, (0,45,0,-45) <sub>s4</sub> specimen at a late stage of damage development under the low load level .....	129
Figure 56. Radiographs of a double-edge-notched, AS4/1808, (0,45,0,-45) <sub>s4</sub> specimen near high-load fatigue failure .....	132
Figure 57. SPATE thermographs of matrix crack development .....	139
Figure 58. SPATE thermograph of a 0-deg. surface ply fracture .....	142
Figure 59. SPATE thermographs of four center-notched, AS4/1808, (0,45,90,-45) <sub>s4</sub> specimens during high-load fatigue .....	144

Figure 60. SPATE signal along Section B-B' in three center-notched, AS4/1808, (0,45,90,-45) <sub>s4</sub> specimens during high-load fatigue .....	146
Figure 61. SPATE thermographs of four center-notched, AS4/1808, (0,45,0,-45) <sub>s4</sub> specimens during high-load fatigue .....	149
Figure 62. SPATE signal along Section C-C' in three center-notched, AS4/1808, (0,45,0,-45) <sub>s4</sub> specimens during high-load fatigue .....	151
Figure 63. SPATE thermographs of four center-notched, AS4/3501-6, (0,45,0,-45) <sub>s4</sub> specimens during high-load fatigue .....	154
Figure 64. SPATE thermographs of three center-notched, AS4/1808, (0,45,90,-45) <sub>s4</sub> specimens during low-load fatigue .....	158
Figure 65. SPATE thermographs of AS4/3501-6, (0,45,0,-45) <sub>s4</sub> , DEN specimens during high-load fatigue .....	160
Figure 66. SPATE thermographs of four double-edge-notched, AS4/1808, (0,45,90,-45) <sub>s4</sub> specimens during high-load fatigue .....	163
Figure 67. Normalized residual strength of center-notched, AS4/1808, (0,45,90,-45) <sub>s4</sub> specimens during high-load fatigue .....	168
Figure 68. Normalized residual strength of center-notched, AS4/1808, (0,45,90,-45) <sub>s4</sub> specimens during low-load fatigue .....	169
Figure 69. Normalized residual strength of double-edge-notched, AS4/1808, (0,45,90,-45) <sub>s4</sub> specimens during high-load fatigue .....	173
Figure 70. Normalized residual strength of center-notched, AS4/1808, (0,45,0,-45) <sub>s4</sub> specimens during high-load fatigue .....	175
Figure 71. Normalized residual strength of center-notched, AS4/1808, (0,45,0,-45) <sub>s4</sub> specimens during low-load fatigue .....	176
Figure 72. Schematic illustration of 0-deg. ply fracture and delamination in AS4/1808, (0,45,0,-45) <sub>s4</sub> specimens after residual strength tests .....	178
Figure 73. Normalized residual strength of center-notched, AS4/3501-6, (0,45,0,-45) <sub>s4</sub> specimens during high-load fatigue .....	181
Figure 74. Flow diagram of the critical element approach. ....	190
Figure 75. Calibration curves for the ellipticity ratio as a function of stiffness reduction across the hole. ....	192
Figure 76. Stiffness reduction of off-axis plies for two loading levels. ....	194
Figure 77. Illustration of remaining strength concept. ....	195
Figure 78. Summation equation used for the calculation of remaining strength. ....	197
Figure 79. Predicted and observed residual strength for a quasi-isotropic laminate. ....	198
Figure 80. Predicted and observed residual strength for a (0,45,0,-45) <sub>s</sub> laminate. ....	199

## List of Tables

Table 1. Thermoelastic properties for carbon epoxy .....	48
Table 2. Force equilibrium assessment in the micromechanical model .....	51
Table 3. Monotonic strength of virgin specimens .....	58
Table 4. Cyclic load levels ( $R = -1$ ) for fatigue tests .....	62
Table 5. Tensile and compressive stiffnesses of virgin specimens .....	64
Table 6. Actual and expected normalized tensile strengths of center-notched, AS4/1808 specimens during high-load fatigue .....	148
Table 7. Normalized residual stiffness and strength of center-notched, AS4/1808, (0,45,90,-45) <sub>s4</sub> specimens .....	167
Table 8. Averaged, normalized, residual strength data .....	170
Table 9. Normalized residual stiffness and strength of double-edge-notched, AS4/1808, (0,45,90,-45) <sub>s4</sub> specimens .....	172
Table 10. Normalized residual stiffness and strength of center-notched, AS4/1808, (0,45,0,-45) <sub>s4</sub> specimens .....	174
Table 11. Normalized residual stiffness and strength of center-notched, AS4/3501-6, (0,45,0,-45) <sub>s4</sub> specimens .....	180
Table 12. Calibration values for critical element model. ....	201



# I

## Executive Summary

### 1.1 *Summary*

This is the final report of research results generated under grant number 85.0087 from the Air Force Office of Scientific Research, monitored by Lt. Col. George Haritos. This report includes some work from the total effort, but focuses on the results completed in the last year of the program (September 1987 to August 1988). Other results can be found in the literature and in the periodic reports submitted to the AFOSR during the contract period. A list of publications in which those results appear follows.

1. Bakis, C.E. and Reifsnider, K.L., "Nondestructive Evaluation of Fiber Composite Laminates by Thermoelastic Emission," Review of Progress in Quantitative Nondestructive Evaluation, Vol. 7B, D.O. Thompson and D.E. Chirrenti, Eds., Plenum Publishing Corp., 1988

2. Bakis, C.E., Yih, H.R., Stinchcomb, W.W., and Reifsnider, K.L., "Damage Initiation and Growth in Notched Laminates Under Reversed Cyclic Loading," in "Fatigue and Fracture of Composite Materials," ASTM STP, American Society for Testing and Materials (Cinn., OH, May 1987), in press.
3. Reifsnider, K.L. and Stinchcomb, W.W., "Critical Element Concepts for Composite Life Prediction," Proc. ASME Winter Annual Meeting, Anaheim, CA, 7-13 December 1986.
4. Reifsnider, K.L., "A Hybrid Approach to Composite Component Life Prediction," Proc. Intl. Conf. on Composite Materials and Structures, 10-13 June, 1986, Beijing, China, Technomic (1986) pp. 688-697.
5. Reifsnider, K.L., and Bakis, C.E., "Modeling Damage Growth in Notched Composite Laminates," Proc. Japan-U.S. Symposium on Composite Materials, 22-24 June, 1986, Tokyo, Japan.
6. Reifsnider, K.L., "Critical Element Concepts for Residual Strength and Life Prediction," Proc. Am. Soc. Composites, First Tech. Conf., 7-9 Oct, 1986, Dayton, OH, Technomic (1986) pp. 387-403.
7. Reifsnider, K.L., "A Philosophy for Prediction the Remaining Life of Materials that have Inhomogeneous Response," Submitted to J. Composites Technology and Research.
8. Bakis, C.E., Simonds, R.A., and Stinchcomb, W.W., "A Test Method to Measure the Response of Composite Materials Under Reversed Cyclic Loads," Symposium on Test Methods and Design Allowables for Fiber Composites, ASTM, 3-4 Nov. 1986, Phoenix, AZ. (STP in press)

9. Reifsnider, K.L., "Life Prediction Analysis: Directions and Divagations," plenary paper, ICCM VI / ECCM 2, Imperial College, London, U.K., 20-24 July, 1987, Elsevier Applied Science, Vol. 4, (1987) pp.4.1-4.39.
10. Reifsnider, K.L., "Damage and Damage Analysis," in *Fatigue of Composite Materials*, K.L. Reifsnider, Editor, Elsevier, in press.
11. Simonds, R.A., Bakis, C.E., and Stinchcomb, W.W., "Effects of Matrix Toughness on Fatigue Response of Graphite Fiber Composite laminates," in *"Fatigue and Fracture of Composite Materials,"* ASTM STP, American Society for Testing and Materials (Cinn., OH, May 1987), in press.
12. Bakis, C.E., Simonds, R.A., Vick, L., and Stinchcomb, W.W., "Matrix Toughness, Long Term Behavior and Damage Tolerance of Graphite Fiber Reinforced Composite Materials," in *Composite Materials: Testing and Design, 9th Symp.*, ASTM STP, Sparks, NV, April, 1988, in press.

In addition, several publications are in press. Appendix A contains a copy of a paper which was presented for an ASTM conference, which should be in print shortly, and Appendix B contains a copy of a dissertation which was developed in part with support from the subject contract effort.

The current report attempts to identify the methods used to obtain results, to outline the nature of the physical data generated by the experimental program, to summarize salient findings, and to present a description of how the experimental results were used in a modeling effort to describe remaining strength and life under long-term loading.

Among the major thrusts and results of the program are the following:

- The program developed the most extensive data base available in the literature to define the initiation and development of damage in the region of notches in composite laminates under fully reversed cyclic loading.
- That data base includes data from two geometries (*edge notched and center notched*), two stacking sequences (quasi-isotropic and quasi-orthotropic ), and two contrasting material systems (AS4/3501-6 and AS4/1808). Hence the effect of geometry, laminate type, and material type was extensively investigated.
- Residual strength variations and stiffness changes were recorded during testing. Extensive nondestructive testing was conducted during testing to monitor damage initiation and growth.
- Deply methods and scanning electron microscope examinations were used to examine the internal details of damage development.
- The first dynamic thermoelastic stress analysis patterns of damage development were recorded, analyzed, and interpreted.
- A performance simulation model called MRLife was constructed to represent, mechanistically, the damage development process and to predict the remaining strength and life of notched laminates under arbitrary loading and long-term exposure to mechanical and thermal loads.

The salient findings of the program include the following.

- Under uniaxial cyclic loading, two rather distinctive regions of damage develop; one of them contributes primarily to the redistribution of global stress resulting in an increase in remaining tensile strength, while the other contributes primarily to the reduction of remaining tensile and compressive strength.

- The difference between center notched and edge notched results was noticeable but not fundamental, while the differences in the results from different stacking sequences and different material systems were large and fundamental in some cases.
- Quasi-static "properties" such as "toughness" do not have the same interpretation under fatigue loading as they do under static conditions. "Tougher" materials under static conditions may be more likely to develop large dominant single cracks under cyclic loading which can make them "brittle" in that sense and inferior to statically "less tough" materials for fatigue applications. That result was strongly evident in the results of the present program and was corroborated by results from a related research program.
- The classical description of thermoelastic emission in the literature does not correctly describe the emission from the surface of composite laminates. The micromechanical description developed during the course of the present program does correctly describe those emissions, a major fundamental advance in our understanding of that phenomenon and in our ability to use it for dynamic stress analysis.
- The critical element modeling concept developed by the Materials Response Group at Virginia Tech has been successfully applied to the description of the remaining strength and life of composite laminates under long-term cyclic loading. This performance simulation code is mechanistic, allowing it to be used to assess the influence of micro-details and macro-geometry on the subsequent performance of the laminates, as well as to "design" material systems. The resulting MRLife code is unique, and represents a new direction in material modeling.

The details of the program results follow.

## **II**

# **Investigative Approach**

## **2.1 Experiments**

### **2.1.1 Mechanical Testing**

Mechanical tests were carried out on servo controlled, hydraulically actuated, MTS load frames equipped with hydraulically actuated wedge grips. Hydraulic wedge grips are essential for the through-zero loading of the flat coupon-type specimens chosen for the present study for reasons of practicality and economy. Monotonic strength tests were carried out in the stroke control mode of operation with a displacement rate of 0.06 in./min. Stroke control was selected to avoid crushing the specimen after a compressive strength measurement. Monotonic tension and compression tests were carried out on virgin and fatigue-damaged specimens to characterize the strength components of the laminates throughout the lifetime. Residual strengths were measured at the "early," "middle," and "late" stages of fatigue

damage development (to be defined in the characterization of basic material properties). Most strength tests were carried out in triplicate to evaluate the amount of scatter in the data and to establish some statistical significance to the results.

Fatigue tests were carried out with a constant amplitude, fully-reversed ( $R=-1$ ), sinusoidal loading regime in load control. Reversed cyclic loads are considered by many to be the most detrimental to fiber composites because of the activation of both tensile and compressive damage modes. Depending on the relative competition of these damage modes, either tensile or compressive failure modes ensue. Hence, the fully-reversed loading regime provides a good opportunity to observe different damage mechanisms in composite laminates. To obtain static stiffness data or document damage development during the first 100 cycles of a fatigue test, reduced load cycle frequencies were used (1 Hz until 10 cycles, 5 Hz until 100 cycles, and 10 Hz thereafter). No significant differences in material response were observed when the present technique was compared to truly constant 10 Hz tests.

External support along a specimen's gage length prevents global buckling and, to a lesser extent, surface delamination growth, resulting in longer fatigue lifetimes and, in some cases, altered failure modes [66]. The present test methodology, detailed in Ref. [67], is founded on the tenets that damage should be allowed to develop in an unconstrained manner in the gage length, much the same as damage grows in engineering structures, and that competing failure modes may not be manifested under the influence of external constraint devices. The gripping arrangement is shown schematically in Figure 1. During testing, the specimens were exposed to the ambient, air-conditioned, laboratory environment.

Two fully-reversed cyclic load levels were chosen such that the load-dependent fatigue response could be observed. The "high" load, corresponding to a fatigue life of 1K to 30K cycles, and the "low" load, corresponding to a fatigue life of 300K to 3M cycles, bracketed the range of fatigue lives over which it was practical to obtain data in the laboratory. Higher loads often resulted in fatigue failures before the load span on the test frame was accurately set,

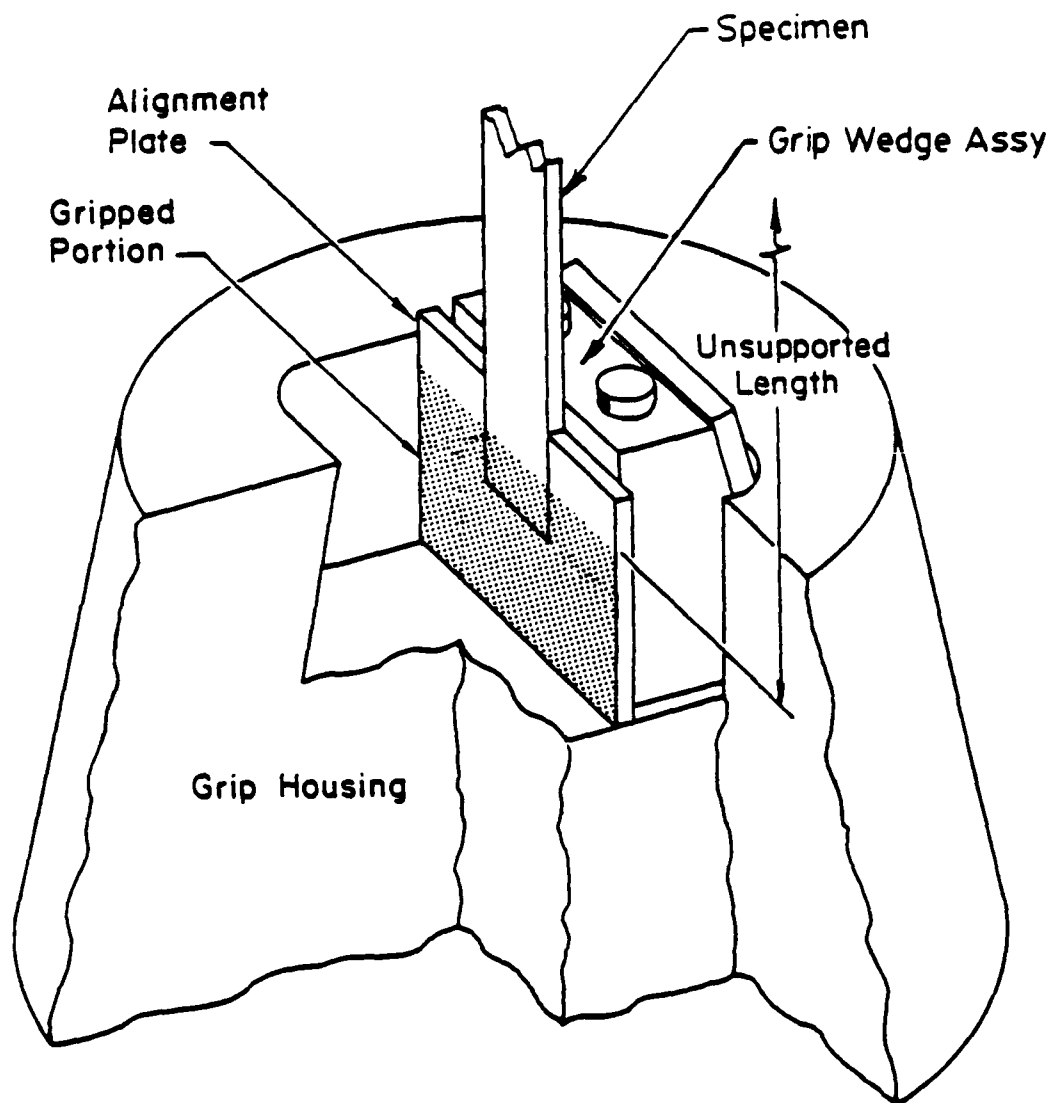


Figure 1. Test specimen gripping arrangement



and lower loads resulted in no different fatigue mechanisms and, in many cases, infinite fatigue lives.

### 2.1.2 Test Specimens

Two carbon epoxy material systems were chosen to provide contrasting material responses under cyclic loading. The Hercules AS4/3501-6 material is representative of "first generation" CFRP materials because of the relatively brittle nature of the 3501 epoxy resin. A newer CFRP formulation, American Cyanamid's AS4/1808, has a relatively ductile epoxy matrix, and is therefore considered a "second generation" or "toughened epoxy" composite [68]. The relatively ductile Cycom 1808 epoxy resin is supposed to exhibit less cracking and delamination prior to laminate failure than the relatively brittle 3501-6 resin [69]. Much of the data in the present investigation was produced with the AS4/1808 center-notched specimens. However, since the objective of the present work is to identify different fatigue responses and their causes, the other material system and notch geometry was included for generality and to provide contrasts.

Ply orientation and stacking sequence have been shown to be important in the damage development, residual strength, and failure mode of notched laminates [4,10,70]. The two layups chosen for the present investigation —  $(0/45/90/-45)_{s4}$  and  $(0/45/0/-45)_{s4}$  — are representative of practical structural material configurations. (The 0-deg. direction is defined to be parallel to the loading axis. Positive ply orientations are measured clockwise looking at the "front" side of the specimen.) The first layup has quasi-isotropic planar elastic properties, and the second has orthotropic properties. The differing amounts of 90- and 0-deg. plies in the two configurations provided contrasting material responses to fatigue damage development. For brevity, the  $(0,45,90,-45)_{s4}$  laminate was denoted the "A" laminate, and the  $(0,45,0,-45)_{s4}$  laminate was denoted the "B" laminate.

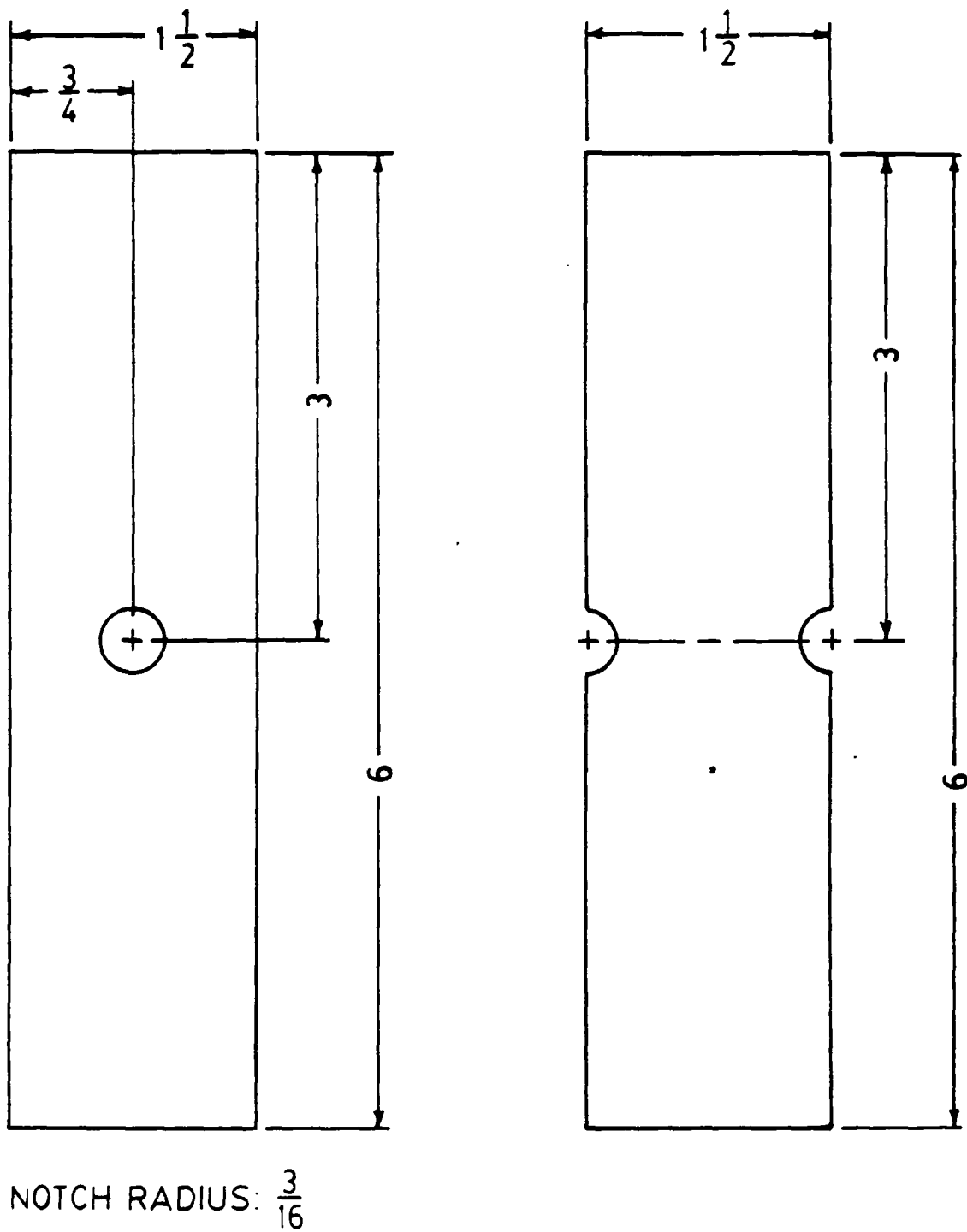


Figure 2. Test specimen configurations

After nondestructively inspecting the laminated plates with an ultrasonic C-scan unit (as described later), the specimens were machined with diamond-coated abrasive circular wheels and core-drills. The test specimen configurations are illustrated in Figure 2. The width and notch radius were selected such that the radius to half-width diameter was equal to 0.25, facilitating the use of closed-form solutions for strains in an infinite plate with an elliptical opening to approximate the strains in the coupons. The length of the coupons was selected according to the test procedure detailed in [67]. Briefly, the procedure specifies that an unsupported length that provides the maximum compressive strength of undamaged material is the length to be used in the fatigue tests. Typically, there is an upper limit on such a length above which compressive strength is reduced due to global buckling effects. Below the buckling length, compressive strength is nearly independent of unsupported length. The results of the compression tests with various unsupported lengths indicated that 2.5-in. would be an appropriate unsupported length for the fatigue tests [71].

The primary notch configuration is a center hole, chosen because of the availability of closed form solutions for the approximate stresses and strains in the test specimens and because it is fairly representative of typical cutouts in structural applications. For comparison, some tests were performed with double semi-circular edge notches, but no closed-form stress solution exists for this configuration (to the author's knowledge). An advantage of the edge-notched configuration over the center-notched configuration is that all damage growth emanates from the notches. In the center-notched specimens, damage growing inward from the straight edges of the specimen late in the fatigue life frequently complicates the analysis of damage growth near the notch. However, the interaction of damage zones emanating from the opposing notches is a problem with the edge notched configuration. For brevity, the center-notched specimens were denoted "CN", and the double-edge-notched specimens were denoted "DEN".

Specimens were labelled according to their matrix type, stacking sequence, panel identification number, specimen identification number within the panel, and notch type. For ex-

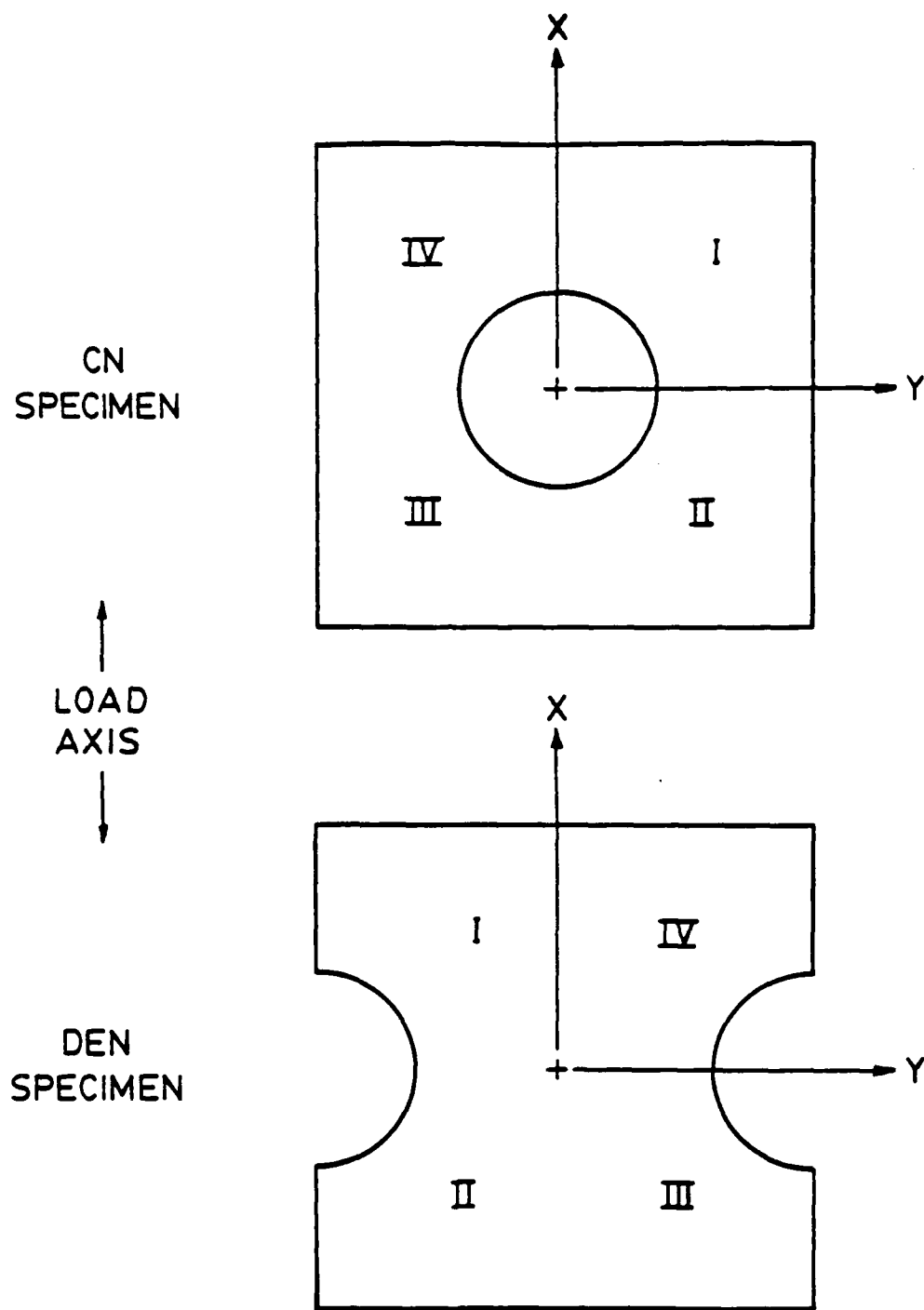


Figure 3. Specimen axis and quadrant notations

ample, "3501-A-1-2-CN" designates the AS4/3501-6 material system, the quasi-isotropic stacking sequence, panel 1, specimen 2, center notch. Another possibility is "1808-B-1-2-DEN", signifying the AS4/1808 material system, the orthotropic stacking sequence, panel 1, specimen 2, double edge notch. Axis and quadrant notations used in the description of damage are illustrated for the two specimen geometries in Figure 3. The seemingly backward quadrant notation for the DEN specimen is intended to facilitate comparisons with CN specimens. (For example, note that quadrant I in the CN case is located at the same position relative to the notch as quadrant I in the DEN case.) Quadrant numbers become reversed left-to-right if the back side of the specimen is being viewed. The sequential numbering of plies and their interfaces progresses from the front to the back of the specimens.

### **2.1.3 Stiffness Measurement**

Stiffness change has been shown to be an effective nondestructive means of monitoring damage growth in carbon epoxy laminates [72-74]. As damage initiates and grows in the material, the stiffness decreases due to internal load redistributions.

In the present investigation, effective tensile and compressive stiffnesses were measured with a 1-in. gage-length extensometer located on the geometric center of the specimens. The knife-edges of the extensometer were positioned firmly on V-notched aluminum tabs bonded to the specimen with silicone adhesive, as detailed in [75]. The dimensions of these tabs were 5/16-in. long (along the V-notch), 5/32-in. wide, and 1/16-in. thick. Different sized tabs will result in different effective stiffness measurements due to the strain gradient near the notch. Dynamic stiffness was continuously monitored during fatigue tests, and static stiffness was periodically measured when a change in dynamic stiffness indicated the need to do so.

Previous investigations revealed that a characteristic stiffness response exists for a given material, stacking sequence, notch configuration and load level [75,76]. That is, the fraction of life consumed in a particular experiment can be roughly estimated by monitoring the specimen's stiffness. Given the typically large amount of scatter in fatigue lifetimes of composite laminates (as much as one order of magnitude), the ability to make such estimates helps establish the actual "age" of the specimen prior to a destructive test, such as deply (described later) or residual strength measurement. To reduce the effect of bending on stiffness measurements in DEN specimens, effective stiffnesses in some tests were computed by averaging strains recorded with extensometers attached to the front and back surfaces.

#### **2.1.4 Ultrasonic C-Scan**

Prior to machining, the laminated panels were nondestructively inspected for irregularities using a Sperry/Automation laboratory C-scanning device. The Panametrics transducer, operated in the pulse-echo mode, had a nominal frequency of 15 MHz, a tip diameter of 0.25 in., and a focal length of 1.0 in. During C-scanning, ultrasonic sound waves are passed through the material by a sweeping transducer such that a full-field map of transmitted signal amplitude is obtained. Nonuniformities in the material, such as voids, cracks, or delaminations, attenuate the transmitted sound waves in proportion to the severity of those nonuniformities. Three separate scans of each plate were carried out with progressively higher gate thresholds to obtain three contours of different attenuation. The three thresholds used most often were 80, 50 and 10 percent of the maximum signal on the plate. A plate with substantial regions of less than 80 percent signal strength was rejected for the test program.

### 2.1.5 X-Ray Radiography

The primary nondestructive technique for evaluating damage mechanisms throughout the fatigue life was liquid-penetrant-enhanced X-ray radiography. The penetrant — zinc iodide in a carrier of water, ethyl alcohol, and Kodak Photo-Flo (wetting agent) — highlighted damaged regions of the laminate by blocking the transmission of X-rays [76-78]. Only those areas of damage with connectivity to the surface of the specimen were highlighted. Once the penetrant was applied to the surface of the specimen, it was allowed to soak in for approximately 15 minutes while the specimen was cycled at 1 Hz ( $R=-1$ ) with a maximum load of about 25 percent of the maximum fatigue load. If the specimen had no prior application of penetrant, the penetrant was allowed to soak in for an additional 12-hour period with no applied load. If penetrant was previously introduced to the specimen, the specimen could be radiographed without the additional 12-hour soak-in period. The specimens were placed directly on top of the Kodak Industrex SR5 (single emulsion, fine grain) film inside a Hewlett Packard 43805N Faxitron Series X-ray cabinet. With the aid of a 3-in.-high adjustable tilt platform, the specimens were radiographed three times with the X-ray beam impinging at angles of 0, 15, and 90 degrees to the specimens's plane. In this manner, some three-dimensional information on the damage distribution could be obtained. The distance between the X-ray tube and the specimen was the maximum possible — approximately 45 in. without the platform. Shorter distances resulted in blurred images of the specimen's edges, particularly in the 90-deg. view. Exposure settings were 3 minutes at 43 kVp (approximately 2.5 mA) for the 0- and 15-deg. radiographs, and 4 minutes at 85 kVp (approximately 2.5 mA) for the 90-deg. radiographs.

Areas permeated with zinc iodide appear as relatively dark areas in positive prints of radiograph negatives. In the 0-deg. view, matrix cracks parallel to the fibers are fine lines, while delaminations are broad, dark areas, (the darkness depends on the thickness of the layer of zinc iodide). Large, dark, rectangular areas above and below the notch in some radiographs are the aluminum tabs used to attach the extensometer to the specimen. In the

90-deg. view, delaminations are lines extending along the length of the specimen. Matrix cracks are visible only in the 90-deg. plies in the 90-deg. view since the other ply orientations are oblique to the X-ray beam.

### **2.1.6 Laminate Deply**

Laminate deply is a destructive damage evaluation technique developed by Freeman [79] that enables the "destacking" of a laminate by pyrolyzing the resin-rich zone between plies of different orientation. The pyrolyzation was carried out at 785° F for two hours in an argon atmosphere (in order to prevent oxidation). A liquid penetrating marking agent (eg., a gold chloride solution) applied before pyrolyzation enabled the detection of regions of the laminate that contained matrix damage. It was found during the course of the present investigation that zinc iodide residue from previous X-ray radiographs provided sufficient contrast to observe delaminated areas. Fiber damage on the surface of each ply was detected by optical and electron microscopy. Tracings of optically visible damage patterns at each interface were used to map damage patterns at various times in the fatigue lifetime. Compared to X-ray radiography, the deply technique facilitated a higher resolution of fiber damage modes and a more accurate spatial resolution of damage (especially through the thickness). On the other hand, it was generally difficult to identify any evidence of matrix cracks on the deplyed laminae.

Specimens were deplyed at the same early, middle, and late stages of fatigue lifetime chosen for residual strength measurements. Only AS4/1808 specimens were successfully deplyed. Several attempts to deply AS4/3501-6 specimens were unsuccessful due to the excessive amount of matrix residue that prevented separation of the plies without causing additional fiber damage.



## **2.1.7 Adiabatic Thermography**

The adiabatic thermoelastic effect in elastic solids is the small, reversible temperature change resulting from the dilatational deformation of matter. If cyclic extensional strains are applied at a rate that is high enough to preclude heat transfer between elements of the material and their surroundings (i.e., ensuring adiabatic conditions), the temperature of the material will vary with the same wave form and frequency as the applied load. Pointwise temperature changes can then be related to stress and strain on the surface with the theory of thermoelasticity. This technique is not to be confused with dissipative thermography, where the quasi-steady-state temperature measurements reflect the heat generated in the material due to hysteretic effects such as viscous damping or friction near defects. Stress patterns measured via adiabatic thermography during the fatigue process provide an essential "bridge" between damage data and residual strength data by allowing the investigator to observe the global stress redistributions resulting from damage growth in notched laminates. A new, micromechanical model of the adiabatic thermoelasticity of laminated fiber composites developed as part of this investigation will be presented in the analysis section of this chapter. Since adiabatic thermography is a new experimental technique and little information on the application of the technique to composite materials is available in the literature, the experimental apparatus and procedure used in the present investigation will be presented next. Aspects of the procedure not detailed in the SPATE operator's manual will be emphasized. The manual should be consulted for routine procedures.

### **2.1.7.1 Thermographic Apparatus**

Modern infrared radiometers have the sensitivity and response time required to measure temperature changes on the surface of a dynamically-stressed material. The radiometer used in the present investigation is marketed by Ometron Inc. under the trade name SPATE (Stress

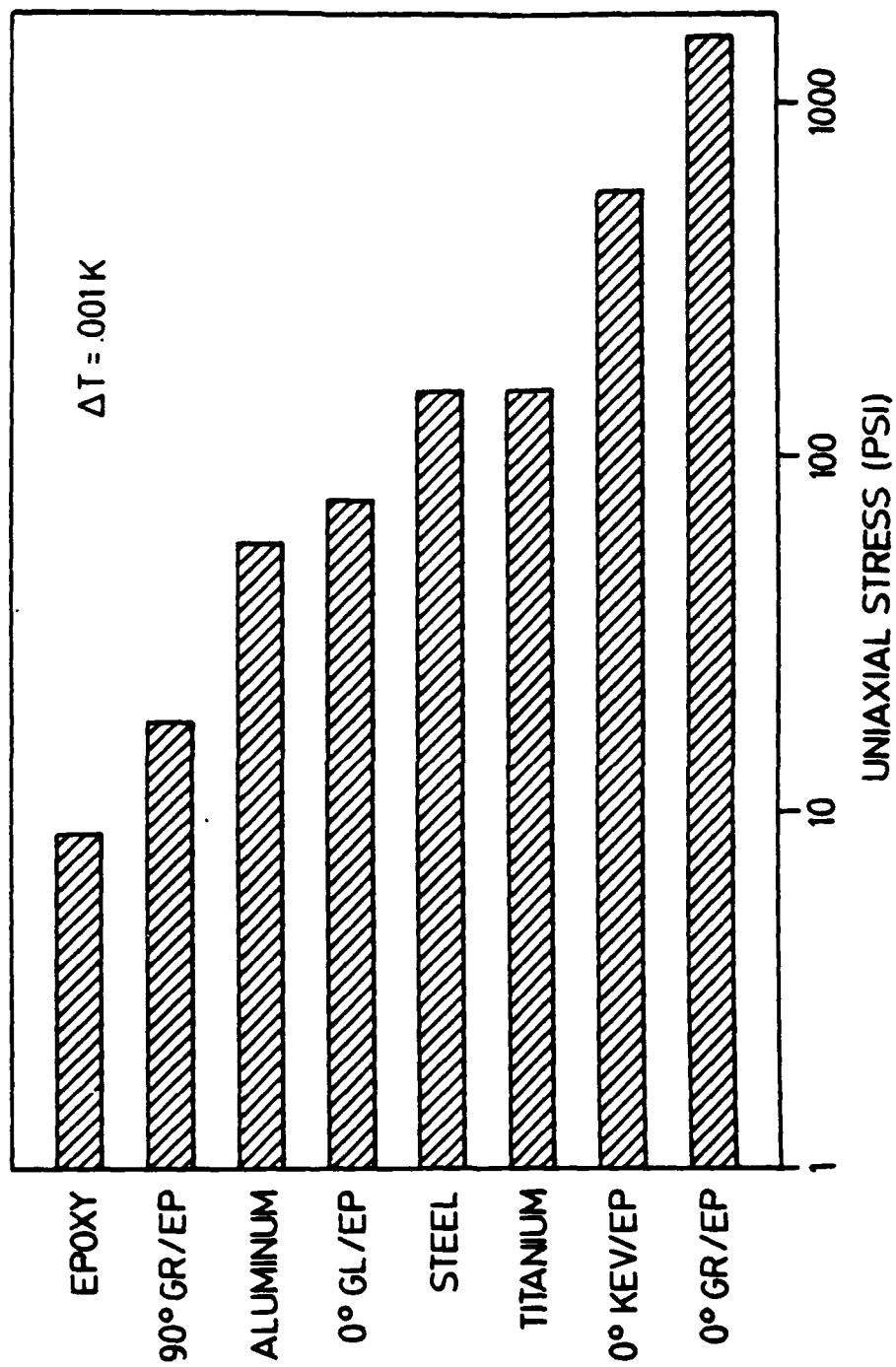


Figure 4. Theoretical stress sensitivity of SPATE with various materials

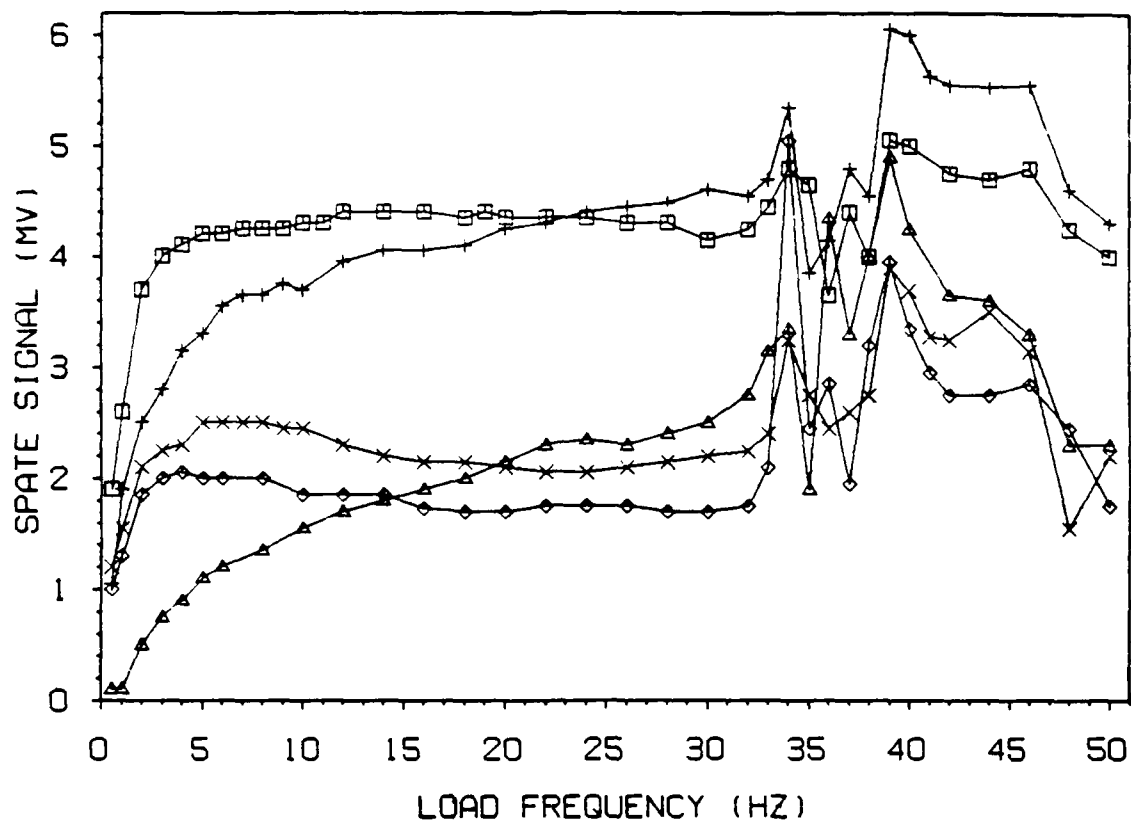
Pattern Analysis by Thermal Emission), specifically for full-field stress measurements. The SPATE apparatus has been used previously with homogenous materials and, more recently, nonhomogeneous materials, to quickly evaluate stress and strain fields in a non-contact manner [80]. The SPATE 8000 consists of a scanning infrared photon detector coupled to a correlator (lock-in amplifier) and computer. The temperature sensitivity of the system is 0.002 °F. The uniaxial stresses corresponding to a temperature change of 0.002 °F in several materials are illustrated in Figure 4. The functions of the computer and correlator are to control the camera's scan activities and to condition the measured photon emittance such that the sinusoidal temperature variation occurring at the same frequency as the sinusoidal load can be determined. The correlator rejects a temperature variation having no sinusoidal content at the test frequency, such as that caused by dissipative heating. The camera scans the test specimen pointwise in a raster-like manner, enabling the computer to store the recorded signal at each point as a digital quantity. The smallest area that can be sampled at each point in the scan area is a 0.02-in.-diameter circle. If the raster scan takes a long time to complete (up to two hours is common), it is necessary to apply a cyclic load amplitude that is low enough to inhibit damage development during the scan. Two factors influencing the scan time are the scan resolution (the number of data points to be recorded over a given area) and the sample time (the amount of time spent acquiring data at a single position on the specimen). In situations where the measured signal is small, electronic averaging must be applied over a selectable time period associated with a filter "time constant" to reduce high frequency noise. Averaging is necessary since only a single value of temperature change is recorded at each point. As the time constant increases, the amount of time spent sampling data at a particular point on the specimen must also increase. Once a scan has been completed, the digital information may be stored on a magnetic disk for future examination. A video monitor enables the operator to observe the results of the scan as each point in the scan is sequentially displayed on a color-coded contour map of temperature change.

A variety of material systems, including carbon epoxy, carbon PEEK, aramid epoxy, boron aluminum, and glass epoxy, to name a few, have been studied with the SPATE apparatus. Of these, fiber-dominated carbon epoxy and aramid epoxy are the most difficult to examine because of their relatively low temperature change during cyclic loading (Figure 4). A detailed review of the procedure for obtaining high quality, repeatable data with fiber reinforced composites follows.

#### **2.1.7.2 Mechanical Excitation**

Any source of periodic mechanical excitation can be used with the SPATE 8000 apparatus, although the high cyclic load amplitudes required to obtain a good temperature signal-to-noise ratio with fiber-dominated carbon epoxy laminates are most readily obtained via a servo-hydraulic load frame equipped with a function generator. Because the SPATE lock-in amplifier output is proportional to the sinewave content of the temperature change, it is essential to maintain a constant load form for quantitative experiments. Unless specifics of the test dictate otherwise, one should maintain a load that does not cause damage growth during the scan. It is also important to maintain loads within the linear-elastic range of the material if stresses or strains are to be computed with the linear theory reviewed in the analysis section of this chapter; otherwise, modifications to the theory must be made to account for the inelastic deformation. In most instances, a sinusoidal load with a maximum of 30-40% of the specimen's tensile strength is appropriate.

To ensure adiabatic deformations and the validity of the theory, it is necessary to increase the load frequency until no further increase in the SPATE signal is realized. Frequency-dependent thermal emission was observed with several unnotched AS4/3502 carbon epoxy laminates (Figure 5), but this phenomenon may be peculiar to the specific laminates interrogated. For example, Potter [81] reported a constant thermal emission for frequencies above



LEGEND: □ ALUMINUM, 4235 PSI  
 ▲ (0)8T GR/EP, 45090 PSI  
 ◇ (+45/-45)2S GR/EP, 9950 PSI  
 + (90/0)2S GR/EP, 19510 PSI  
 × (0/90)2S GR/EP, 20510 PSI

Figure 5. SPATE signal in AS4/3502 laminates as a function of loading frequency

5 Hz with XAS/914 carbon epoxy. It is therefore desirable to maintain a constant loading frequency in quantitative comparisons of data.

In the present investigation, cyclic loadings for the SPATE scans were all carried out with a frequency of 5 Hz. For  $(0,45,90,-45)_{s4}$  laminates, the maximum and minimum loads were 4100 and 100 lb., respectively. For  $(0,45,0,-45)_{s4}$  laminates, the maximum and minimum loads were 5100 and 100 lb., respectively. These load amplitudes provided correlator signals between +10 and -10 mV.

#### **2.1.7.3 Specimen Preparation**

A flat-finish paint was applied to the specimen in order to obtain a high and uniform surface emissivity in the infrared spectrum and to reduce the possibility of reflected heat sources being modulated at the test frequency. Krylon ultra-flat black spray paint applied in two thin coats, for example, serves this purpose well [80], and is easily removed with acetone. Where possible, it is wise to avoid the use of paint since investigators have observed an attenuation of the photon emittance due to the paint's thickness. This effect is especially evident at increased frequencies ( $>20$  Hz) and paint thicknesses ( $>12$  spray passes) [82,83]. Black-colored composites (eg. carbon epoxy) that have a rough, non-reflecting surface finish do not require any surface preparation.

#### **2.1.7.4 SPATE Setup**

It is advantageous to maximize the spatial resolution (i.e., minimize the distance between the detector and specimen) in order to observe the effect of localized damage that typically occurs in composites prior to catastrophic failure. A constant distance of 12 in. from the detector to the specimen was maintained in order to minimize variations in the attenuation of the

infrared radiation over the distance between the detector and the specimen. With a proper surface preparation, the angle of obliquity between the detector and the specimen can be as high as 55 deg. before measurement inaccuracies become significant [82], though, for the present investigation, such angles were kept less than approximately 10 deg.

When analyzing carbon epoxy or aramid epoxy composites, typical output voltage amplitudes from the lock-in amplifier range from 0 to  $\pm 10$  mV. The low-pass filter time constant for this range of signal should be at least 0.1 to 0.3 sec. to produce an adequate signal-to-noise ratio and stable output. The sample time should be 3 to 10 times greater than the time constant for an accurate spatial resolution of temperature change on the color monitor. If the sample time is too short, the output cannot stabilize before the camera advances to the next sample point. Hence, sample times of 0.3 to 3 sec. are typical — leading to very long scan times with these "worst-case" material systems.

Adjustment of the electronic "zero" on the lock-in amplifier is essential for accurate stress analysis. This can be done quickly by performing line scans across several sections of the area of interest with no load applied to the specimen (a reference signal must still be supplied to the lock-in amplifier, though, to scan the specimen). If there is a signal variation along any section of the specimen, the optimum adjustment is such that the average signal is zero.

During a scan, one can expect to obtain spurious data when the focal area lies partly on and partly off of an edge of the specimen (particularly along the top and bottom portions of the notch). These data points are inaccurate because the stressed material cyclically enters and leaves the focal area, resulting in a false apparent temperature change.

Calibration of the SPATE's thermal emission scale can be accomplished with the use of high sensitivity, low response time thermocouples placed at several locations on the specimen (though, this was not done for the present investigation). Care must be exercised, how-

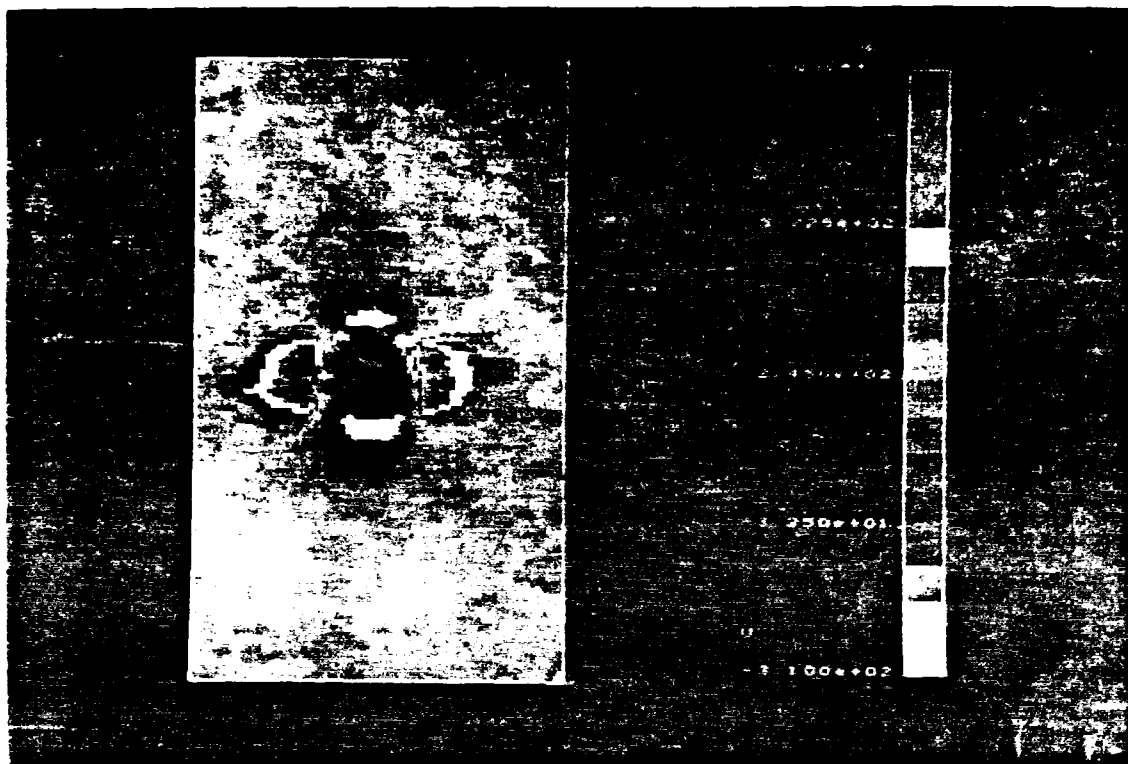
ever, to ensure that all test variables previously mentioned are held constant for a particular calibration.

#### **2.1.7.5 Interpretation of Results**

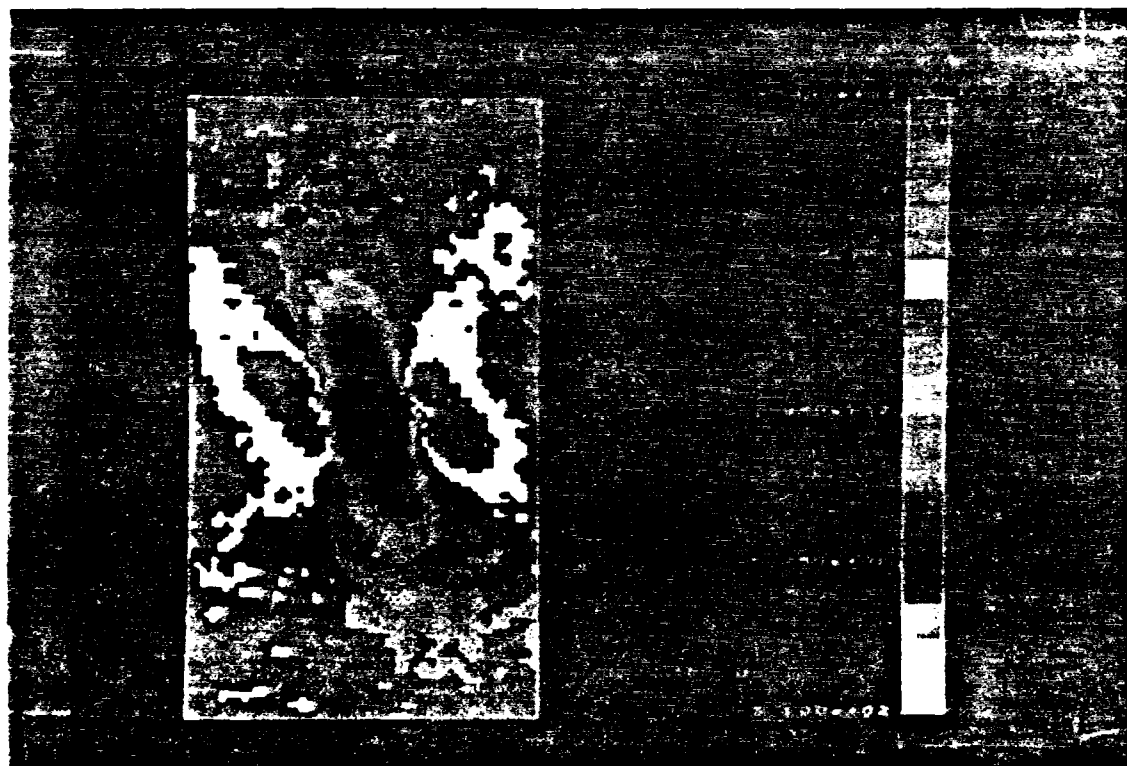
Due to the adiabatic nature of the SPATE technique, the surface ply dominates infrared temperature measurements. Figure 6 illustrates this phenomenon in two undamaged, center-notched quasi-isotropic, carbon epoxy laminates with different stacking sequences:  $(0,90,45,-45)_s$  and  $(45,90,-45,0)_s$ . The black color on the thermal emission scale corresponds to no temperature change during the load cycle. Colors above black quantify the amount of (uncalibrated) cooling during positive load increments (commonly associated with tensile stresses), while colors below black quantify heating (commonly associated with compressive stresses) during positive load increments. In the first laminate, the disturbance in the temperature field caused by the stress concentration was symmetric about the hole, while in the second laminate the pattern was unsymmetric. Despite the identical, symmetric global strains in these laminates, the unsymmetric thermal emission pattern in Figure 6b can be predicted by considering the unsymmetric stress pattern about the hole in the 45-deg. surface ply (as will be shown later in the analysis).

The utility of the SPATE technique for monitoring damage development in fiber composite laminates is exemplified by the penetrant-enhanced X-ray radiographs and SPATE thermographs of fatigue damaged carbon epoxy laminates in Figure 7 and Figure 8. The first example involves the same  $(0,90,45,-45)_s$  carbon epoxy laminate as in Figure 6a. The advanced damage condition around the notch resulted in a very low temperature change during the load cycle. Based on the information obtained in the radiograph, it is known that the 0-deg. surface ply was delaminated near the notch and had several associated cracks parallel to the fibers. It is therefore obvious that delaminated regions of this ply were under a nearly-pure uniaxial stress state because of the lack of transverse constraint from the ad-



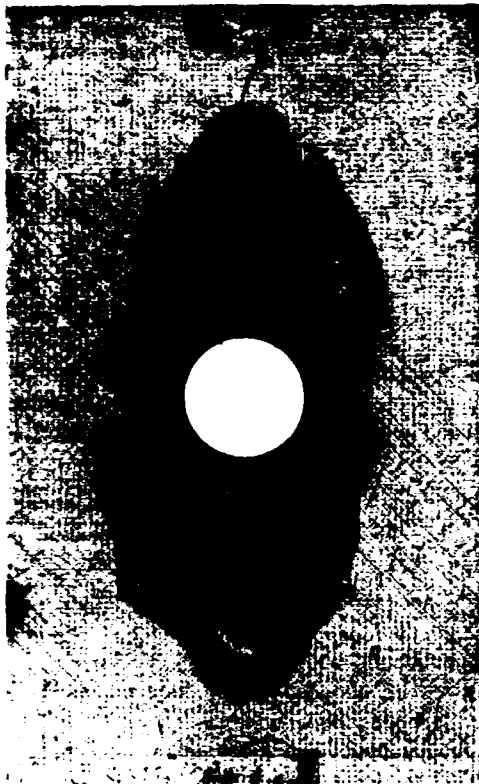


(a)

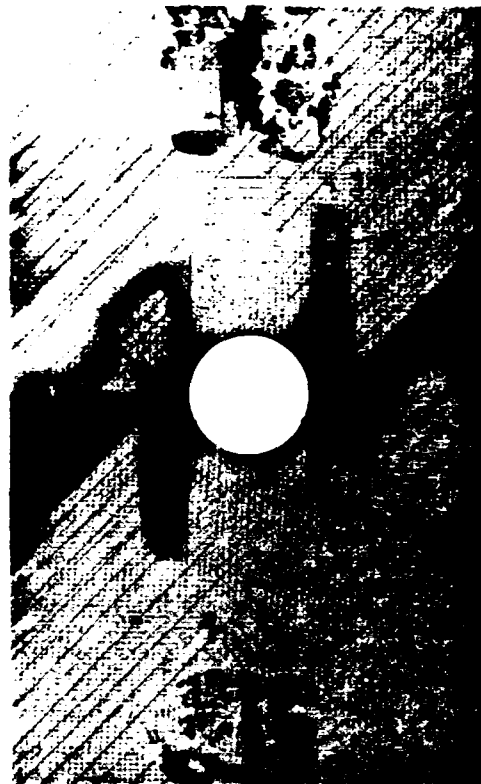


(b)

Figure 6. SPATE thermographs of 8-ply carbon epoxy laminates: (a) (0.90,45,-45)<sub>s</sub>; (b) (45,90,-45)<sub>s</sub>.



( a )



( b )

Figure 7. Radiographs of 8-ply carbon epoxy laminates with fatigue damage: (a)  $(0,90,45,-45)_s$  and (b)  $(45,90,-45,0)_s$  laminates

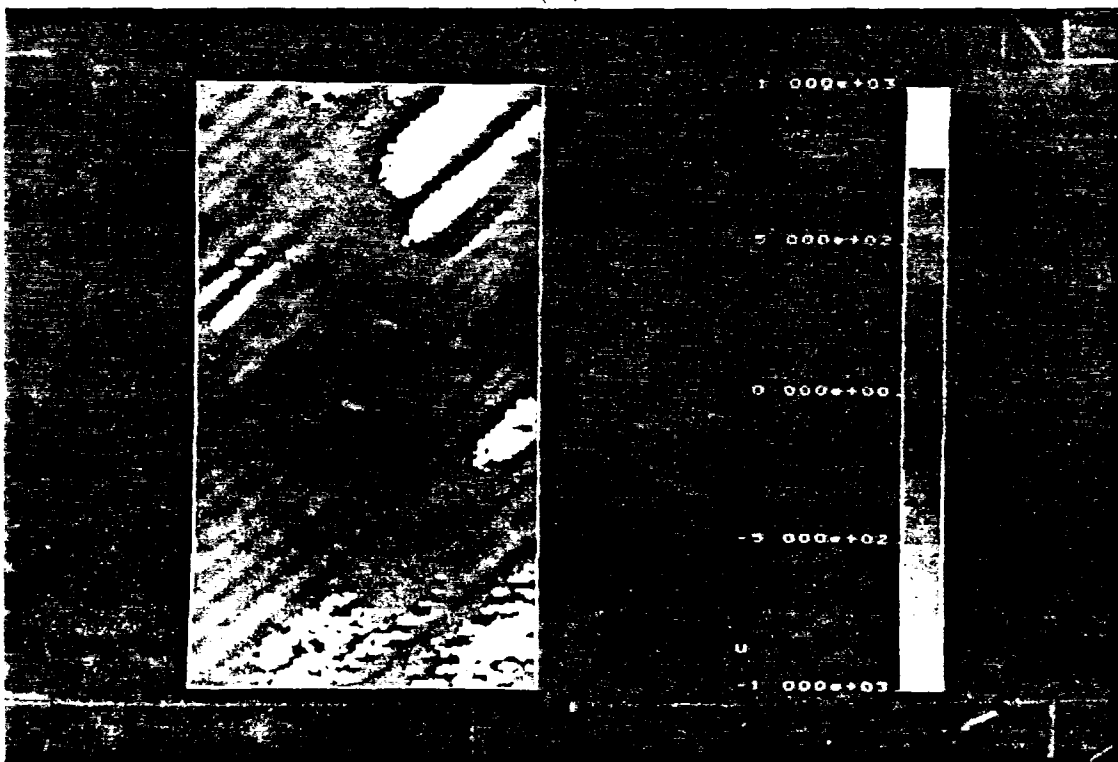


Figure 8. SPATE thermographs of 3-ply carbon epoxy laminates with fatigue damage: (a)  $[0/90/45/-45]_3$ , and (b)  $[45/90/-45/0]_3$  laminates from Figure 7

joining sublaminates. The very low temperature change measured near the notch was caused not by the total absence of stress in the surface ply, but by the absence of transverse stress in that ply. The surface ply continued to bear load in the 0-deg. fiber direction, but since the coefficient of thermal expansion in this material system is extremely low in the fiber direction, there was little resultant thermal emission.

Consider next the radiograph and SPATE thermograph of the fatigue-damaged (45,90,-45,0)<sub>s</sub> carbon epoxy laminate in Figure 7b and Figure 8b. This is the same laminate shown in the undamaged state in Figure 6b. Damage in the surface ply consisted of matrix cracks and delaminations. Due to the relaxation of stresses transverse to the cracks in the surface ply, each matrix crack on the surface of observation appeared as a line of low thermal emission in the thermograph. Delaminated portions of the surface ply that were bounded on three sides by the hole boundary and two parallel matrix cracks in the surface ply carried no load and, therefore, had no thermal emission.

In summary, reduced thermal emissions in carbon epoxy laminates can be due to a relaxation of some or all components of stress in the surface ply. Another cause for pointwise variations of the thermal emission in composites is the existence of manufacturing irregularities — in particular, nonuniform phase and void distribution. For example, matrix-rich regions of a composite can be resolved from matrix-poor regions because of their different thermoelastic responses [84]. Additional papers demonstrating the applicability of adiabatic thermoelastic emission as an effective nondestructive testing technique for CFRP materials can be found in Refs. [85-88].

## 2.2 Analysis

### 2.2.1 Adiabatic Thermoelastic Effect

**Nomenclature:** Superscripts  $f$ ,  $m$ , and  $\ell$  refer to fiber, matrix, and lamina, respectively. Subscripts  $L$  and  $T$  refer to longitudinal and transverse directions of the lamina relative to the fibers. Subscripts 1, 2, 3 and  $x$ ,  $y$ ,  $z$  refer to lamina- and laminate-aligned coordinates, respectively.

The adiabatic thermoelastic effect was first explained by Thomson (later to become Lord Kelvin) in 1853 [89,90]. Using fundamental laws of thermodynamics, he derived Eq. (1), which relates the pointwise change in infinitesimal extensional strain components,  $\varepsilon_i$  ( $i = 1,2,3$ ), in homogeneous, isotropic, linear-elastic matter and the small, reversible, adiabatic temperature change,  $\Theta$ ,

$$\Theta = - \frac{3 T_0 \alpha K}{c_\sigma} (\varepsilon_1 + \varepsilon_2 + \varepsilon_3) \quad (1)$$

where  $T_0$  is the initial temperature of the material,  $\alpha$  is the linear thermal expansion coefficient,  $K$  is the bulk modulus, and  $c_\sigma$  is the *volumetric* specific heat at constant stress. Equation (1) can be written in terms of the change in extensional stress components,  $\sigma_i$ , as in Eq. (2):

$$\Theta = - \frac{T_0 \alpha}{c_\sigma} (\sigma_1 + \sigma_2 + \sigma_3) \quad (2)$$

Two well-known implications of Eqs. (1) and (2) are: (a) the temperature of isotropic matter with a positive thermal expansion coefficient increases with a negative dilatation, and decreases with a positive dilatation; and (b) a state of pure shear strain or stress produces no

adiabatic thermoelastic temperature change in isotropic matter. The accuracy of Thomson's thermoelastic relationship has been verified with metals by numerous investigators, including Joule [91], Compton and Webster [92], Dillon and Tauchert [93], Belgen [83], and Stanley and Chan [94]. Gilmour, et al. [95] showed that several glassy polymers, including epoxy resin, obeyed Eq. (1) if elastic deformations were maintained. Haward and Trainor [96] demonstrated the validity of (1) for poly(methyl methacrylate) (PMMA) for tensile and compressive loads below the creep threshold. Deviations in the measured temperature change from (1) have been attributed to plasticity in metals by Jordan and Sandor [97], Enke and Sandor [98], and Stanley and Chan [82], and to viscoelasticity in polymers by Higuchi and Imai [99]. In situations where adiabatic conditions are not maintained, the temperature variation is not reversible, and additional terms must be included in Eqs. (1) and (2) to account for heat transfer.

Biot gives the counterpart of Eq. (1) for anisotropic solids as:

$$\Theta = - \frac{T_0}{c_\epsilon} \alpha_{kl} C_{ijkl} \epsilon_{ij} \quad (3)$$

where  $\alpha_{kl}$  is the linear thermal expansion tensor,  $c_\epsilon$  is the volumetric specific heat at constant strain,  $C_{ijkl}$  is the stiffness tensor, and  $\epsilon_{ij}$  is the linear strain tensor [100]. The volumetric specific heat at constant stress or strain is related to the corresponding mass specific heat,  $c'$ , by the expression  $c = \rho c'$ , where  $\rho$  is the mass density. Rewriting Eq. (3) in terms of the stress tensor, we have:

$$\Theta = - \frac{T_0}{c_\epsilon} \alpha_{kl} \sigma_{kl} \quad (4)$$

The difference between  $c_\sigma$  and  $c_\epsilon$  for anisotropic solids, though quite small, is given by Eq. (5) [101]:

$$c_\sigma - c_\epsilon = T_0 \alpha_{ij} \alpha_{kl} C_{ijkl} \quad (5)$$

Equations (3) and (4) imply that a state of pure shear strain or stress in anisotropic matter can result in a non-zero adiabatic thermoelastic temperature change only if there exists a non-zero shear-extension coupling term in the thermal expansion tensor or the stiffness tensor. Unidirectionally-reinforced fiber composite materials have no such shear-extension coupling, and, furthermore, are considered to be transversely isotropic. Equation (3) for such materials then becomes

$$\Theta = -\frac{T_0}{c_\epsilon} \{ \alpha_L [C_{11}\epsilon_1 + C_{12}(\epsilon_2 + \epsilon_3)] + \alpha_T [2 C_{12}\epsilon_1 + (C_{22} + C_{23})(\epsilon_2 + \epsilon_3)] \} \quad (6)$$

where the contracted notation has been employed on the indices of the elastic constants and strain components, and the thermal expansion coefficients have been expressed in terms of the longitudinal and transverse components. An additional simplification for isotropic materials is given by Eq. (7):

$$\Theta = -\frac{T_0}{c_\epsilon} \alpha (C_{11} + 2C_{12})(\epsilon_1 + \epsilon_2 + \epsilon_3) \quad (7)$$

where only one thermal expansion coefficient and two elastic constants are required.

Equations (1-4) can be recast in the form given by Eq. (8) in order to express the adiabatic thermoelastic temperature change in terms of the two planar components of extensional stress acting on the surface of a unidirectional fiber-reinforced material:

$$\Theta = K_1\sigma_1 + K_2\sigma_2 \quad (8)$$

Here,  $K_1$  and  $K_2$  represent the influence of the thermoelastic constants in the orthogonal 1 and 2 directions, respectively. The 1 and 2 directions correspond to the principal material directions in orthotropic matter (such as unidirectionally-reinforced composite materials). If the material is isotropic,  $K_1 = K_2$ , and  $\Theta$  is proportional to the sum of the normal stresses; otherwise  $K_1 \neq K_2$ , and  $\Theta$  is proportional to a nonuniformly-weighted sum of the normal stresses. An apparent limitation of the adiabatic thermoelastic measurement technique is that the two

stress components in Eq. (8) cannot be individually calculated from a given temperature change except in special cases where one component is known by some boundary condition [102]. For a series of measured temperature changes,  $\Theta_j$ , the locus of possible combinations of  $\sigma_1$  and  $\sigma_2$  can be graphically represented by one of a series of parallel lines in the  $\sigma_1$ - $\sigma_2$  plane (Figure 9). The line passing through the origin suggests that, in addition to the null stress state, there are an infinite number of stress states resulting in no adiabatic thermoelastic temperature change.

Equation (8) can be used to describe the "smeared" thermoelastic response of a composite material if the effective (average) thermoelastic constants of the material are known. In those situations where the constitution or relative amount of each phase of the composite is variable, a more general approach is to evaluate the temperature change in each constituent separately using Eq. (3) or (4), and to combine these changes in some manner to derive the net temperature change of the composite. Expression (9) represents one method of computing a weighted average of the several temperature changes in a non-layered composite,

$$\Theta^{\text{net}} = \Theta^j X^j \quad (9)$$

where  $\Theta^j$  is the temperature change of the  $j$ -th constituent and  $X^j$  is an "influence factor" for the  $j$ -th constituent (such as the volume fraction). A difficulty associated with using Eq. (9) is that an accurate micromechanical model for constituent extensional strains or stresses is required to compute each  $\Theta^j$ .

Considering that photons from a depth of only a few microns reach the infrared detector [103] and that there is no heat transfer between layers of a laminate during an adiabatic deformation, it is obvious that SPATE measurements are sensitive to the deformation of just the top ply on the surface of observation. (A typical ply thickness is approximately 0.005 in.). Since the deformations and resulting temperature changes of the constituent phases of the composite will differ in layers of dissimilar orientation, laminate stacking sequence must be known to interpret the measurements. That is, Eq. (9) needs to be evaluated only for the



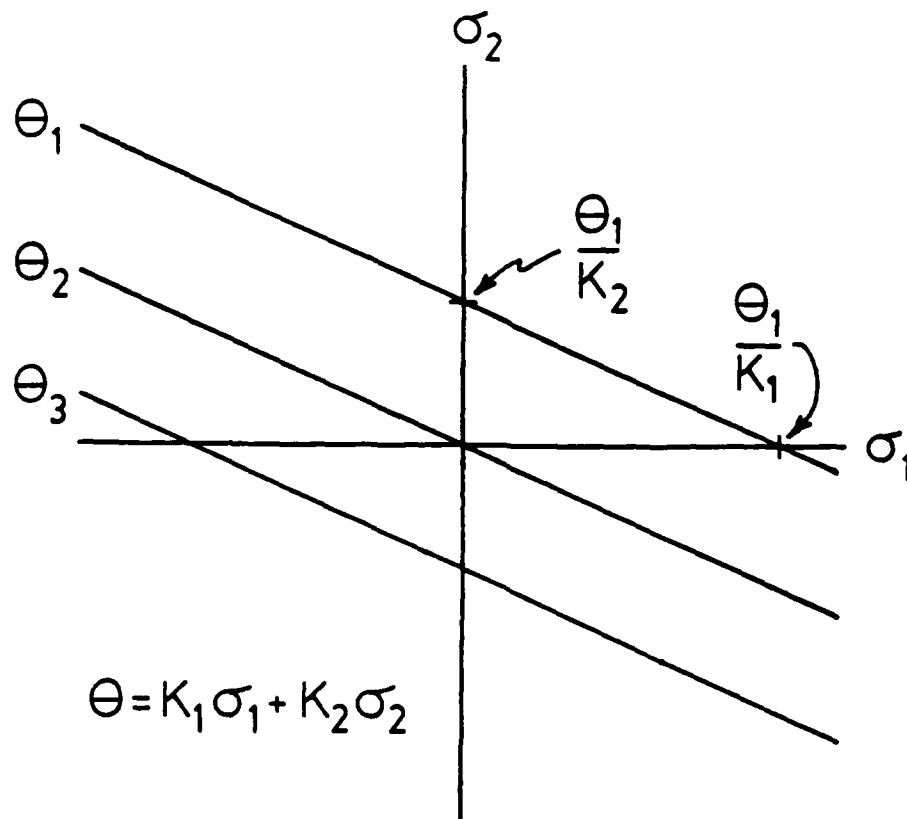


Figure 9. Dependence of adiabatic thermoelastic temperature change on in-plane stress components

surface ply. Of course, the deformation of the surface ply reflects the deformation of the entire laminate if the plies remain bonded together during the measurement. If heat generation, heat conductance, and heat capacitance are taken into account during a mechanical excitation, stresses a small distance below the surface of observation can be computed as well [104].

The approach taken to develop a micromechanical model of the adiabatic thermoelastic effect in undamaged fiber composites is to begin with Lekhnitskii's elasticity solution for global strains in an infinite, homogeneous, anisotropic plate with an elliptical opening [30], realizing that those strains are valid only in regions away from the free edges in a laminated plate. After transforming those strains to the surface ply's local coordinates, a simple micromechanical model of fiber and matrix deformation is used to compute the temperature change in those constituents. Finally, a rule of mixtures relation, such as Eq. (9), is used to compute the net temperature change of the surface ply.

In the micromechanical analysis of strains in the constituents, "mechanics of materials" assumptions [105] will be invoked to maintain simplicity. The problem is formulated by first identifying the unknown quantities to be computed, which, for Eq. (3), would be the three extensional stresses and strains in the fibers and matrix:  $\sigma_i^f$ ,  $\sigma_i^m$ ,  $\epsilon_i^f$ , and  $\epsilon_i^m$  ( $i=1,2,3$ ). In the most general three-dimensional case, the assumed force equilibrium equations in the longitudinal and transverse directions of a representative volume (or area) of material in a plane state of stress (Figure 10) are given by Eqs. (10-12),

$$V^f \sigma_1^f + V^m \sigma_1^m = \sigma_1^{\ell} \quad (10)$$

$$\sigma_2^f = \sigma_2^{\ell} \quad \text{and} \quad \sigma_2^m = \sigma_2^{\ell} \quad (11a,b)$$

$$\sigma_3^f = 0 \quad \text{and} \quad \sigma_3^m = 0 \quad (12a,b)$$

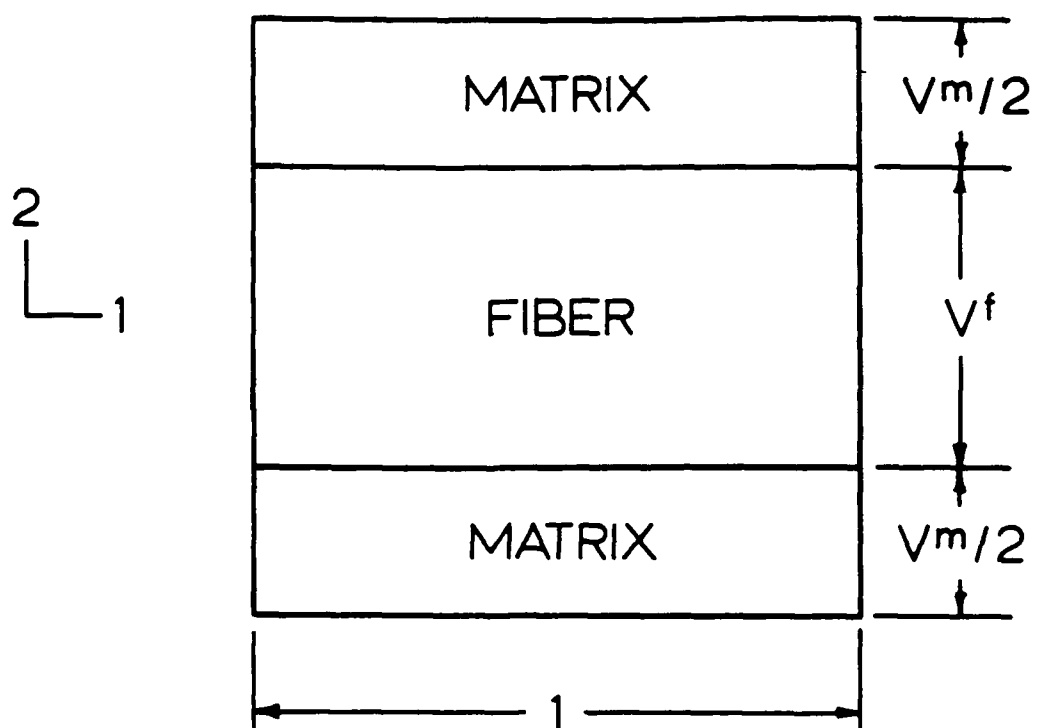


Figure 10. Representative area of a fiber composite material

where  $V^f$  and  $V^m$  are volume fractions of the fibers and matrix, respectively. The assumed kinematic relations in the longitudinal and transverse directions are given by Eqs. (13-15):

$$\varepsilon_1^f = \varepsilon_1^\ell \quad \text{and} \quad \varepsilon_1^m = \varepsilon_1^\ell \quad (13a,b)$$

$$\varepsilon_2^f V^f + \varepsilon_2^m V^m = \varepsilon_2^\ell \quad (14)$$

$$\varepsilon_3^f V^f + \varepsilon_3^m V^m = \varepsilon_3^\ell \quad (15)$$

The constitutive relations between normal stresses and strains in transversely isotropic media are given by Eq. (16):

$$[\sigma_1 \ \sigma_2 \ \sigma_3]^T = [C] [\varepsilon_1 \ \varepsilon_2 \ \varepsilon_3]^T \quad (16)$$

where  $C_{ij}$  are elements of the stiffness matrix given by Eq. (17):

$$[C] = \begin{bmatrix} \frac{1}{E_L} & -\frac{\nu_{LT}}{E_L} & -\frac{\nu_{LT}}{E_L} \\ -\frac{\nu_{LT}}{E_L} & \frac{1}{E_T} & -\frac{\nu_{TT}}{E_T} \\ -\frac{\nu_{LT}}{E_L} & -\frac{\nu_{TT}}{E_T} & \frac{1}{E_T} \end{bmatrix}^{-1} \quad (17)$$

Implicit in Eq. (16) is the assumption of no shear coupling in any plane of the material. This assumption is based on the fact that the 1, 2, and 3 axes coincide with the principal directions of orthotropy. Of course, in the isotropic matrix material the transverse and longitudinal directions are immaterial. It will also be assumed that hygrothermal self-stresses have no dynamic variation during cyclic loading and that intralaminar stress gradients due to the mismatch of fiber and matrix thermoelastic properties are negligible. Edge-induced interlaminar stresses will not be considered in the micromechanical analysis since the global solution for strain near an edge is invalid there.

Including the six constitutive relations for the fibers and matrix implied by (16), there are now fifteen equations for twelve unknowns. Clearly, the formulation is overdetermined due to the redundant nature of several of the equations. The formulation must therefore be altered to obtain a tractable system of equations. To this end, only the six extensional strains are to be computed through the use of Eqs. (13a,b), (14), and three conditions given by Eqs. (18), (19), and (20):

$$C_{12}^f \epsilon_1^f + C_{22}^f \epsilon_2^f + C_{23}^f \epsilon_3^f = C_{12}^m \epsilon_1^m + C_{22}^m \epsilon_2^m + C_{23}^m \epsilon_3^m \quad (18)$$

$$C_{13}^f \epsilon_1^f + C_{23}^f \epsilon_2^f + C_{33}^f \epsilon_3^f = 0 \quad \text{and} \quad C_{13}^m \epsilon_1^m + C_{23}^m \epsilon_2^m + C_{33}^m \epsilon_3^m = 0 \quad (19,20)$$

Equation (18) results from equating the in-plane transverse stress components of the matrix and fibers ( $\sigma_2^f = \sigma_2^m$ ), and does not require that the transverse constituent stresses equal the transverse lamina stress. This potential violation of equilibrium is inevitable with the present formulation. Equations (19) and (20) are the conditions of vanishing stress normal to the surface of the material ( $\sigma_3^f = 0$  and  $\sigma_3^m = 0$ ), and are chosen to represent the stress state of particles of material near the surface of the test specimen that most strongly influence the adiabatic thermoelastic emission of infrared radiation. Solving Eqs. (19) and (20) for the out-of-plane strains, we find:

$$\epsilon_3^f = -\frac{1}{C_{33}^f} (C_{13}^f \epsilon_1^f + C_{23}^f \epsilon_2^f) \quad \text{and} \quad \epsilon_3^m = -\frac{1}{C_{33}^m} (C_{13}^m \epsilon_1^m + C_{23}^m \epsilon_2^m) \quad (21,22)$$

The assumption of homogeneous strain in the longitudinal direction of all constituents, given by Eqs. (13a,b), can be used to replace  $\epsilon_1^f$  and  $\epsilon_1^m$  in the previous equations with the known lamina strain,  $\epsilon_1^f$ . Expressing Eq. (18) in terms of  $\epsilon_2^m$ ,  $\epsilon_1^f$ , and  $\epsilon_2^f$  with the use of Eqs. (13), (14), (21), and (22), we have:

$$\begin{aligned}
C_{12}^f \varepsilon_1^f + \frac{C_{22}^f}{V^f} (\varepsilon_2^f - V^m \varepsilon_2^m) - \frac{C_{23}^f}{C_{33}^f} \left[ C_{13}^f \varepsilon_1^f + \frac{C_{23}^f}{V^f} (\varepsilon_2^f - V^m \varepsilon_2^m) \right] \\
= C_{12}^m \varepsilon_1^f + C_{22}^m \varepsilon_2^m - \frac{C_{23}^m}{C_{33}^m} (C_{13}^m \varepsilon_1^f + C_{23}^m \varepsilon_2^m)
\end{aligned} \tag{23}$$

Solving Eq. (23) for  $\varepsilon_2^m$  in terms of  $\varepsilon_1^f$  and  $\varepsilon_2^f$  results in Eq. (24),

$$\varepsilon_2^m = D_1 \varepsilon_1^f + D_2 \varepsilon_2^f \tag{24}$$

where  $D_i$  are unitless material constants defined by:

$$\begin{aligned}
D_1 &= \frac{C_{12}^f - C_{12}^m - \frac{C_{23}^f C_{13}^f}{C_{33}^f} + \frac{C_{23}^m C_{13}^m}{C_{33}^m}}{C_{22}^m - \frac{(C_{23}^m)^2}{C_{33}^m} + \frac{V^m}{V^f} \left[ C_{22}^f - \frac{(C_{23}^f)^2}{C_{33}^f} \right]} \\
D_2 &= \frac{C_{22}^f - \frac{(C_{23}^f)^2}{C_{33}^f}}{V^f \left[ C_{22}^m - \frac{(C_{23}^m)^2}{C_{33}^m} \right] + V^m \left[ C_{22}^f - \frac{(C_{23}^f)^2}{C_{33}^f} \right]}
\end{aligned}$$

Substituting Eqs. (13b) and (24) into Eq. (22) provides the remaining unknown matrix strain component in terms of the in-plane lamina strains,

$$\varepsilon_3^m = D_3 \varepsilon_1^f + D_4 \varepsilon_2^f \tag{25}$$

where

$$D_3 = -\frac{1}{C_{33}^m} (C_{13}^m + C_{23}^m D_1) \quad \text{and} \quad D_4 = -\frac{C_{23}^m}{C_{33}^m} D_2$$

The volume change of the matrix material per unit original volume is given by the sum of the infinitesimal, extensional strains in Eqs. (13b), (24), and (25),

$$\varepsilon_1^m + \varepsilon_2^m + \varepsilon_3^m = D_5 \varepsilon_1^f + D_6 \varepsilon_2^f \quad (26)$$

where  $D_5 = (1 + D_1 + D_3)$  and  $D_6 = (D_2 + D_4)$ .

It is assumed that the fibers are transversely isotropic in elastic as well as thermal expansion properties, with the plane of isotropy being perpendicular to the fiber longitudinal axis. For the present, we ignore the contradiction of this assumption with the "mechanics of materials" assumptions stated earlier. The in-plane, transverse component of fiber strain is expressed in terms of the known lamina and matrix strains by rearranging Eq. (14):

$$\varepsilon_2^f = \frac{1}{V^f} (\varepsilon_2^f - V^m \varepsilon_2^m) \quad (27)$$

Equations (13a) and (27) are used to express the out-of-plane, transverse component of fiber strain in Eq. (21) as

$$\varepsilon_3^f = -\frac{1}{C_{33}^f} \left[ C_{13}^f \varepsilon_1^f + \frac{C_{23}^f}{V^f} (\varepsilon_2^f - V^m \varepsilon_2^m) \right] \quad (28)$$

The strain  $\varepsilon_2^m$  in Eqs. (27) and (28) can be eliminated using Eq. (24) to finally arrive at the expressions for the extensional fiber strains in terms of the in-plane lamina strains,

$$\begin{aligned} \varepsilon_1^f &= \varepsilon_1^f \\ \varepsilon_2^f &= D_7 \varepsilon_1^f + D_8 \varepsilon_2^f \\ \varepsilon_3^f &= D_9 \varepsilon_1^f + D_{10} \varepsilon_2^f \end{aligned} \quad (29)$$

where the unitless material constants  $D_i$  are given by

$$\begin{aligned} D_7 &= -\frac{V^m}{V^f} D_1 & D_8 &= \frac{(1 - V^m D_2)}{V^f} \\ D_9 &= \frac{1}{C_{33}^f} (D_1 C_{23}^f \frac{V^m}{V^f} - C_{13}^f) & D_{10} &= \frac{C_{23}^f}{C_{33}^f V^f} (D_2 V^m - 1) \end{aligned}$$

In the application of Eq. (6), relating temperature change to strain in a transversely isotropic material, it is convenient to group the transverse fiber strains as in Eq. (30)

$$\varepsilon_2^f + \varepsilon_3^f = D_{11} \varepsilon_1^f + D_{12} \varepsilon_2^f \quad (30)$$

where

$$D_{11} = \frac{1}{C_{33}^f} \left[ D_1 \frac{V^m}{V^f} (C_{23}^f - C_{33}^f) - C_{13}^f \right] \quad \text{and} \quad D_{12} = \frac{1}{V^f} (1 - V^m D_2) \left[ 1 - \frac{C_{23}^f}{C_{33}^f} \right]$$

Up to this point, the equations expressing the three extensional components of micro-constituent strains in terms of the in-plane lamina strains have been developed. The temperature change of the fibers and matrix can now be obtained simply by substituting the proper material properties and lamina strains into Eqs. (6) and (7), respectively.

The last remaining step in calculating the effective lamina temperature change is to combine the constituent temperature changes. Within the context of adiabatic, reversible temperature change, it is natural to combine the constituent temperature changes based on the area fraction of each micro-constituent material influencing the temperature sensor. For the present discussion, the effective lamina temperature change is approximated with the rule of mixtures expression, Eq. (31):

$$\Theta^f = \Theta^f V^f + \Theta^m V^m \quad (31)$$

Substitution of Eqs. (6) and (7) into Eq. (31) provides the final expression for the effective temperature change of the lamina in terms of the in-plane strains from classical laminated plate theory:

$$\Theta^f = D_{13} \varepsilon_1^f + D_{14} \varepsilon_2^f \quad (32)$$

where  $D_{13}$  and  $D_{14}$  are material constants given by:



$$D_{13} = -T_0 \left[ \frac{V^f}{c_\epsilon^f} \{ \alpha_L^f [C_{11}^f + C_{12}^f D_{11}] + \alpha_T^f [2 C_{12}^f + (C_{22}^f + C_{23}^f) D_{11}] \} + \frac{V^m}{c_\epsilon^m} \alpha^m D_5 (C_{11}^m + 2 C_{12}^m) \right]$$

$$D_{14} = -T_0 \left\{ \frac{V^f}{c_\epsilon^f} D_{12} [\alpha_L^f C_{12}^f + \alpha_T^f (C_{22}^f + C_{23}^f)] + \frac{V^m}{c_\epsilon^m} \alpha^m D_6 [C_{11}^m + 2 C_{12}^m] \right\}$$

To illustrate the effect of surface ply orientation on the thermoelastic temperature change measured via infrared thermography, several theoretical calculations for continuous fiber carbon epoxy laminates are considered next. (Experimental data were not available, and could differ somewhat from the present predictions which were calculated using Eq. 32). The highly anisotropic thermoelastic constants of unidirectional laminae of carbon epoxy were taken from Ref. [106]. Figure 11 is a prediction of the effect of ply orientation on the adiabatic temperature change for a unidirectional ply under constant axial stress or strain change. There is a monotonic increase in temperature change as the ply orientation,  $\theta$ , is changed from 0-deg. to 90-deg. Analogous behavior is predicted for  $\pm\theta$  angle-ply laminates (Figure 12). Note that there are two values of  $\theta$  resulting in no thermal emission for angle-ply laminates, according to the calculations. The global transverse strains of a laminate vary with  $\theta$  because of the dependence of the global Poisson's ratio on  $\theta$ . In order to separate the effects of surface ply orientation and global Poisson's ratio, the surface ply angle in a quasi-isotropic laminate was varied while a constant global strain field was maintained (Figure 13). Again, the temperature change is greatest when the surface ply orientation is perpendicular to the load direction. As a final example, the effect of laminate Poisson's ratio on the temperature change in a 0-deg. surface ply under a constant longitudinal strain change is considered (Figure 14). The temperature change of the surface ply can be either greater than zero, less than zero, or equal to zero, depending on the magnitude of the transverse strain. This effect is caused by the opposite signs of a carbon epoxy ply's thermal expansion coefficients in the longitudinal and transverse directions (typically,  $-0.43 \mu/^\circ\text{F}$  and  $13.5 \mu/^\circ\text{F}$ , respectively).

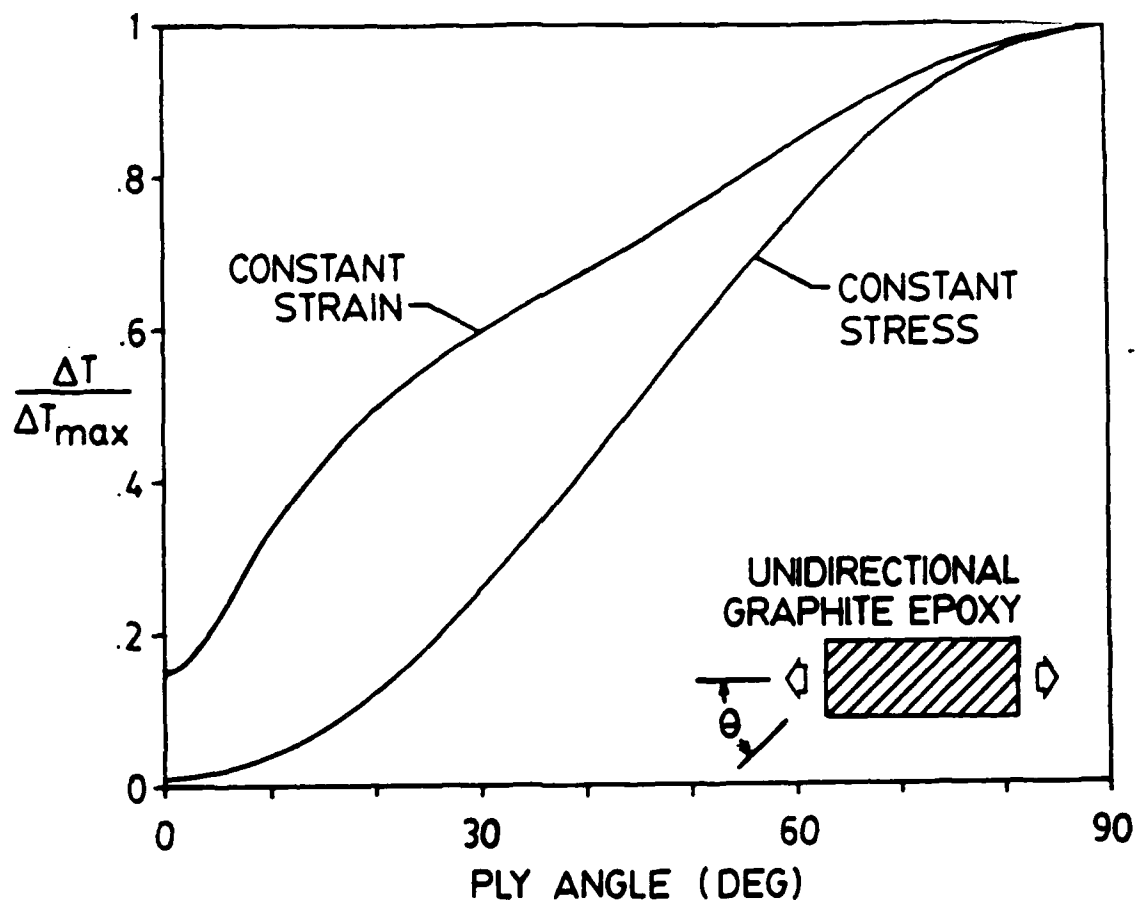


Figure 11. Effect of ply orientation on the temperature change in a unidirectional ply under constant axial stress or strain

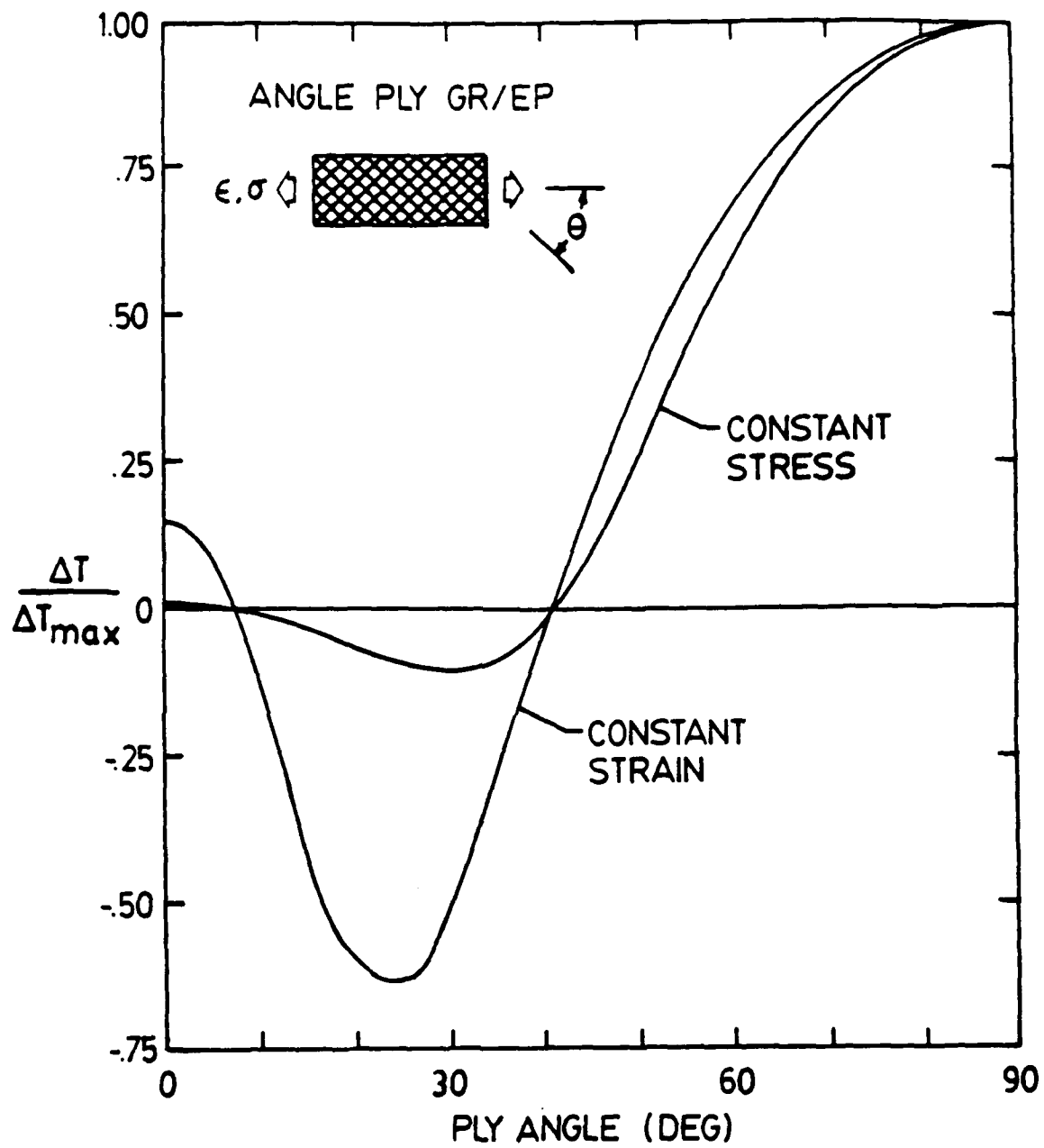


Figure 12. Effect of ply orientation on the temperature change in an angle-ply laminate under constant axial stress or strain

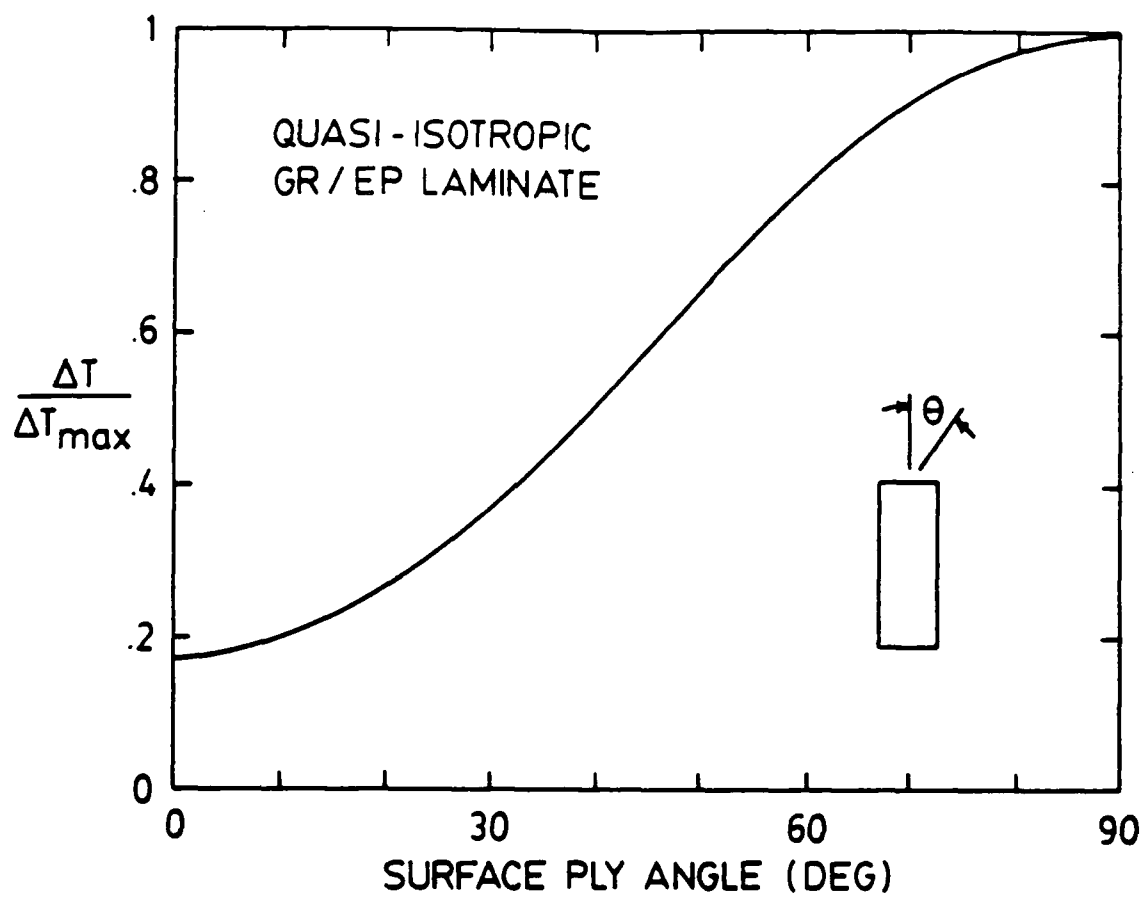


Figure 13. Effect of ply orientation on the temperature change in a quasi-isotropic laminate under a constant global strain field

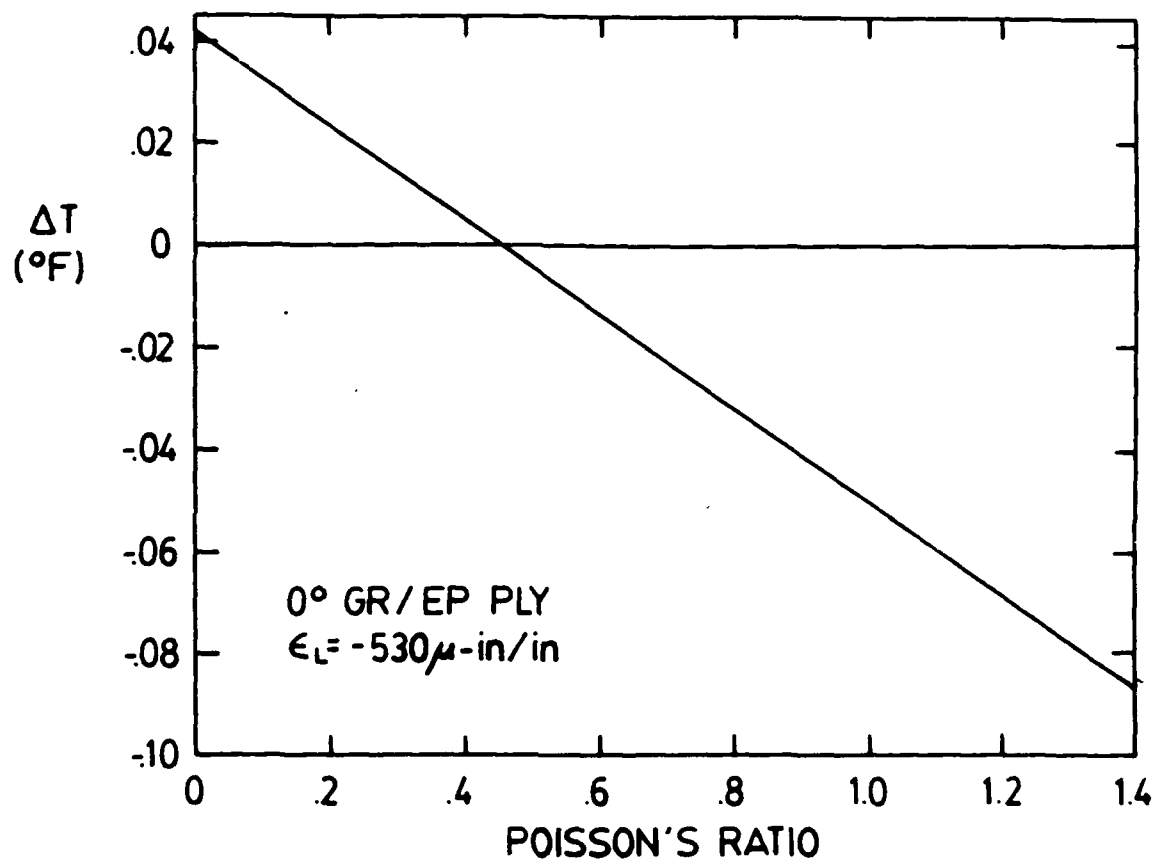


Figure 14. Effect of laminate Poisson's ratio on the temperature change in a 0-deg. ply under a constant longitudinal strain

The generality of the present analysis for thermoelastic temperature changes in laminated fiber composites with arbitrary properties and constitution facilitates our understanding of laboratory measurements by enabling the prediction of the effect of various material properties on the measurements. For instance, using the micromechanical expressions for effective elastic properties of a lamina given by Chamis [106] in conjunction with the present model for adiabatic thermoelastic response, the effect of the fiber volume fraction on the adiabatic temperature change during a constant longitudinal stress or strain a 0-deg. carbon epoxy lamina can be predicted (Figure 15). Under constant strain, the temperature change varied linearly with  $V^f$ . Under constant stress, however, the variation was nonlinear due to the increased longitudinal stiffness of the material at higher fiber volume fractions. In this particular calculation, a fiber volume fraction of 0.67 resulted in no temperature change. Lower fiber volumes resulted in cooling under tensile loads, and higher fiber volumes resulted in heating under tensile loads.

To verify the accuracy of the analysis, the predicted and measured thermoelastic emissions in two center-notched, quasi-isotropic, T300/5208 laminates with either a 0 or 45-deg. surface ply were compared. Global stresses from Lekhnitskii's elasticity solution [30] were used in conjunction with the present micromechanical model to compute constituent strains and the average adiabatic temperature change in the surface ply. The thermoelastic properties in Table 1 were used in the analysis, along with  $V^f = 0.55$  and  $T_0 = 297$  K. Predictions were normalized by their respective far-field values to facilitate comparisons of the patterns. The thermoelastic emission pattern for the (0,90,45,-45)<sub>s</sub> laminate (Figure 16a) was not in very good agreement with the measurement in Figure 6a. On the other hand, the prediction for the (45,90,-45,0)<sub>s</sub> laminate (Figure 16b) was in excellent agreement with the measurement in Figure 6b. Laminates with 0-deg. surface plies were the most challenging to model since there was great variation from one material system to another, and from one stacking sequence to another. Seemingly, the order of the interior plies influenced measurements more than would be expected in a purely adiabatic process. Given that the analytical results of Figure 16 re-

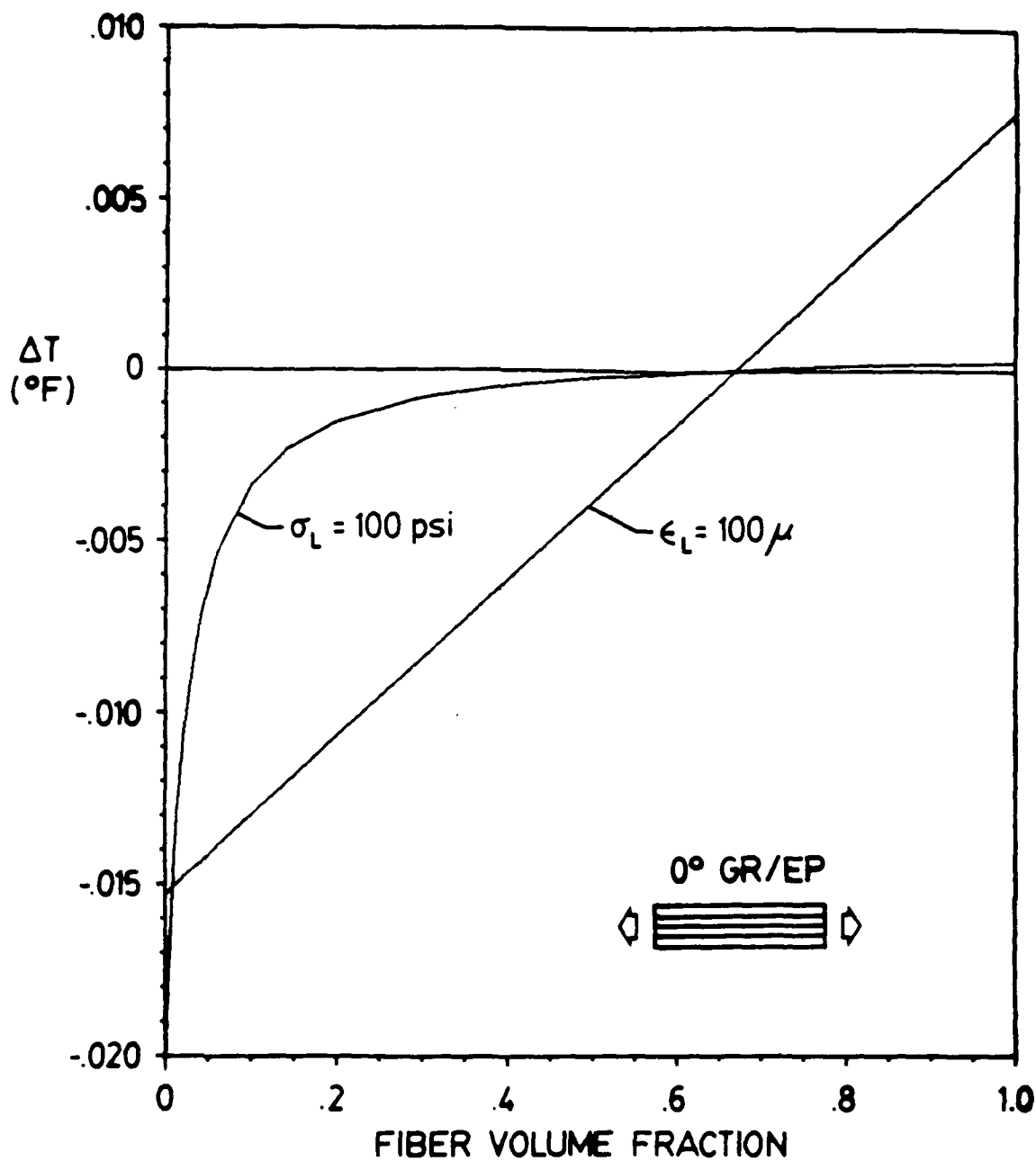


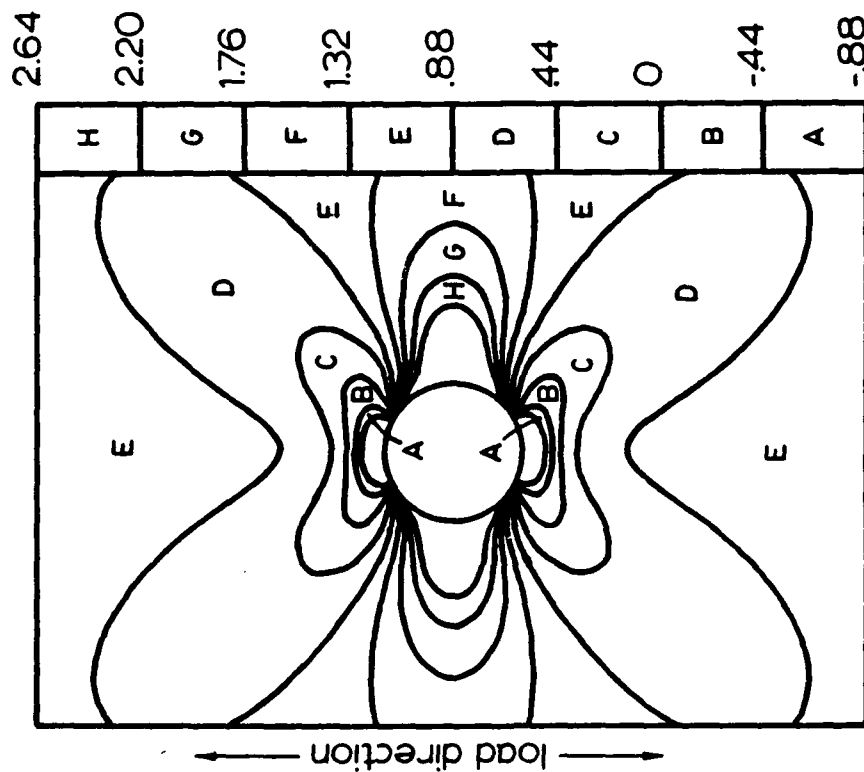
Figure 15. Effect of fiber volume fraction on the adiabatic temperature change in a 0-deg. carbon epoxy lamina under constant longitudinal stress or strain

Table 1. Thermoelastic properties for carbon epoxy

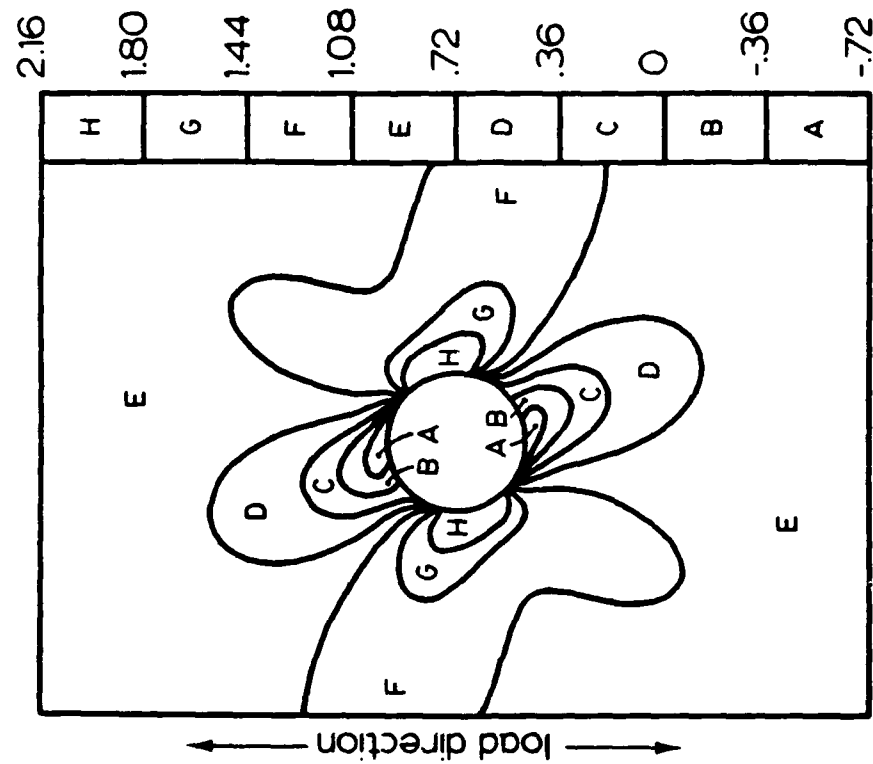
Fiber	Matrix	Lamina
$E_L^f = 33.6 \text{ Msi}$	$E^m = .78 \text{ Msi}$	$E_L^f = 18.8 \text{ Msi}$
$E_T^f = 2.1 \text{ Msi}$	$\nu^m = 0.35$	$E_T^f = 1.41 \text{ Msi}$
$\nu_{LT}^f = 0.29$	$\alpha^m = 40 \mu/^{\circ}\text{F}$	$G_{LT}^f = 0.782 \text{ Msi}$
$\nu_{TT}^f = 0.49$	$c_e^m = 105 \text{ lb./in.}^2/^{\circ}\text{F}$	$\nu_{LT}^f = 0.308$
$\alpha_{LL}^f = -0.55 \mu/^{\circ}\text{F}$		
$\alpha_{TT}^f = 5.6 \mu/^{\circ}\text{F}$		
$c_e^f = 125 \text{ lb./in.}^2/^{\circ}\text{F}$		

Taken from Refs. [106,107].





(a)



(b)

Figure 16. Predicted SPATE patterns in two center-notched carbon epoxy laminates: (a)  $(0,90,45,-45)_s$ ; (b)  $(45,90,-45,0)_s$

presented the temperature change of only the surface ply, and that there was fair-to-very good correlation of the analysis and experiments, it can be concluded that the assumptions of the analysis are reasonable, but could be improved by addressing several uncertainties. The notched (0,90,45,-45)<sub>s</sub> laminate was chosen for these additional exploratory-type analyses because the theory and experiments disagreed most severely for laminates with 0-deg. surface plies.

There are several plausible causes for the discrepancy between the measured and predicted thermoelastic emissions. By computing stresses in the fibers and matrix with strains evaluated in the micromechanical analysis, and checking force equilibrium in the longitudinal and transverse directions (Eqs. 10 and 11), it is found that the analysis produced constituent stresses that were quite consistent with the lamina stress state on an absolute scale, but, in some instances, significantly in error on a percentage basis for several simple laminates (Table 2). (The carbon epoxy material properties used in the calculations for Table 2 were slightly different than those given in Table 1. However, for the present discussion this does not matter.) Furthermore, the accuracy of the constituents' thermoelastic properties are questionable for the dynamic problem at hand. An inaccuracy in any one of the thermoelastic properties or micro-stress components could cause the discrepancies. It may also be necessary to alter expression (31) to account for the actual contributions of the individual constituent phases (perhaps in adjacent plies) on the infrared radiation under conditions that may not be purely adiabatic.

A second modeling uncertainty was addressed by modifying a test specimen. Specifically, the resin-rich layer of epoxy on the surface of the notched (0,90,45,-45)<sub>s</sub> T300/5208 laminate in Figure 6a was removed by sanding until bare fibers were visible with an optical microscope. In this manner, it could be determined whether or not the resin-rich layer was masking the temperature variation of the fibers. The SPATE scan of the sanded specimen is shown in Figure 17. Despite the increased surface fiber area visible to the infrared detector, the overall magnitude of thermoelastic emission increased. There was also a slight change in the con-

Table 2. Force equilibrium assessment in the micromechanical model

Laminate†	$\sigma_1^f$ ‡	$\sigma_2^f$ ‡	$(V^f \sigma_1^f + V^m \sigma_1^m)$ ‡	$\sigma_2^f$ and $\sigma_2^m$ ‡
(0) <sub>8t</sub>	20.00	0	20.39	-.09
(90) <sub>8t</sub>	0	1.31	-.09	1.36
(0/90) <sub>2s</sub>	20.12	.36	20.49	.29
(90/0) <sub>2s</sub>	-.45	1.29	-.54	1.35
(±45) <sub>2s</sub>	2.97	.25	3.02	.25

† Applied longitudinal strain ( $\epsilon_x$ )  $\approx 1000\mu$ .

‡ Units of stress are ksi.

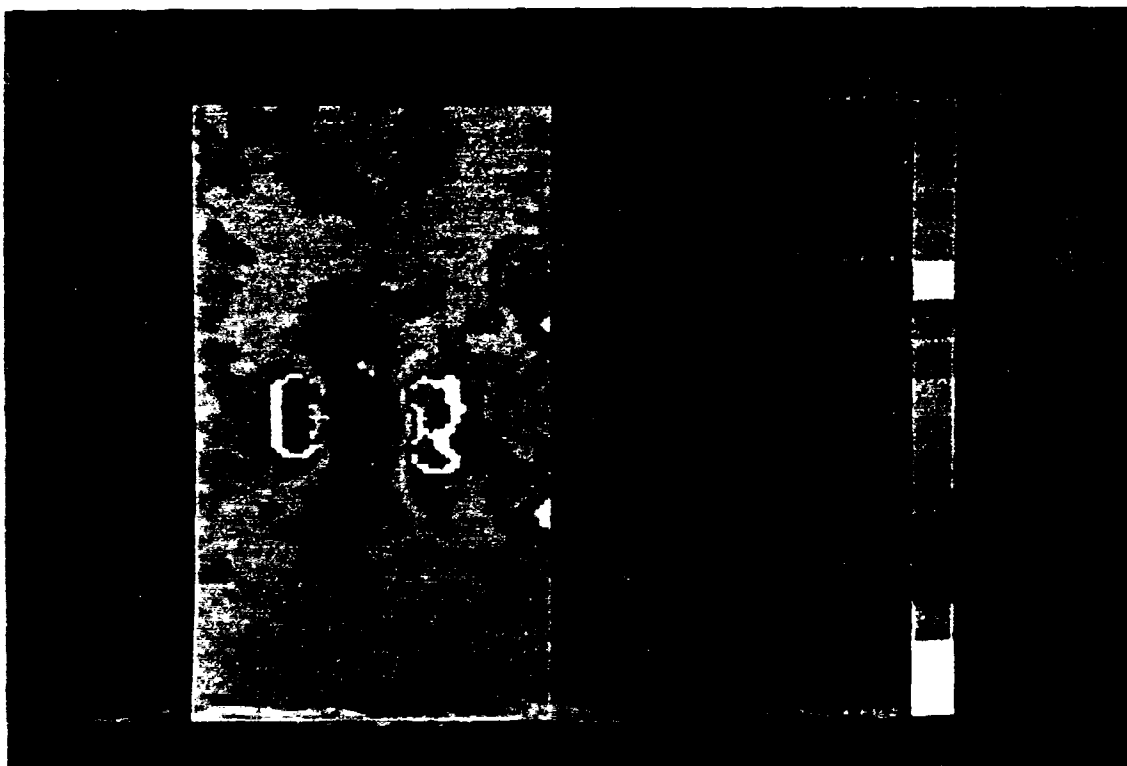
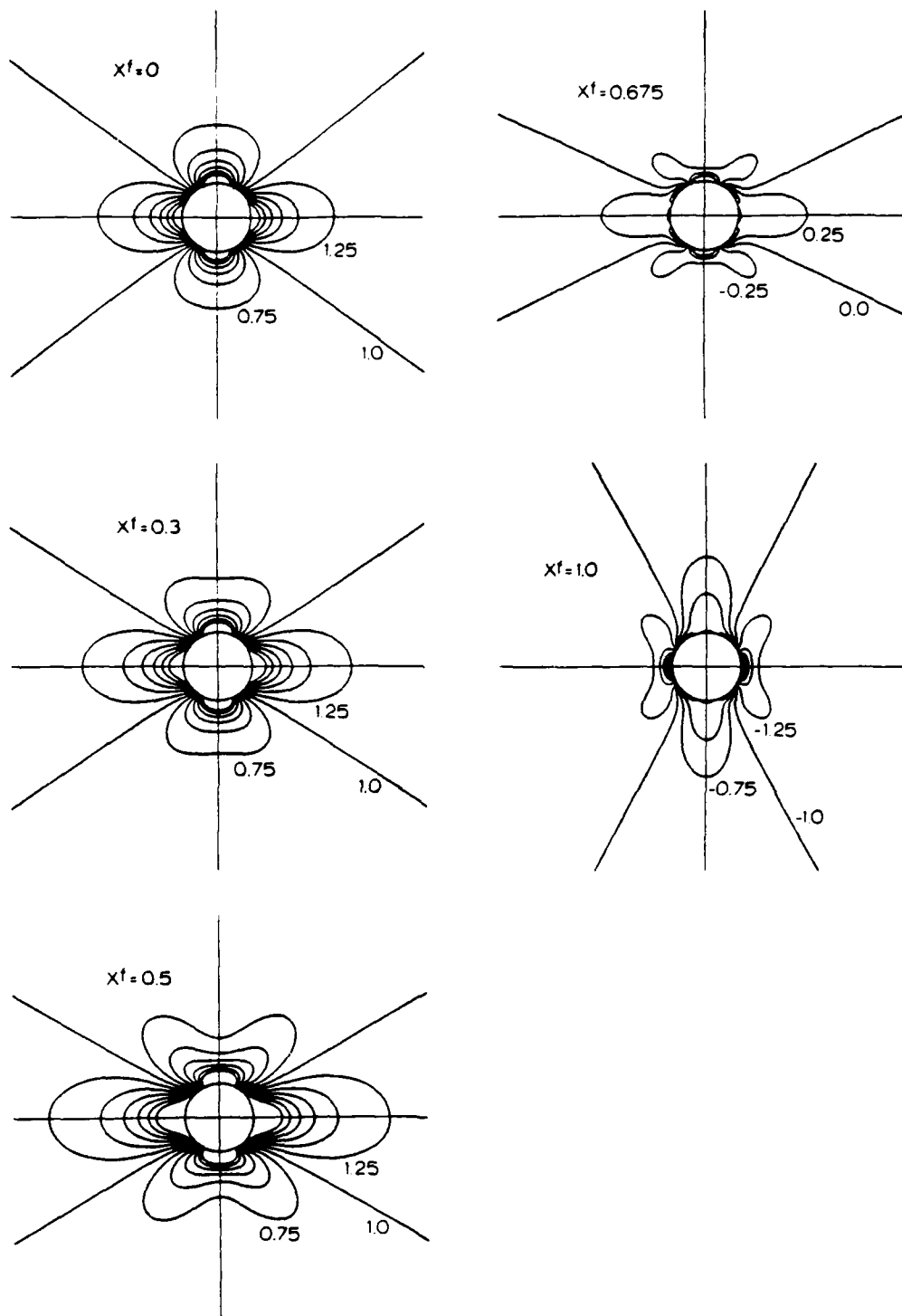


Figure 17. SPATE thermograph of a  $(0,90,45,-45)_s$  carbon epoxy laminate with the resin-rich surface layer removed: (c.f. Figure 6a)

tour pattern, although disagreement with the prediction (Figure 16a) persisted. The analysis was then modified to allow the specification of different contributions of the fibers and matrix to the rule of mixtures expression for net temperature change ( Eq. 31). The results of this modification are shown in Figure 18, where the contribution of the fibers varied from zero to 100 percent. At 67.5 percent fiber contribution, the predicted far-field thermoelastic emission was zero. Above 67.5 percent fiber contribution, the far-field thermoelastic emission was greater than zero under tensile loads, and below 67.5 percent it was less than zero. Since the measurements indicated that the far-field thermoelastic emission was less than zero under tensile loads, the theory predicted that the fibers must contribute less than 67.5 percent to the measurements. In any case, none of the patterns shown in Figure 18 agree remarkably with the measurements before or after sanding.

The third modeling uncertainty addressed was the influence of interply heat conduction. A fully-three-dimensional analysis of in-plane and out-of-plane conduction with the sole source of heat generation being the adiabatic thermoelastic effect in various layers was beyond the scope of the present investigation. Hence, the temperature changes of the outermost one to four plies were averaged with unequal weights. The justification for neglecting intraply conduction was that the thickness of the plies (0.005 in.) was very small, providing a short conduction path relative to those distances involved in intraply conduction that were likely to affect the contour patterns. The results, shown in Figure 19 for the (0,90,45,-45)<sub>s</sub> laminate, were calculated using  $V^f = 0.55$  in the rule of mixtures expression (31) as well as in the computed material constants. The prediction using a 70 percent first ply contribution, and 30 percent second ply contribution agreed best with the measurements, although there is still room for improvement. It is interesting to note that, on a point-to-point basis, the average of the adiabatic temperature changes in the 0- and 90-deg. plies equaled that for the +45- and -45-deg. plies, which also equaled the average for all eight plies in the laminate.

Despite the difficulties in predicting SPATE measurements discussed above, we still face the ill-posed problem of computing the state of deformation in the material from temperature



**Figure 18. Predicted SPATE patterns in a center-notched (0,90,45,-45), carbon epoxy laminate with varied contributions of the constituents in the surface ply**

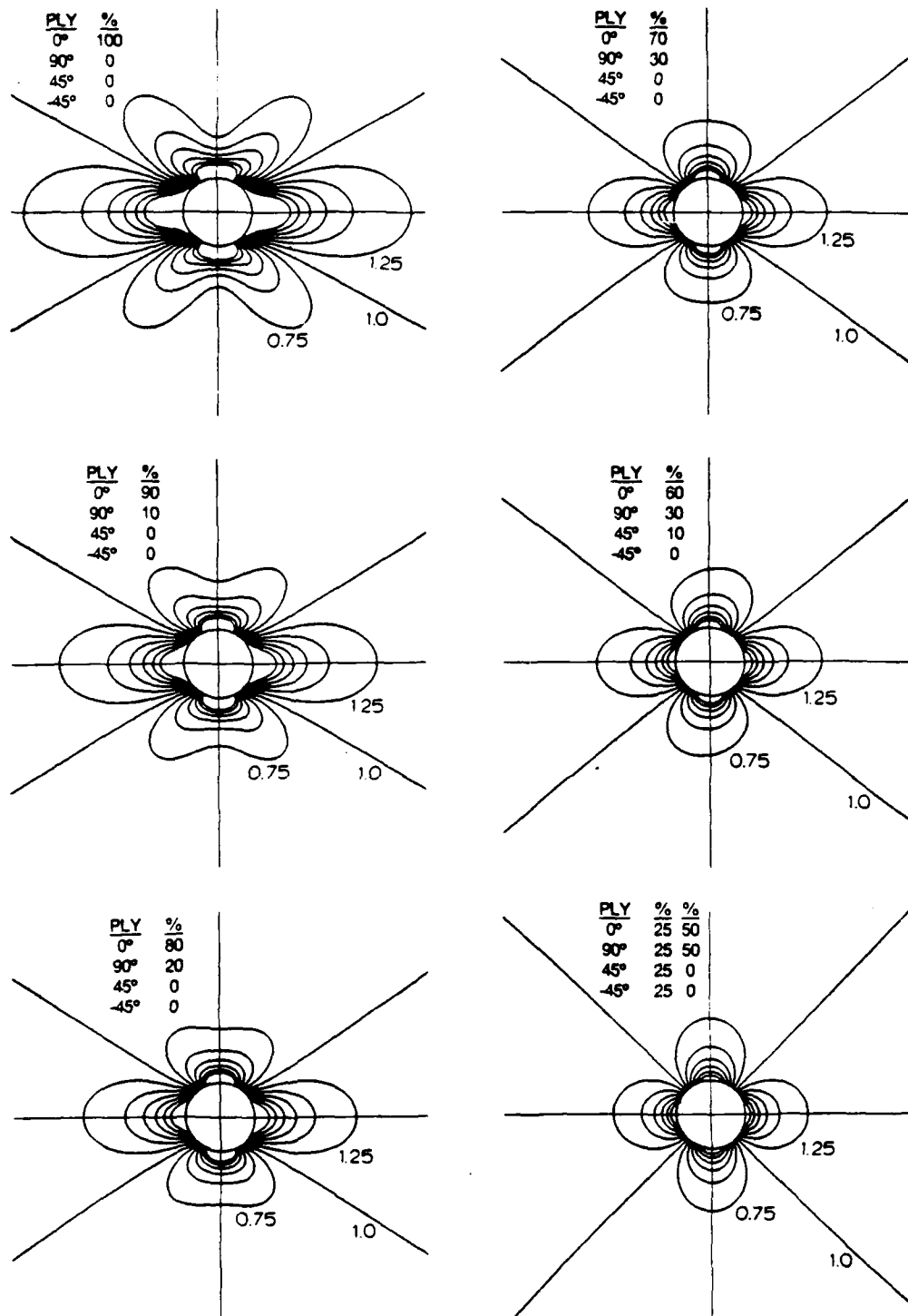


Figure 19. Predicted SPATE patterns in a center-notched (0,90,45,-45), carbon epoxy laminate with varied ply influences

change measurements. Recalling Figure 9 on page 33, there are infinitely-many combinations of stress components that produce the same temperature change. This fact is especially problematic when damage is introduced into the specimen and the evaluation of the stress or strain field associated with the damage is attempted. Therefore, the evaluation of stress or strain redistribution due to damage is to be approached with this limitation in mind.



### III

## Basic Material Characterization

### 3.1 *Monotonic Strength*

As was mentioned in the description of specimen design, a series of compression tests with different unsupported gage lengths revealed that a 2.5-in. gage length would be sufficiently small to avoid the weakening effects of column-type buckling in all specimens. A longer unsupported length could have been used with the orthotropic stacking sequence, but a uniform length was chosen for all specimens for simplicity of fabrication. The orthotropic stacking sequence occasionally exhibited an in-plane, shearing failure mode along a -45 deg. angle, which, in the case of DEN specimens, would extend into the grips if the specimen was shorter than 2.4 inches. The tensile and compressive strengths of virgin specimens loaded monotonically to failure are listed in Table 3. Specimens with an unsupported length (UNSL) of 2.4 or 2.5 in. were used to compute the mean, standard deviation and variance of the ultimate gross section stress for each specimen type [71]. A few noteworthy items from these data are highlighted below.

**Table 3. Monotonic strength of virgin specimens**

Specimen Type	Tensile Strength, $S_t^o$ (ksi)*			Compr. Strength, $S_c^o$ (ksi)*		
	$\bar{x}$	s	var, %	$\bar{x}$	s	var, %
3501-A-CN	42.3	3.8	9.1	-43.8	.95	2.2
3501-A-DEN	45.8	2.4	5.2	-44.2	3.2	7.3
3501-B-CN	59.2	1.9	3.2	-52.8	.32	.6
3501-B-DEN	64.9	2.2	3.4	-53.6	1.3	2.5
1808-A-CN	39.4	.81	2.0	-45.2	1.0	2.3
1808-A-DEN	42.5	2.7	6.2	-48.1	3.8	7.9
1808-B-CN	54.1	2.8	5.1	-55.2	1.7	3.0
1808-B-DEN	55.9	1.6	2.8	-56.6	2.9	5.1

\* Stresses computed over the gross, unnotched cross-sectional area. Data include mean ( $\bar{x}$ ), standard deviation (s), and variance (var); sample size is three.

- The quasi-isotropic 3501-6 material was stronger in compression than in tension, while the opposite situation prevailed with the orthotropic layup. One may surmise that the in-plane shear failure mode of the orthotropic laminate in compression may contribute to the relative lack of compressive strength, but no such relationship between tensile and compressive strengths was observed in the orthotropic 1808 material. Indeed, 1808 specimens of either stacking sequence were always stronger in compression than in tension.
- In tension, 3501-6 specimens were about 10% stronger than analogous 1808 specimens. In compression, 1808 specimens were slightly stronger than 3501-6 specimens.
- A lower local strain (measured by a small strain gage near the notch) was measured near failure in the orthotropic layup of both material systems [71]. The orthotropic layup was also approximately 50% stronger in tension and 25% stronger in compression than the quasi-isotropic layup for both materials.
- Near failure, there was less local strain near the notch tip in the DEN configuration than in the analogous CN configuration [71].

Briefly, failure modes in tension consisted of clean laminate fractures (little delamination) initiating at the point of highest stress concentration near the notch or adjacent to but not directly in contact with the notch. In the latter mode, the surface 0-deg. ply fractured along an underlying +45 deg. ply direction, beginning at the point where the large matrix cracks tangent to the notch in these two plies intersect. In the DEN configurations, failure almost always initiated at one of the notches first (with audible acoustic emissions and visible fiber breaks in the surface ply). In some cases, failure was instantaneous after the first notch failure, and in other cases the specimen continued to bear additional load after the first acoustic event.

Under compression loading, delaminations were widespread in all specimen types. There were also signs of local crushing and ply buckling near the notches. As described earlier, the orthotropic laminates occasionally exhibited an in-plane shear mode of failure which either extended entirely or partially across the specimen width. The fracture surface of the outer-

most 0-deg. ply in the shear failures was either a staircase-type or extremely smooth. In all specimen types except 1808-B, there was at least one compression failure where a portion of the surface 0-deg. ply was intact, but delaminated.

## 3.2 Fatigue Life

Plots of applied stress amplitude versus fatigue lifetime for the eight specimen types are shown in Figure 20. Each figure illustrates the S-N data for a particular material system and lamination arrangement (both notch configurations) on a semi-log scale. If it is hypothesized that the data must pass through one of the components of strength (either tensile or compressive, depending on the failure mode) for failure during the first cycle, it is obvious that a more complete data set would have either a knee or a gradual bend to achieve the necessarily concave-down appearance of a continuous curve. The data would appear more linear without the semi-log scale. Comparing the data, it can be seen that the S-N curve of the (0,45,0,-45)<sub>s4</sub> laminate is steeper than that of the (0,45,90,-45)<sub>s4</sub> laminate for both materials and notch types. The DEN data points fall either on or above the CN points, which is consistent with the superior monotonic strength of virgin DEN specimens.

In Table 4, the two load levels chosen for the primary tests of each specimen type are listed in two forms: absolute units, and normalized by the corresponding monotonic tensile and compressive strength of virgin specimens. Except for the high-load, quasi-isotropic, CN specimens, there were no large differences in the normalized load levels for the AS4/3501-6 and AS4/1808 materials. The higher high load level in the AS4/3501-6 (0,45,90,-45)<sub>s4</sub> CN specimens compared to similar AS4/1808 specimens resulted in shorter fatigue lifetimes in the AS4/3501-6 specimens (about 1K cycles vs. 10K cycles). To obtain the targeted high- and low-load fatigue lifetimes, normalized loads had to be higher in the (0,45,0,-45)<sub>s4</sub> laminates

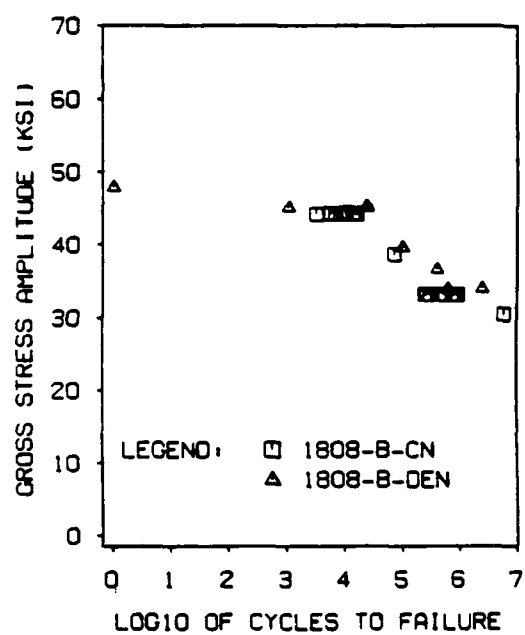
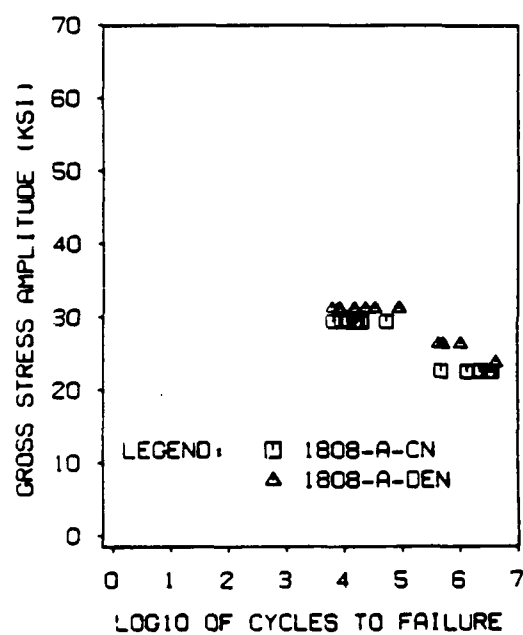
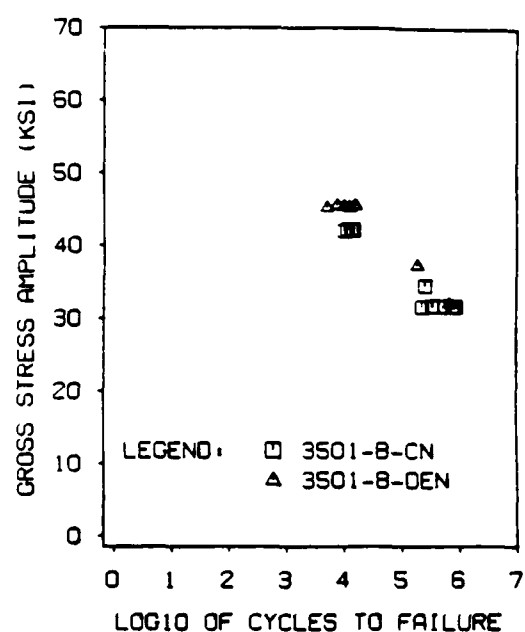
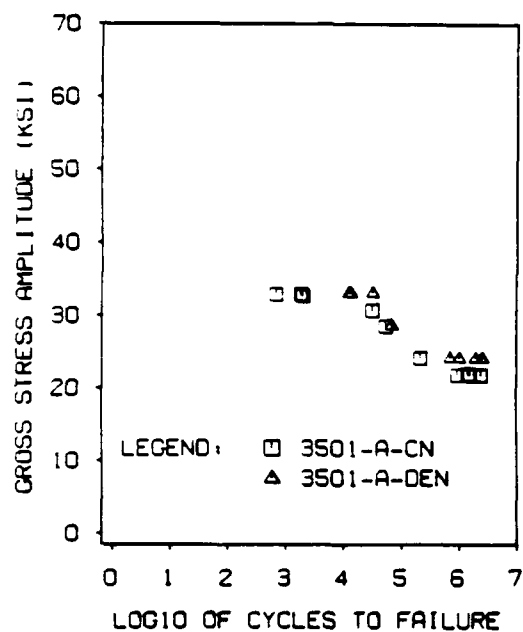


Figure 20. Stress vs. life data for test specimens

**Table 4. Cyclic load levels (R=-1) for fatigue tests**

Material	Stack	Notch	High Load, $S_a$			Low Load, $S_a$		
			ksi	$S_a/S_t^o$	$S_a/S_c^o$	ksi	$S_a/S_t^o$	$S_a/S_c^o$
AS4/3501-6	(0/45/90/-45) <sub>s4</sub>	CN	32.8	.78	.75	21.9	.52	.50
		DEN	33.2	.72	.75	24.3	.53	.55
	(0/45/0/-45) <sub>s4</sub>	CN	42.2	.71	.80	31.7	.54	.60
		DEN	45.6	.70	.85	32.2	.50	.60
AS4/1808	(0/45/90/-45) <sub>s4</sub>	CN	29.4	.75	.65	22.6	.57	.50
		DEN	31.3	.74	.65	26.5	.62	.55
	(0/45/0/-45) <sub>s4</sub>	CN	44.2	.82	.80	33.1	.61	.60
		DEN	45.3	.81	.80	34.0	.61	.60

than in the  $(0,45,90,-45)_{s4}$  laminates, especially for the high load level. This requirement is consistent with the steeper S-N curve of the  $(0,45,0,-45)_{s4}$  specimens.

### **3.3 Stiffness Measurements**

Initial stiffness measurements of virgin specimens during the first load cycle of fatigue tests are given in Table 5. Due to the slight non-linearity of the stress-strain behavior of the notched specimens, stiffness measurements at the low and high load amplitudes are listed separately. The AS4/3501-6 material was slightly stiffer than the AS4/1808 material in all cases. The tensile stiffness of the AS4/3501-6 material increased slightly with increased load, while that of the AS4/1808 material remained approximately the same. In both material systems, the compressive stiffness decreased with higher loads. Scatter in the measurements was higher in the DEN specimens than in the CN specimens. A possible explanation of this observation is that the in-plane deformations directly over the notch dominate the slight, though inevitable, out-of-plane deformations, reducing the scatter when the extensometer is positioned across the notch.

Throughout each fatigue test, tensile and compressive stiffness measurements were normalized by their respective values recorded during the first load cycle of the subject specimen. Typical stiffness records during the lifetime of each of the eight specimen types during high-load and low-load fatigue are illustrated in Figure 21 and Figure 22, in which high-load tests are indicated by (H), and low-load tests are indicated by (L). The horizontal axes in the stiffness plots are normalized life axes obtained by dividing the actual number of cycles by the number of cycles to failure for that particular specimen. Stiffness curves recorded with CN specimens and low-load levels were more repeatable than those recorded with DEN specimens and high load levels. In fact, variations caused by the unsymmetric development of

**Table 5. Tensile and compressive stiffnesses of virgin specimens**

Specimen Type	High Load						Low Load					
	$E_t^p$ (Msi)*			$E_c^p$ (Msi)*			$E_t^p$ (Msi)*			$E_c^p$ (Msi)*		
	$\bar{x}$	s	n	$\bar{x}$	s	n	$\bar{x}$	s	n	$\bar{x}$	s	n
3501-A-CN	4.59	.06	12	4.20	.13	12	4.51	.14	7	4.21	.17	7
3501-A-DEN	6.33	.29	6	5.84	.49	6	6.28	.21	4	5.90	.34	4
3501-B-CN	6.28	.22	14	5.45	.26	14	6.20	.12	6	5.73	.14	6
3501-B-DEN	9.69	.36	13	8.50	.50	13	9.42	—	1	8.56	—	1
1808-A-CN	4.57	.11	22	4.18	.13	22	4.59	.07	23	4.28	.09	23
1808-A-DEN	6.26	.10	21	5.67	.19	21	6.19	.16	3	5.74	.15	3
1808-B-CN	6.25	.15	23	5.56	.19	23	6.26	.15	22	5.70	.12	22
1808-B-DEN	9.46	.18	3	8.34	.23	3	9.31	.37	3	8.61	.41	3

\* Measured with a front-mounted, 1-in. extensometer. Data include mean ( $\bar{x}$ ), standard deviation (s), and sample size (n).



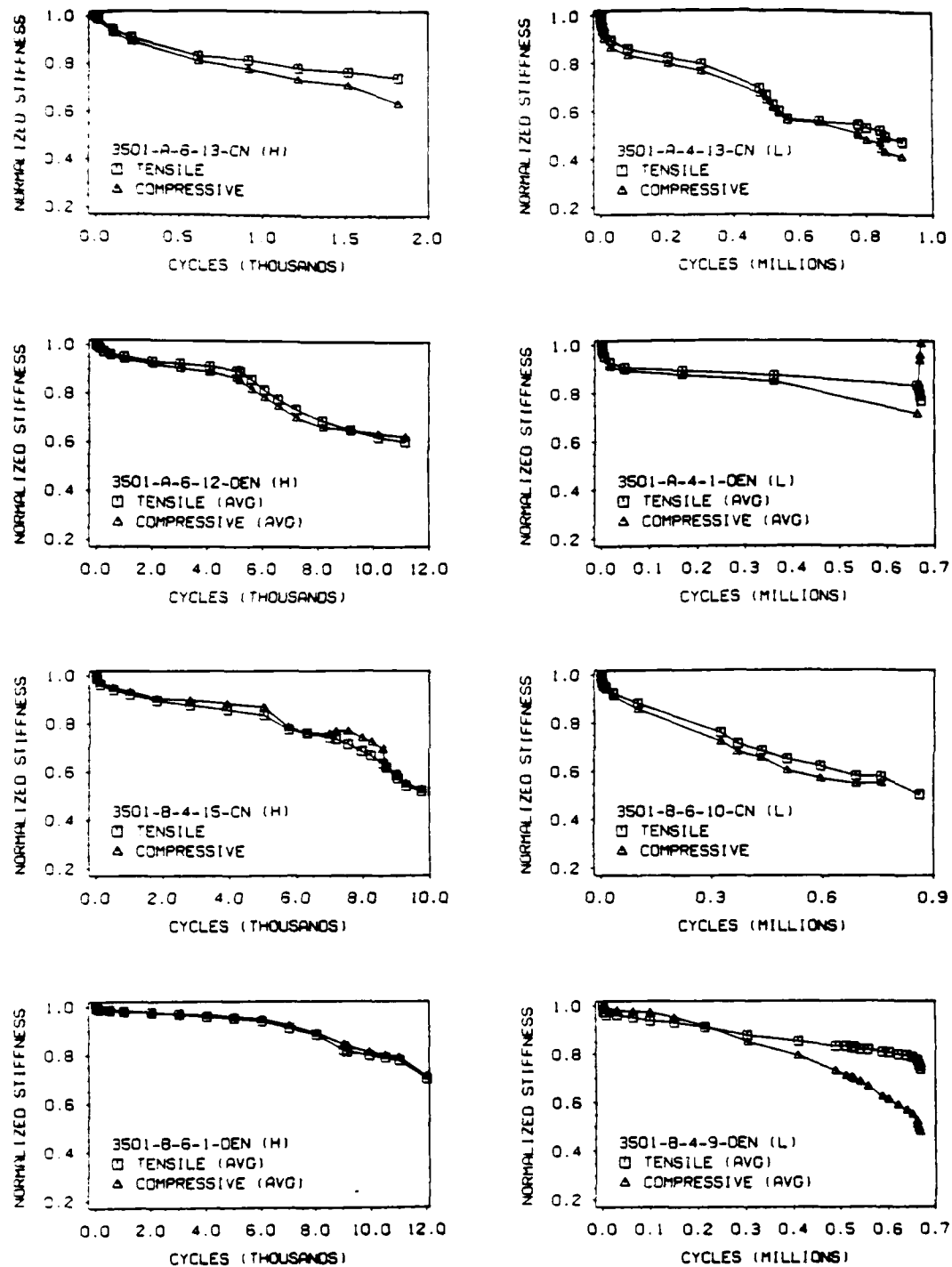


Figure 21. Stiffness change in AS4/3501-6 specimens

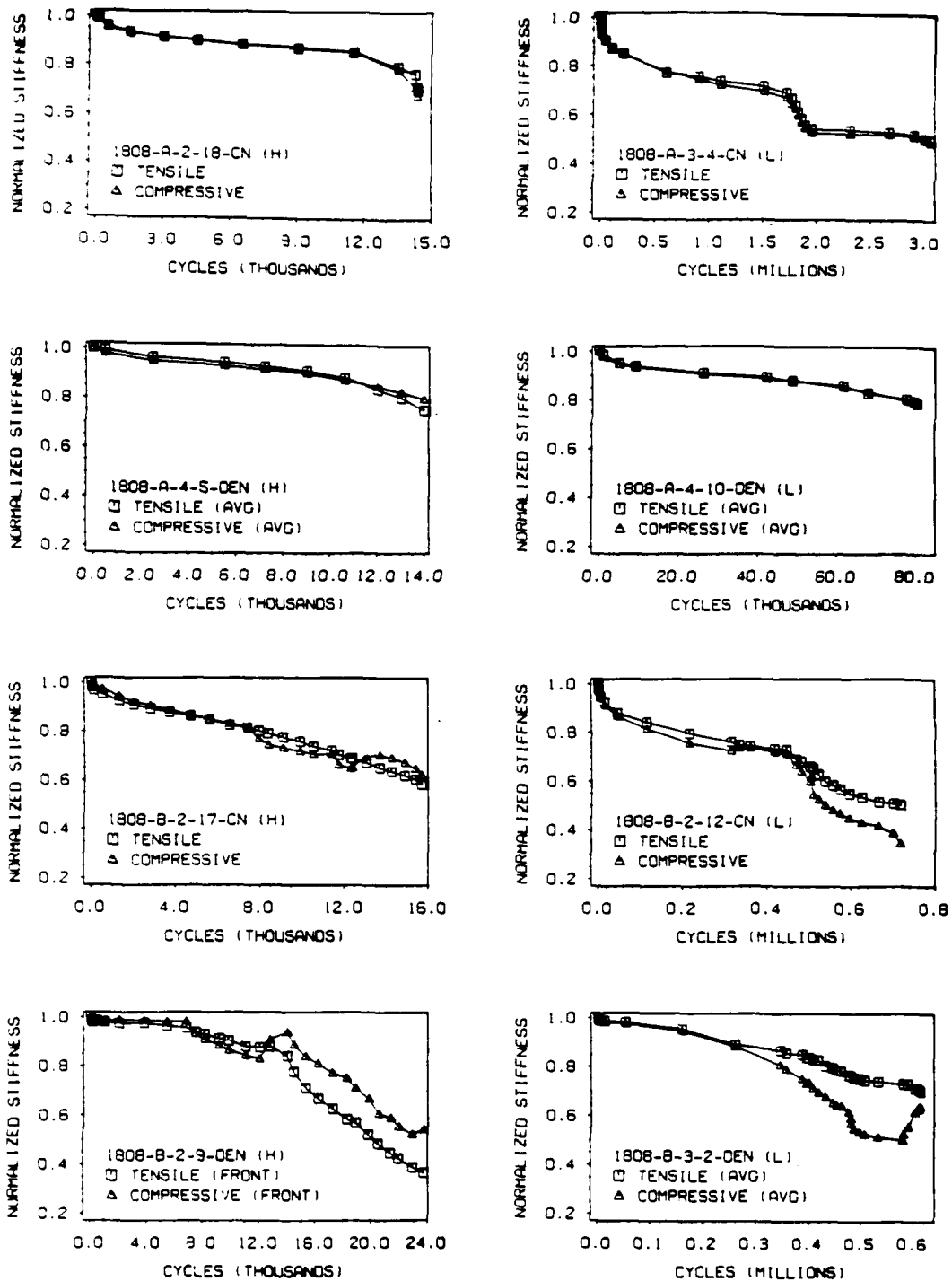


Figure 22. Stiffness change in AS4/1808 specimens

damage in DEN specimens were so great that strains measured by front- and back-mounted extensometers had to be averaged to eliminate the bending strain component. The large in-plane deformations across the notch prevented the relatively small out-of-plane deformations from becoming a problem in CN specimens. Most of the stiffness data for DEN specimens in Figure 21 and Figure 22 were computed by averaging front and back surface strains (indicated by "AVE"), though, in some cases, only front surface stiffnesses were available (indicated by "FRONT"). Stiffness changes in high-load specimens reflected the highly concentrated nature of damage growth in those specimens. For example, damage that initiated first in one area of the specimen (eg. front side) grew most rapidly in that same area and led to failure of the specimen before damage at analogous locations in the laminate (eg. back side) initiated and grew an equal amount. These variations in damage growth paths caused variations in the stiffness curves as well. Because of its more symmetric nature, low-load fatigue damage resulted in less stiffness variation among specimens.

In general, the rates of change of stiffness corresponded well with the associated rates of damage growth. Separate periods (or stages) of damage growth could be identified during a fatigue test by observing the slope of the stiffness versus cycles curves. The occurrence of rapid damage initiation and growth near the notch(es) was easily identified by the rapid, but slowing, stiffness drop at the beginning of each test. The DEN specimens had less stiffness drop during this first stage of damage development than the CN specimens, especially in the orthotropic laminates. Part of this behavior can be attributed to the more remote location of the extensometer relative to the damage initiation sites in the DEN specimens, and part to the lesser tendency of  $(0,45,0,-45)_{s4}$  laminates to delaminate during "stage I" damage development.

After stage I was complete, stiffness measurements were greatly influenced by the particular patterns of damage growth that appeared in the different specimen types. For example, after a second period of relatively slow matrix cracking during low-load fatigue, the center-notched  $(0,45,90,-45)_{s4}$  laminates usually underwent a third period of rapid delamination

growth in the longitudinal direction, resulting in a short-lived period of rapid stiffness decline. A fourth period of slower matrix cracking ensued, followed by a fifth stage reflecting the rapid delamination growth that typically preceded fatigue failure in this type of test. In contrast, during high-load tests of  $(0,45,90,-45)_{s4}$  CN specimens, there were only three stages of damage growth and stiffness change during the lifetime. Among the specimen types investigated presently, the difference between high- and low-load fatigue response was most dramatic in  $(0,45,90,-45)_{s4}$  CN specimens.

The  $(0,45,0,-45)_{s4}$  laminates had about the same net stiffness drop at failure as the  $(0,45,90,-45)_{s4}$  laminates; their rate of change, however, was more uniform. A prominent feature of all tests, especially those involving  $(0,45,0,-45)_{s4}$  laminates, was that the second half of fatigue life was characterized by a "bumpy" stiffness curve due to the non-symmetric appearance of delaminations near the front and back surfaces of the specimens. This "bumpiness" occurred at a relatively larger fraction of life during high-load tests.

The three stopping points for destructive testing techniques — the early, middle, and late stages of fatigue life — were estimated using the characteristic stiffness curves and damage development patterns recorded with X-ray radiography. The early stopping point, about 5-10 percent of life, was at or slightly before the stabilization of the stiffness decline at the end of stage I. The middle stopping point was the most difficult to find due to the lack of repeatable stiffness values or changes in rate of the stiffness decline between 40 and 60 percent of life in many tests. Most often, the beginning of the undulations of the stiffness curves (especially compressive stiffness) and the attainment of a particular cumulative stiffness change were used to predict the middle-life stopping point. The late-life stopping point was also difficult to detect because the actual stiffness values near the end of life were typically scattered over 10-30 percentage points in CN specimens (more in DEN specimens, due to bending effects). To avoid this problem, late life was estimated based on the fairly-predictable sudden increase in damage growth, audible acoustic emissions, and stiffness change during the last 10 percent

of life. In cases where the percentage of life based on stiffness was in doubt, X-ray radiographs usually provided definitive information.

## **IV**

### **Fatigue Damage Mechanisms**

In the following description of fatigue damage mechanisms in notched specimens, certain orientations and locations are referred to repeatedly. The longitudinal direction is along the load axis of the specimen, coinciding with the 0-deg. fiber direction. The transverse direction is oriented at 90 degrees to the longitudinal direction, in the plane of the specimen.

Specific damage mechanisms are also referred to often in the text. Among the more ubiquitous damage types are primary and secondary matrix cracks parallel to the fibers in a particular ply. Primary matrix cracks are those which emanate directly from any boundary of the specimen, including the notch(es) and straight edges. Secondary matrix cracks are the remainder of the cracks that do not directly intersect a boundary. Incremental, step-wise ply fractures denote the through-the-ply fracture of fibers that occur in short, sudden steps in certain specimens.

This documentation of fatigue damage mechanisms in notched composite laminates is based on the large experimental program discussed earlier. Of course, due to the nature of experimental investigations, there is some degree of variability in the results. The results

included herein represent *typical* behaviors, and are not meant to be comprehensive. Descriptions of damage initiation and growth in center-notched specimens of each material-laminate combination are presented in detail. Similarities in damage mechanisms in specimens with different notch configurations are used to reduce the volume of material presented. Hence, the most complete descriptions are to be found in the sections on CN specimens. The effects of material system, lamination arrangement, load level, and notch configuration on fatigue damage mechanisms are discussed in the summary at the end of this chapter. For organizational reasons, the discussions of stress redistribution and residual strength during the fatigue process are presented in separate sections.

## **4.1 AS4/3501-6, Quasi-Isotropic Laminate**

### **4.1.1 Center-Notched Specimens**

#### **4.1.1.1 High Load Level**

The high load level chosen for the CN (0,45,90,-45)<sub>s4</sub>, AS4/3501-6 specimens, 32.8 ksi, resulted in fatigue lifetimes of approximately 500 to 2000 cycles. Fatigue damage under this high amplitude loading was evident in a radiograph taken after the first full load cycle of a test (Figure 23). Primary matrix cracks were present in all plies adjacent to the notch. The off-axis plies had secondary matrix cracks as well. The 15-deg. radiograph (not shown) indicated the presence of 0-deg. ply pull-out (delamination) in the four corners formed where the 0-deg. tangent cracks meet the hole boundary.

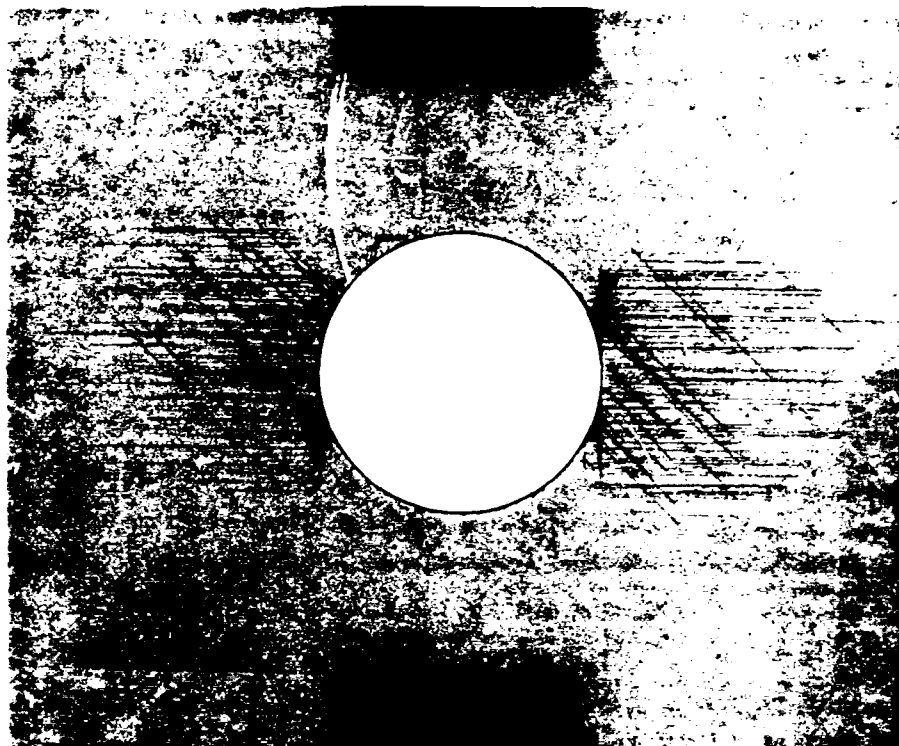


Figure 23. Radiograph of a center-notched, AS4/3501-6,  $(0,45,90,-45)_{s4}$  specimen after one high-level load cycle

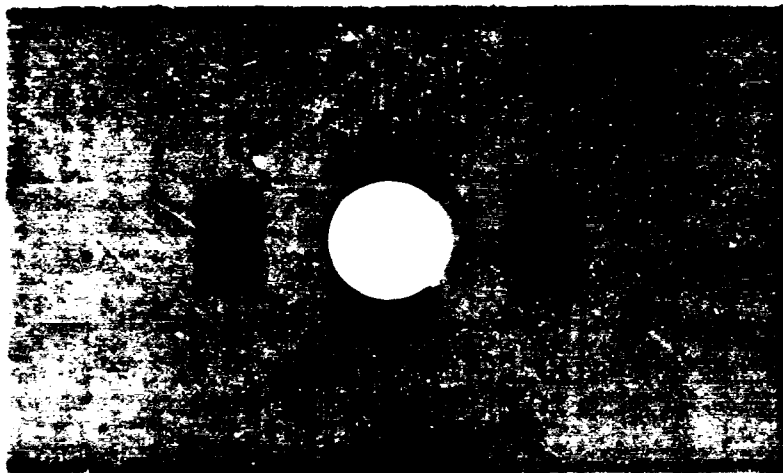


Typical 0- and 90-deg. radiographs of early-life residual strength specimens are shown in Figure 24a and Figure 25a, respectively. Off-axis matrix cracks had reached the straight edges of the specimen, and incremental fractures of the surface 0-deg. ply were growing in a step-wise manner along the large +45-deg. matrix cracks tangent to the hole boundary. Based on visual and audible information obtained during the slow loading of the specimen for stiffness measurements, the 0-deg. ply fractures are believed to occur only during the compressive portion of the load cycle, probably by the mechanism of microbuckling. Immediately after a 0-deg. ply fracture occurred, a 0-deg. matrix crack formed at the tip of the new crack, and a delamination initiated and grew between the parallel matrix cracks at each end of the new "step" (Figure 26a). In some instances, narrow strips of the surface 0-deg. ply delaminated without the presence of 0-deg. ply fracture. Delaminations in these instances apparently prevented ply fractures from occurring during the remainder of the lifetime by decoupling damage in adjacent plies. Delaminations on all the 0/45 interfaces through the thickness can be seen in the early-life edge radiograph. Interior 0/45 interface delaminations were all approximately the same size in the longitudinal direction, but they were shorter than the 0/45 interface delaminations involving the surface 0-deg. plies.

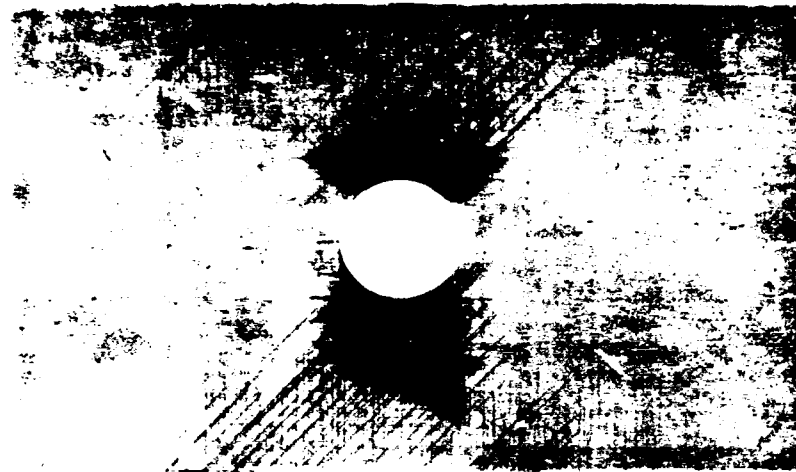
Radiographs of typical middle-life specimens are shown in Figure 24b and Figure 25b. Zero-deg. fiber fractures initiated in the next-to-outermost 0-deg. ply groups (plies 8, 9, 24, and 25). Delaminations also initiated and grew on all interfaces adjacent to the 90-deg. plies. During subsequent cycling, off-axis matrix cracks initiated and grew at the straight edges. All 0<sub>2</sub> ply groups fractured near the transverse centerline of the hole. Zero-deg. ply fracture paths still followed underlying +45-deg. matrix cracks, but jumped to different +45-deg. cracks such that a generally transverse direction of growth was maintained (i.e., the 0-deg. ply fracture paths remained close to the transverse centerline through the notch. Delaminations on 0/45 interfaces remained only slightly longer at locations closer to the surface).



(a)



(b)



(c)

Figure 24. Radiographs of center-notched, AS4/3501-6, (0,45,90,-45)<sub>s4</sub> specimens during high-load fatigue: (a) early; (b) middle; and (c) late life

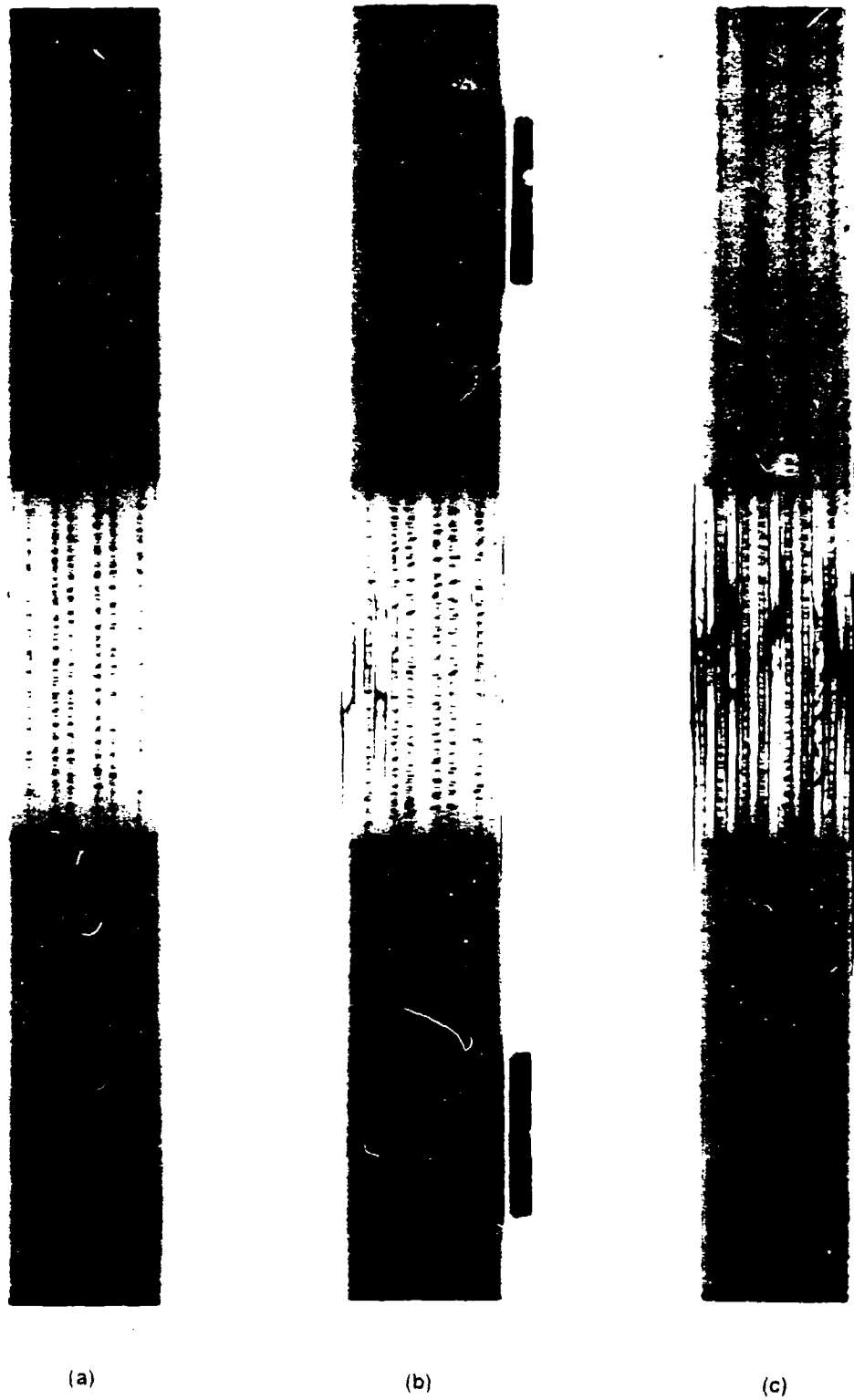
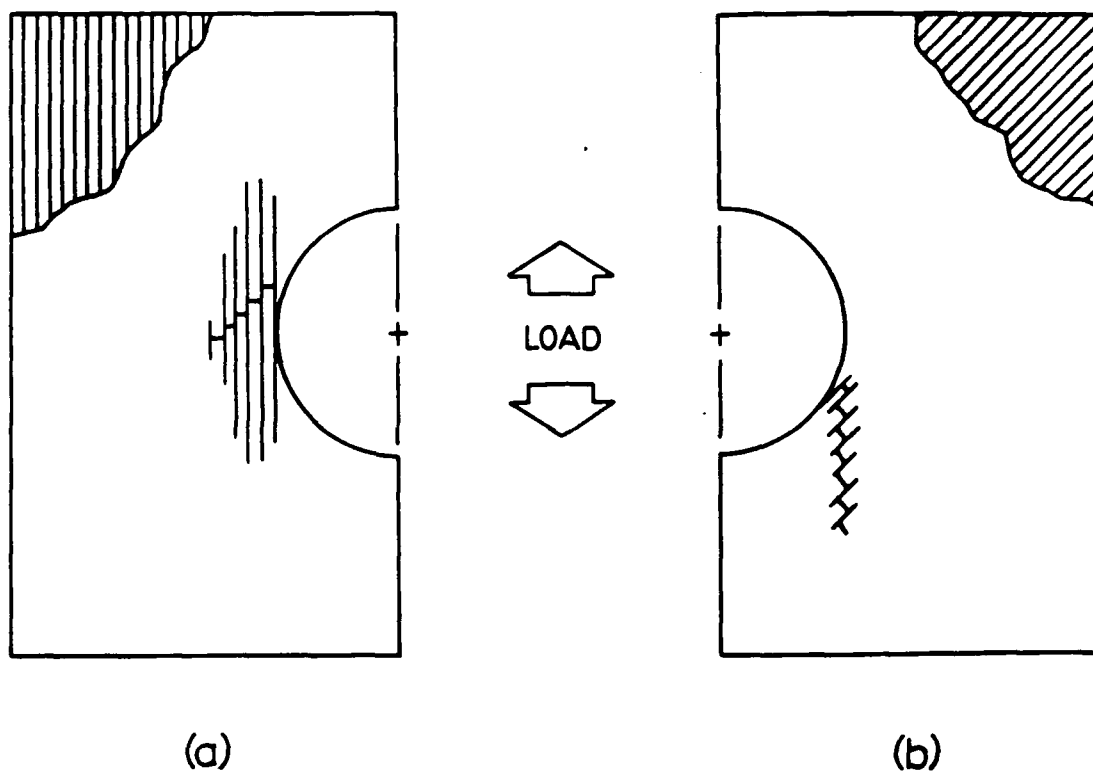


Figure 25. Edge radiographs of center-notched, AS4/3501-6, (0,45,90,-45)<sub>s4</sub> specimens during high-load fatigue: (a) early; (b) middle; and (c) late life



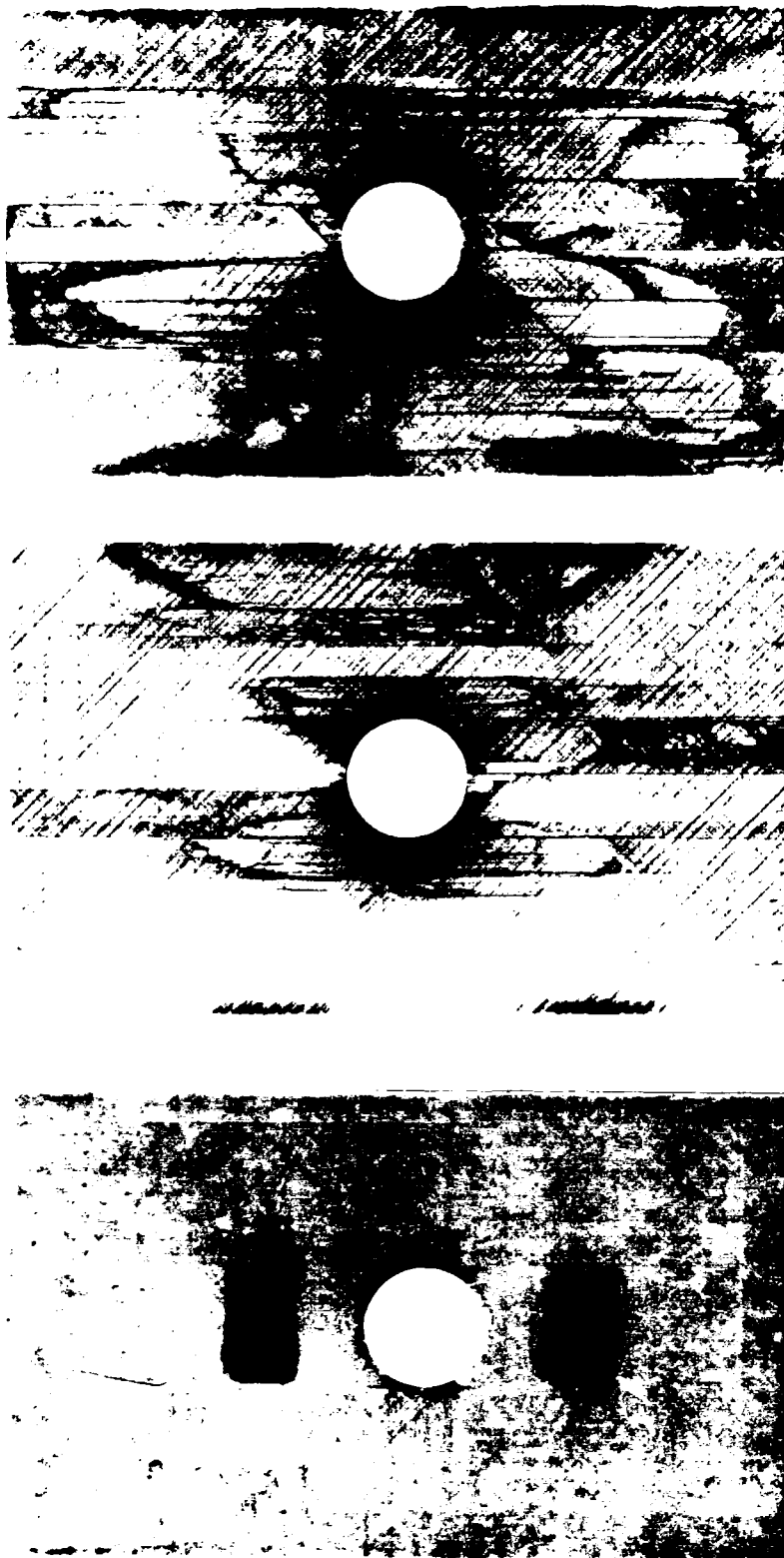
**Figure 26. Schematic of incremental, step-wise surface ply fractures influenced by matrix cracks in adjacent plies: (a) 0-deg. ply in  $(0,45,90,-45)_{s4}$  and  $(0,45,0,-45)_{s4}$  laminates; (b) 45-deg. ply in  $(0,45,0,-45)_{s4}$  laminates**

At the late-life residual strength measurement point (impending fatigue failure), typical radiographs were as shown in Figure 24c and Figure 25c. Fatigue failure of the specimens was by crushing, followed by delamination.

#### **4.1.1.2 Low Load Level**

Fatigue lifetimes under the low amplitude cyclic load, 21.9 ksi, were between 900K and 2.4M cycles. On the first load cycle, primary matrix cracks initiated in the 0-, -45-, and 90-deg. plies near the notch. Soon after this time, primary matrix cracks appeared in the +45-deg. plies near the notch, followed by secondary 90-deg. matrix cracks along primary -45-deg. cracks. By about one thousand cycles, delaminations initiated at the 0/45 interfaces through the thickness, although those involving the surface plies were longer in the longitudinal direction. This type of delamination initiated in the small area of material bounded on three sides by the hole and the 0- and 45-deg. primary matrix cracks tangent to the hole in the second and third quadrants. Additional delaminations on the 45/90 and 90/-45 interfaces also initiated by 1K cycles, at first near the surface, and later closer to the laminate's midplane (Figure 27a and Figure 28a). Secondary matrix cracks in the +45- and -45-deg. plies occurred later, as did surface 0-deg. ply fractures along underlying +45-deg. matrix cracks. Zero-deg. ply matrix cracks and delaminations occurred immediately after the occurrence of incremental 0-deg. ply fractures, which were limited to the surface plies until near fatigue failure. Occasionally, narrow strip-like delaminations of the surface 0-deg. plies initiated along the paths of the primary +45-deg. matrix cracks that originated tangent to the hole and grew in the longitudinal direction. Zero-deg. ply fractures did not occur in these delaminated strips of 0-deg. ply.

The damage growth rate slowed markedly until approximately half of the fatigue lifetime passed (as indicated in the stiffness records in Figure 21 on page 65). After that time, near-surface 0/45 interface delaminations, particularly in the even quadrants, grew rapidly from the



(a)

(b)

(c)

Figure 27. Radiographs of center-notched, AS4/3501-6, (0,45,90,-45)<sub>s</sub> specimens during low-load fatigue: (a) early; (b) middle; and (c) late life

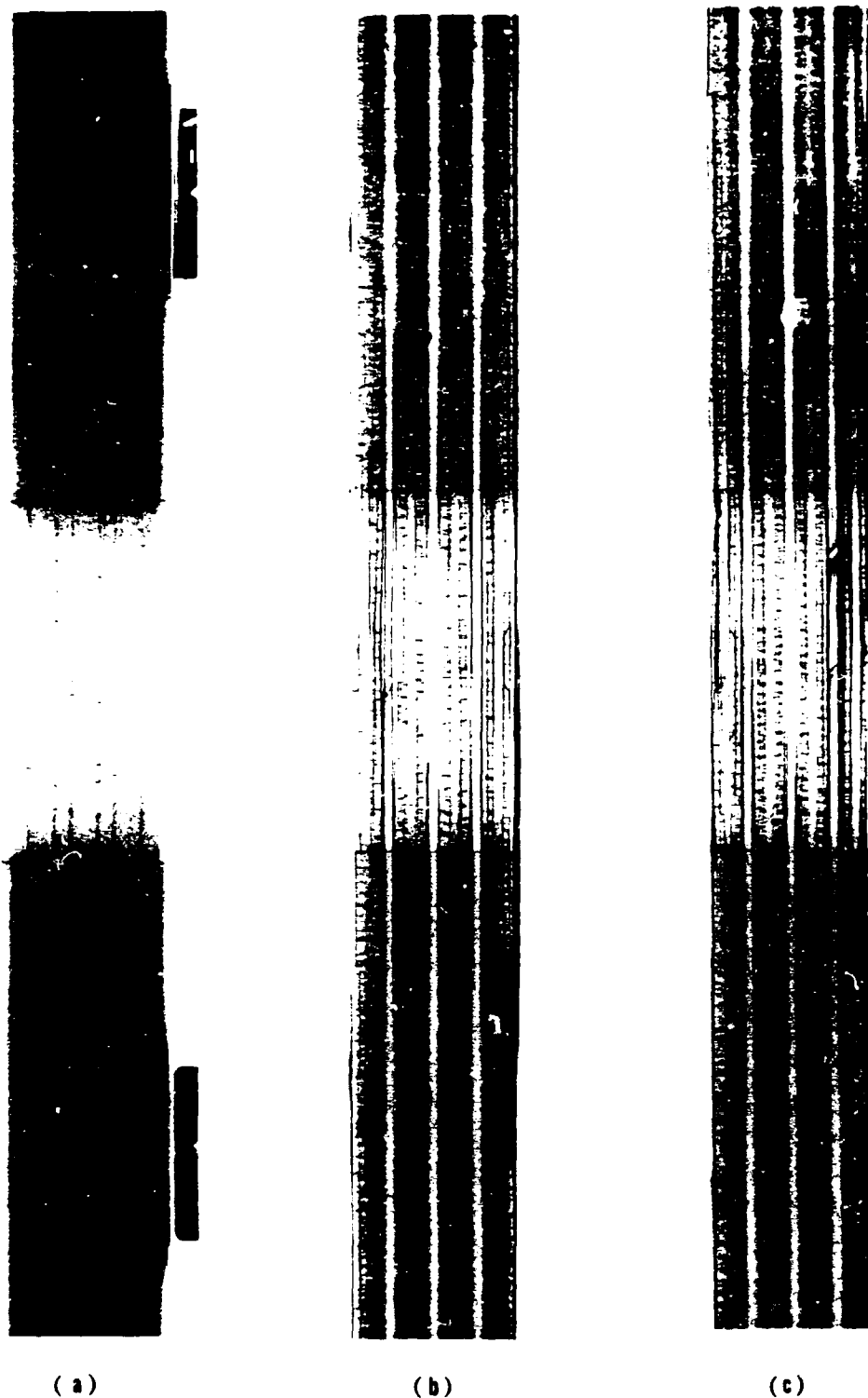


Figure 28. Edge radiographs of center-notched, AS4/3501-3, (0,45,90,-45)<sub>s4</sub> specimens during low-load fatigue: (a) early; (b) middle; and (c) late life

notch in the longitudinal direction until they reached the gripped portion of the specimen. This period of rapid damage growth was used as an easy-to-find stopping point for middle-life residual strength measurements. Off-axis matrix cracks in the middle-life specimens were located throughout the gage-length (Figure 27b and Figure 28b). Delaminations were on all interfaces involving a 0- or 90-deg. ply, although those closer to the surface were longer in the longitudinal direction than those closer to the midplane. Only the 0/45 interface delaminations closest to the surface spanned the hole centerline in the 90-deg. radiograph. Damage growth rate slowed again after the middle-life residual strength measurement point, as indicated in Figure 21b.

Near the end of the fatigue lifetime, delaminations initiated at several interfaces near the straight edges in regions of dense matrix cracks. As with the delaminations that initiated at the notch, edge delaminations favored interfaces closest to the surface of the laminate. In specimens close to fatigue failure, delaminations of the surface 0-deg. plies spanned the distance between the notch and one or both of the straight edges, and the second-outermost 0<sub>2</sub> ply groups fractured in a manner similar to the step-wise fracture of the surface 0-deg. plies described earlier (Figure 27c and Figure 28c). Step-wise 0-deg. ply fractures on the surface initiated near straight-edge-induced 0/45 interface delaminations and grew toward the longitudinal centerline of the specimen. The rate of damage development near the end of the fatigue lifetime increased dramatically, as indicated by the radiographs, the stiffness record (Figure 21b), and audible acoustic emissions during the test. The low-load fatigue failure mode was unstable delamination growth, followed by crushing of the less delaminated plies. The primary contrast in damage between the two load levels was the greater longitudinal extent of matrix damage and lesser amount of 0-deg. ply fracture with the low load.



### 4.1.2 Double-Edge-Notched Specimens

Damage mechanisms in the double-edge-notched, AS4/3501-6, (0,45,90,-45)<sub>s4</sub> specimens under the high (33.2 ksi) and low (24.3 ksi) load levels were essentially similar to those in the center-notched specimens under their respective high and low load levels. The fatigue lifetimes of the high- and low-load specimens ranged between 12K-31K, and 670K-2.5M cycles, respectively.

Since the DEN high-load specimens had slightly longer fatigue lifetimes than the CN high-load specimens, they also had a slightly greater amount of longitudinal delamination growth, and less internal 0-deg. ply fracture. A typical late-life specimen is shown in Figure 29. In this case, there were no internal 0-deg. ply fractures. The fatigue failure mechanism was unstable delamination growth near the surface and crushing in the interior region near the notches.

Under the low load level, longitudinal delaminations grew faster in the even quadrants around the notches than in the odd quadrants. Fiber fracture sometimes occurred in the second-outermost 0-deg. ply groups by the end of the lifetime (Figure 30). Fatigue failure in the low-load specimens occurred shortly after a delamination adjacent to the outermost 90-deg. ply grew rapidly (typically during 1 load cycle) across the distance between the notches. The low-load fatigue failure mode was the same as the high-load fatigue failure mode.

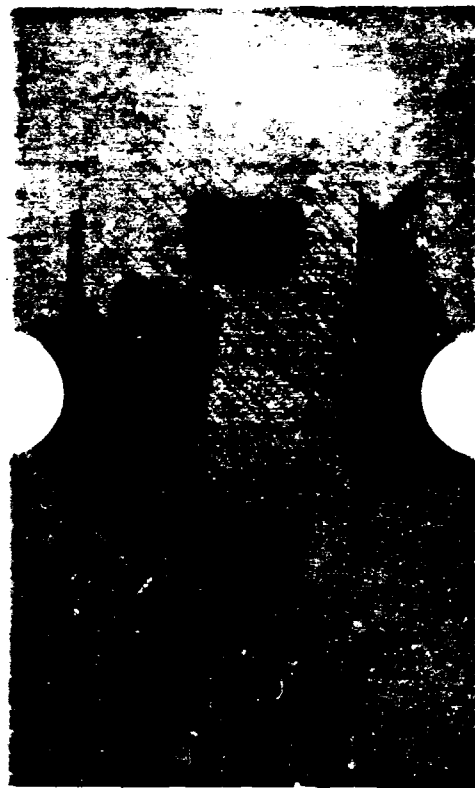


Figure 29. Radiographs of a double-edge-notched, AS4/3501-6, (0,45,90,-45)<sub>34</sub> specimen near high-load fatigue failure



**Figure 30. Radiographs of a double-edge-notched, AS4/3501-6, (0,45,90,-45)<sub>24</sub> specimen near low-load fatigue failure**

## **4.2 AS4/3501-6, Orthotropic Laminate**

### **4.2.1 Center-Notched Specimens**

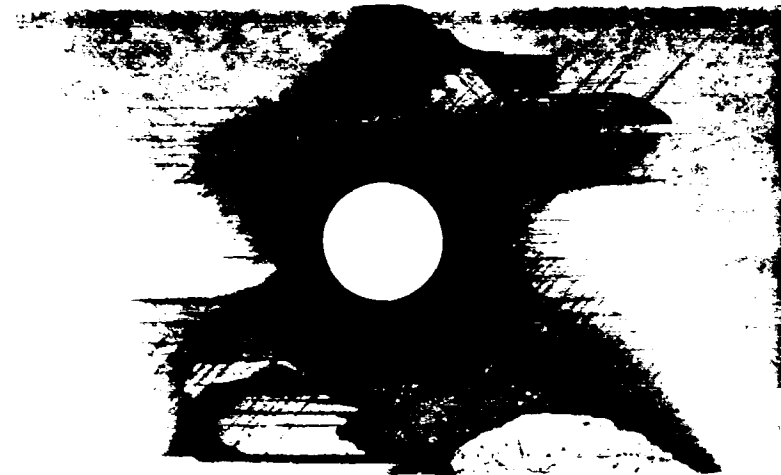
#### **4.2.1.1 High Load Level**

The high load level for AS4/3501-6, (0,45,0,-45)<sub>s4</sub>, CN specimens, 42.2 ksi, resulted in fatigue lifetimes of 10K-14K cycles. After two load cycles, matrix cracks in all plies were evident around the hole. Zero-deg. ply matrix cracks appeared tangent to the hole and nearly perpendicular to the hole, as were matrix cracks in the +45- and -45-deg. plies. Also, secondary +45-deg. matrix cracks initiated along the 0-deg. tangent cracks. No delaminations were seen on the second load cycle, yet, surface 0-deg. ply fracture — a frequent cause of 0/45 interface delamination — was seen at that time (Figure 26a). Note that the 0-deg. ply fracture path did not initiate on the hole boundary. Instead, the localized fracture began at the intersection of the 0-deg. and 45-deg. matrix cracks tangent to the hole, suggesting the importance of the stress concentration associated with the crossing cracks. Based on audible acoustic emissions and visual observations during the manual load ramping required for stiffness measurements, it is known that the 0-deg. ply fractures occurred during the compressive portion of the load cycle. Occasionally, a short, narrow strip of surface 0-deg. ply delaminated tangent to the hole before the occurrence of 0-deg. ply fracture. In such situations, 0-deg. ply fracture did not occur in that delaminated strip for the remainder of the fatigue lifetime. A second mode of through-the-ply fiber fracture appeared as soon as the first or second cycle in the +45-deg. plies in the second and fourth quadrants (Figure 26b). This mode of ply fracture was caused by the stress concentration imposed on the +45-deg. plies along the 0-deg. matrix cracks tangent to the hole. The -45<sub>2</sub> ply groups are less likely to fracture along the 0-deg. matrix cracks than the +45-deg. plies because of their greater thickness. Fractures

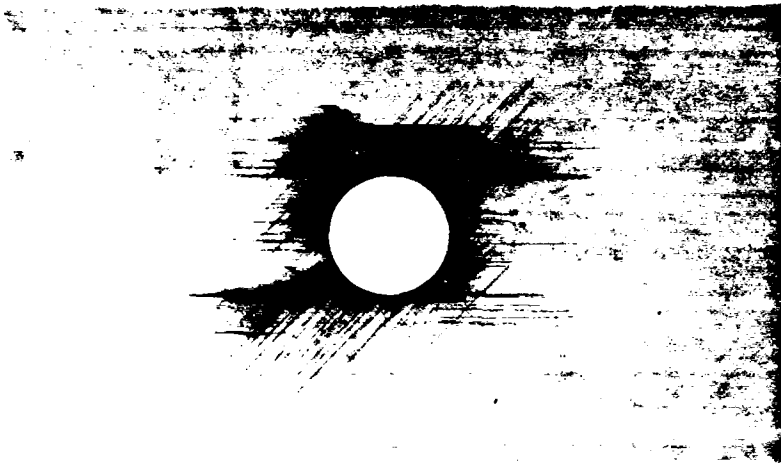
in the +45-deg. plies occurred only in the even quadrants because of the high stresses borne by the fibers tangent to the hole in those quadrants (the +45-deg. fibers in the odd quadrants intersect the hole boundary and, thus carried little load).

With further load cycles, secondary 0-deg. cracks initiated and grew at the tip of the 0-deg. ply fracture paths, leading to strip-like 0/45 delaminations growing longitudinally from the fracture site. Delaminations at the next two or three interfaces frequently followed the appearance of surface 0-deg. ply fractures. In addition to the delaminations induced by 0-deg. ply fracture, other delaminations soon initiated at the hole boundary where the 45- and -45-deg. plies tend to "pull out" (where their fibers are nearly tangent to the hole). Interior delaminations were all of equal length in the longitudinal direction during this delamination initiation period, but later became longer at the interfaces closest to the surface. The 0-deg. matrix cracks in the second and fourth quadrants were longer than those in the first and third quadrants due to their interaction with the 45-deg. ply fracture paths in adjacent plies in the even quadrants. Radiographs of a typical early-life residual strength specimen are shown in Figure 31a and Figure 32a.

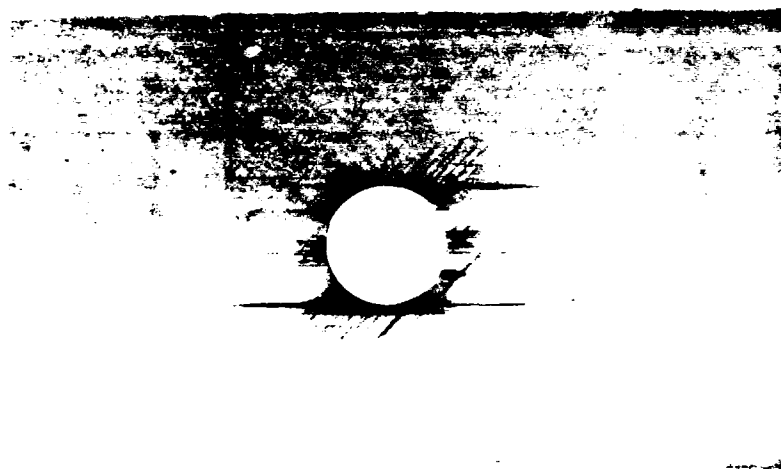
During the second stage of fatigue lifetime, delaminations adjacent to the -45<sub>2</sub> ply groups continued to grow longitudinally and, to a lesser extent, transversely from the notch. In specimens used for middle-life residual strength measurements, delaminations had grown in the transverse direction either with or without the assistance of 0-deg. ply fractures. New delamination growth along -45<sub>2</sub> ply groups occurred at this time at the tips of the 0-deg. tangent cracks in the even quadrants. (Figure 31b and Figure 32b). In several instances, 0-deg. ply fractures were observed in the third ply from the surface, at the intersection of matrix cracks tangent to the hole in the subject 0-deg. ply and the adjacent -45-deg. ply. These 0-deg. ply fractures were followed by delaminations along the broken plies that grew in all directions and prevented additional step-wise fractures of the 0-deg. ply.



(a)



(b)



(c)

Figure 31. Radiographs of center-notched, AS4/3501-6, (0,45,0,-45)<sub>s4</sub> specimens during high-load fatigue: (a) early; (b) middle; and (c) late life

AD-A207 623

INVESTIGATION AND MODELING OF DAMAGE GROWTH IN  
COMPOSITE LAMINATES. (U) VIRGINIA POLYTECHNIC INST AND  
STATE UNIV BLACKSBURG MATERIALS.

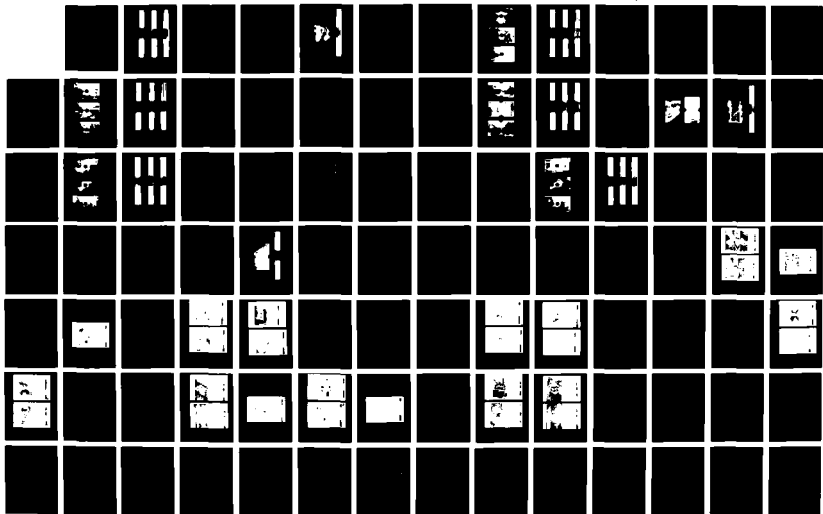
2/5

UNCLASSIFIED

K L REIFSNIDER ET AL 25 SEP 88

F/G 11/4

NL



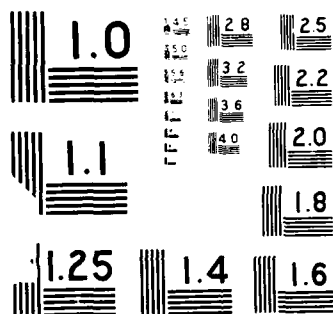






Figure 32. Edge radiographs of center-notched, AS4/3501-6,  $(0,45,0,-45)_{s4}$  specimens during high-load fatigue: (a) early; (b) middle; and (c) late life

Late in the second half of the fatigue lifetime, 0-deg. surface ply fracture paths and their associated delaminations began to grow more rapidly toward the straight edges of the specimen, and delaminations closest to the surface of the specimens continued to grow faster than those in the interior. Near the end of the fatigue lifetime, large surface ply delaminations extended across the entire width of the specimen on one or both surfaces. Most interior 0-deg. plies were not yet broken, and the 0/45-interface delaminations were still much smaller than those on the -45-deg. ply interfaces (Figure 31c and Figure 32c). Failure of this type of specimen in all observed cases was by the unstable growth of near-surface delaminations and crushing of the interior plies. Which of these two damage mechanisms occurred first could not be ascertained.

#### **4.2.1.2 Low Load Level**

The low load level, 31.7 ksi, resulted in fatigue lifetimes between 200K and 900K cycles. Damage after the first cycle consisted of matrix cracks tangent to the hole in the 0-deg. plies and nearly perpendicular to the hole in +45- and -45-deg. plies. At around 100 cycles, matrix cracks in the 45- and -45-deg. plies initiated and grew tangentially to the hole, setting the stage for delamination initiation at the intersection of the 0-, 45-, or -45-deg. matrix cracks and the hole boundary. Delaminations were first visible in the radiographs after 1000 cycles, and were located at all interfaces through the thickness, in all four quadrants. Also at 1K cycles, ply fractures initiated in the 45-deg. plies along the adjoining 0-deg. matrix cracks tangent to the hole. Unlike similar ply fractures in high-load specimens, 45-deg. ply fractures in low-load specimens favored interior ply locations, and never did occur at all possible locations through the thickness of the laminate. The difference in length of the even and odd quadrant 0-deg. tangent cracks was therefore less in low load specimens than in high-load specimens.

At 10K cycles, most new delamination growth occurred in the even quadrants, along the large 0-deg. matrix cracks tangent to the hole. Such delamination growth was fastest on

interfaces closest to the surface of the specimen. Matrix cracks in the 0-deg. plies and, eventually, 0/45 interface delaminations at the outermost interfaces, formed in all four quadrants near the tips of the 0-deg. tangent cracks, suggesting the presence of substantial shearing or transverse ply stresses in those areas. Up to this point, only two mechanisms of delamination in the ligaments of material transverse to the hole existed — 0/45 delamination due to surface 0-deg. ply fracture, and 0/45 interface delamination at the tips of the 0-deg. tangent cracks.

During the second half of life, most additional delamination growth was in the ligaments of material transverse to the notch. Near the end of life, the surface ply fracture paths reached the straight edges, and the associated delaminations grew longitudinally toward the grips. Interior delaminations of the  $-45_2$  ply groups also approached the grips, resulting in a largely delaminated specimen. In only one instance was interior 0-deg. ply fracture observed. Hence, failure was by compressive instability of the sublaminates formed by the delaminations. The most prominent difference between the late-life radiographs of high- and low-load specimens was the greater extent of delamination in low-load specimens.

#### 4.2.2 Double-Edge-Notched Specimens

Double-edge-notched, AS4/3501-6,  $(0,45,0,-45)_{s4}$  specimens under the high load level, 45.6 ksi, had fatigue lifetimes of about 5K to 15K cycles. Damage mechanisms were similar to CN specimens. Zero-deg. ply fractures initiated and grew along either  $+45$ - or  $-45$ -deg. matrix cracks in an adjacent ply, tangent to the notches. Near the end of the fatigue lifetime, 0-deg. ply fractures crossed near the longitudinal centerline of the specimen (Figure 33). Delaminations on the outermost 0/45 interfaces also extended across nearly the entire width of the specimen. Fatigue failure of these specimens was by unstable delamination growth near the surface and crushing of the interior plies between the notches. Insufficient data was available



Figure 33. Radiographs of a double-edge-notched, AS4/3501-6, (0,45,0,-45)<sub>s4</sub> specimen near high-load fatigue failure

at the time of this writing to discuss low-load fatigue damage development in the double-edge-notched, AS4/3501-6,  $(0,45,0,-45)_{s4}$  specimens.

### **4.3 AS4/1808, Quasi-Isotropic Laminate**

#### **4.3.1 Center-Notched Specimens**

##### **4.3.1.1 High Load Level**

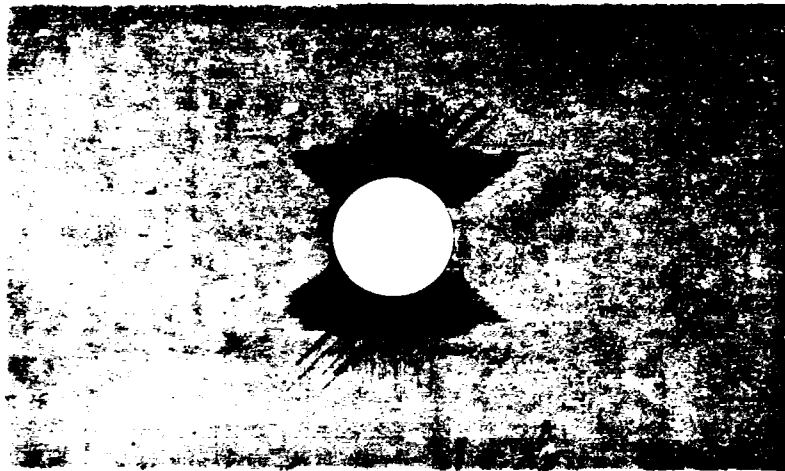
The high load level for center-notched, AS4/1808,  $(0,45,90,-45)_{s4}$  laminates, 29.4 ksi, resulted in fatigue lifetimes between 6K and 50K cycles. During the first one or two cycles, matrix cracks appeared almost perpendicular to the hole in all off-axis plies, and tangent to the hole in the 0-deg. plies. In the next 100 cycles, secondary matrix cracks initiated first in the 45-deg. plies along the 0-deg. tangent cracks, and next in the 90-deg. plies along the -45-deg. cracks. The first occurrence of delamination was at the outermost 0/45 interface at the corner formed by the 0- and 45-deg. matrix cracks and the hole boundary in the even quadrants. At the time of early-life residual strength measurement, step-wise 0-deg. surface ply fractures began to form during compression at the point where the primary 0- and 45-deg. matrix cracks tangent to the hole boundary intersect, a small distance away from the hole. These small, incremental fractures followed a 45-deg. path as they grew away from the notch (Figure 26a). Zero-deg. ply matrix cracks soon followed the incremental fractures, as did strip-like, longitudinal delaminations between those matrix cracks (Figure 34a and Figure 35a). Occasionally, strip-like 0-deg. surface delaminations initiated without the presence of 0-deg. ply fractures. Such delaminations initiated along a +45-deg. matrix crack emanating from the hole (like the step-wise 0-deg. ply fractures), and grew in the longitudinal

direction. However, when a 0/45 interface delamination occurred before a 0-deg. ply fracture, decoupling between the 0- and 45-deg. plies isolated the 0-deg. ply from the stress concentration of the 45-deg. matrix crack and prevented fracture of the 0-deg. ply. Delaminations at this early time in the fatigue life appeared on all 0-deg. ply interfaces throughout the thickness, but those on the outermost 0/45 interfaces were larger than those in the interior, as shown in the damage sketches obtained from a deplied specimen (Figure 36). The deply data also revealed the existence of delaminations where the 45- and -45-deg. plies "pulled out" tangent to the hole, along the 90-deg. plies nearest to the surface.

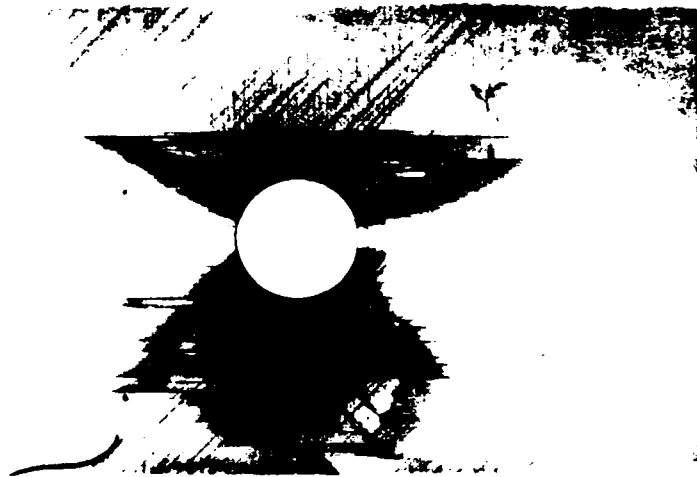
After additional load cycles, delaminations adjacent to the 90-deg. plies stabilized in size, while those along the 0-deg. plies continued to grow, albeit slower than before. During this second stage of life, the rate of damage growth, as evidenced by the stiffness record in Figure 22 on page 66, was slower than at other times in the fatigue lifetime. Off-axis matrix cracks emanating from the hole reached off-axis matrix cracks growing inward from the edges, and some interior 0<sub>2</sub> ply groups fractured locally near the hole. Two general types of damage patterns became evident at this time in the fatigue lifetime. The first was characterized by the longitudinal growth of 0/45 delaminations, particularly at the interfaces closest to the surface, and also by little or no 0-deg. ply fracture in the interior of the laminate. The second type of damage pattern was characterized by the fracture of all 0-deg. plies near the hole, and a more transversely-oriented direction of damage associated with those 0-deg. ply fractures. Apparently, the "high" load level chosen for the current test program was on the transition between load levels that caused dramatically different damage patterns. Cyclic load levels above 29.4 ksi favored 0-deg. ply fracture and the transverse mode of damage growth, while loads below 29.4 ksi favored the longitudinal mode of damage growth and little 0-deg. ply fracture until the second half of the fatigue lifetime (see the next section on low-load damage mechanisms). Radiographs of a typical middle-life residual strength specimen are shown in Figure 34b and Figure 35b. This particular example illustrates the fiber fracture dominated mode of damage growth, as evidenced by the broken 0-deg. ply groups in the in-



(a)



(b)



(c)

Figure 34. Radiographs of center-notched, AS4/1808, (0,45,90,-45)<sub>s</sub> specimens during high-load fatigue: (a) early; (b) middle; and (c) late life



(a)

(b)

(c)

Figure 35. Edge radiographs of center-notched, AS4/1808, (0,45,90,-45)<sub>s4</sub> specimens during high-load fatigue: (a).early; (b) middle; and (c) late life



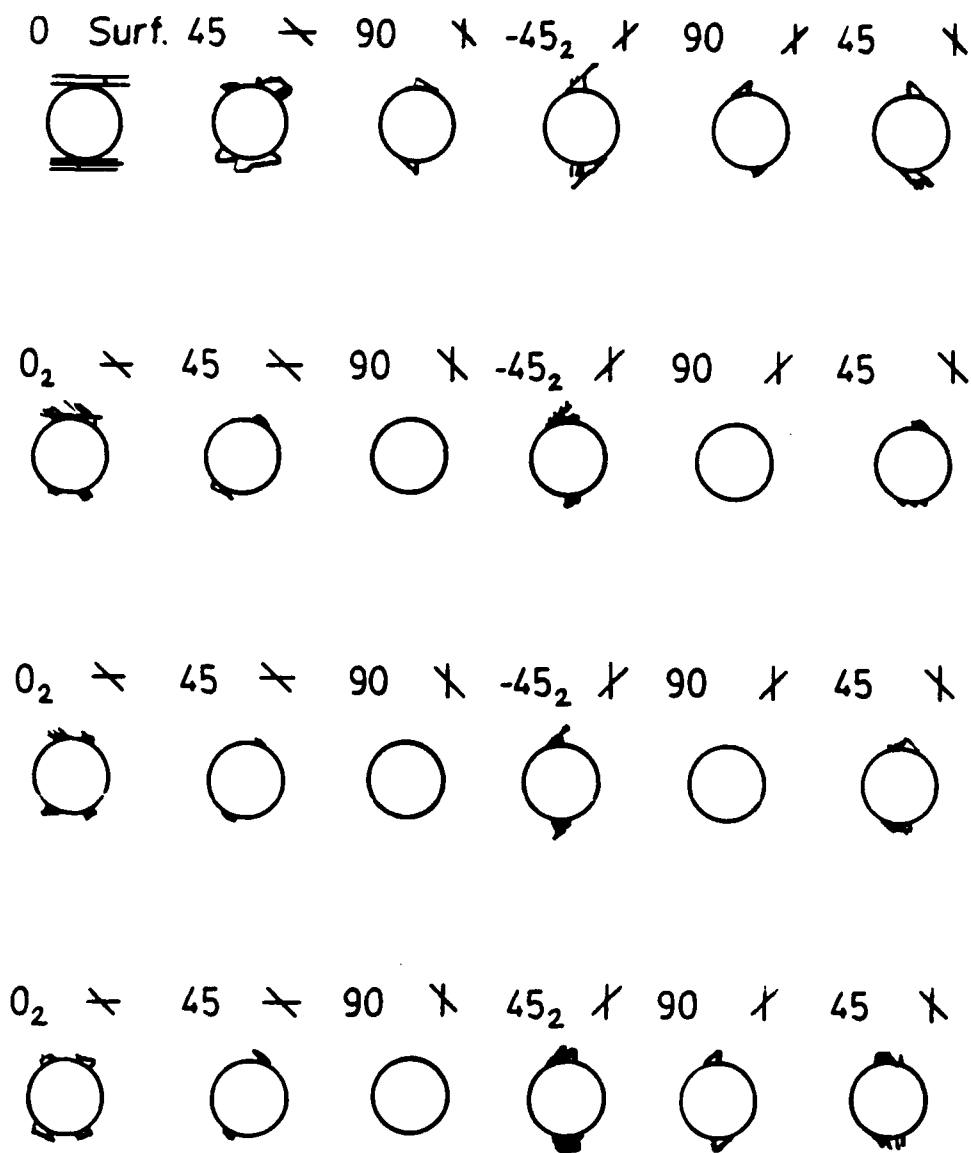


Figure 36. A depled, center-notched, AS4/1808, (0,45,90,-45)<sub>s4</sub> specimen at an early stage of damage development under the high load level

terior of the laminate (see the edge view radiograph). The several interfaces adjoining a 0-deg. ply group fracture site delaminated faster than the remaining interfaces, resulting in an unstable-type of non-symmetric damage growth and compressive instability.

Near the end of the high-load fatigue lifetime, most of the 0-deg. ply groups fractured near the hole. Some of these internal 0-deg. ply fracture paths grew away from the hole in the same manner as the surface 0-deg. ply fractures described earlier. The ply fracture paths and associated matrix damage, however, covered a larger area in the surface plies. The rate of damage growth during the last 10 percent of life accelerated greatly, as evidenced by the stiffness data in Figure 22a. In a typical late-life residual strength specimen (Figure 34c and Figure 35c), delaminations extended across nearly the entire width. Sketches of damage on the interfaces of a depled late-life specimen near fatigue failure are shown in Figure 37. Numerous ply fractures in the 0-, 45-, and -45-deg. plies formed a nearly continuous crack through the thickness of the specimen near the transverse centerline through the hole. The close association between internal ply fractures and delaminations was also indicated in the depley data. In all observed cases, fatigue failure was by delamination of the outer plies and crushing of the less-delaminated interior plies.

#### **4.3.1.2 Low Load Level**

The low load level, 22.6 ksi, resulted in fatigue lifetimes of 500K to 3.5M cycles. As early as the first cycle, 0-deg. matrix cracks initiated and grew tangent to the hole and off-axis ply matrix cracks initiated and grew roughly perpendicularly to the hole. These were followed by -45- and +45-deg. matrix cracks tangent to the hole. In the first 1000 cycles, delaminations initiated on the outermost 0/45 interfaces in all four quadrants around the notch (usually beginning in the even quadrants) and on the outermost 90-deg. ply interfaces. Eventually, all 0/45 interfaces delaminated in a similar fashion through the thickness, as did the 90-deg. ply interfaces. The near-surface 0/45 delaminations remained larger, though, for the remainder

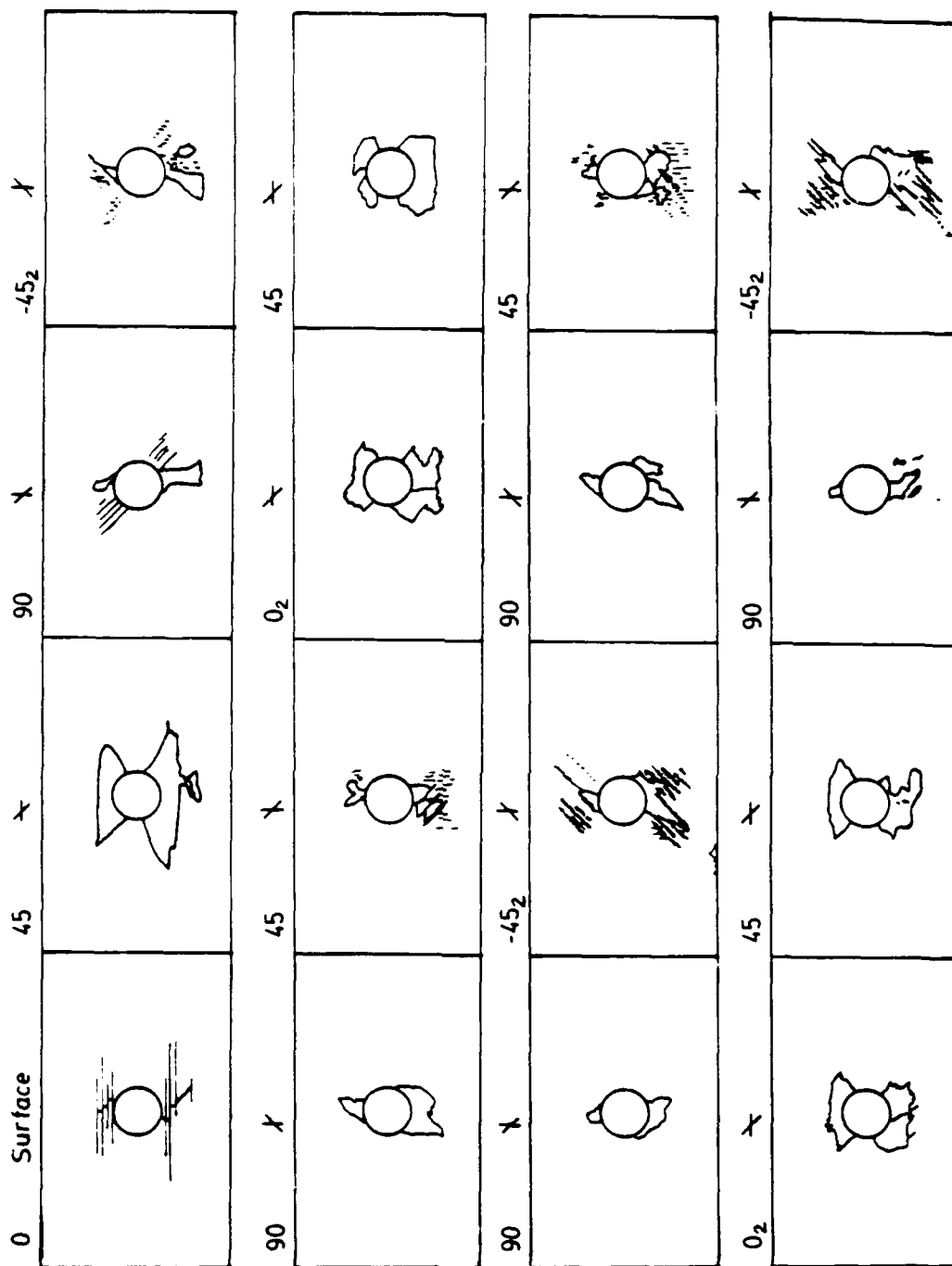


Figure 37. A depled, center-notched, AS4/1808, (0,45,90,-45)<sub>s4</sub> specimen at a late stage of damage development under the high load level

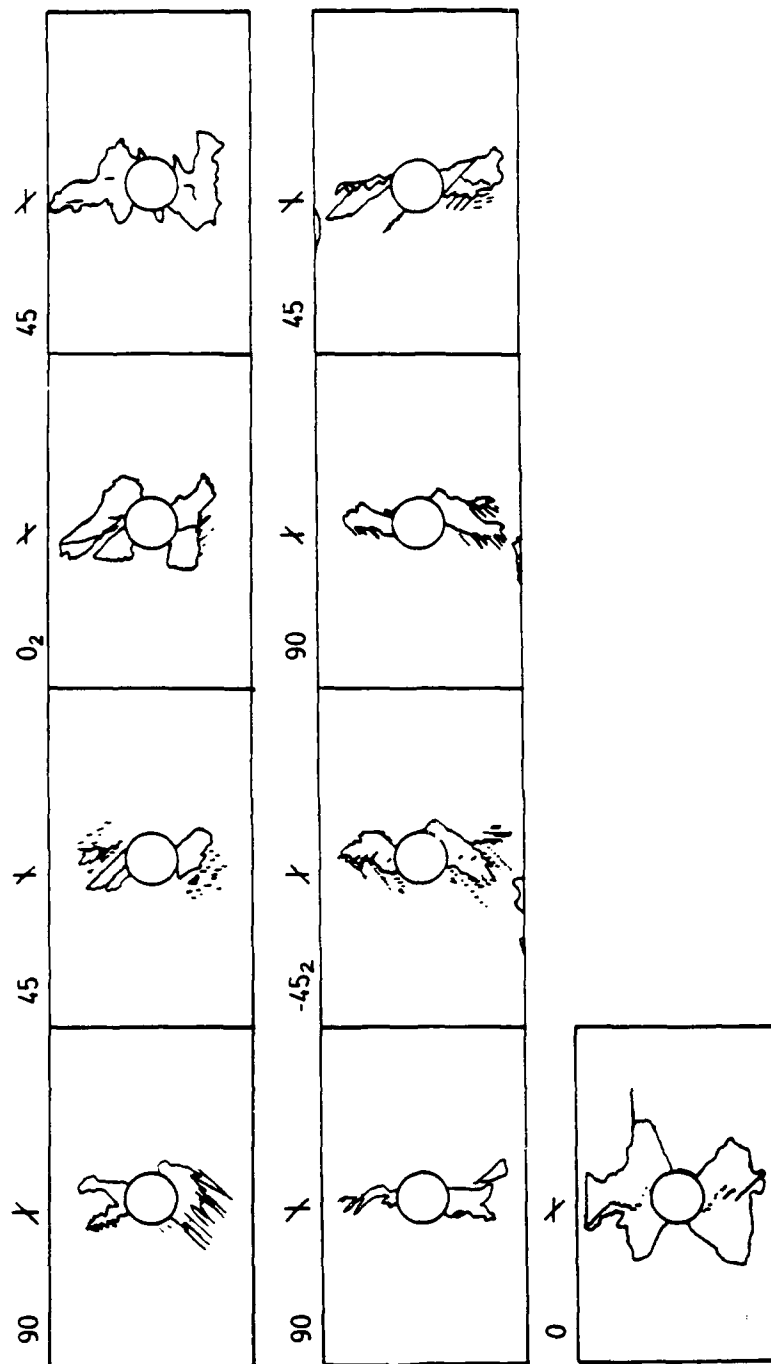
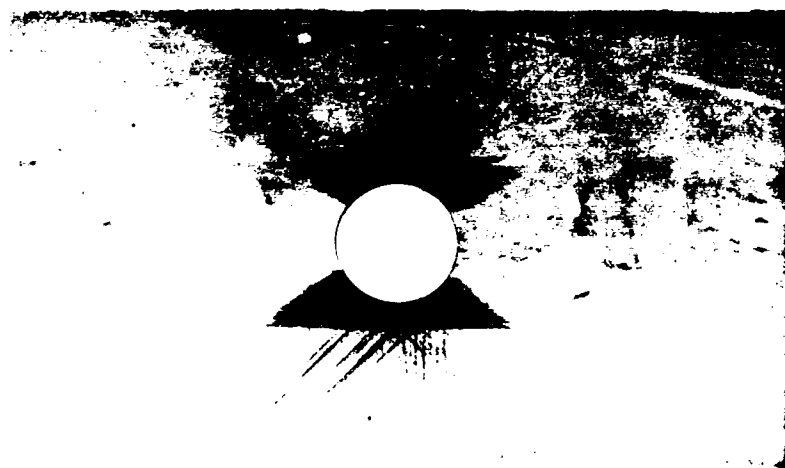


Figure 37 (Concluded)

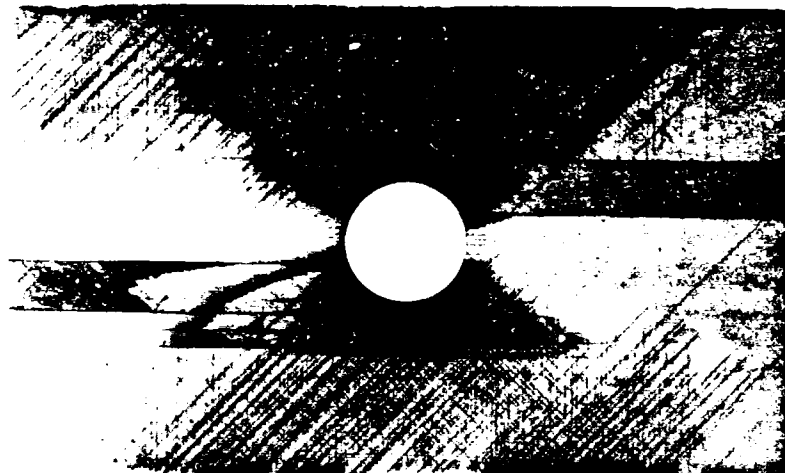
of the lifetime. At the time of the early-life residual strength measurement, incremental step-type fractures in the surface 0-deg. plies had formed along the underlying 45-deg. matrix cracks, though they were less pervasive than in the high-load specimens (i.e., they were interspersed with 0-deg. strip delaminations which prevented their occurrence) (Figure 38a and Figure 39a). Sketches of damage in a depled, early-life specimen (Figure 40) indicated that 0/45 interface delaminations were larger when closer to the surface, but 45/90 and 90/-45 interface delaminations were about the same size through the thickness.

Additional load cycles caused continued growth of the 0/45 interface delaminations, especially at locations closer to the surface. The 90-deg. ply delaminations remained confined to the area bounded by the 45- and -45-deg. matrix cracks tangent to the hole boundary for much of the second stage of the fatigue lifetime. In the third of five observed stages of the fatigue lifetime in these specimens, the sudden, rapid change in stiffness shown in Figure 22 on page 66 at approximately 40-60 percent of the lifetime was caused by the rapid growth (and subsequent arrest) of strip-like delaminations on the outermost 0/45 interface between the hole and the grips, particularly in the even quadrants. Typical radiographs of middle-life residual strength specimens resembled those shown in Figure 38b and Figure 39b. Usually, delaminations under one or both of the surface 0-deg. plies extended outward to at least one straight edge. However, only occasionally had 0/45 interface delaminations in the interior of the laminate grown transversely to the hole at half of the lifetime.

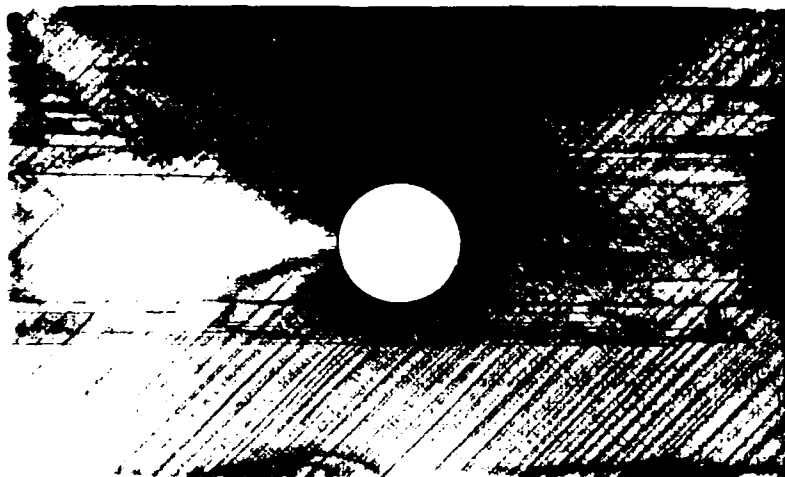
In the fourth stage of fatigue lifetime, matrix damage intensified in the ligaments of material adjacent to the notch (little stiffness change occurred during this time). During the last (fifth) stage of life, interior 0-deg. ply fractures occurred near the notch and surface ply delaminations grew rapidly toward the straight edges. As in other cases mentioned earlier, these delaminations initiated along an underlying +45-deg. matrix crack and rapidly formed strip-like delaminations along longitudinal 0-deg. matrix cracks. Frequently, 0-deg. ply fractures and straight edge delaminations associated with the surface plies grew such that, when combined with the delaminations growing outward from the hole, a continuous delamination



(a)

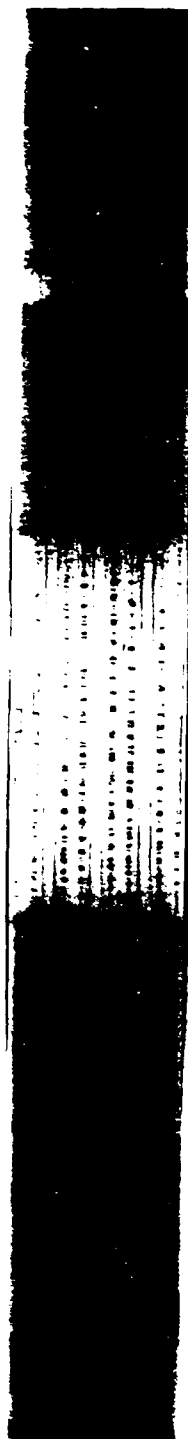


(b)

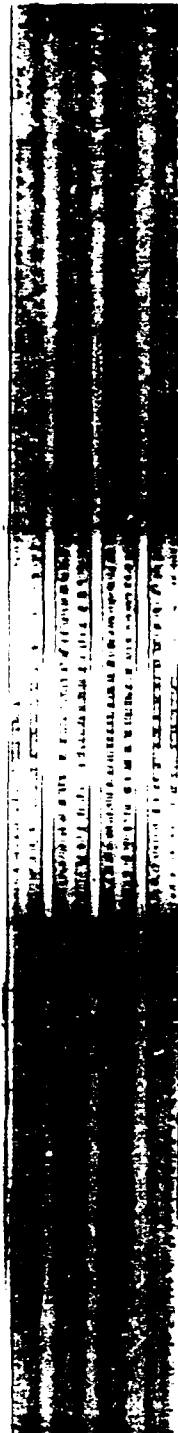


(c)

Figure 38. Radiographs of center-notched, AS4/1808, (0,45,90,-45)<sub>s</sub> specimens during low-load fatigue: (a) early; (b) middle; and (c) late life



(a)



(b)



(c)

Figure 39. Edge radiographs of center-notched, AS4/1808, (0,45,90,-45)<sub>s4</sub> specimens during low-load fatigue: (a) early; (b) middle; and (c) late life

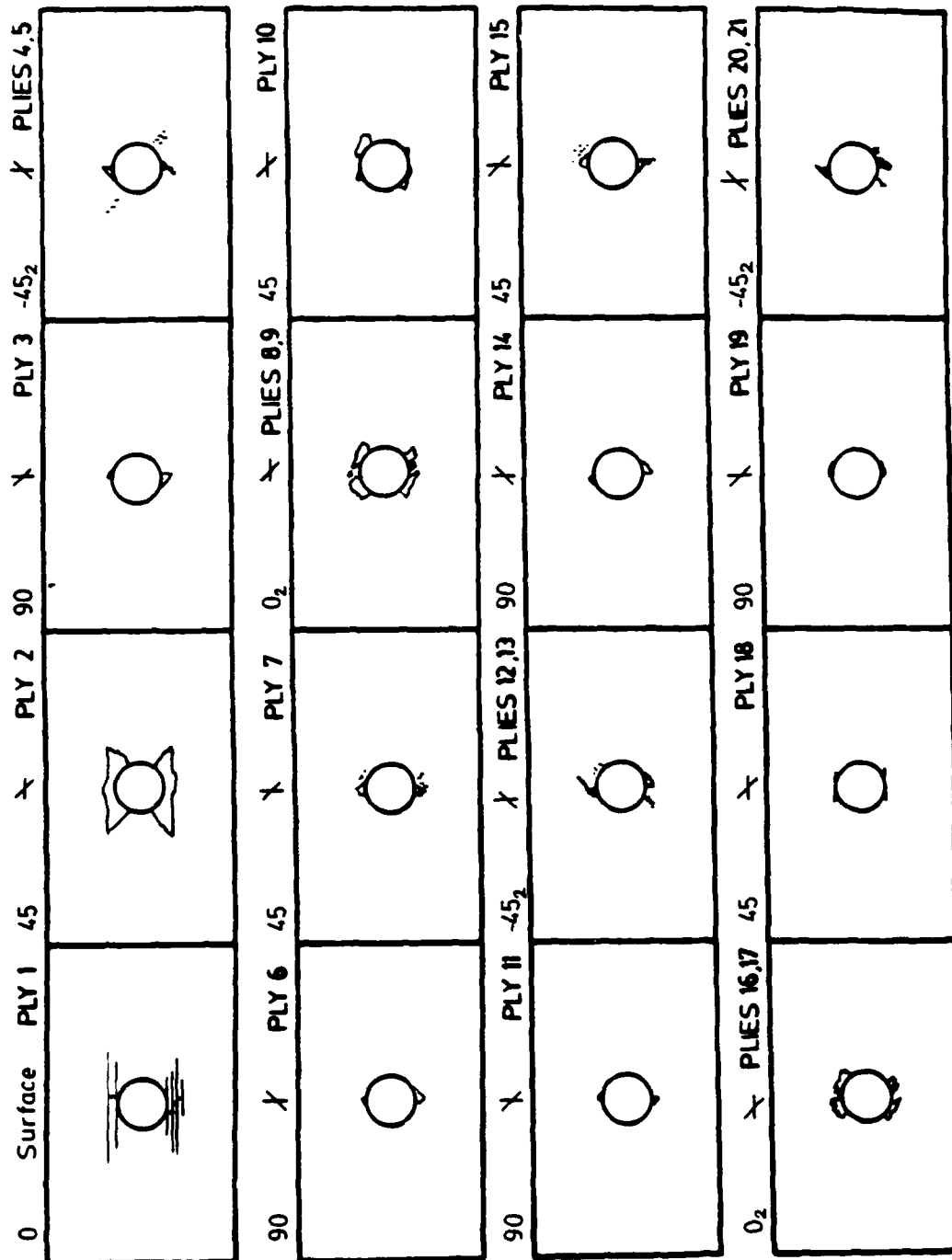


Figure 40. A depled, center-notched, AS4/1808, (0,45,90,-45)<sub>4</sub> specimen at an early stage of damage development under the low load level



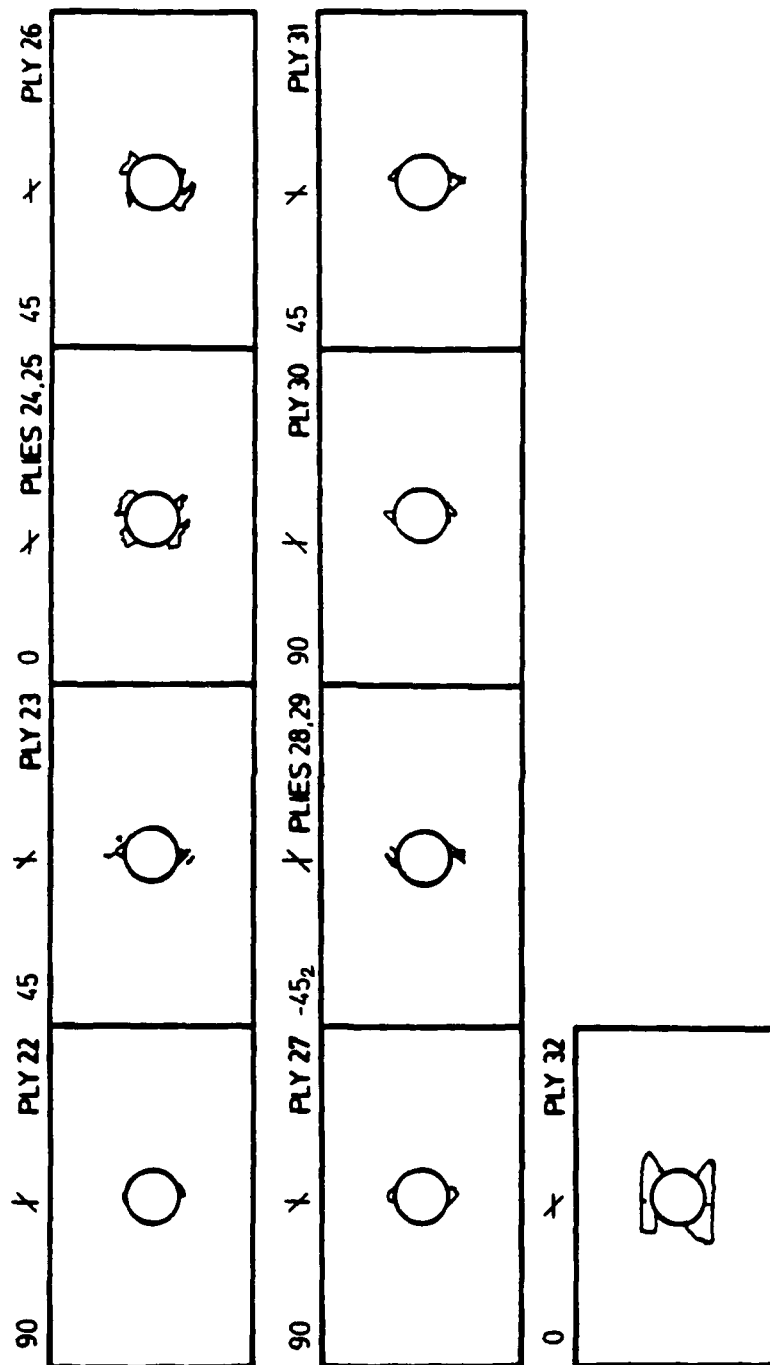


Figure 40 (Concluded)

extending from the notch to one or both of the straight edges, along the entire gage length was formed. Interior interface delaminations also grew longitudinally near the end of life, as shown in the radiographs of a typical late-life residual strength specimen in Figure 38c and Figure 39c.

Sketches of damage seen in a depled late-life specimen reinforced the radiographic data by also indicating a larger extent of delamination on interfaces closer to the surface (Figure 41). Compared to the high-load specimens, there was a greater difference in the extent of near-surface versus interior delaminations in the low-load specimens. Near failure, delaminations beyond the third or fourth interfaces from each surface were similar in shape and size with both load levels. Ply fractures in most 0-deg. plies in the laminate initiated and grew close to the longitudinal centerline of the hole. As indicated by the stiffness record in Figure 22 on page 66, the rate of damage growth accelerated rapidly near the end of life. Failure of all specimens under the low load level was by delamination of the exterior plies and crushing of the interior plies.

## **4.3.2 Double-Edge-Notched Specimens**

### **4.3.2.1 High Load Level**

The high load level for double-edge-notched, AS4/1808, (0,45,90,-45)<sub>s4</sub> specimens, 31.3 ksi, resulted in fatigue lifetimes between 6K and 80K cycles. The unusually wide disparity in fatigue lifetimes was caused by the same type of failure mode transition seen in the CN specimens. Overall, damage mechanisms in DEN specimens were similar to those in CN specimens. However, since these particular DEN specimens were analyzed for stress redistribution and residual strength data, radiographs of specimens at all three residual strength stopping points have been included in Figure 42 and Figure 43.

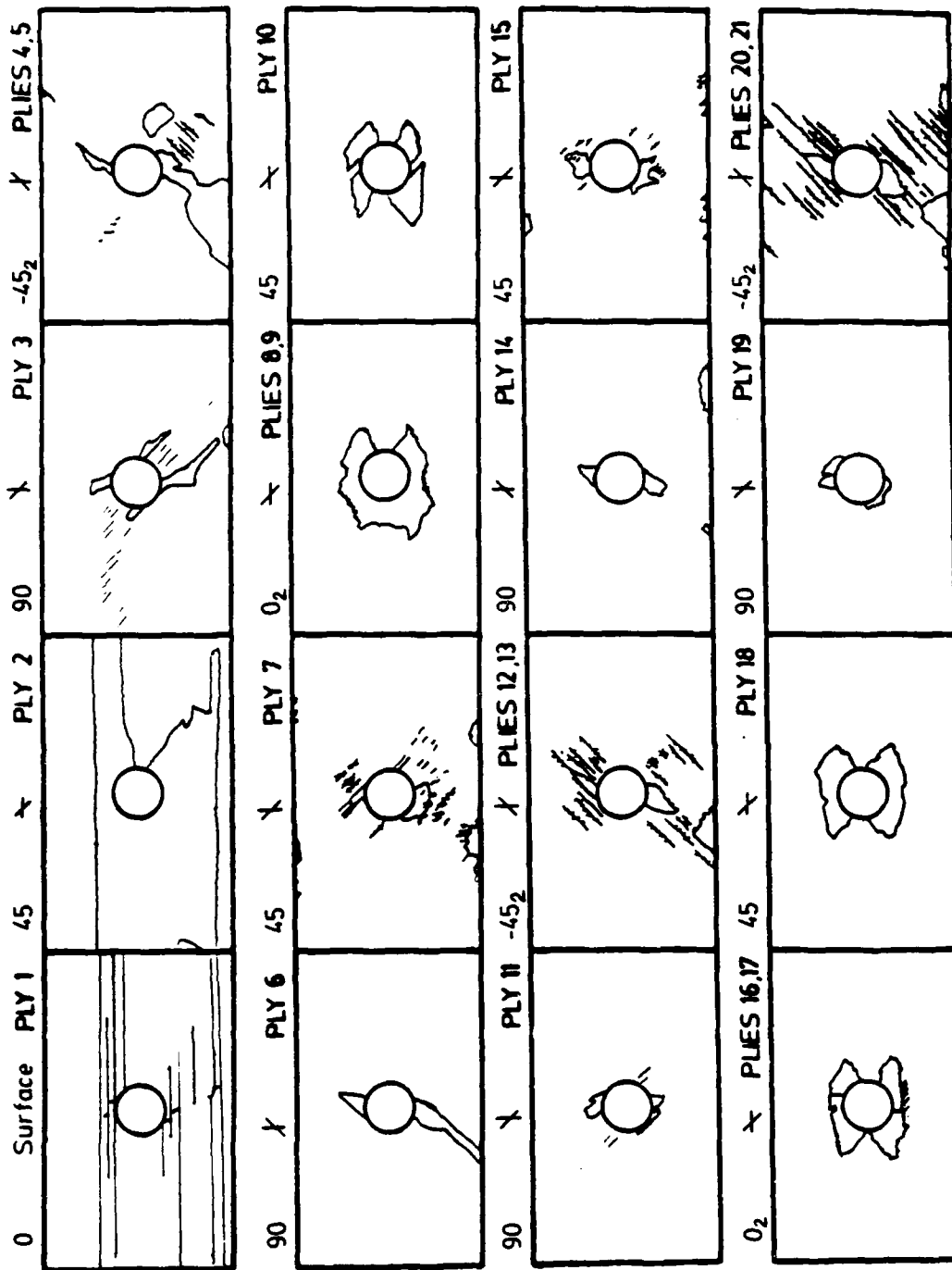


Figure 41. A depleted, center-notched, AS4/1808, (0,45,90,-45)<sub>4</sub> specimen at a late stage of damage development under the low load level

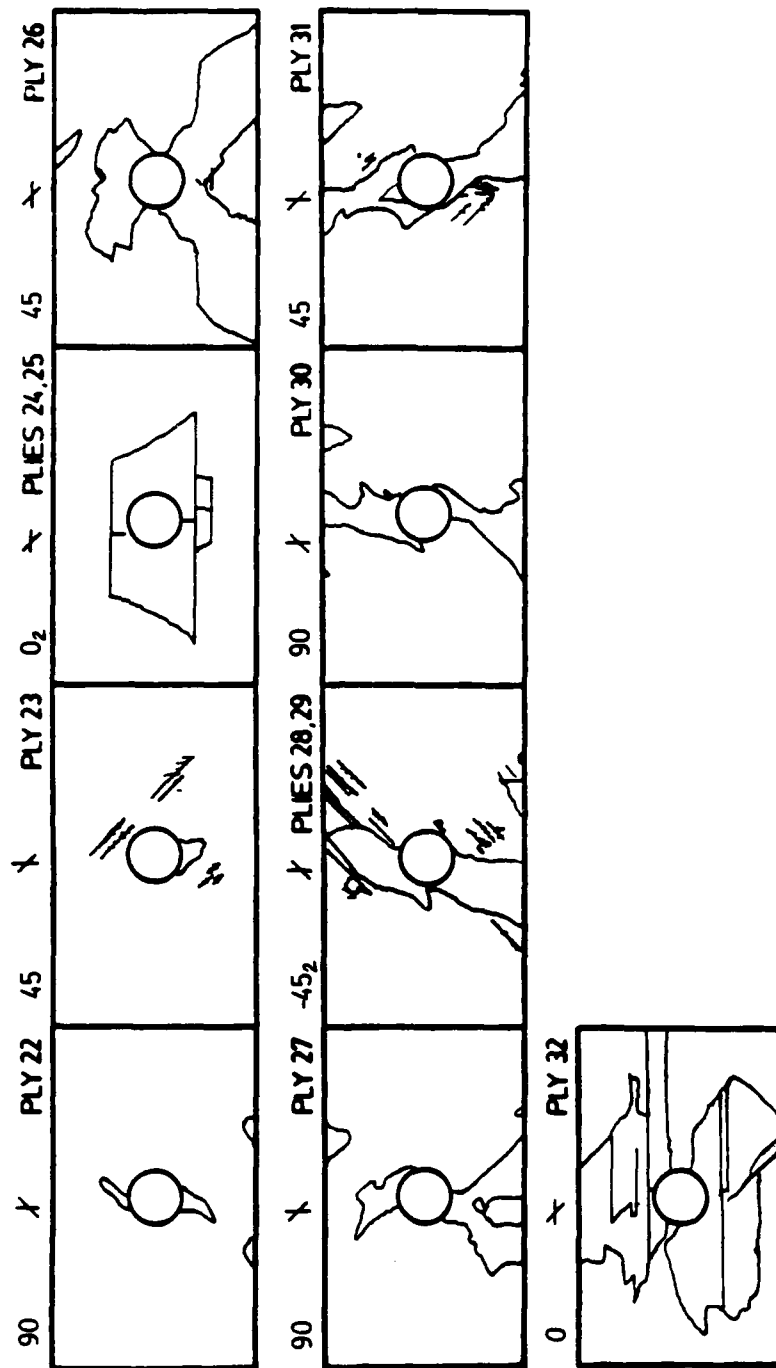
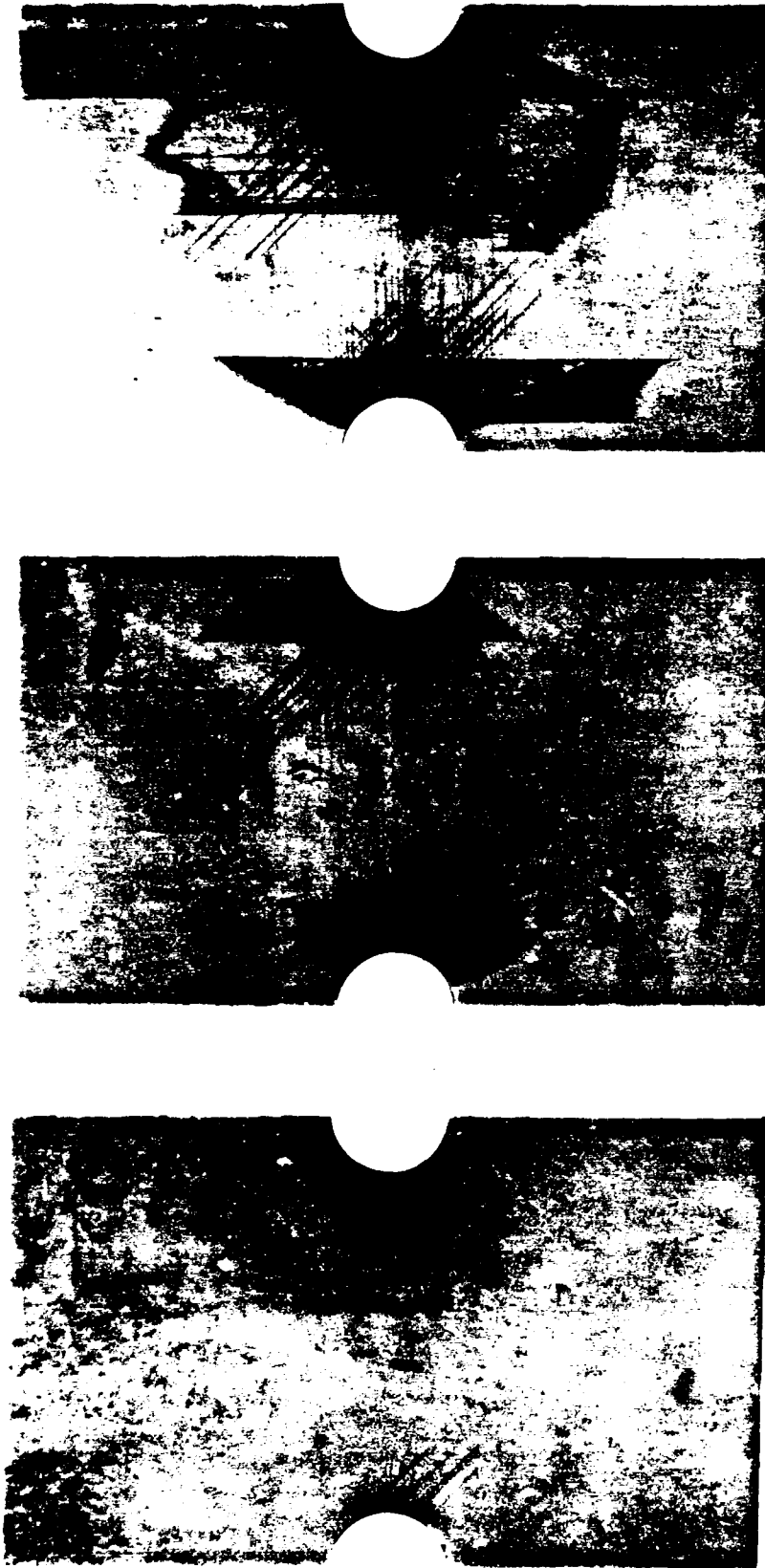


Figure 41 (Concluded)



(a)

(b)

(c)

Figure 42. Radiographs of double-edge-notched, AS4/1808, (0,45,90,-45)<sub>s4</sub> specimens during high-load fatigue: (a) early; (b) middle; and (c) late life

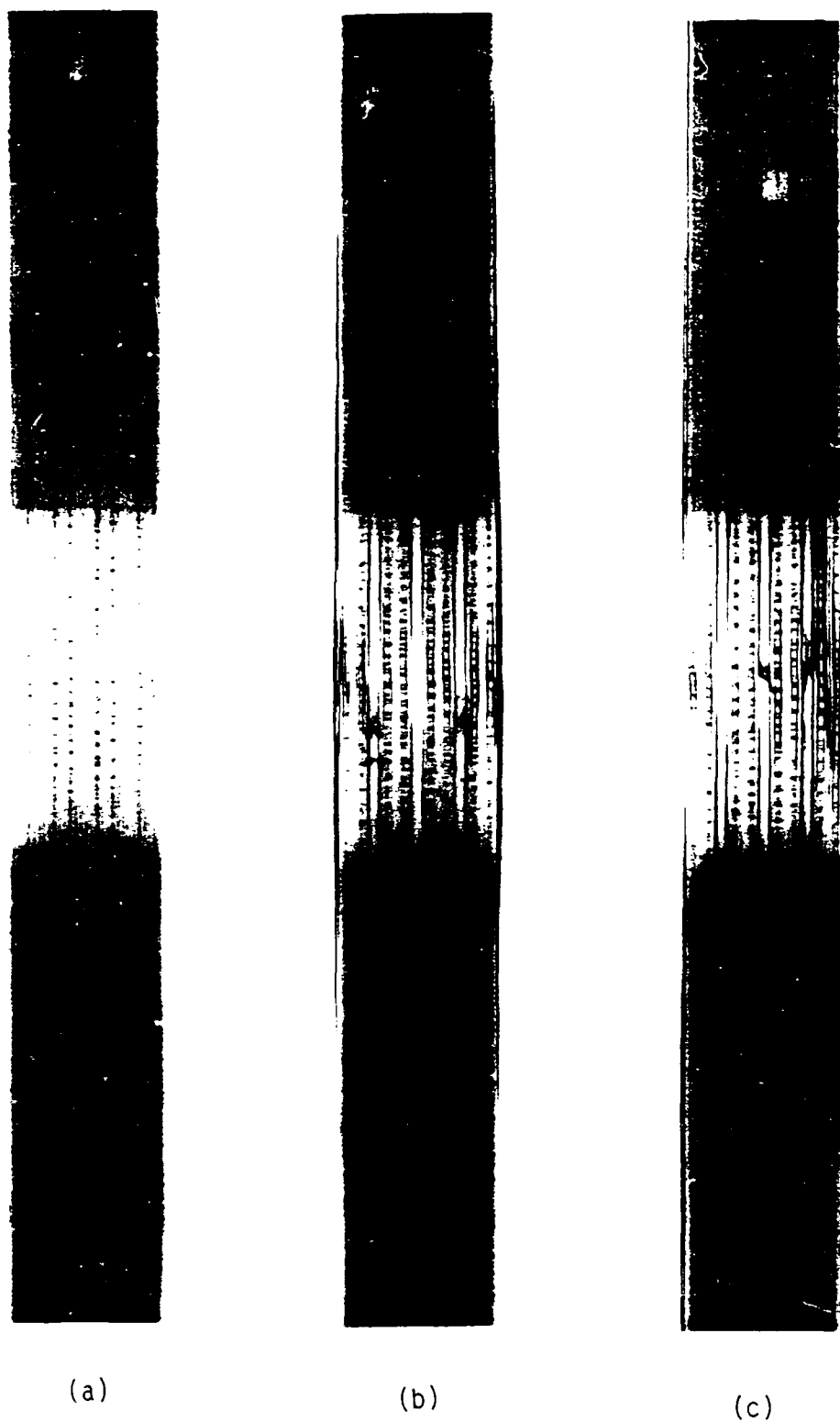


Figure 43. Edge radiographs of double-edge-notched, AS4/1808, (0,45,90,-45)<sub>s4</sub> specimens during high-load fatigue: (a) early; (b) middle; and (c) late life

Early-life specimens contained incremental fractures of the surface 0-deg. plies along the +45-deg. directions, tangent to the notches. Longitudinal delaminations extending from the notches grew faster in the even quadrants than in the odd quadrants, as shown in the middle-life radiographs.

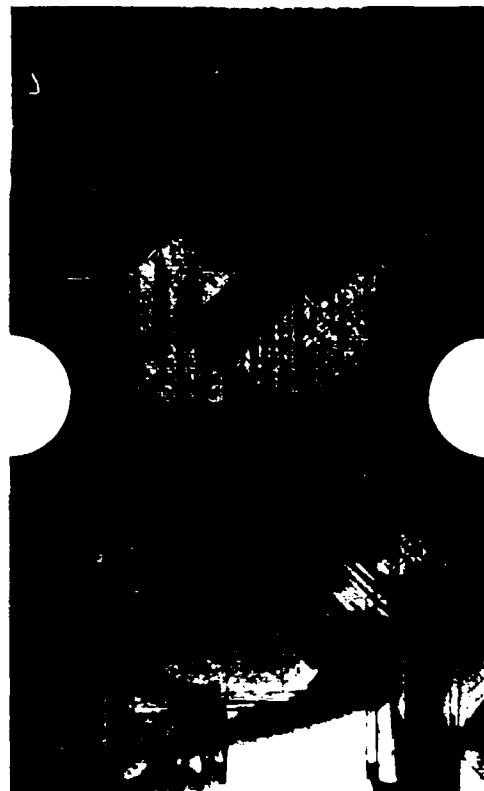
Radiographs of middle-life specimens showed signs of the failure mode transition seen previously in CN specimens. As was the case with CN specimens, the "high" load level chosen for DEN specimens was on the transition between ply fracture dominated behavior and delamination dominated behavior. Those specimens with the "high"-load mode of damage contained ply fractures near the notches in the outermost and second outermost 0-deg. plies by 50 percent of life. Those specimens with the "low"-load mode of damage had no internal 0-deg. ply fractures at this same percentage of life. The middle-life specimen shown in Figure 42b and Figure 43b is following the low-load type behavior.

Late-life specimens typically had 0-deg. ply fractures in one or more of the internal 0-deg. ply groups. Delaminations on the outermost 0/45 interfaces generally spanned most or all of the distance between the notches. Specimens dominated by 0-deg. ply fracture, such as the one shown in Figure 42c and Figure 43c, had less longitudinal growth of delaminations, more internal 0-deg. ply fractures, and significantly shorter fatigue lifetimes than those dominated by near-surface 0/45 interface delaminations. Failure in all high-load tests was compressive, however. Figure 44 shows the post-failure appearance of specimens with each of the two types of damage development. Note that the delamination-dominated specimen failed across a section of material that does not pass through the notches. In both cases, though, the failure mode was delamination of the outermost plies, and crushing of the internal, less delaminated plies.

#### **4.3.2.2 Low Load Level**



(a)



(b)

**Figure 44.** Radiographs of double-edge-notched, AS4/1808,  $(0,45,90,-45)_{34}$  specimens after fatigue failure: (a) ply fracture domination; (b) delamination domination



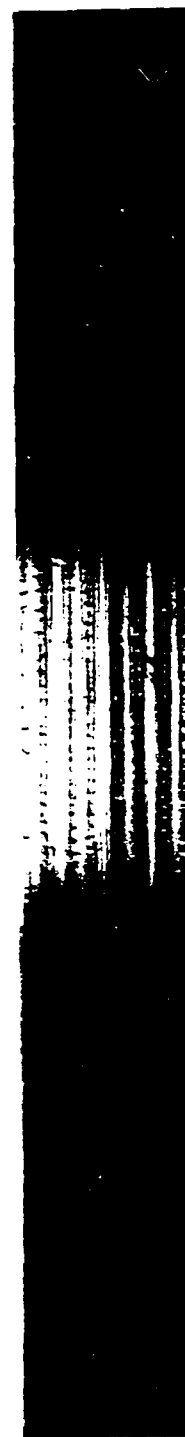
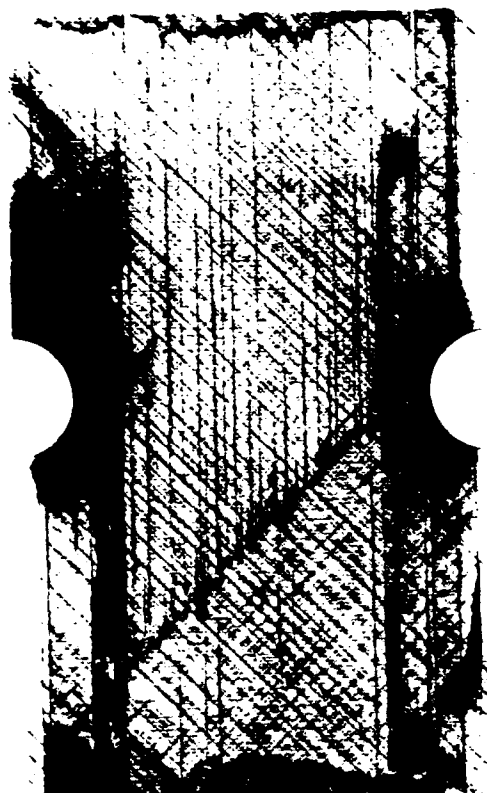


Figure 45. Radiographs of a double-edge-notched, AS4/1808, (0,45,90,-45)<sub>s4</sub> specimen near low-load fatigue failure

The low-load level in double-edge-notched, AS4/1808, (0,45,90,-45)<sub>s4</sub> specimens, 26.5 ksi, resulted in fatigue lifetimes between 400K and 1M cycles. Only preliminary data were available on this type of test as of this writing, but it can be said with confidence that damage mechanisms were similar to the low-load CN specimens. The late-life radiograph shown in Figure 45 indicates that large delaminations under the 0-deg. surface ply extended over the entire gage length of the specimen. In addition to the usual 0-deg. surface ply step-wise fractures along the +45-deg. direction, this particular specimen had one additional 0-deg. ply fracture at the second-outermost 0-deg. ply group. Fatigue failure of this type of specimen was in compression after near-surface delaminations grew unstably and interior plies were crushed.

## **4.4 AS4/1808, Orthotropic Laminate**

### **4.4.1 Center-Notched Specimens**

#### **4.4.1.1 High Load Level**

The high load level for center-notched, AS4/1808, (0,45,0,-45)<sub>s4</sub> specimens, 44.2 ksi, resulted in fatigue lifetimes of 3K to 16K cycles. After one load cycle, matrix cracks appeared in all plies around the notch. The 0-deg. matrix cracks initiated and grew tangentially to the hole, and were longest in the even quadrants. Secondary +45-deg. matrix cracks initiated along the 0-deg. tangent cracks, as did +45 deg. ply incremental fractures (Figure 26b). The 45-deg. ply fracture paths were approximately half as long as the 0-deg. matrix cracks they paralleled. Delaminations occurred within the next 10 cycles at the outermost 45/0 and 0/-45<sub>2</sub> interfaces in the second and fourth quadrants where the 0-deg. tangent cracks met the hole boundary.

Within the next 100 cycles, delaminations existed on all interfaces between plies of different orientation. Delaminations adjacent to the outermost  $-45_2$  ply groups were the largest of all delaminations in the longitudinal direction. The interaction of 0-deg. matrix cracks and adjacent  $+45$ -deg. ply fracture paths that occurred in the even quadrants did not materialize in the odd quadrants because the  $+45$ -deg. plies bear significant load only in the even quadrants (i.e. those quadrants where the  $+45$ -deg. fibers do not intersect the hole boundary). The  $-45$ -deg. plies did not fracture near adjacent matrix cracks due to their double thickness in this lamination arrangement. In radiographs of an early-life residual strength specimen (Figure 46a and Figure 47a), a small 0-deg. ply fracture step appeared in the first quadrant, at the intersection of the 0- and  $-45$ -deg. matrix cracks tangent to the hole. In the edge-view radiograph, it can be seen that this fracture step extends through the first three plies. This fracture likely initiated in the third ply because of the stress disturbance caused by the adjacent  $-45$ -deg. matrix crack. Based on audible acoustic emissions and visual observations, it is known that the step-wise 0-deg. ply fractures occurred during compressive load excursions. Sketches of the damage seen in a depled early-life specimen (Figure 48) indicated that, in the absence of surface ply fracture, the patterns of matrix damage through the thickness of the specimen were nearly identical.

With additional load cycles, delaminations along the  $-45_2$  ply groups grew along the large 0-deg. matrix cracks in the even quadrants. Delaminations on  $-45$ -deg. ply interfaces farther from the surface grew slower than those closer to the surface during the first half of fatigue life. Delaminations on the 0/45 interfaces grew little, if at all, unless a 0-deg. ply fracture was present, in which case substantial growth resulted. By the middle-life strength measurement point, delaminations near the tip of the 0-deg. tangent cracks in the even quadrants had typically initiated and grown a short distance from the notch (Figure 46b and Figure 47b). Near the points where  $-45$ -deg. matrix cracks tangent to the hole intersected the 0-deg. tangent cracks and their associated  $+45$ -deg. ply fracture paths in the even quadrants, the second 0-deg. ply from the surface often broke during a compressive load excursion and caused a



(a)



(b)



(c)

**Figure 46.** Radiographs of center-notched, AS4/1808, (0,45,0,-45)<sub>2</sub>4 specimens during high-load fatigue: (a) early; (b) middle; and (c) late life



Figure 47. Edge radiographs of center-notched, AS4/1808, (0,45,0,-45)<sub>s4</sub> specimens during high-load fatigue: (a) early; (b) middle; and (c) late life

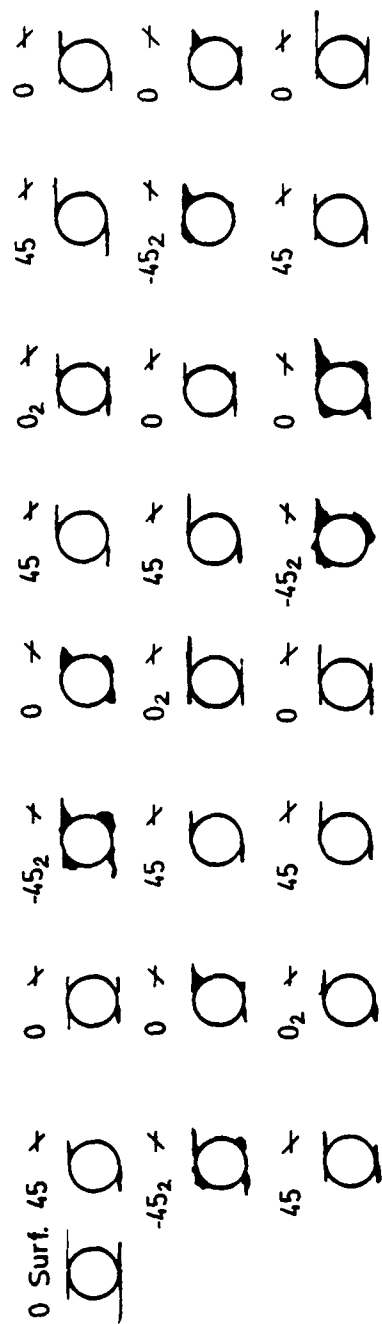


Figure 48. A depled, center-notched, AS4/1808, (0,45,0,-45)<sub>3,4</sub> specimen at an early stage of damage development under the high load level

dynamic crack to propagate to the surface of the specimen. In Figure 47b, however, the crack did not propagate to the surface, but, instead, caused delaminations on the two outermost interfaces. In general, the initiation of 0-deg. ply fractures occurred near large matrix cracks in the 45- and -45-deg. plies. Growth of 0-deg. ply fracture paths was along either the +45- or -45-deg. direction (or both, in alternate fashion), depending on the peculiar orientations of the plies adjacent to the 0-deg. ply and the local stress fields associated with damage in those plies.

Sketches of a deplied middle-life specimen (Figure 49) indicated that delaminations along the -45<sub>2</sub> ply groups were growing along 0-deg. matrix cracks tangent to the hole in the even quadrants. Ply fracture paths in the 45-deg. plies were nearly as long as the 0-deg. matrix cracks which they followed. There was little difference in the damage patterns through the thickness of the laminate.

During the second half of the fatigue life, up to approximately the last 10 percent of life, delaminations along the -45<sub>2</sub> plies grew at a somewhat constant rate. During this time, 0-deg. ply fractures on the surfaces, along with the associated matrix cracking and delamination of the surface 0-deg. plies, approached the straight edges of the specimen. During the last 10 percent of life, delamination growth rates accelerated greatly, and crushing of the interior plies caused fatigue failure of the specimen. Figure 46c and Figure 47c show a typical late-life damage state, just prior to fatigue failure. Most late-life damage growth occurred in the even quadrants, remote from the hole. The difference in the longitudinal extents of delamination as a function of distance from the surface decreased toward the end of life.

Sketches of the damage seen in a deplied, late-life specimen (Figure 50) revealed that delaminations initiated and grew near 0-deg. ply fracture sites in the two outermost 0-deg. plies. The 45-deg. ply fracture paths were still the same length as the 0-deg. matrix cracks tangent to the hole. Ply fracture paths in 0-deg. plies bounded by only +45-deg. plies always

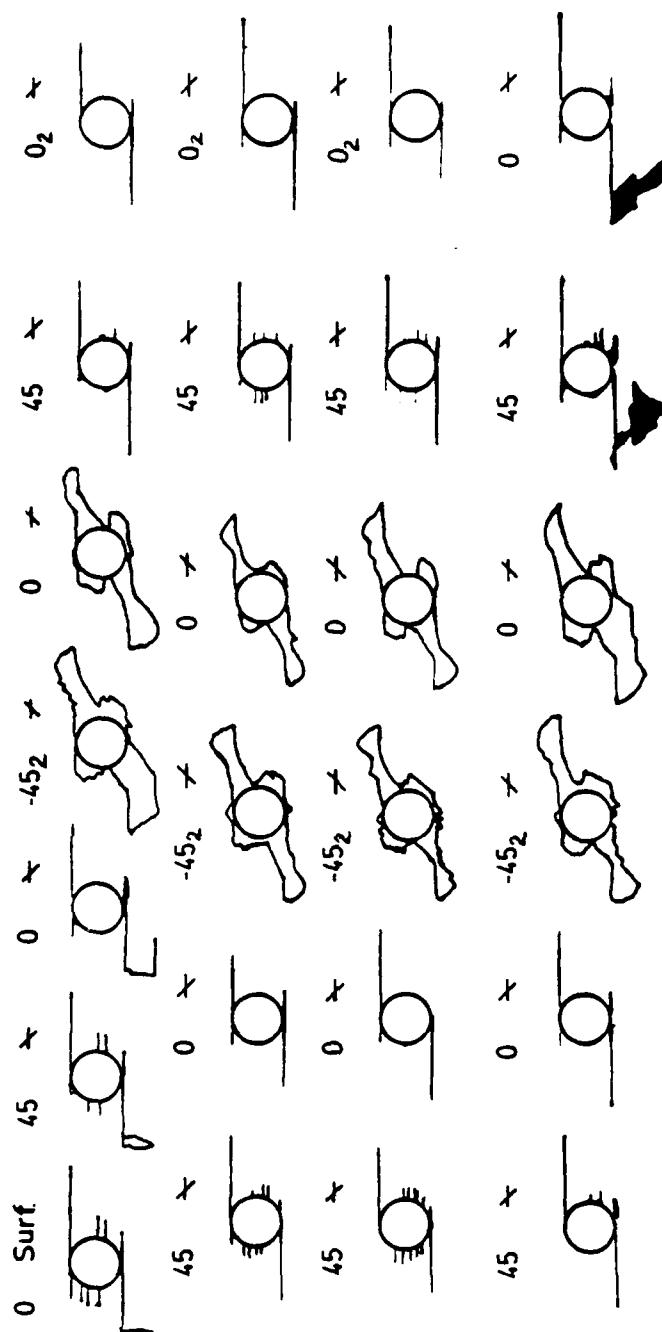


Figure 49. A depled, center-notched, AS4/1808, (0,45,0,-45)<sub>4</sub> specimen at a middle stage of damage development under the high load level



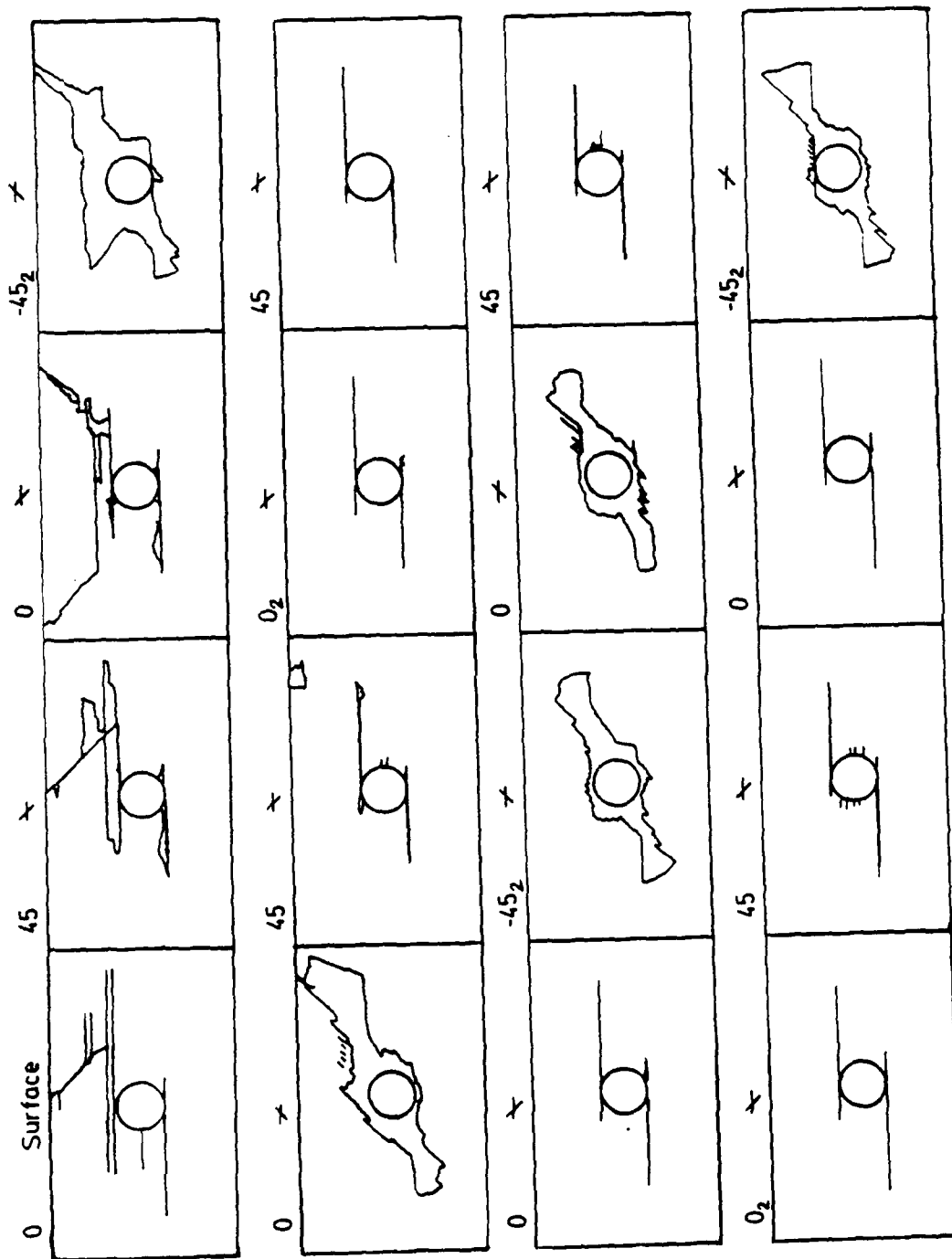


Figure 50. A depletted, center-notched, AS4/1808, (0,45,0,-45)<sub>2</sub> specimen at a late stage of damage development under the high load level

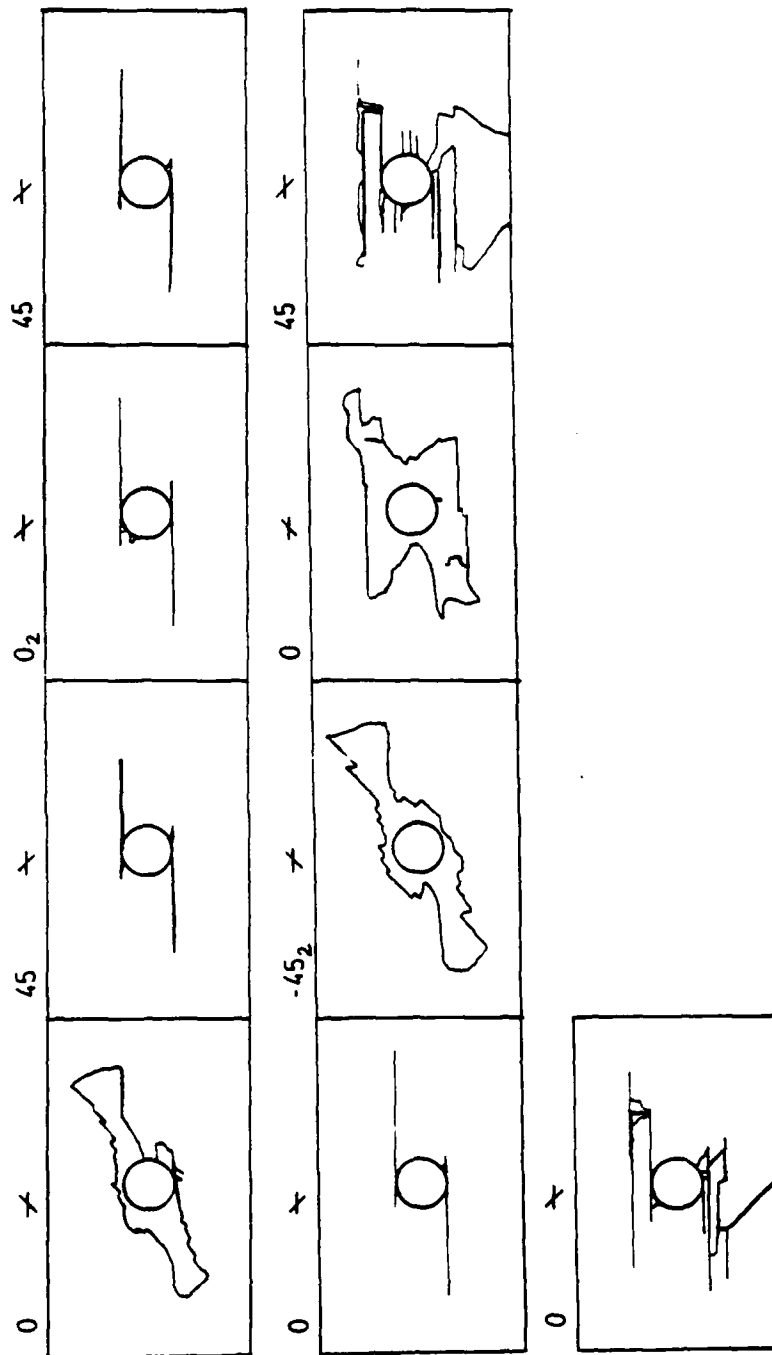


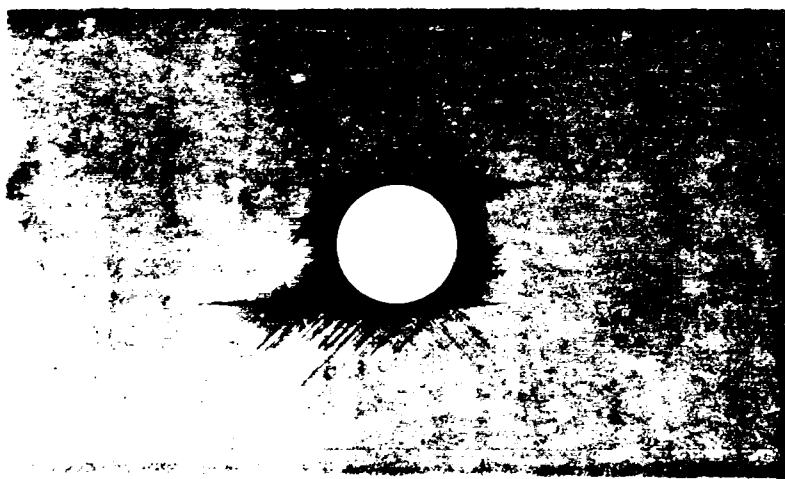
Figure 50 (Concluded)

followed the +45-deg. direction, while those in 0-deg. plies bounded by +45- and -45-deg. plies followed either the +45- or -45-deg. directions.

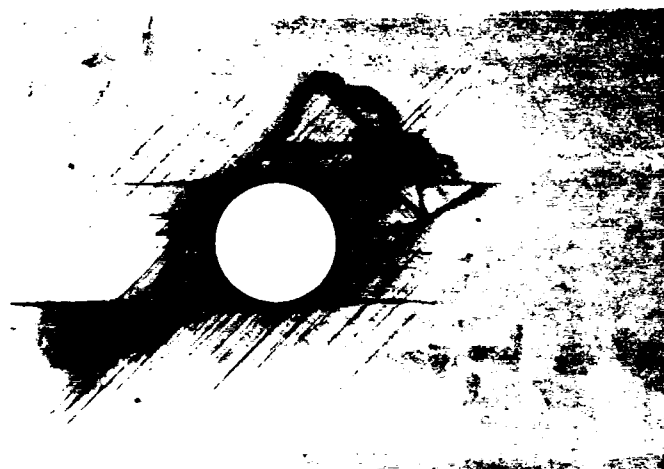
#### **4.4.1.2 Low Load Level**

The low load level for center-notched, AS4/1808, (0,45,0,-45)<sub>s4</sub> specimens, 33.1 ksi, resulted in fatigue lifetimes of 200K to 900K cycles. During the first load cycle, -45-deg. matrix cracks initiated and grew nearly perpendicularly to the hole, and 0-deg. matrix cracks initiated and grew tangentially to the hole. During the next 10 cycles, +45-deg. matrix cracks initiated nearly perpendicularly to the hole. After about one thousand cycles, delaminations initiated in all four corners formed by the intersection of the 0-deg. tangent cracks and the hole boundary, on the outermost 0/45 and 0/-45 interfaces. The length of the 0-deg. tangent cracks in all four quadrants up to this time were roughly equivalent. After about 5K cycles, these cracks became longer in the even quadrants as the +45-deg. plies began to fracture along the 0-deg. tangent cracks in those quadrants. Compared with the high-load specimens, the 45-deg. ply fracture paths followed behind the tips of the 0-deg. tangent cracks more in the low-load specimens. At the early-life residual strength measurement point, delaminations were located mostly between the 0-deg. tangent cracks, adjacent to the -45-deg. ply groups (Figure 51a and Figure 52a), although these delaminations did extend somewhat into the ligaments of material transverse to the hole. Also at this time, delaminations were longest on the outermost -45-deg. ply interfaces (Figure 53).

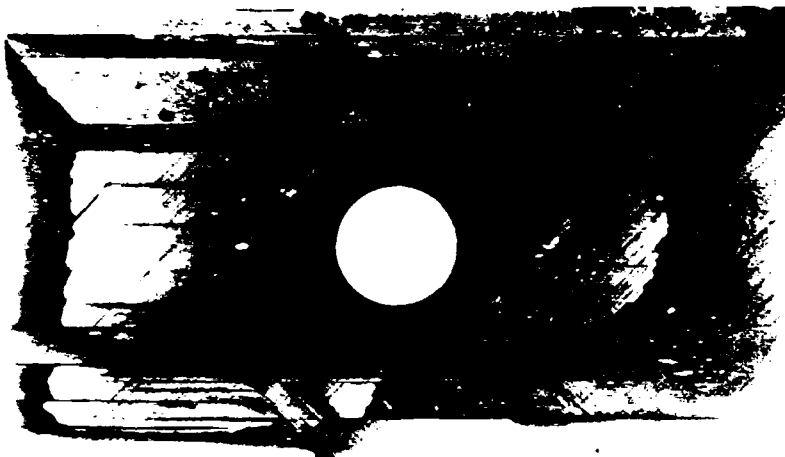
Before half of the fatigue lifetime was exceeded, 0/45 interface delaminations beneath the surface 0-deg. plies overtook the -45<sub>2</sub> ply-group delaminations in length because of the presence of delamination-inducing 0-deg. ply fractures on the surfaces. At the middle-life residual strength measurement point, delaminations adjacent to the -45-deg. plies were growing transversely to the hole, as evidenced by the continuous dark lines crossing the centerline of the notch in the edge radiograph (Figure 51b and Figure 52b). The deply data also indicated



(a)



(b)



(c)

Figure 51. Radiographs of center-notched, AS4/1808,  $(0, 45, 0, -45)_{ss}$  specimens during low-load fatigue: (a) early; (b) middle; and (c) late life



(a)

(b)

(c)

**Figure 52.** Edge radiographs of center-notched, AS4/1808,  $(0,45,0,-45)_{s4}$  specimens during low-load fatigue: (a) early; (b) middle; and (c) late life

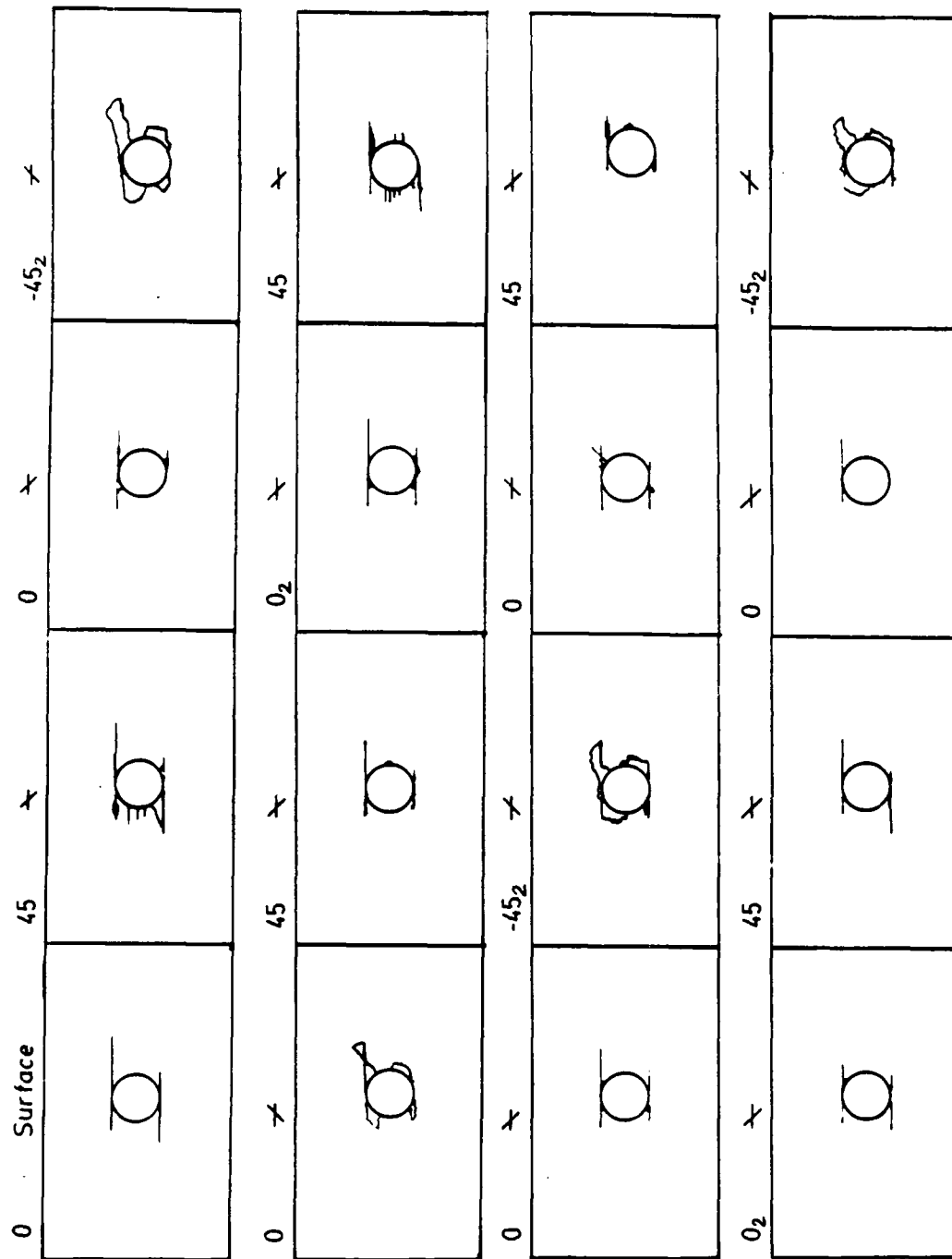


Figure 53. A depled, center-notched, AS4/1808, (0,45,0,45)<sub>s,4</sub> specimen at an early stage of damage development under the low load level

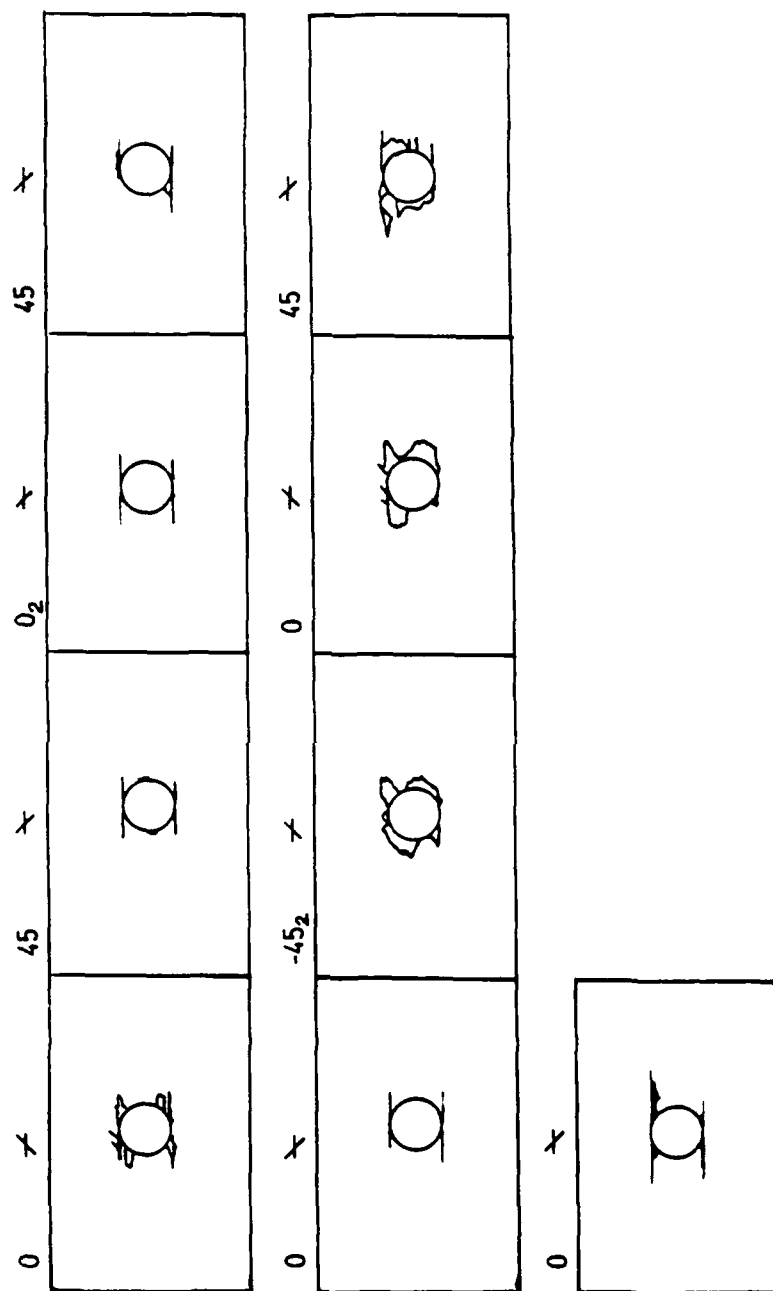


Figure 53 (Concluded)

a disparity in the damage patterns as a function of distance from the surface that emerged by half of the lifetime (Figure 54). The tips of the 45-deg. ply fracture paths lagged behind the 0-deg. tangent cracks, particularly in the plies farthest from the surface (unlike the high-load specimens). Zero-deg. ply fracture paths initiated and grew closer to the hole centerline than in the high-load specimens.

During the second half of the fatigue life, 0/-45 interface delaminations near the tips of the 0-deg. matrix cracks constituted most of the new damage growth. Matrix cracks, surface 0-deg. ply incremental fracture paths along the 45-deg. direction, and delaminations adjacent to the surface 0-deg. plies grew into the load-bearing ligaments of material aside the notch. In a typical late-life residual strength specimen (Figure 51c and Figure 52c), surface ply delaminations extended almost entirely over the specimen's gage length. No interior 0-deg. ply fractures were seen in the low-load specimens. Therefore, the only fiber fracture mechanism observed in the interior of the laminate was +45-deg. ply fracture. Fatigue failure of the specimens was by unstable delamination growth and crushing of the interior, less-delaminated plies.

Deply data (Figure 55) supported the above observations, and indicated that the paths of fiber fracture along the 0-deg. tangent cracks in the 45-deg. plies were shorter in the low-load specimens than in the high-load specimens. In the low-load, late-life deply specimen, there was also a larger disparity in the damage patterns as a function of location through the thickness, compared to specimens at an earlier stage of life or specimens cycled at the high load level.

#### **4.4.2 Double-Edge-Notched Specimens**



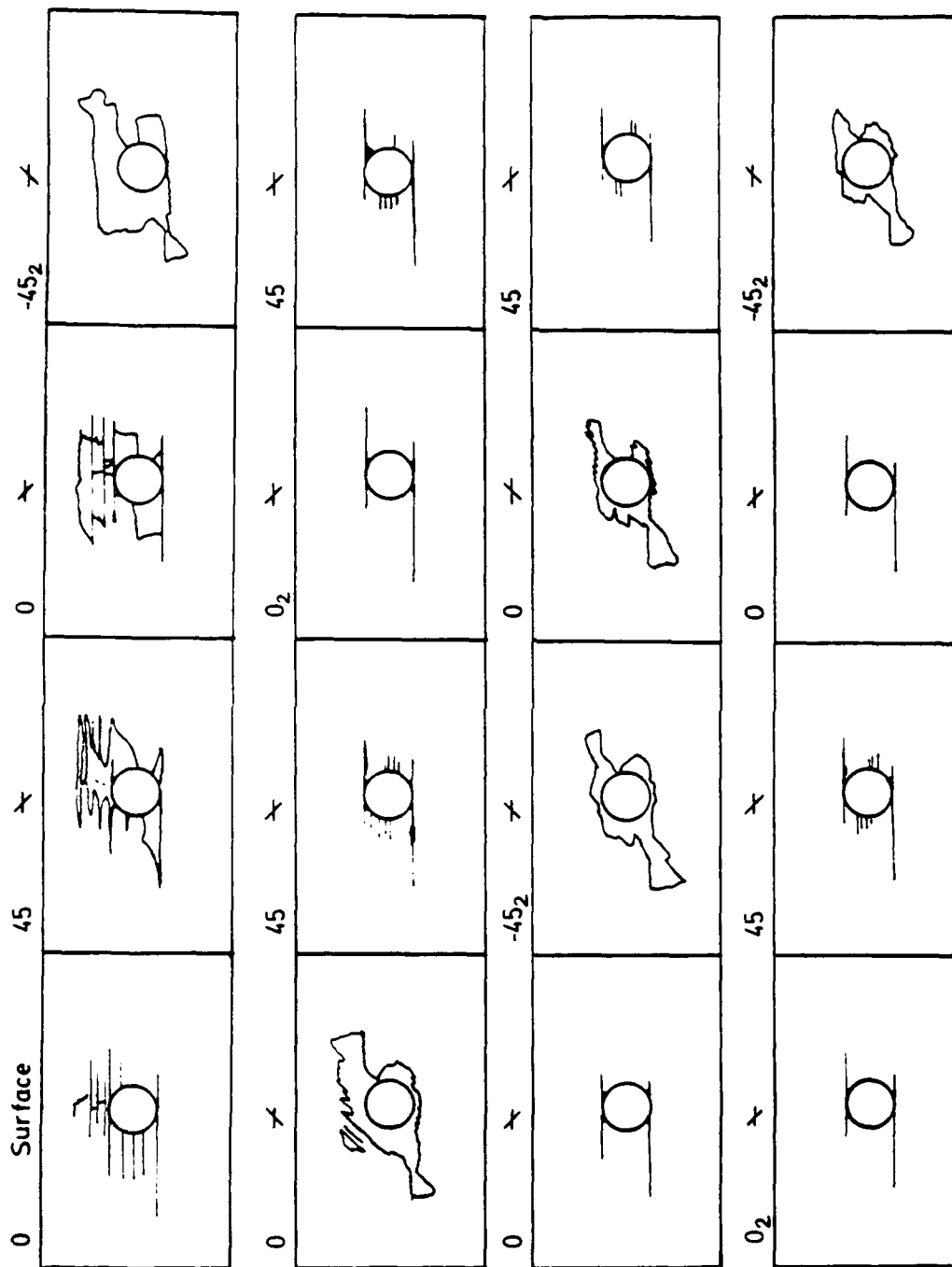


Figure 54. A depleted, center-notched, AS4/1808, (0,45,0,-45)<sub>2,4</sub> specimen at a middle stage of damage development under the low load level

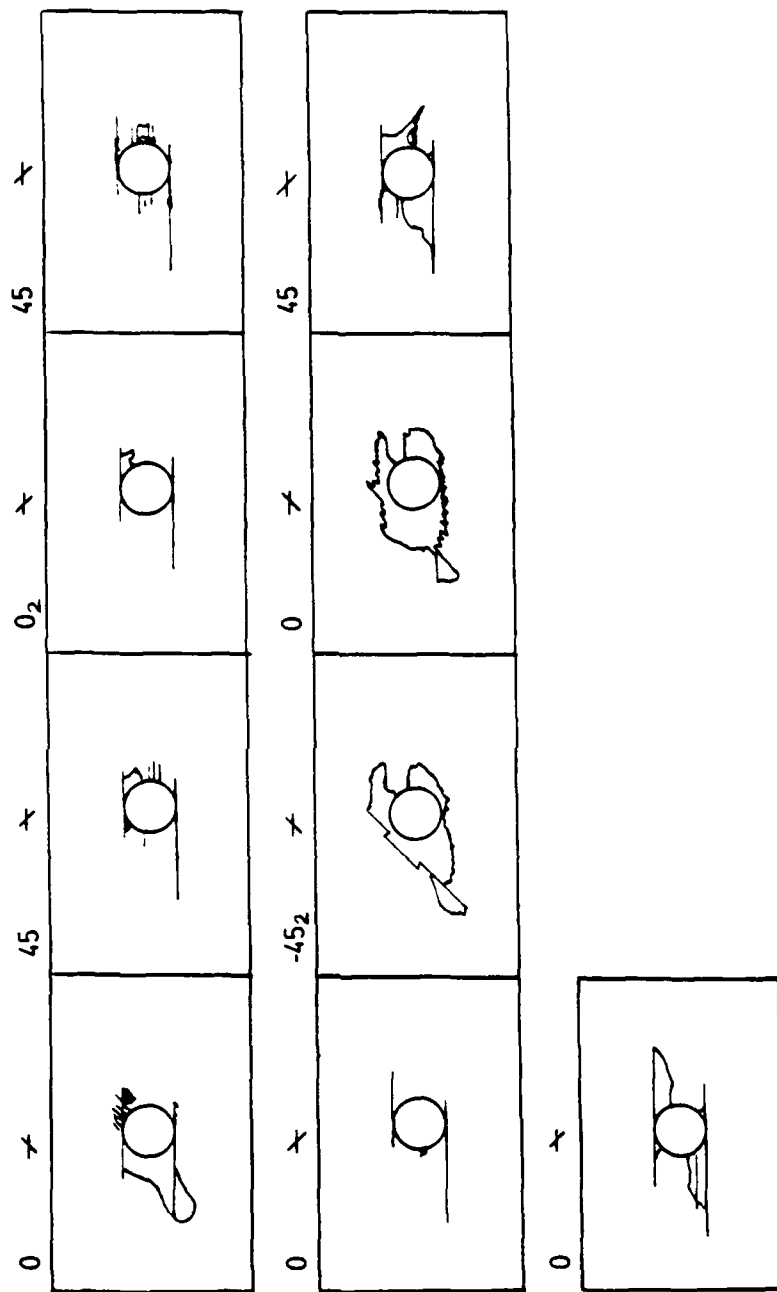


Figure 54 (Concluded)

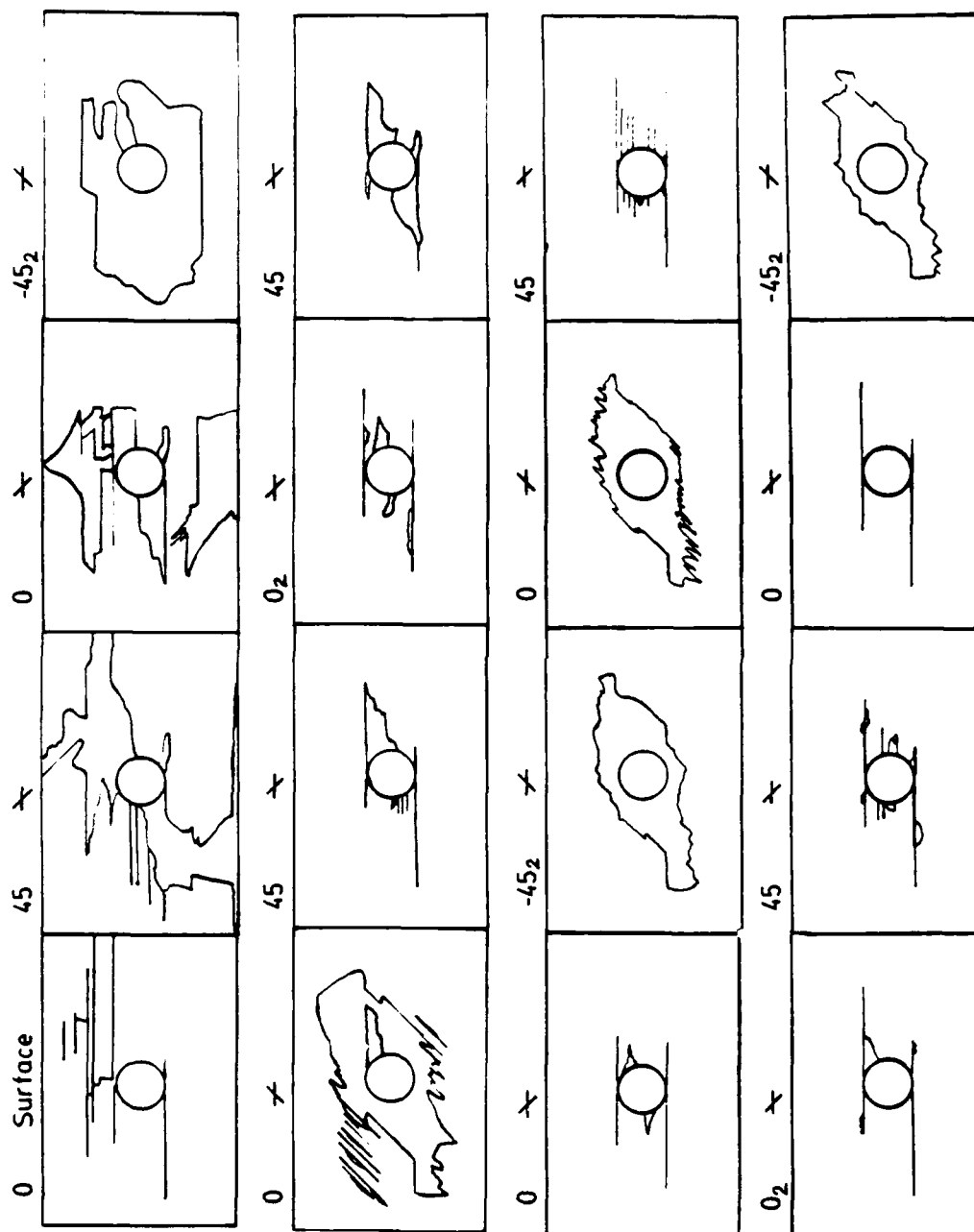


Figure 55. A deploded, center-notched, AS4/1808, (0,45,0,-45)<sub>24</sub> specimen at a late stage of damage development under the low load level

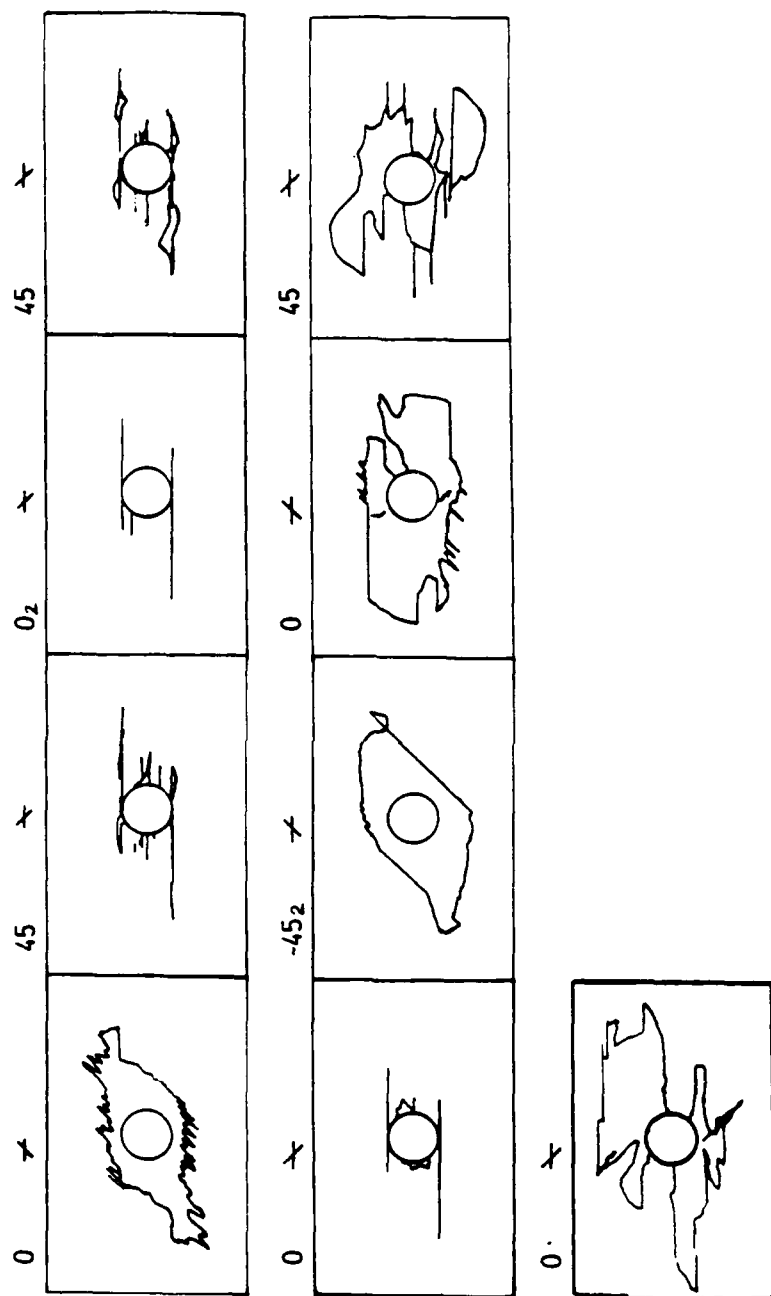


Figure 55 (Concluded)

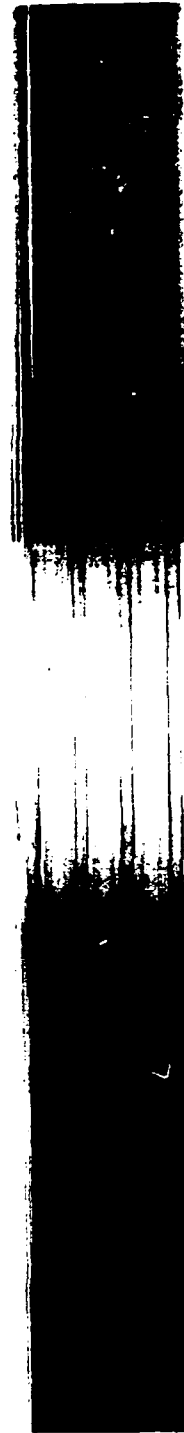


Figure 56. Radiographs of a double-edge-notched, AS4/1808, (0.45,0,-45)<sub>24</sub> specimen near high-load fatigue failure

Data for double-edge-notched, AS4/1808,  $(0,45,0,-45)_{s4}$  specimens were available for only the high load level, 45.3 ksi. Fatigue lives with this load level were between 1K and 24K cycles. Damage and failure mechanisms were similar to those reported for CN specimens under the high load level. Stepwise, 0-deg. ply fractures initiated and grew along both +45- and -45-deg. ply matrix cracks tangent to the notches. The late-life specimen shown in Figure 56 contains delaminations at the first four interfaces that extend, in varying amounts, across the distance between the notches.

## **4.5 Summary of Damage Mechanisms**

Damage mechanisms in the two materials investigated presently, AS4/1808 and AS4/3501-6, were fundamentally similar for a particular load level and lamination arrangement. Matrix cracks, delaminations, and ply fractures were evident in all cases studied, but the distribution, relative quantity, and interaction of these damage types depended, in order of decreasing influence, on the lamination arrangement, load level, material system, and notch configuration.

### **4.5.1 Effect of Lamination Arrangement**

Damage in the  $(0,45,0,-45)_{s4}$  specimens was more directional than damage in the  $(0,45,90,-45)_{s4}$  specimens due to the more highly anisotropic strength properties of the orthotropic laminate. Specifically, lines of intense damage tangent to the notch in the load direction were more prominent in the orthotropic laminate because of this laminate's lower in-plane shear strength along this path. The early presence of large matrix cracks tangent to the notch in all 0-deg. plies caused failure of the +45-deg. plies along this tangent path in the

even quadrants around the notch, in cases where the +45-deg. fibers carried a significant load. Once the +45-deg. plies broke along the 0-deg. matrix cracks in the even quadrants and interacted with the matrix cracks, these 0-deg. tangent damage zones grew more rapidly than the odd quadrant damage zones. Delaminations in the orthotropic laminate were largest along the -45<sub>2</sub> ply groups in the even quadrants. Smaller delaminations were noted along the 0-deg. ply interfaces. The concentration of damage at the tips of the 0-deg. tangent damage zones in the even quadrants resulted in essentially undamaged ligaments of material adjacent to the notch. This situation existed until the last stage of fatigue lifetime, when delaminations grew over much of the gage length.

Incremental compressive fractures of the surface 0-deg. plies along the +45-deg. direction occurred in both laminates. Later in the fatigue lifetime, similar fracture paths occurred in interior 0<sub>2</sub> ply groups located between +45-deg. plies. Single-thickness 0-deg. plies in the interior of the orthotropic laminate were located adjacent to +45- and -45-deg. plies, and fractured in compression near the intersection of the 0- and -45-deg. matrix cracks that originated tangent to the notch. These internal ply fractures grew incrementally along either the +45- or -45-deg. direction (or both, in alternate fashion), and served as precursors for the transverse growth of delamination in the orthotropic laminate near the end of life.

The damage pattern in the (0,45,90,-45)<sub>s4</sub> specimens reflected the influence of the off-axis plies (comprising 75 percent of the thickness of this laminate). Matrix crack growth in the 90-deg. plies led to a more transversely-oriented growth of delamination from the notch at an earlier fraction of life. The implications of these significant differences in delamination characteristics shall become evident in the discussions on residual strength later. The incidence of step-wise 0-deg. ply fracture was higher in the quasi-isotropic laminate, especially in the internal 0-deg. ply groups. Both laminates failed during a compressive load cycle after near-surface delaminations grew in an unstable manner and the internal plies crushed near the notch(es).

#### 4.5.2 Effect of Load Level

The high load level resulted in a more concentrated, or localized, damage pattern than the low load level. Though the fundamental damage modes present in both loading regimes were identical, their relative abundance and degree of interaction depended highly on the maximum load level (or, perhaps, the loading rate, since all tests were run at the same frequency, not stress rate). For instance, in all specimens studied, damage under the high load was more directionally-oriented than under the low load. With low loads, incremental ply fractures and delaminations near the surface of the specimens were significantly more extensive than similar damage modes farther from the surface. This difference was less evident under high loads.

In  $(0,45,90,-45)_{s4}$  specimens, damage grew preferentially along the transverse centerline through the notch during high-load fatigue. Damage in low-load fatigue specimens grew by essentially the same mechanisms, but over a larger area of the specimen, often resulting in nearly-completely delaminated surface plies. Delaminations on 0/45 interfaces closer to the surface had greater longitudinal dimensions than similar interfaces located in the interior of the laminate. This difference was greater in low-load specimens than in high-load specimens. Only the low-load specimens developed longitudinal delaminations of the 0-deg. surface ply that extended from the notch to the grips (usually in the even quadrants, at first), causing a large middle-life stiffness reduction. Conceptually, the critical size for unstable delamination growth should be higher during lower compressive load excursions. Lower loads should, therefore, result in more delamination since fatigue failure in all cases was by the unstable delamination of near-surface 0-deg. plies and the resulting overload of interior plies. Matrix cracks always appeared over a larger area in the low-load specimens. The last important difference between high- and low-load damage mechanisms in  $(0,45,90,-45)_{s4}$  laminates was the earlier occurrence of interior 0-deg. ply fracture under high loads. If such fractures occurred at all in the low-load specimens, they occurred during the last 10 percent of life.



In high-load  $(0,45,0,-45)_{s4}$  specimens, 0-deg. ply fracture was seldom blunted by the occurrence of delaminations that isolated the subject 0-deg. ply from its cracked, off-axis neighbors. Instead, through-the-thickness fractures in principal load bearing plies (along with delamination in their wake) continued to grow, eventually causing compressive fatigue failure. In the low-load specimens, 0-deg. ply fractures near the tips of the 0-deg. tangent cracks were frequently preempted by delaminations along the  $-45_2$  ply groups in this same locale. Without the influence of a bonded neighboring ply, 0-deg. ply fractures were never observed. The same can be said for the  $+45$ -deg. ply fracture paths that followed the adjacent 0-deg. matrix cracks tangent to the notch in the even quadrants. No such fractures occurred after the growth of delaminations between the 0- and  $+45$ -deg. plies.

Under low-level cyclic loads, there was less interaction of damage modes in adjacent plies in the  $(0,45,0,-45)_{s4}$  laminate. For example, the 45-deg. ply fracture paths tangent to the notch were nearly the same length as the 0-deg. ply matrix cracks that they paralleled in high-load specimens. However, the 45-deg. ply fracture paths in low-load specimens were much shorter than the 0-deg. matrix cracks. In low-load fatigue, there was more matrix damage (transverse cracks and delaminations) than in high-load fatigue, and that damage was more evenly represented in all four quadrants around the notch. Damage in the high-load specimens was relatively more concentrated in the even quadrants, especially in the first half of the fatigue lifetime.

#### **4.5.3 Effect of Material System**

Transverse matrix cracks appeared over a greater area and with a greater density in the 3501-6 material than in the 1808 material. Delaminations were approximately equivalent in location, size, and extent in both materials. More precisely, the 1808 high-load specimens had larger surface ply delaminations than the 3501-6 high-load specimens, but this effect could

have been caused by the slightly longer fatigue lives in the 1808 material at the chosen high load levels (longer fatigue lives corresponded with larger delaminations). The 1808 specimens displayed 0- and 45-deg. ply fracture modes earlier and over a larger area than did the 3501-6 specimens. Therefore, the competing, strip-like delaminations of the surface 0-deg. plies were more likely to occur in the 3501-6 specimens than in the 1808 specimens.

In the  $(0,45,0,-45)_{s4}$  specimens, material comparisons could be made only at the high load level. The skewed appearance of the damage patterns was more pronounced in the 1808 material than in the 3501-6 material in the second half of the fatigue lifetime. The 1808 material was also more likely than the 3501-6 material to exhibit ply fracture in the second-outermost 0-deg. ply and growth of such fractures along the -45-deg. direction. These results suggest that matrix damage in adjacent off-axis plies had a stronger influence on the fracture of the 0-deg. plies in the 1808 material.

#### **4.5.4 Effect of Notch Configuration**

There was more scatter in the fatigue lives of DEN specimens than of CN specimens due to the greater variability of damage in the DEN specimens. For example, the AS4/1808,  $(0,45,90,-45)_{s4}$  DEN specimens tested under the high load level exhibited greater failure mode transitions than did the CN specimens under the high load level. The non-symmetric development of damage was also more prevalent in DEN specimens, due to their similarity to unnotched specimens (i.e., less notch influence in the damaged specimen).

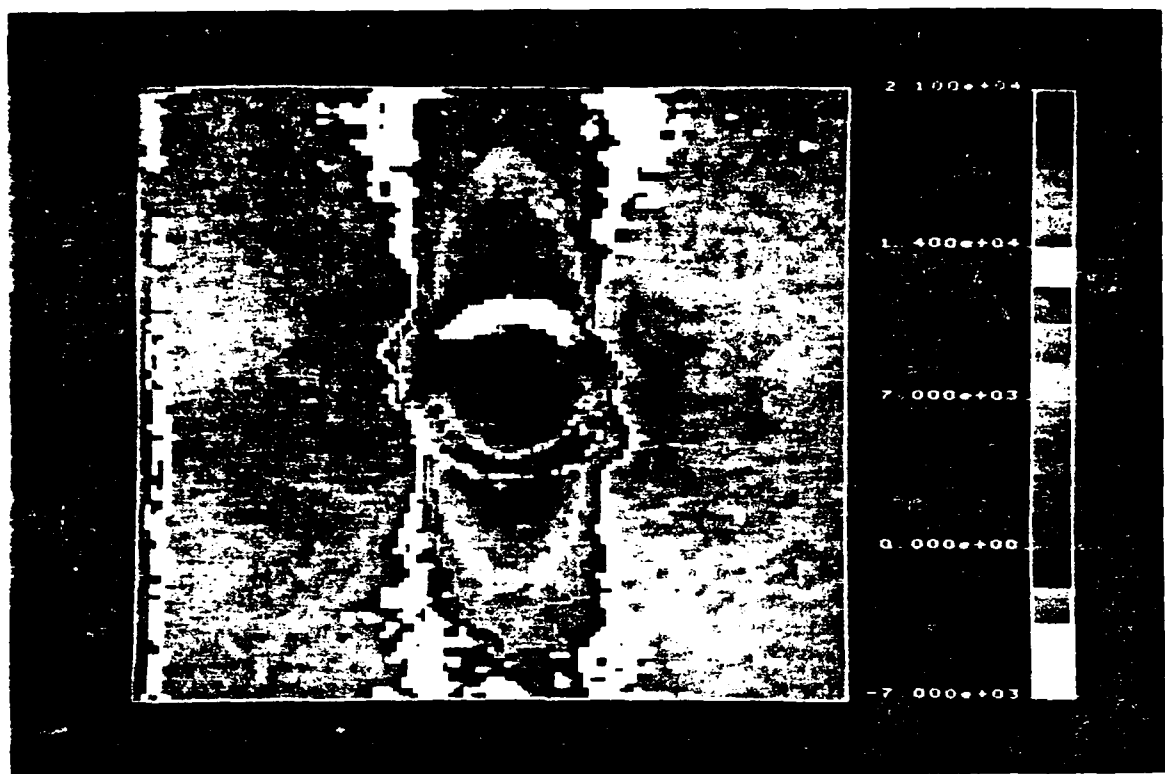
By the end of life, longitudinal surface ply delaminations in DEN specimens were longer in the even quadrants than in the odd quadrants. These differences were less dramatic in the CN specimens. In the DEN  $(0,45,90,-45)_{s4}$  specimens, fatigue failure was often preceded by the appearance of a narrow strip of delamination spanning the distance between the notches

along the outermost 90-deg. ply. Life-limiting delaminations in the CN specimens grew over a shorter distance between the notch and the straight edge(s), but at a slower rate than the life-limiting delaminations in the DEN specimens. Hence, the last stage of fatigue life was longer in the CN specimens than in the DEN specimens (as seen in the stiffness records, Figure 21 and Figure 22).

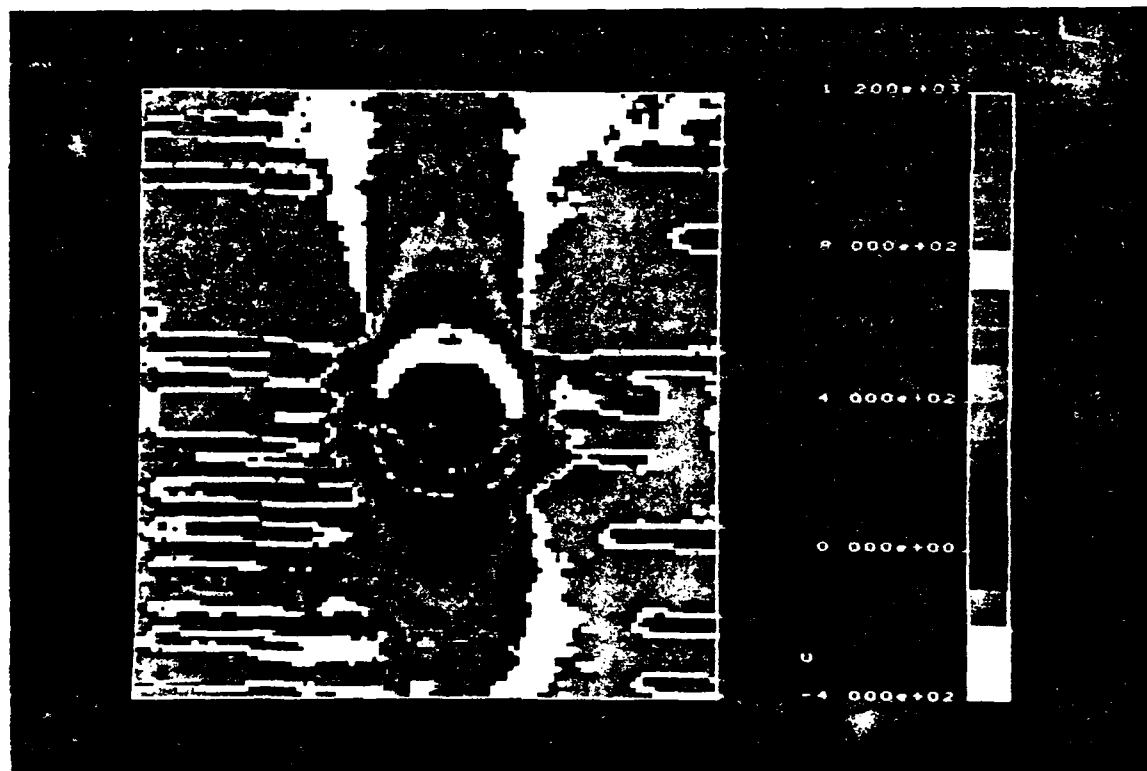
## V

### Stress Redistribution Mechanisms

Matrix cracks, frequently the first damage mode to appear in practical carbon fiber reinforced plastic materials, set the internal stress state for subsequent damage development. Insight into this stress redistribution problem was obtained with a sequence of SPATE thermographs of a center-notched, 42-ply, carbon epoxy laminate with matrix cracks that initiated and grew in the 90-deg. surface ply during tensile cyclic loading (Figure 57). The SPATE sequence shown in Figure 57 includes the undamaged condition, 90-deg. crack initiation, and 90-deg. crack saturation. Also evident in the heavily-damaged specimen was a near-surface delamination corresponding to the black (no temperature change) area surrounding the notch. There are two special features of the SPATE thermographs that should be noted. The first is the reduction in load carried by the material immediately adjacent to and along the length of each 90-deg. matrix crack. The second is the eventual reduction of load carried by the 90-deg. surface ply over the entire gage-length of the specimen as the crack spacing became asymptotically smaller with increasing load cycles. In this manner, stress was increasingly transferred to undamaged plies until a saturated 90-deg. ply crack spacing was approached.

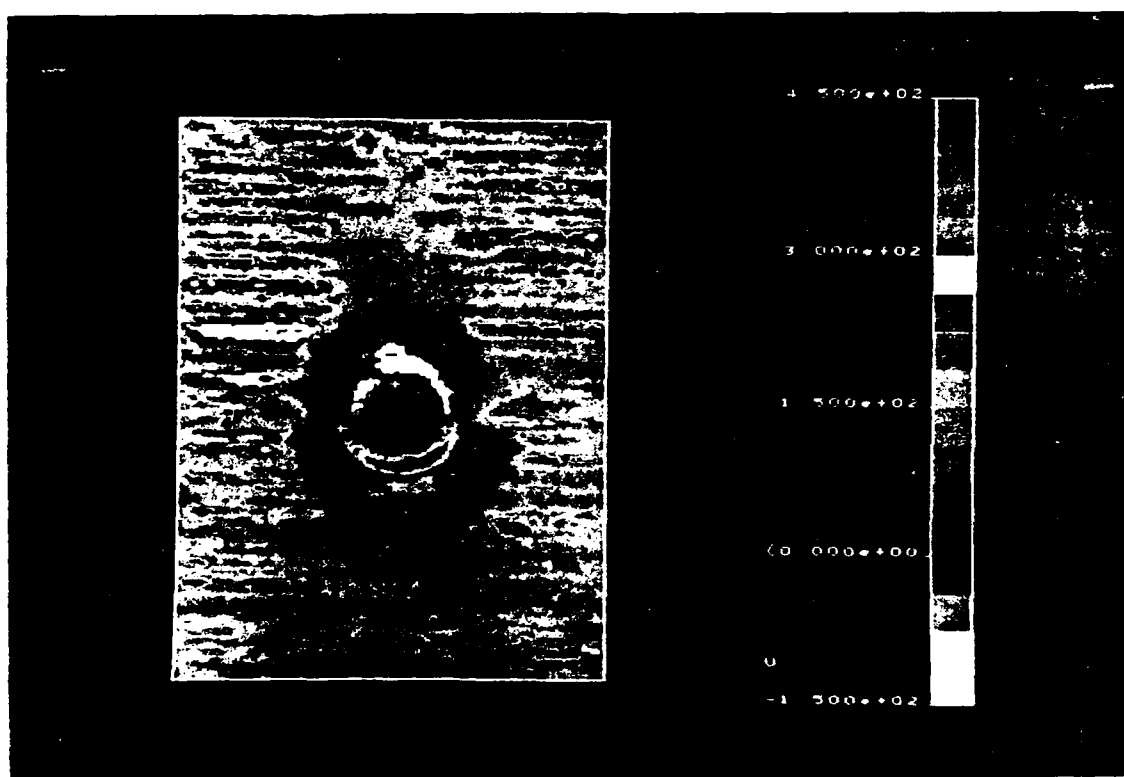


(a)



(b)

Figure 57. SPATE thermographs of matrix crack development: (a) undamaged; (b) after tensile fatigue ( $R=0.1$ ); (c) after tensile-compressive fatigue ( $R=-1$ ), near fatigue failure



(c)

Figure 57. (Concluded)

Although the delamination around the notch in Figure 57c appeared in the SPATE thermograph as an area of negligible temperature change, it would be a misinterpretation to assume that this portion of the surface ply carried no load at all. Recalling the expression for adiabatic temperature change in a ply,  $\Delta T = K_1 \sigma_1 + K_2 \sigma_2$ , it is clear that certain nonzero combinations of stress components result in no net temperature change, as does the null stress state. In this particular case (Figure 57c), additional information obtained via penetrant-enhanced X-ray radiography suggested that the surface ply could still carry load in the fiber direction, but not transverse to the fibers.

Fiber reinforced composites in structural applications are usually designed such that most of the load is carried by the fibers. Therefore, one can expect significant disturbances in the stress field to arise from fiber fracture. For example, recall Figure 26 on page 76 illustrating the incremental, 0-deg. surface ply fracture pattern often seen on the surface of test specimens. Immediately ahead of the crack front, a zone of high stress concentration formed, leading to a repetition of the incremental damage growth process. A better appreciation for the severity of this migrating zone of stress concentration is offered by the SPATE thermograph of a AS4/1808, (0,45,90,-45)<sub>s4</sub> specimen in Figure 58. The adiabatic temperature change near the crack tip was approximately 2.9 times greater than that in the far-field area of the laminate, slightly greater than the typical ratio of 2.8 measured adjacent to the hole in undamaged specimens. Additional experimental evidence obtained using the photoelastic coating technique also revealed the large strain concentration typically seen with this type of damage [58]. Therefore, not only was there a strain concentration in the intact 0-deg. fibers ahead of the crack tip, but at least a portion of the laminate underlying the surface damage zone near the notch was also subjected to a strong strain concentration due to the local reduction in compliance caused by the 0-deg. ply fiber fractures. Two directions of damage growth during cyclic loading, in-plane and through-the-thickness, were thus affected by damage-induced stress redistribution.

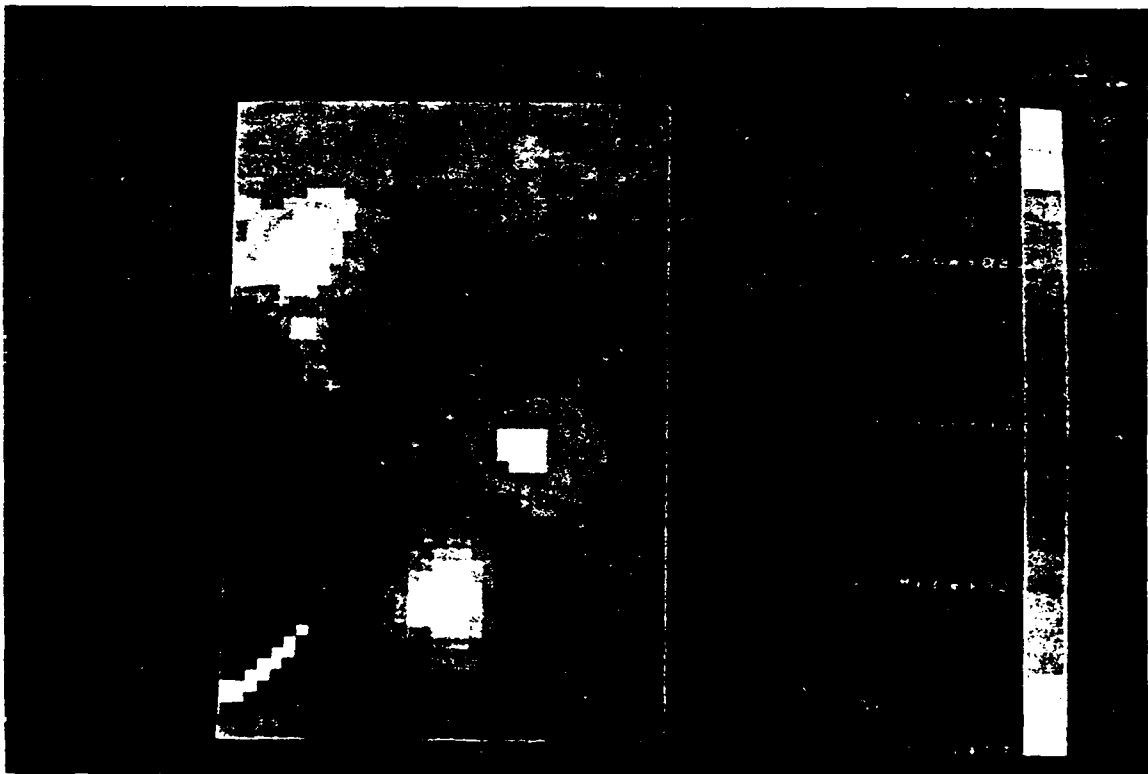


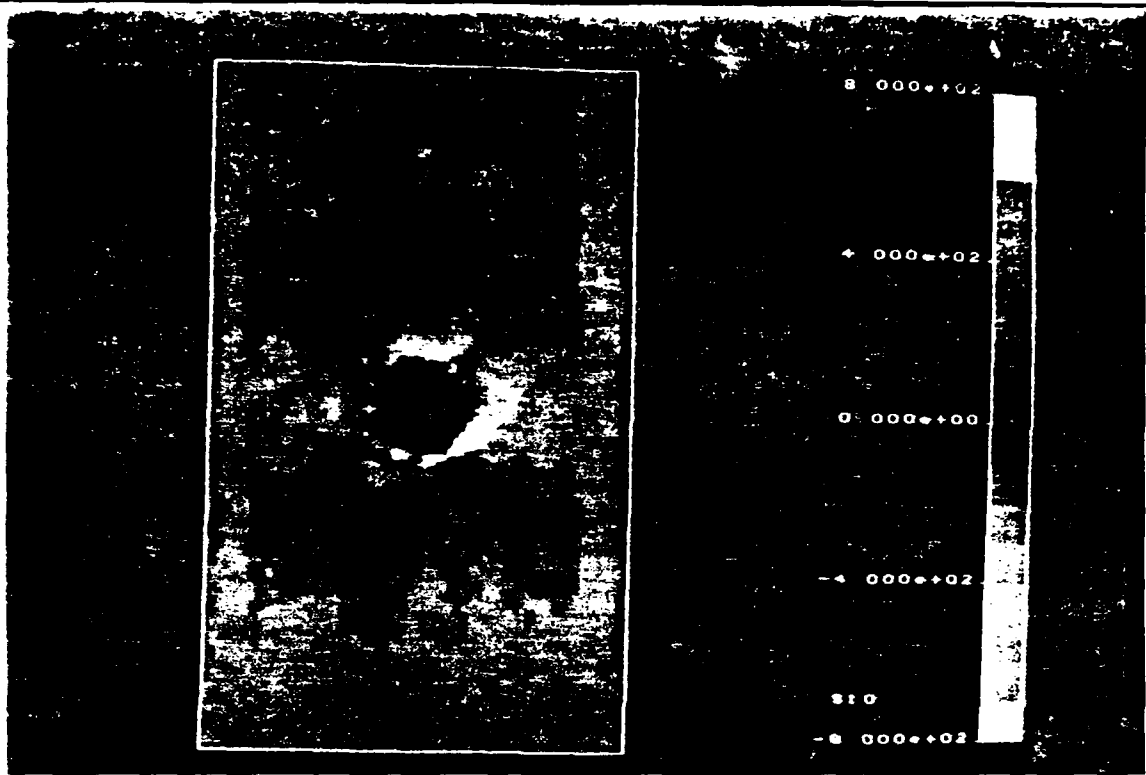
Figure 58. SPATE thermograph of a 0-deg. surface ply fracture



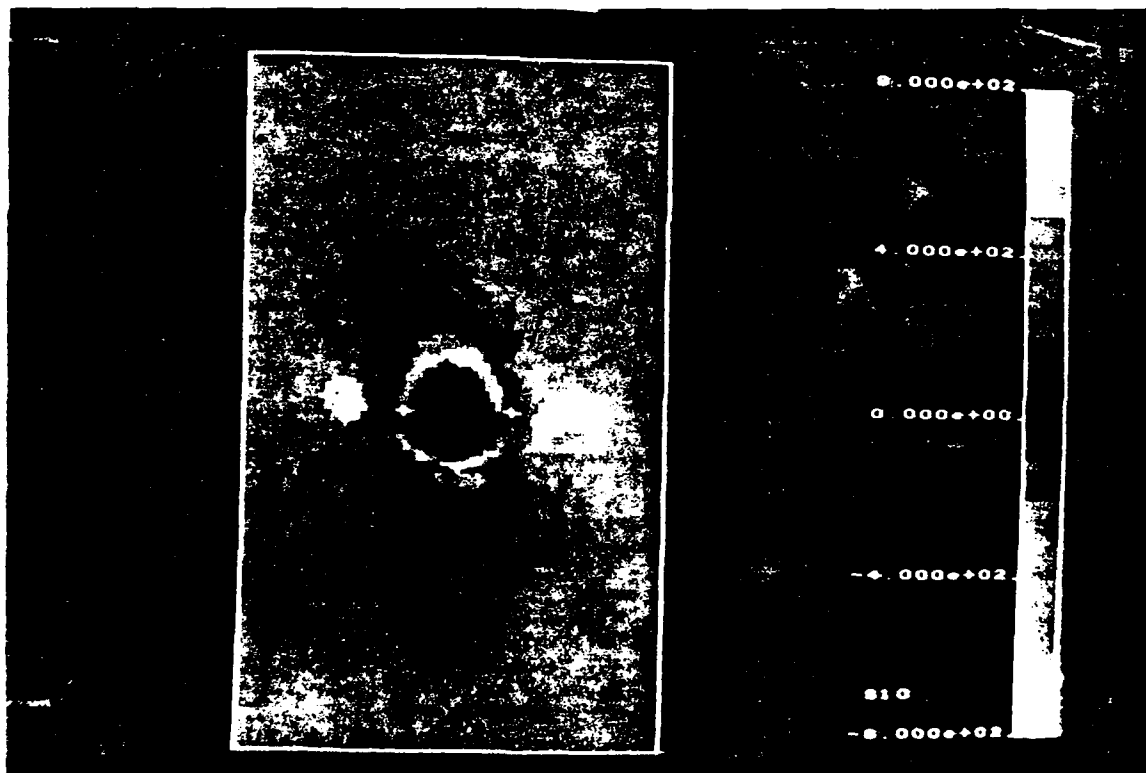
Numerous parameters influence the details of damage development and stress redistribution in fiber reinforced composite laminates during cyclic loading, although only a few have been experimentally investigated. Those that will be discussed next are: lamination arrangement, material system, loading regime, and, to a lesser extent, notch configuration. The discussion will focus on comparisons, not details.

Lamination arrangement influences the damage initiation and growth patterns in CFRP laminates because of the anisotropic strength characteristics of the individual plies. That is, the matrix-dominated shear and transverse strengths are significantly lower than the fiber-dominated longitudinal strength. SPATE thermographs of  $(0,45,90,-45)_{s4}$  and  $(0,45,0,-45)_{s4}$  AS4/1808 laminates obtained at regular intervals in their respective fatigue lifetimes indicated that their different modes of fatigue damage growth resulted in different distributions of stress around the notch.

The highest adiabatic temperature change (ATC) in the surface 0-deg. ply of the  $(0,45,90,-45)_{s4}$  laminate during high-load fatigue occurred adjacent to the notch in the undamaged specimen, but it shifted in the transverse direction such that it remained immediately in front of the 0-deg. ply fiber fracture path or delamination zone (or both) growing from the notch. Concurrently, the ATC within the delaminated zone decreased to a value of nearly zero. Adiabatic thermoelastic emissions in four different specimens at sequential states of fatigue life are shown in Figure 59 and Figure 60. The lower ATC measured within the growing damage zone near the notch was caused by either: (a) an actual decrease in fiber-direction stress in those cases where the surface 0-deg. ply has fractured and delaminated in the incremental fashion of Figure 26 on page 76; or (b) the purely uniaxial load imposed on the delaminated strips of 0-deg. ply adjacent to the notch in the absence of fiber fracture. Photoelastic coating data in either case indicated that strains inside the damage zone increased relative to the undamaged condition, and that areas of high strain concentration also existed immediately ahead of the advancing damage zone [58]. Fatigue damage in the  $(0,45,90,-45)_{s4}$  laminate followed the path of the migrating zones of high strain concentration.

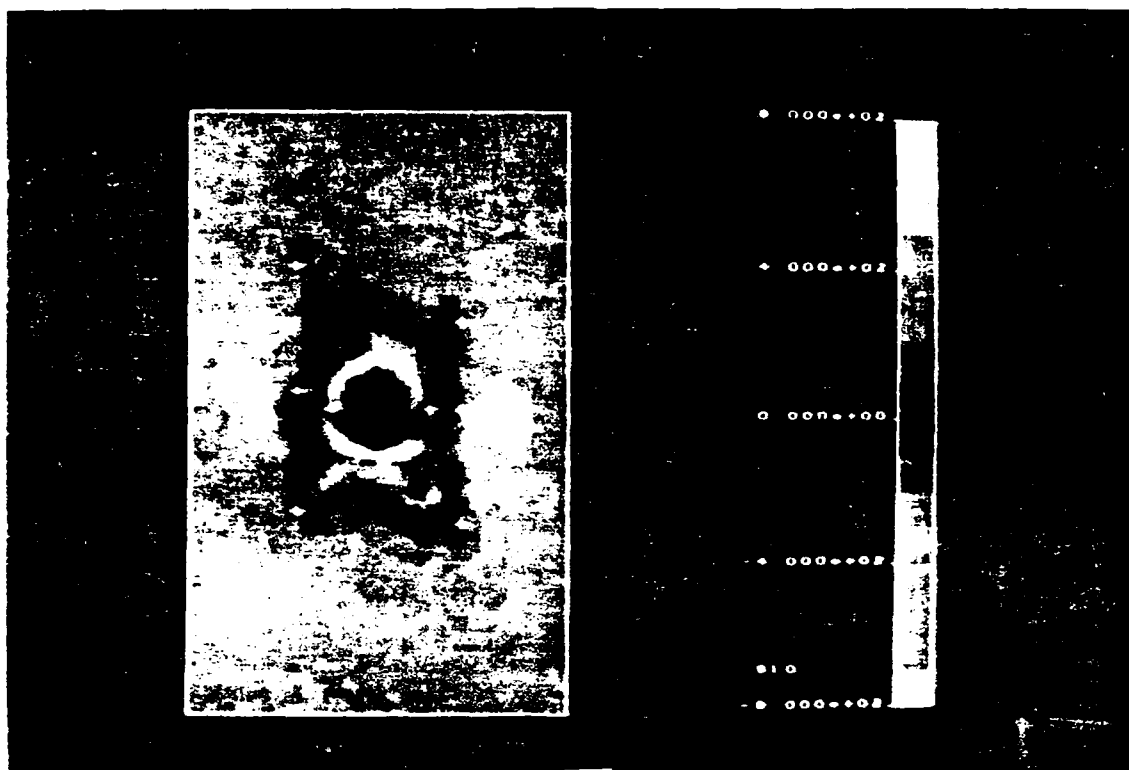


(a)

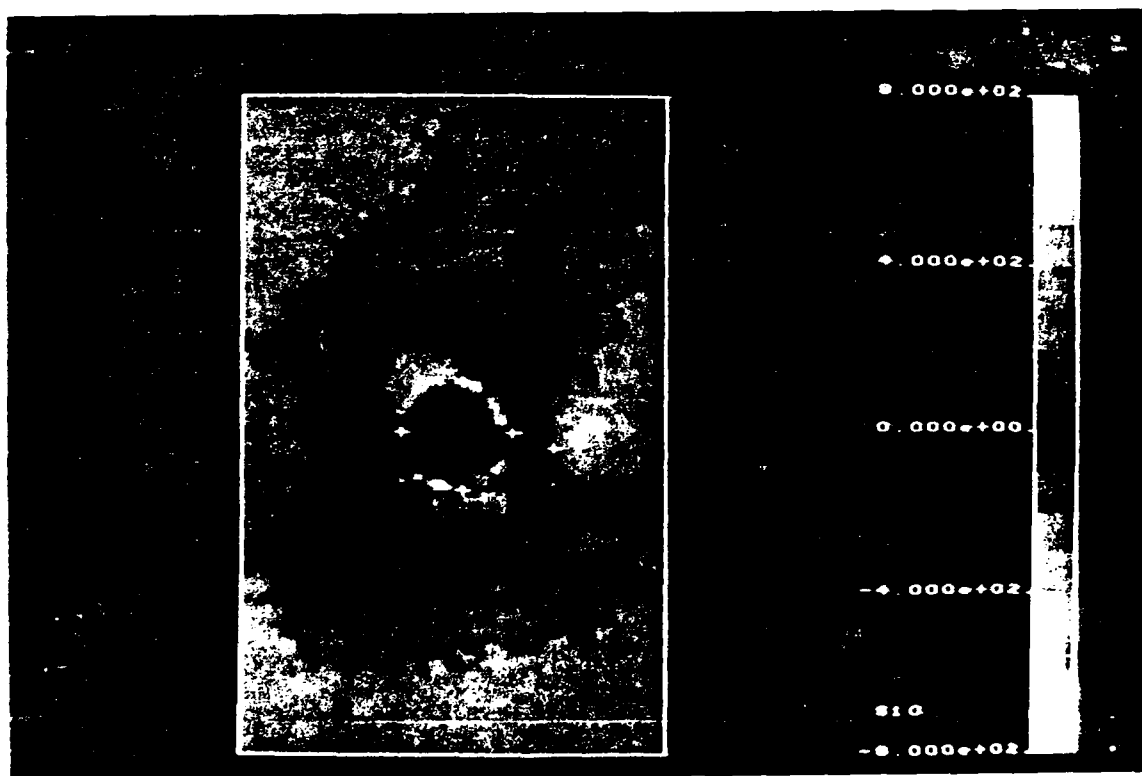


(b)

Figure 59. SPATE thermographs of four center-notched, AS4/1808,  $(0.45, 90, -45)_{s4}$  specimens during high-load fatigue: (a) undamaged (back); (b) early life (front); (c) middle life (front); (d) late life (back)



(c)



(d)

Figure 59. (Concluded)



SPATE data revealed only a small change in the uniformity of the far-field patterns as damage developed, a feature that contrasted with the  $(0,45,0,-45)_{s4}$  laminate.

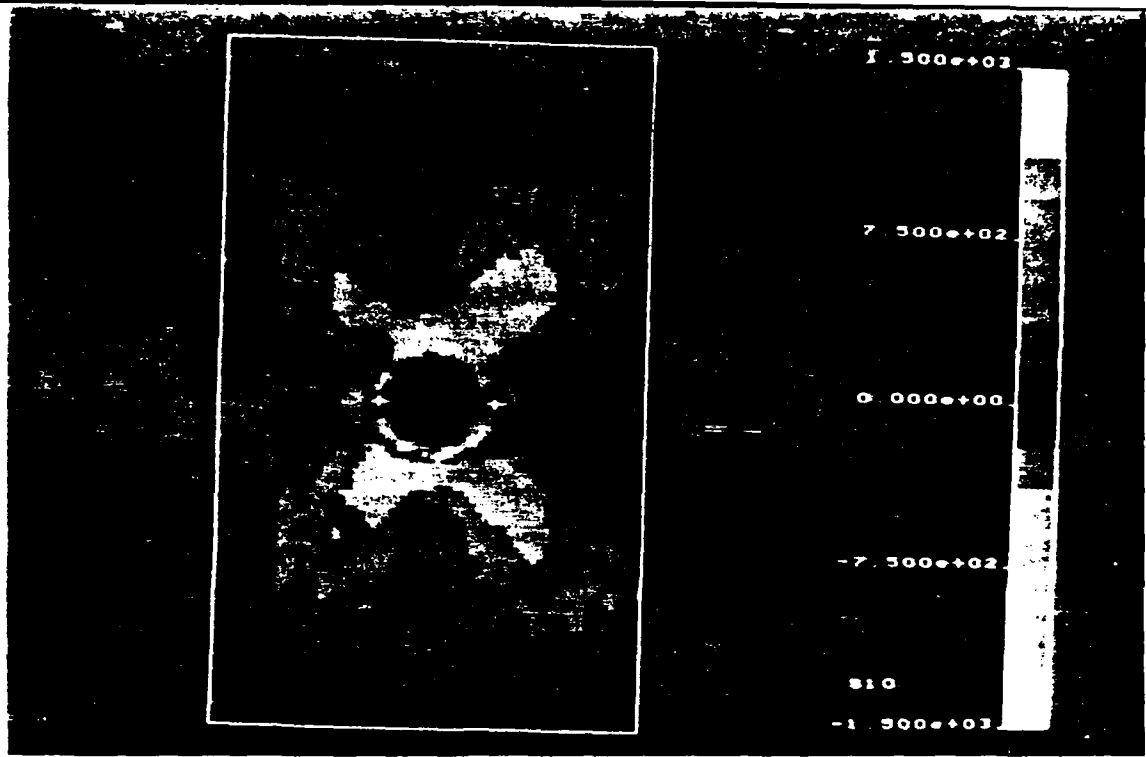
Correlations of the maximum ATC measurements on high-load,  $(0,45,90,-45)_{s4}$  specimens with the tensile strength of those same specimens were quite good once inter-specimen variations in the ATC remote from the notch were eliminated by normalizing the maximum ATC near the notch by the remote ATC. In effect, "ATC concentration factors" were used as measures of worst-case stress concentrations in different specimens. Dividing the ATC concentration factor in the virgin specimen by the ATC concentration factors in the residual strength specimens resulted in the expected strengths listed in Table 6 for the  $(0,45,90,-45)_{s4}$  specimens (the expected strengths for  $(0,45,0,-45)_{s4}$  specimens were computed differently). The actual tensile strengths in Table 6 were normalized by the average strength of virgin specimens. Actual and expected strengths both increased up to half of the fatigue lifetime, and decreased near fatigue failure.

In AS4/1808,  $(0,45,0,-45)_{s4}$  specimens, zones of high ATC moved longitudinally along the large 0-deg. cracks that formed tangent to the notch in the 0- and 45-deg. plies (Figure 61 and Figure 62). Near the tips of these cracks, there were small areas of stress concentration in the load-bearing ligaments of the 0-deg. plies. These zones shifted in the longitudinal direction as the 0-deg. cracks grew, and corresponded closely to the location of tensile fracture in residual strength tests (shown later in the chapter on residual strength). The maximum amplitude of ATC within these small zones was nearly the same as that found adjacent to the notch (over a larger area) in the undamaged specimen. Photoelastic coating data indicated that high shear strain concentrations formed at the 0-deg. tangent crack tips. Also, the photoelastic data showed that regions of material directly above and below the notch (between the 0-deg. tangent cracks) became somewhat decoupled from the remainder of the laminate and carried little load [58]. This information indicates that the stress distribution in the  $(0,45,0,-45)_{s4}$  laminate became increasingly uniform as fatigue damage developed (provided no localized surface damage events occurred), resulting in a reduced notch effect as the

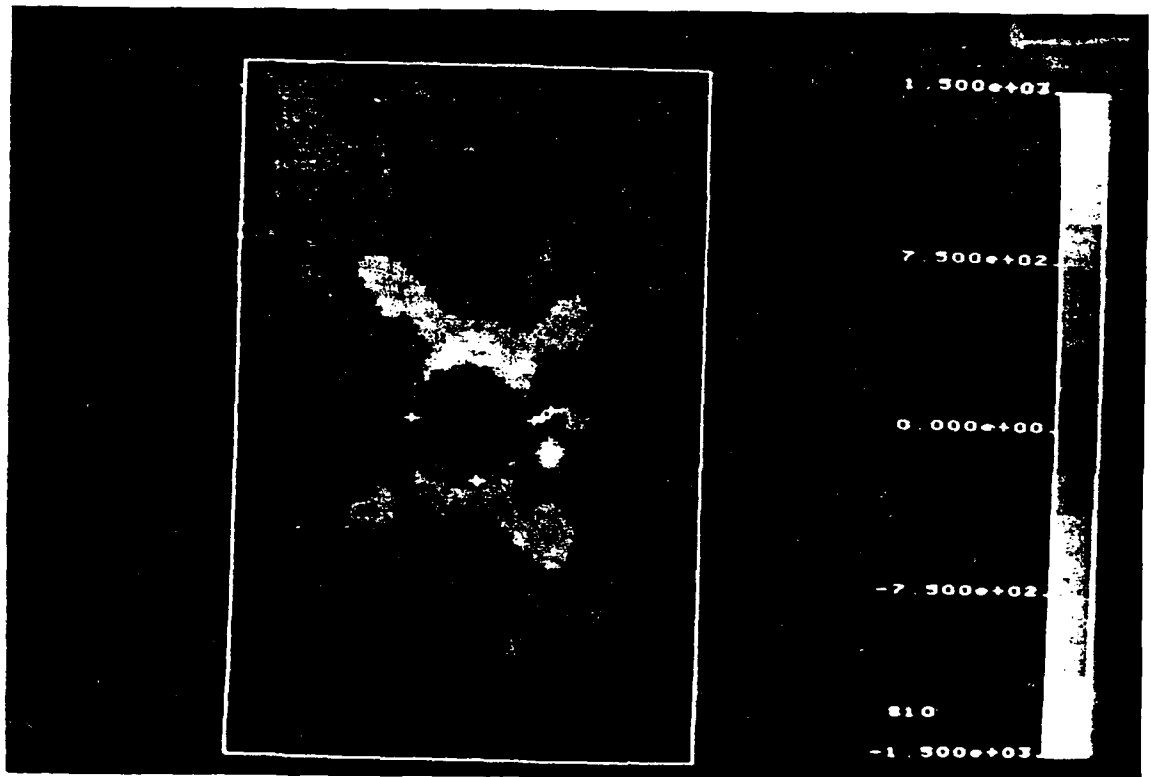
**Table 6. Actual and expected normalized tensile strengths of center-notched, AS4/1808 specimens during high-load fatigue**

Stack	Specimen Identification	Estimated % of Life	Actual $S_f/S_f^\dagger$	Expected $S_f/S_f^\dagger$
(0,45,90,-45) <sub>s4</sub>	3-10	0	1.00	1.00
	3-12	5-10	1.11	1.27
	3-2	40-60	1.19	1.33
	2-3	≥90	.883	1.12
(0,45,0,-45) <sub>s4</sub>	2-11	0	1.00	1.00
	3-3	5-10	1.16	0.71
	3-7	40-60	1.42	1.16
	2-18	≥90	1.10	1.05

† Strengths normalized by the average strength of virgin specimens.

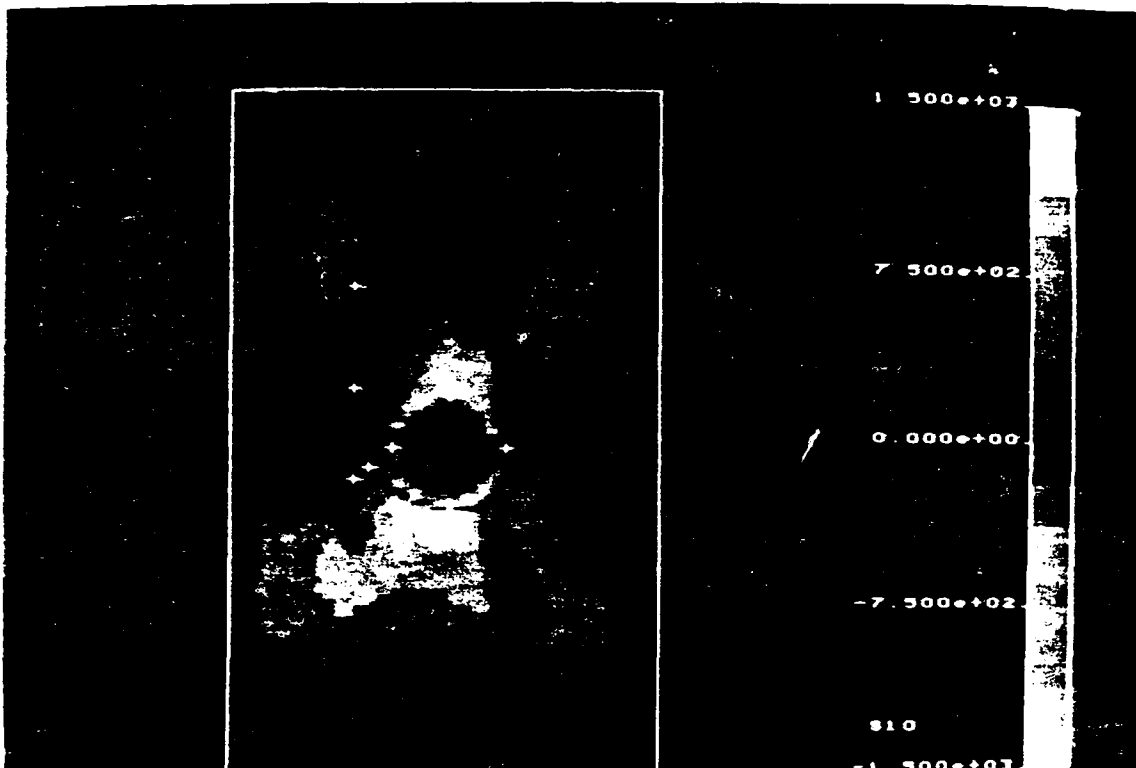


(a)

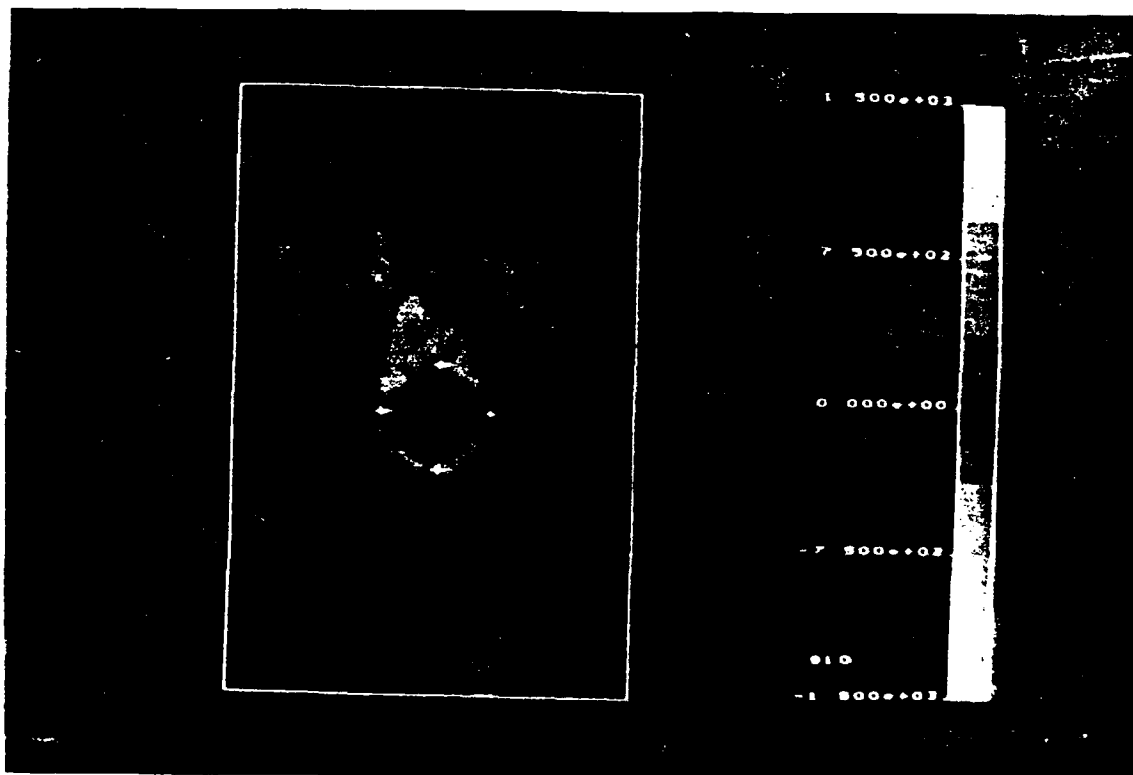


(b)

Figure 61. SPATE thermographs of four center-notched, AS4/1808, (0,45,0,-45)<sub>31</sub> specimens during high-load fatigue: (a) undamaged (back); (b) early life (front); (c) middle life (front); (d) late life (front)



(c)



(d)

Figure 61. (Concluded)



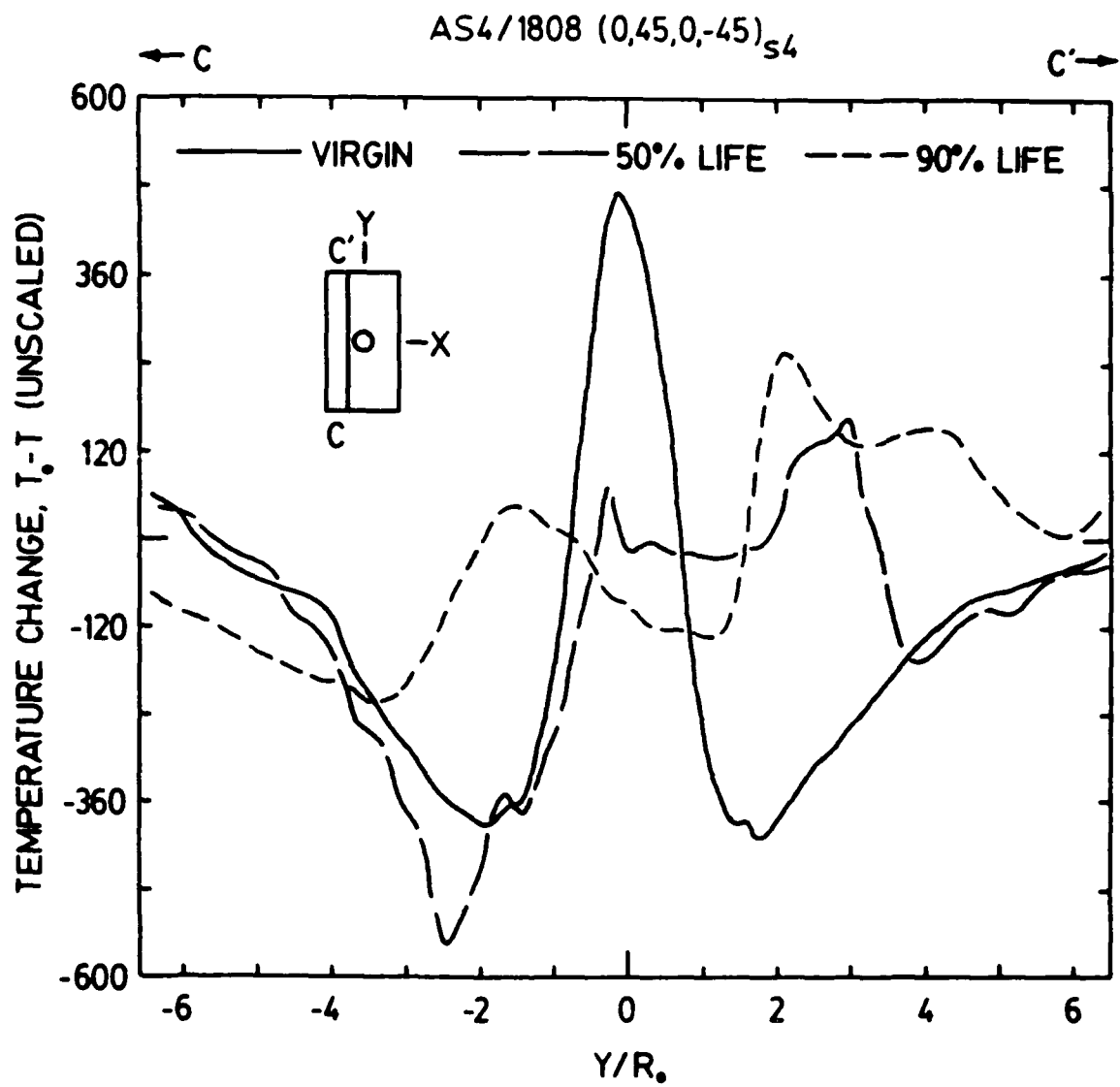


Figure 62. SPATE signal along Section C-C' in three center-notched, AS4/1808, (0,45,0,-45)<sub>S4</sub> specimens during high-load fatigue:  $R_0$  = hole radius.

two ligaments of material adjacent to the notch behaved more like straight-sided coupons. Near the end of life, the maximum ATC within the ligaments increased. This suggests that the surface 0-deg. plies carried an increasing proportion of the load as the stiffness of the ligaments decreased due to off-axis matrix cracking.

Expected strengths of center-notched, AS4/1808,  $(0,45,0,-45)_{s4}$ , residual strength specimens could not be computed as they were for  $(0,45,90,-45)_{s4}$  specimens because the far-field value of ATC was zero in the  $(0,45,0,-45)_{s4}$  specimens. (One cannot compute an ATC concentration factor by dividing the maximum ATC by zero). Consequently, the highest value of ATC measured in the virgin specimen was divided by the highest value of ATC in each residual strength specimen to arrive at the expected strengths listed in Table 6. The effect of inter-specimen variation in ATC was therefore not eliminated in the calculations for orthotropic specimens as it was for quasi-isotropic specimens. Despite this handicap, the expected strengths for all stages of fatigue life except "early" followed the trends in the actual tensile strengths of the test specimens (increasing up to middle life, and decreasing slightly near fatigue failure). The low expected strength of the early-life specimen resulted from the extremely high value of ATC measured at the tip of a short 0-deg. ply fracture adjacent to the hole. Apparently, the small volume of highly stressed material in front of the crack tip did not govern the failure of the specimen.

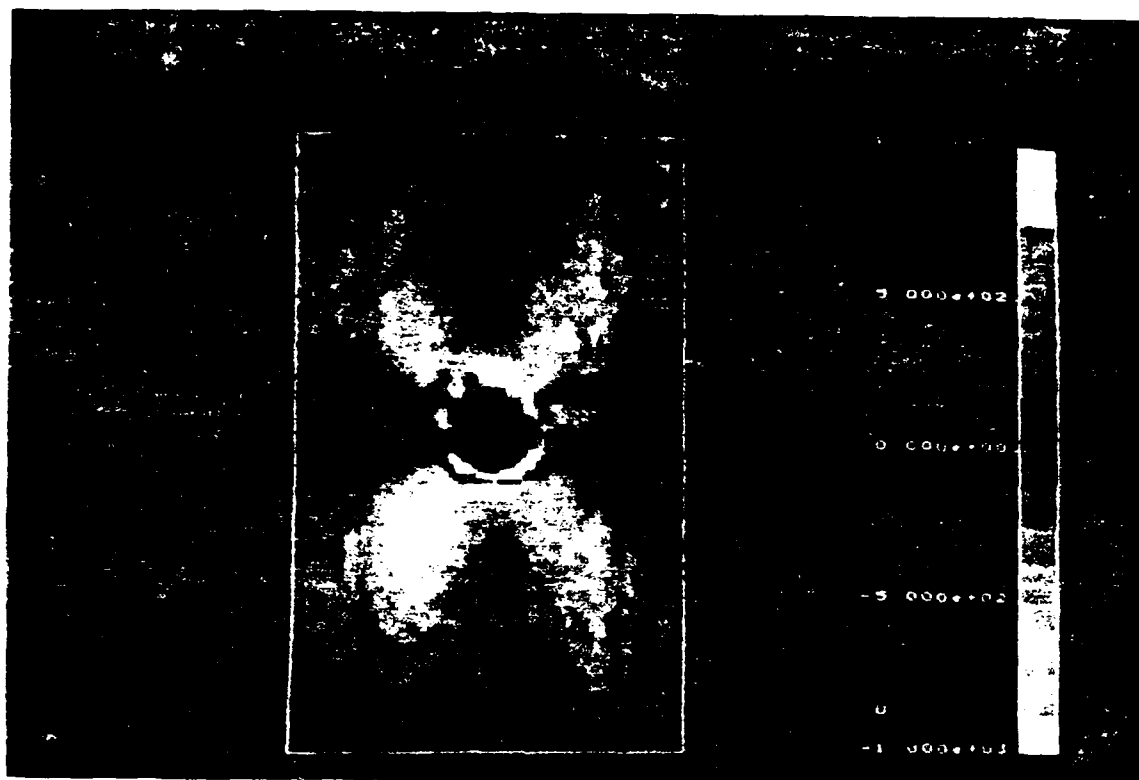
In summary, the statements one can make regarding stress redistribution in the two notched AS4/1808 laminates examined are as follows:

1. Areas of major stress concentration were intrinsically related to the existing damage state.
2. Areas of major stress concentration corresponded to areas of subsequent damage growth.
3. Values of ATC corresponded well with trends in tensile strength during the fatigue life-time.

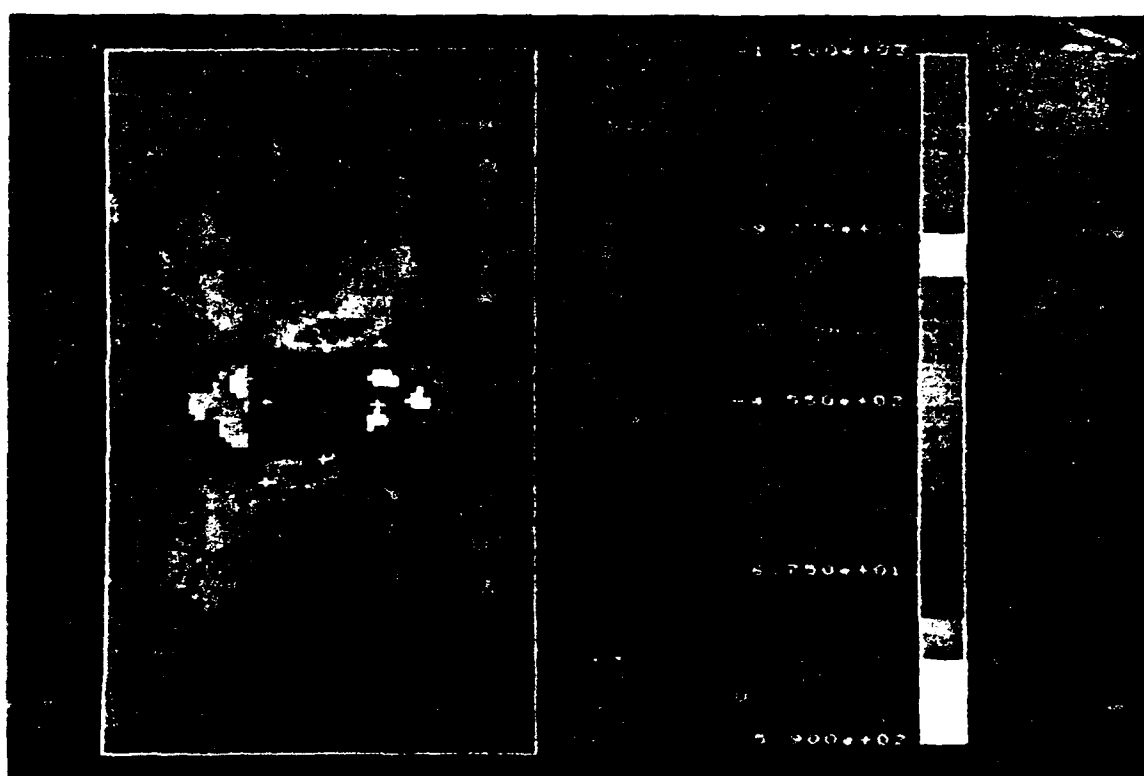
4. The nature of stress redistribution in the orthotropic laminate was such that for a large portion of the fatigue lifetime the two ligaments of material adjacent to the notch saw little stress concentration due to the original notch.

Using SPATE data to predict the tensile strength of specimens is, at best, unreliable. For example, the expected strength increases of the quasi-isotropic specimens in Table 6 were higher than the expected strength increases of the orthotropic specimens. In reality, the orthotropic specimens had higher strength increases than the quasi-isotropic specimens. A possible explanation for this discrepancy is that the interior plies of the laminate may govern strength, particularly when the surface plies are heavily damaged. Hence, stress patterns in the surface plies may lead to inaccurate strength predictions.

The second parameter affecting the damage development and stress redistribution in CFRP laminates is material system. The previous chapter on damage mechanisms described the differences in fatigue response of AS4/3501-6 and AS4/1808 specimens. Presently, stress redistribution mechanisms in center-notched, AS4/3501-6 and AS4/1808, (0,45,0,-45)<sub>s4</sub> specimens during high-load fatigue will be compared. Up to approximately one third of the fatigue lifetime, there was little difference in their respective SPATE thermographs (compare the AS4/3501-6 thermographs in Figure 63 with the AS4/1808 thermographs in Figure 61 on page 149). At approximately one half of each material's respective fatigue lifetime, though, differences emerged. The most prominent among these was the lack of high stress concentrations near the tips of the 0-deg. tangent cracks in the AS4/3501-6 laminate. (Recall that the 0-deg. tangent cracks were shorter and more similar in length in all four quadrants in the AS4/3501-6 specimens.) There was, overall, a more uniform thermoelastic emission in the two ligaments of material adjacent to the notch in the AS4/3501-6 laminate, leading one to expect higher residual tensile strengths than in the AS4/1808 laminate. It will be shown later that the residual tensile and compressive strengths of middle-life AS4/3501-6 specimens were only slightly higher than their AS4/1808 counterparts.

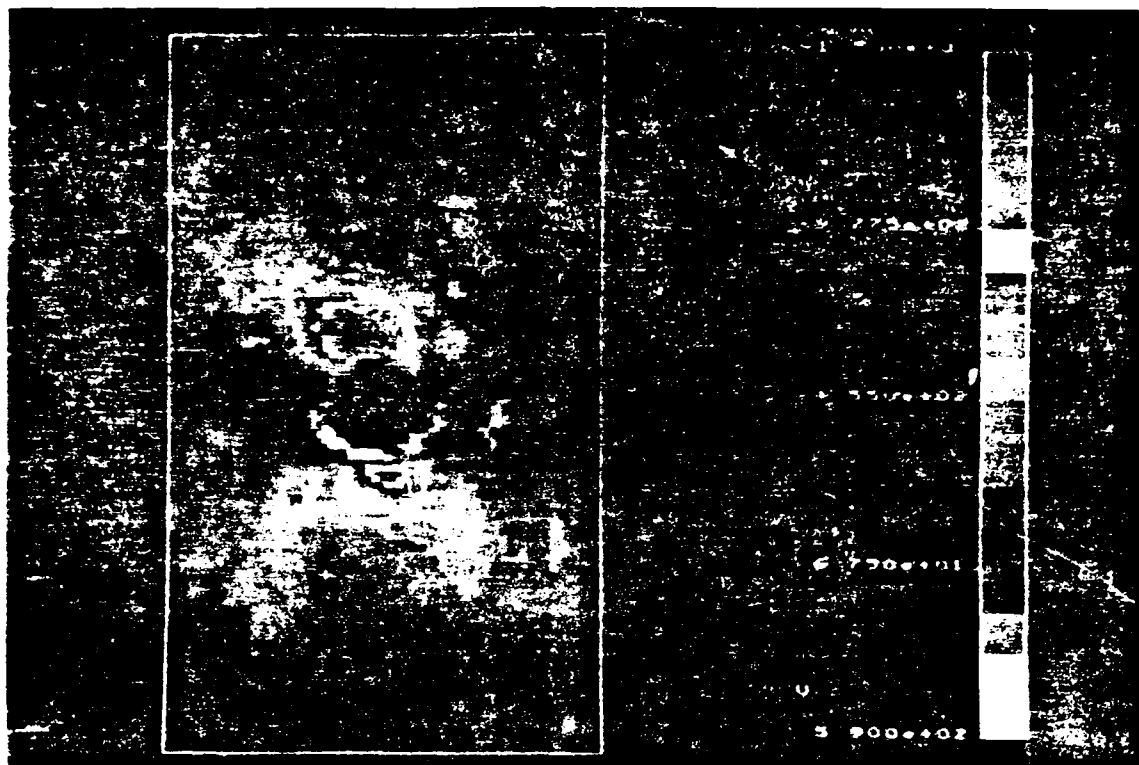


(a)



(b)

Figure 63. SPATE thermographs of four center-notched, AS4/3501-6,  $(0.45,0,-45)_{54}$  specimens during high-load fatigue: (a) undamaged (back); (b) early life (back); (c) middle life (back); (d) late life (back)



60



Figure 63 (Concluded)

Next, the effect of cyclic load excursions on stress redistribution in the notched (0,45,90,-45)<sub>s4</sub> AS4/1808 laminate under the "high" and "low" load levels described earlier. In these cases, compressive failures were precipitated by large amounts of delamination throughout the unsupported gage length, but significant differences were seen in the damage and stress redistribution patterns prior to failure (see Damage Mechanisms).

SPATE thermographs of the low-load specimens taken three times during the fatigue lifetime are shown in Figure 64 for comparison with the high-load specimens shown at comparable fractions of the fatigue lifetime in Figure 59 on page 144. In the early-life thermographs, the primary difference between the load levels was the larger area of reduced ATC adjacent to the notch with the low load level. In both cases, the low ATC area was caused by 0-deg. ply fractures or delaminations under the surface 0-deg. ply (or both). Zero-deg. ply fiber fractures and associated delaminations, which were more likely to form under the high load amplitude, maintained a high stress concentration and resulted in a predominantly transverse direction of damage growth. In the low-load situation, delaminations often occurred in the absence of 0-deg. fiber fractures, resulting in a tendency for longitudinal delamination growth and less stress concentration in the surface ply for most of the fatigue lifetime. This information is supported by the mid-life SPATE thermographs shown in Figure 59c and Figure 64b. In the high-load specimens, the zones of high ATC that shifted in the transverse direction as damage grew away from the notch underwent only a slight change in magnitude throughout the fatigue lifetime. In the low-load specimens, those zones disappeared entirely by mid-life, and reappeared in the last 10 percent of life. The initial decrease and subsequent increase in maximum ATC in the low-load specimens corresponded well with the initial increase and subsequent decrease in residual tensile strength throughout the fatigue lifetime. On the average, the residual tensile strengths of low-load specimens were slightly higher than those of high-load specimens at equal fractions of their respective fatigue lifetimes. Unfortunately, the SPATE data did not represent the entire stress redistribution process in the laminate; only that in the surface plies. For example, the high- and low-load specimen

thermographs at mid-life (Figure 59c and Figure 64b) differed, but the residual tensile strengths of these *particular* specimens were nearly identical (both were 119 percent of the average virgin specimen strength).

Another stress redistribution mechanism existing in laminates subjected to compressive load excursions stems from the tendency of damage, particularly delaminations, to initiate and grow fastest near the free surfaces [2,6,108], as described in the chapter on damage mechanisms. When delaminated outer plies of a laminate buckle under compressive loading, a greater proportion of the load must be carried by the inner, less-delaminated plies since they possess greater lateral support and stiffness. No experimental, through-the-thickness measurements of stress redistributions were obtained in the present investigation, though such measurements would aid the explanation of many anomalous residual strength results (i.e., those where the stress concentration on the surface ply decreased, but the residual tensile strength did not increase).

Due to the compressive load excursions applied to the specimens in the present investigation, slight imperfections in the material and misalignment of the loading axis caused unsymmetric damage development and stress distributions through the thickness. The associated asymmetry of the specimen's stiffness caused out-of-plane bending (especially under compressive loads), and exaggerated the unequal rates of damage development on the opposing surfaces of the specimen. Compared to specimens with a centrally-located notch, damage-induced bending was more prevalent in specimens with double-edge notches. For example, compare the SPATE thermographs of the front and back surfaces of a DEN, AS4/3501-6, (0,45,0,-45)<sub>s4</sub> laminate near the end of its high-load fatigue life with a thermograph of an undamaged specimen (Figure 65). Under a fully-reversed cyclic load history, fiber fractures and delaminations that initiated on the front surface 0-deg. ply led to larger local compressive strains and, consequently, a faster local damage growth rate. Near impending laminate failure — when the thermographs in Figure 65 were obtained — the front surface 0-deg. ply carried little load in the area between the notches, while the back surface 0-deg.

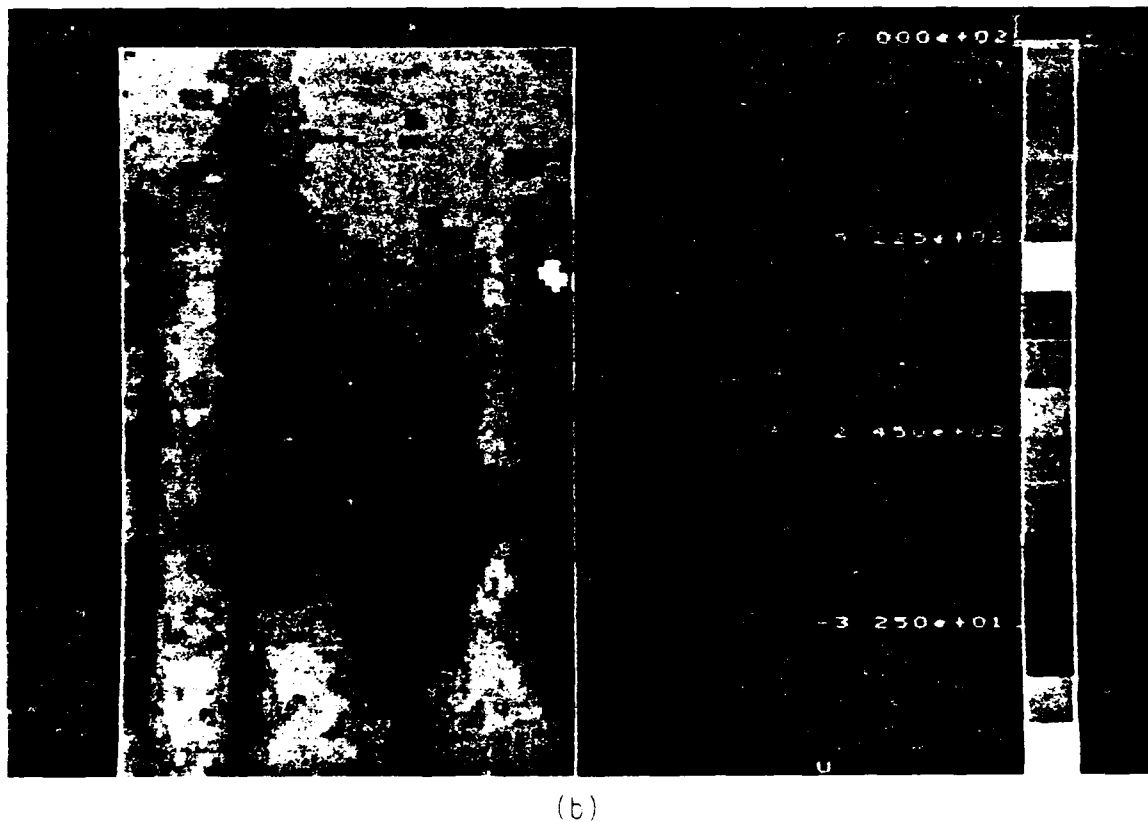
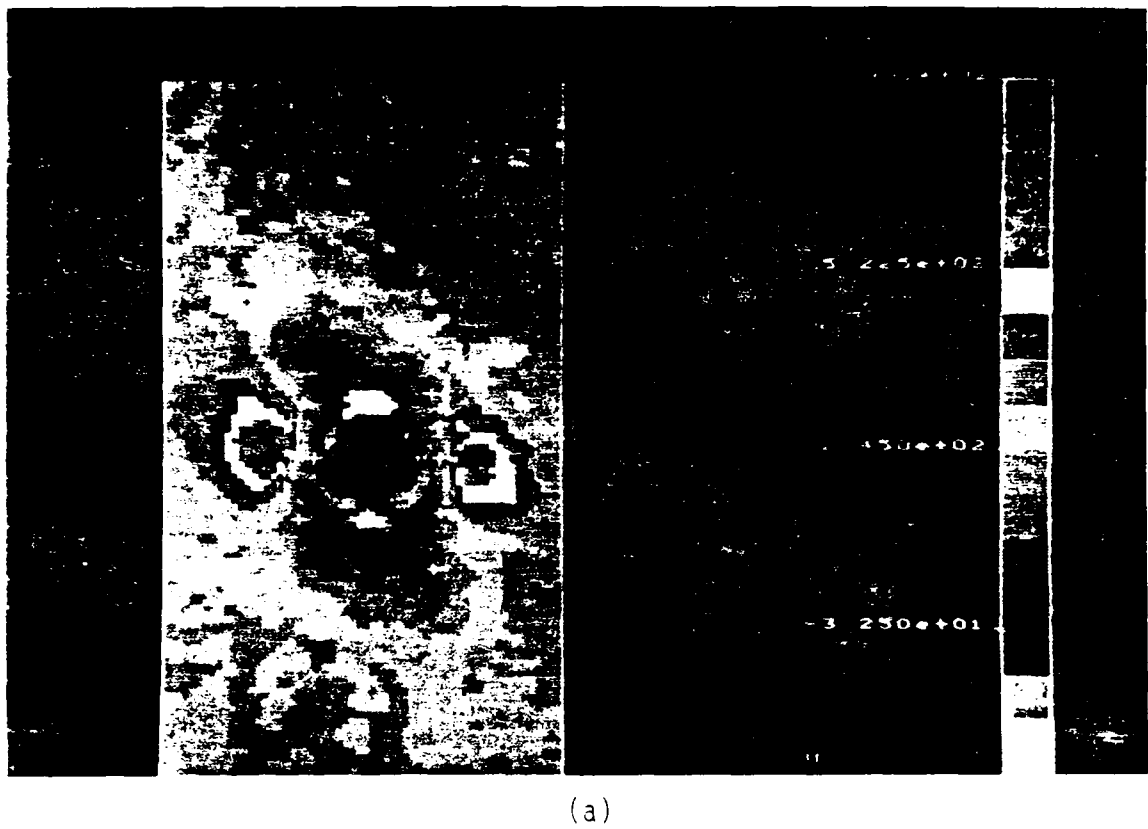
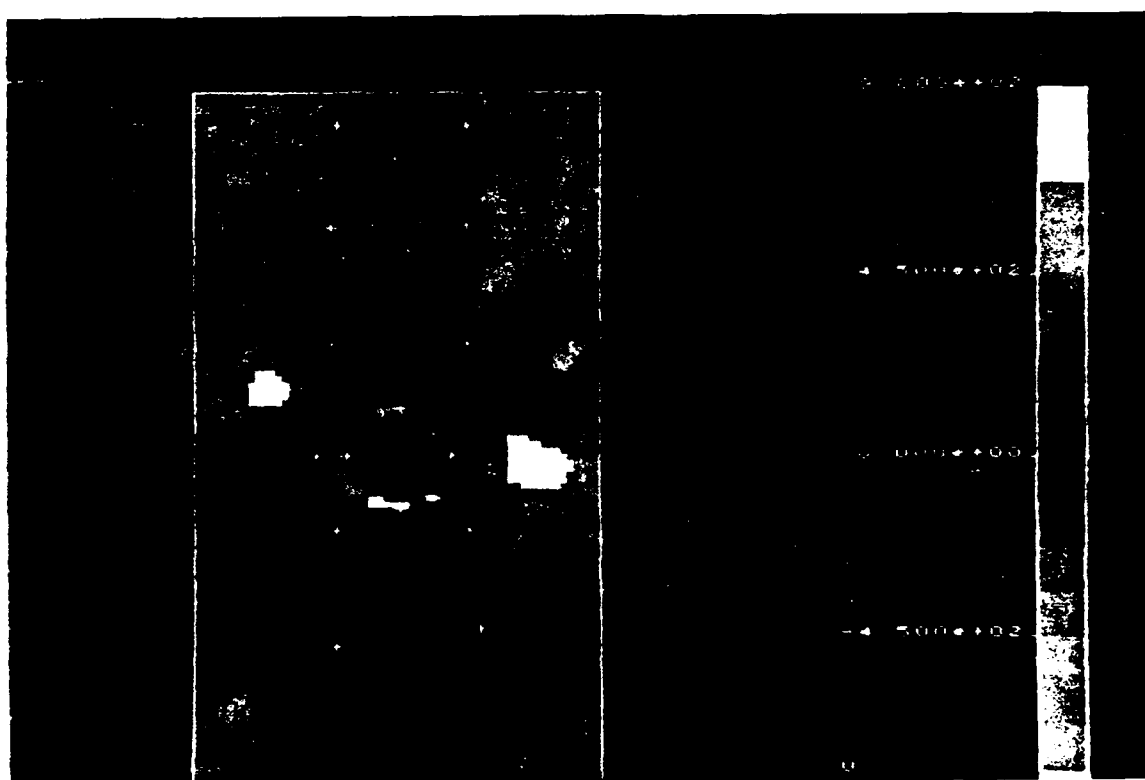


Figure 64. SPATE thermographs of three center-notched, AS4/1808,  $(0,45,90,-45)_4$  specimens during low-load fatigue: (a) early life (front); (b) middle life (front); (c) late life (front)



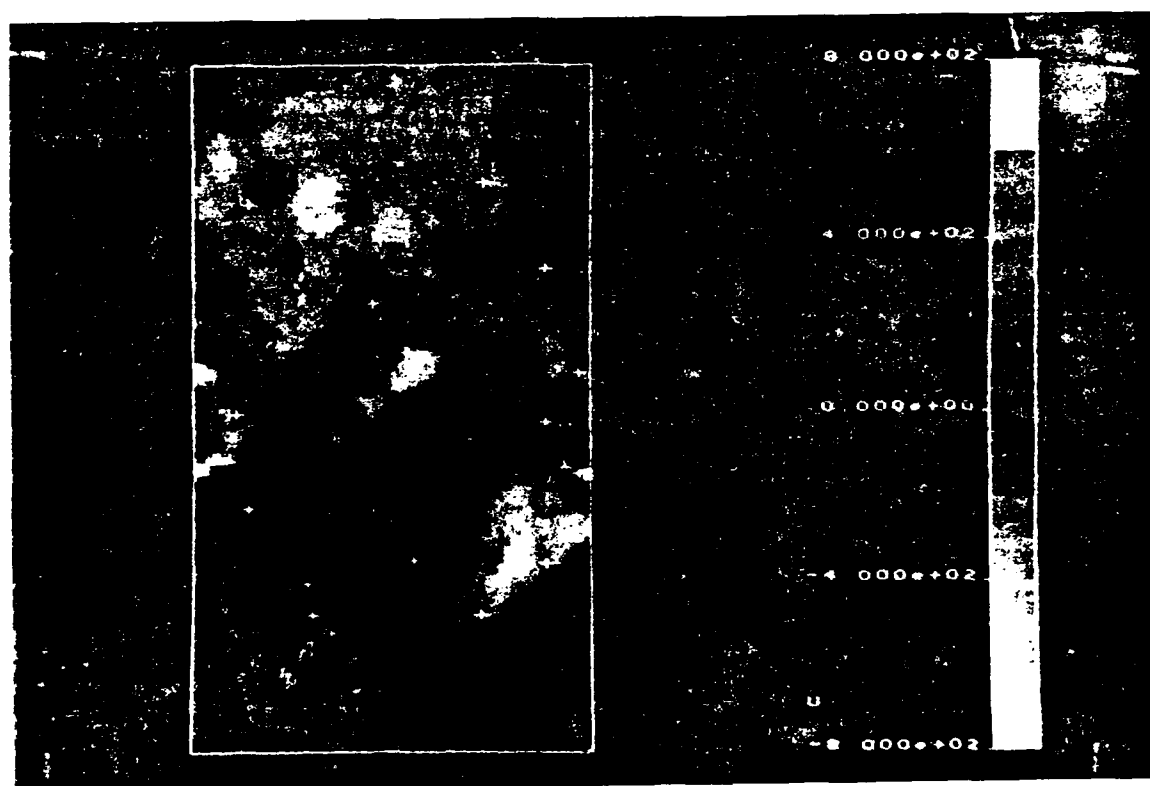


(c)

Figure 64. (Concluded)

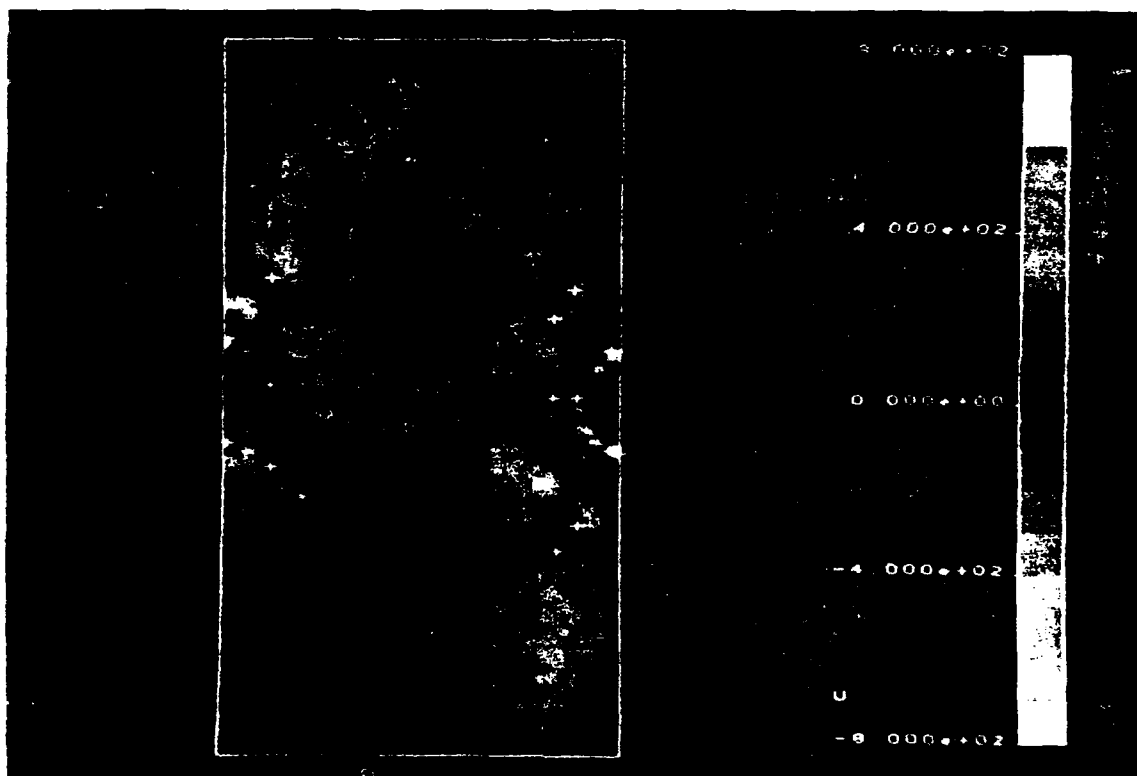


(a)



(b)

Figure 65. SPATE thermographs of AS4/3501-6, (0.45,0,-45)<sub>s</sub>, DEN specimens during high-load fatigue: (a) no. 3-13, back, undamaged; (b) no. 3-4, front, near failure; (c) no. 3-4, back, near failure

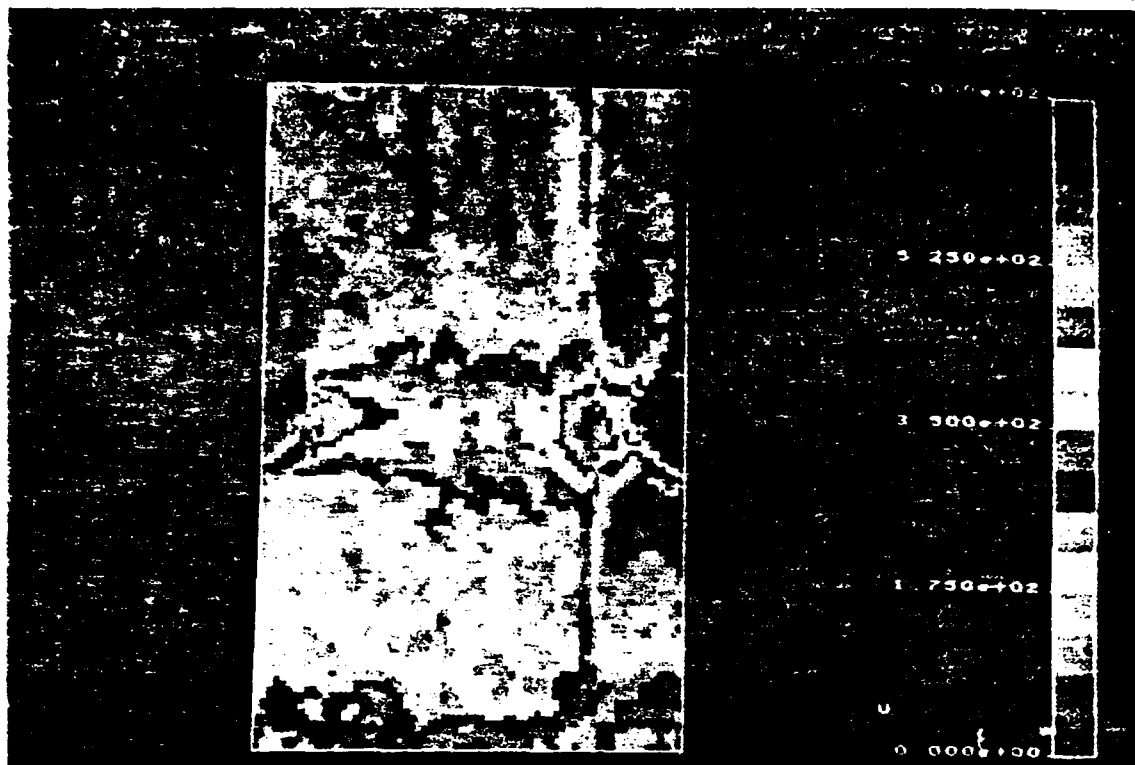


(c)

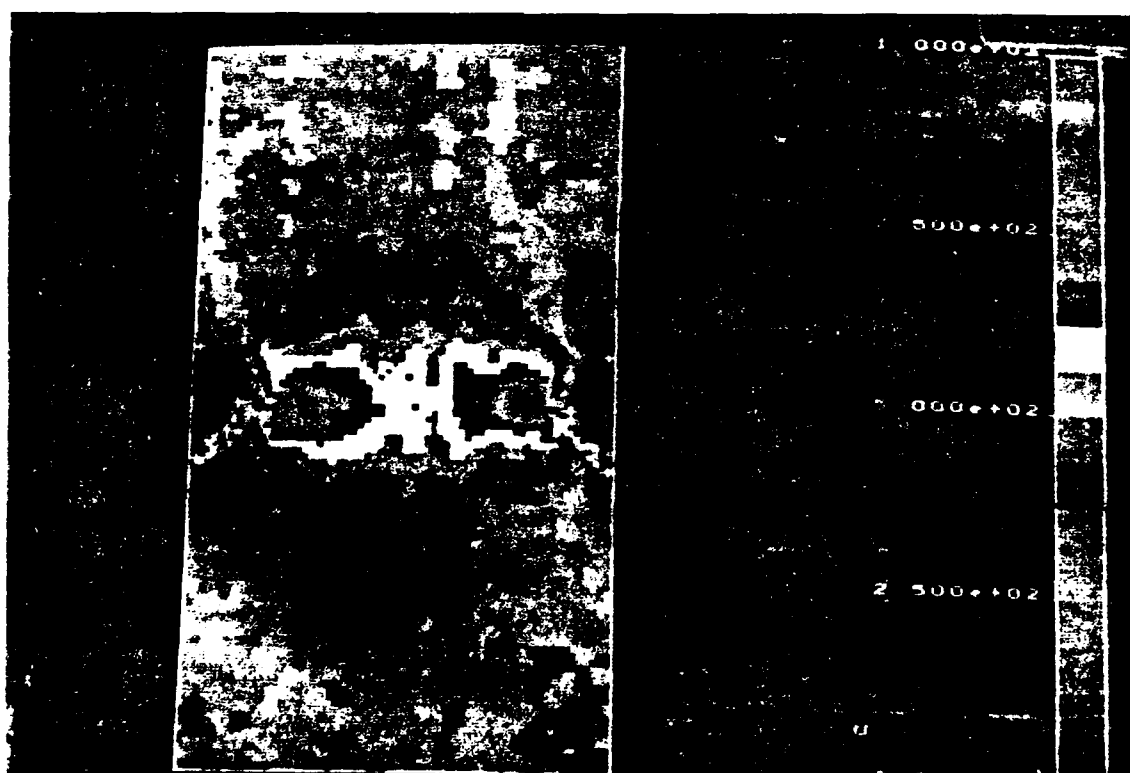
Figure 65. (Concluded)

ply remained relatively intact. Fatigue failure occurred when the interior plies, beginning with the side under the most compression, failed during a compressive load excursion.

Aside from the matter of global laminate bending, the fatigue response of laminates with DEN or CN notch configurations is rather invariant, especially in the late portion of life when additional damage growth is influenced more by the earlier damage pattern than the initial stress concentration caused by the notch itself. Indeed, Morton et al. [109] have shown that circular holes and sharp slits result in different early-life (and undamaged) strengths, but increasingly similar strengths later in the fatigue lifetime. In the present study, high-load fatigue damage development and stress redistribution data for AS4/1808, (0,45,90,-45)<sub>s4</sub> specimens with double semi-circular edge notches were compared to the data obtained from center-notched specimens. It was found that damage initiation and growth for the two notch configurations were nearly the same, as was the failure mode. With a few exceptions, DEN specimens had slightly more longitudinal delamination growth and slightly higher residual tensile and compressive strengths than their center-notched counterparts at comparable fractions of their respective fatigue lifetimes. A sequence of SPATE thermographs of DEN specimens during high-load fatigue development shows the effect of the increased longitudinal delamination on the surface stress pattern (Figure 66). As damage grew, the two regions of high stress initially located adjacent to the notches moved toward the centerline of the specimen and eventually coalesced near fatigue failure.



(a)



(b)

Figure 66. SPATE thermographs of four double-edge-notched, AS4/1808,  $(0,45,90,-45)_{s4}$  specimens during high-load fatigue: (a) undamaged (back), (b) early life (front), (c) middle life (front), (d) late life (front).

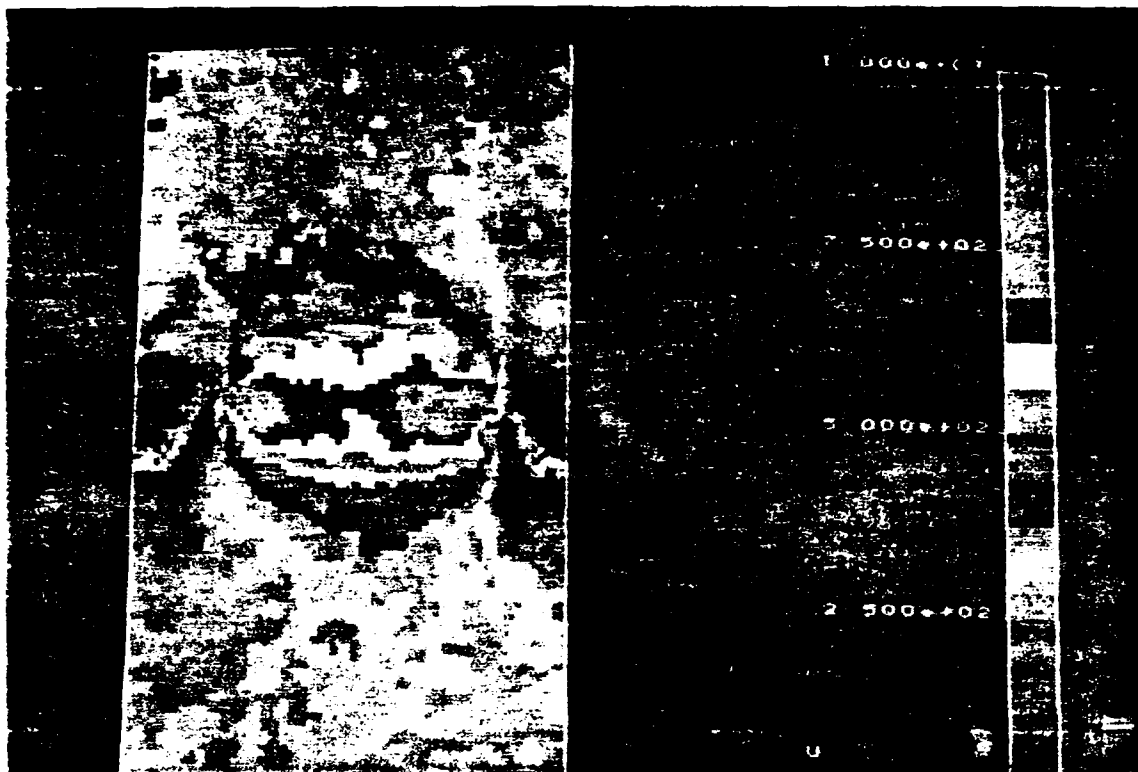


Figure 66. (Concluded)

## VI

### Residual Strength

Residual tensile and compressive strengths ( $S_t$  and  $S_c$ , respectively) and stiffnesses ( $E_t$  and  $E_c$ , respectively) measured at the early, middle, and late stages of fatigue life were normalized by their respective values in virgin specimens given in Table 3 and Table 5. Plots of normalized tensile and compressive strengths versus the estimated fraction of fatigue life are superposed so that trends in the two components of strength can be easily compared. Cyclic load amplitudes, normalized by the tensile and compressive strengths of virgin specimens (refer to Table 4), are indicated on the vertical axes of the strength graphs as points of reference. The discussion of residual strength focuses on the data for six test types studied in detail: 1808-A-CN (high and low load levels); 1808-A-DEN (high load level); 1808-B-CN (high and low load levels); and 3501-B-CN (high load level). Residual strength data for the center-notched AS4/1808 specimens are the most extensive. Therefore, strength data for the DEN and AS4/3501-6 specimens will be compared to this best-characterized data set.

## 6.1 AS4/1808, Quasi-Isotropic Laminate

Normalized residual stiffness and strength data for center-notched, AS4/1808, (0,45,90,-45)<sub>s4</sub> specimens during high- and low-load fatigue are given in Table 7. The strength data are presented graphically in Figure 67 and Figure 68. Averaged, normalized strengths of early-, middle-, and late-life specimens are listed in Table 8 for comparison with other test types.

The tensile strength increased for the early- and middle-life measurement points, and decreased for the late-life measurement point. High-load specimens had lower residual tensile strengths than low-load specimens in the second half of the lifetime, perhaps due to the larger number of broken 0-deg. plies near the notch in high-load specimens during this part of life. The compressive strength decreased monotonically throughout the fatigue lifetime. Values of residual compressive strength between the two loading regimes were comparable until impending failure. At that time, delaminations had grown larger and residual compressive strengths had decreased more in low-load specimens than in high-load specimens.

The rate of compressive strength change during high-load fatigue was similar to the rate of stiffness change (Figure 22); rapid until the end of stage I, slower in stage II, and rapid once again in stage III. The sharp decline in stiffness near the middle of life in low-load tests did not seem to cause any anomalies in the middle-life residual strength measurements. This suggests that the damage that caused the stiffness change (surface 0-deg. ply delamination) was inconsequential to the strength. Judging by the proximity of the late-life compressive strengths to the maximum compressive load excursions ("C," on the graphs), one may conclude that these specimens clearly failed in compression. The failure mode transition that manifested itself after approximately half of the fatigue lifetime in high-load specimens caused two fiber fracture dominated specimens to have significantly lower residual tensile strengths



**Table 7. Normalized residual stiffness and strength of center-notched, AS4/1808, (0,45,90,-45)<sub>s4</sub> specimens**

Spcmn. I.D.	Load Level	No. Cycles	Est. % Life	$E_r/E_i^o$	$E_c/E_c^o$	$S_r/S_i^o$	$S_c/S_c^o$
3-12	high	1305	5-10	.930	.955	1.11	—
7-4	high	1000	5-10	.953	.950	1.03	—
8-10	high	1000	5-10	.960	.961	1.06	—
2-1	high	904	5-10	.935	.924	—	.839
8-9	high	1000	5-10	.932	.953	—	.856
7-3	high	1000	5-10	.956	.964	—	.863
3-2	high	9240	40-60	.850	.918	1.19	—
8-3	high	3500	40-60	.878	.892	.963	—
7-2	high	3500	40-60	.908	.920	1.16	—
3-14	high	9400	40-60	.851	.892	—	.896
8-12	high	3500	40-60	.899	.902	—	.808
7-14	high	2500	40-60	.804	.808	—	.750
2-3	high	11024	≥90	.674	.732	.883	—
8-11	high	6300	≥90	.910	1.58	1.02	—
8-5	high	16514	≥90	.716	.810	1.01	—
2-2	high	8800	≥90	.821	1.14	—	.628
8-1	high	51627	≥90	.688	.729	—	.711
8-4	high	11811	≥90	.637	.583	—	.706
6-6	low	25000	5-10	.917	.910	1.10	—
7-1	low	25000	5-10	.893	.919	1.17	—
7-8	low	24000	5-10	.895	.893	1.10	—
6-4	low	61500	5-10	.876	.868	—	.852
7-7	low	25000	5-10	.901	.898	—	.810
7-6	low	50000	5-10	.919	.898	—	.981
6-10	low	1443000	40-60	.655	.612	1.19	—
7-9	low	1052000	40-60	.757	.786	1.24	—
8-8	low	595000	40-60	.747	.741	1.18	—
6-12	low	2792000	40-60	.724	.771	—	.769
7-11	low	2275240	40-60	.734	.725	—	.795
7-5	low	931200	40-60	.717	.689	—	.853
4-9	low	2115050	≥90	.399	.325	1.18	—
7-10	low	3465800	≥90	.507	.500	1.16	—
7-13	low	453910	≥90	.468	.447	1.03	—
2-15	low	2215030	≥90	.489	.408	—	.541
7-12	low	1253400	≥90	.614	.691	—	.615
8-2	low	1310000	≥90	.679	.744	—	.599

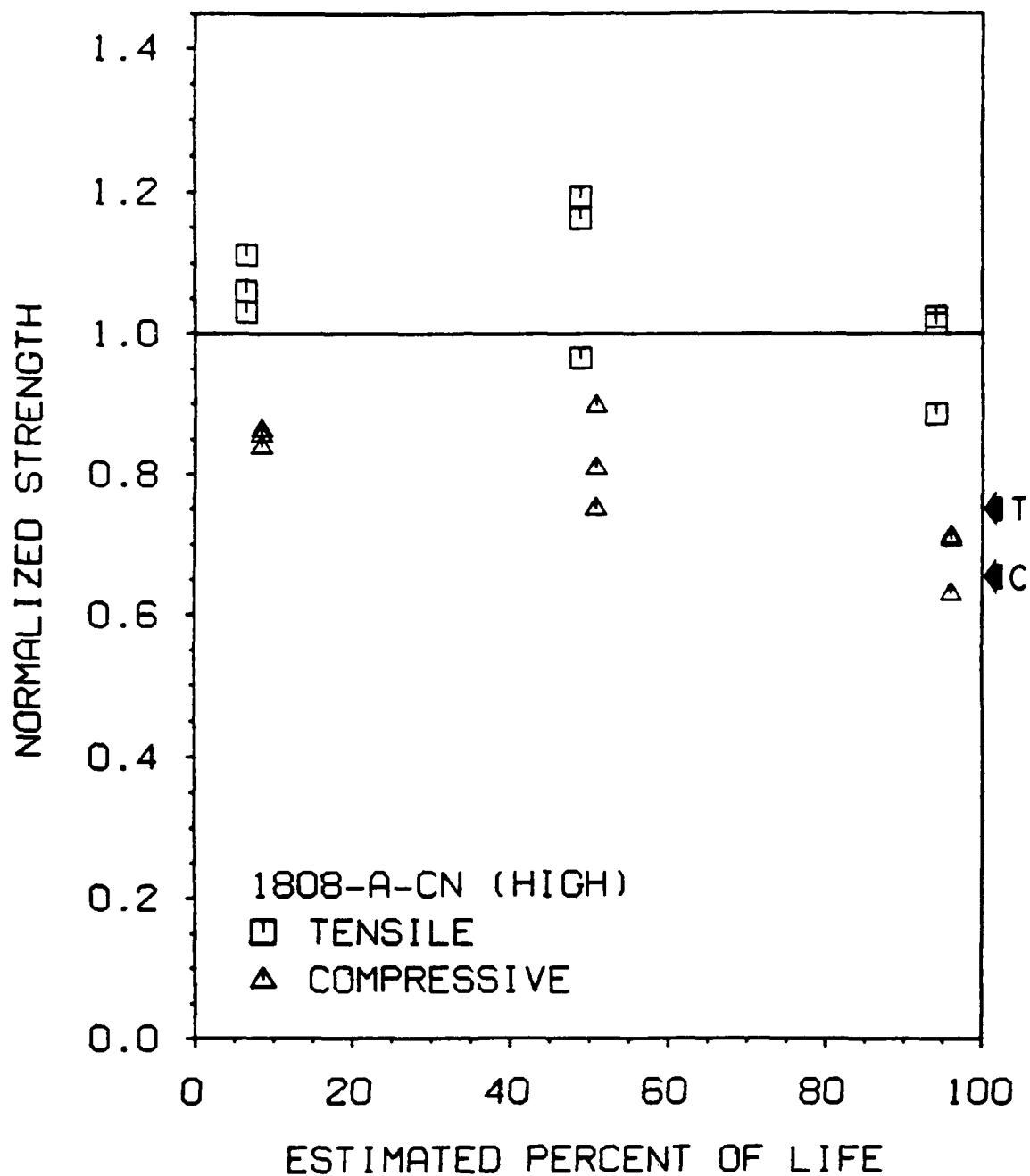


Figure 67. Normalized residual strength of center-notched, AS4/1808, (0,45,90,-45)<sub>s4</sub> specimens during high-load fatigue

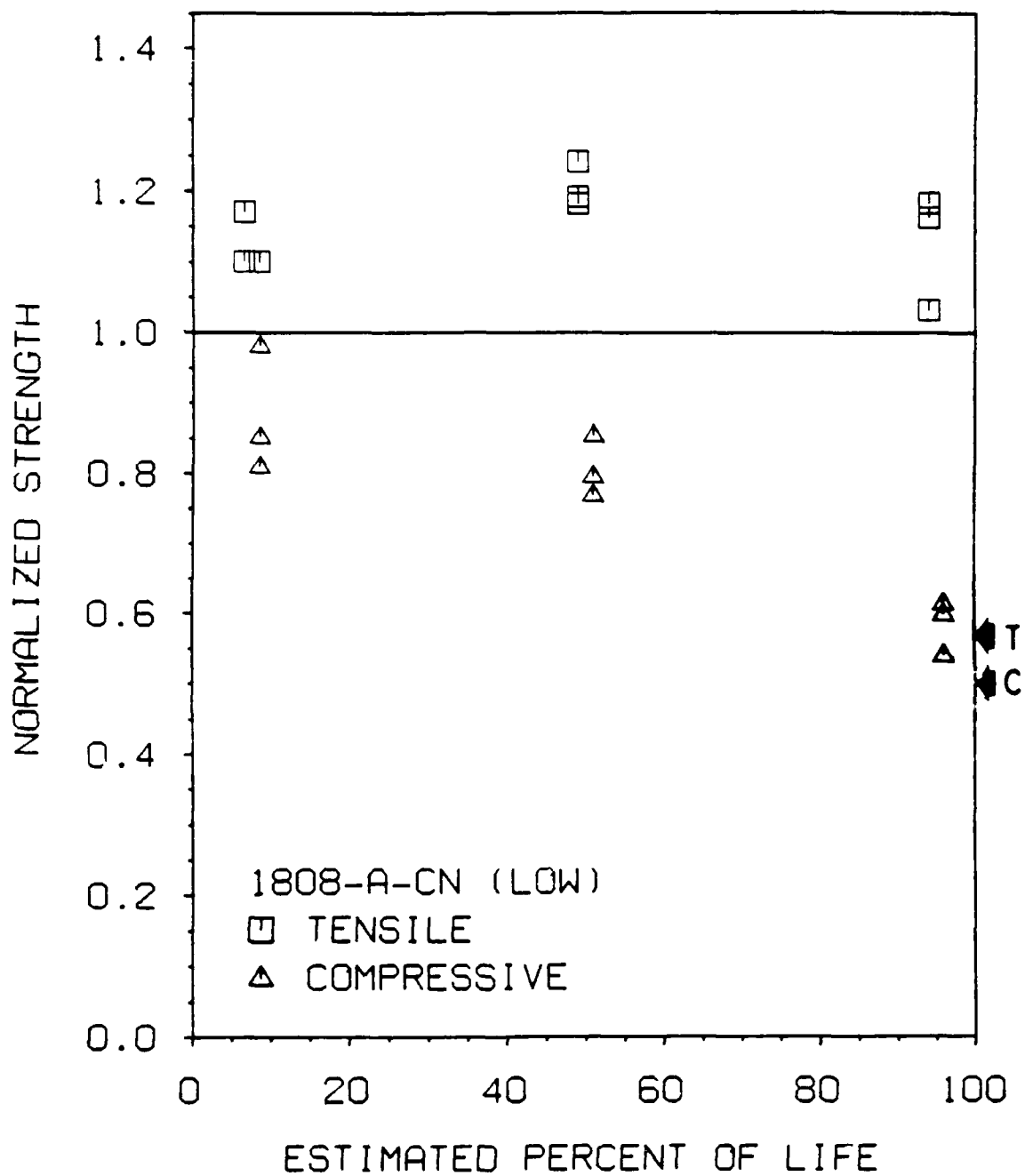


Figure 68. Normalized residual strength of center-notched, AS4/1808, (0,45,90,-45)<sub>S4</sub> specimens during low-load fatigue

Table 8. Averaged, normalized, residual strength data

Specimen Type	Load Level	$S_r/S_r^*$			$S_c/S_c^*$		
		5-10% Life	40-60% Life	$\geq 90\%$ Life	5-10% Life	40-60% Life	$\geq 90\%$ Life
1808-A-CN	High Low	1.07 (3)	1.10 (3)	.971 (3)	.853 (3)	.818 (3)	.682 (3)
		1.12 (3)	1.20 (3)	1.12 (3)	.881 (3)	.806 (3)	.585 (3)
1808-A-DEN	High	1.08 (3)	1.25 (3)	.998 (3)	.885 (3)	.822 (3)	.678 (2)
1808-B-CN	High Low	1.12 (3)	1.27 (3)	1.22 (3)	1.09 (3)	.934 (3)	.882 (2)
		1.14 (3)	1.23 (3)	1.13 (3)	1.11 (3)	.998 (3)	.820 (2)
3501-B-CN	High	1.08 (3)	1.30 (3)	1.28 (2)	1.09 (3)	1.02 (2)	.879 (1)

\* Numbers in parentheses indicate the number of tests performed.

than the remaining delamination dominated specimens during that time period (these were the two tensile data points below 1.0 in the high-load figure).

The fracture appearance of these specimens after strength measurements at three stages of fatigue damage development and under both load levels were essentially similar. Typically, the final fracture paths in the 0-deg. plies passed through the center of the notch, predominantly perpendicular to the load axis. The final tensile fracture paths in specimens with 0-deg. ply fracture paths caused by fatigue grew in the transverse direction from the points where the earlier ply fractures stopped. Specimens with larger delaminations had relatively irregular fracture surfaces. The extent of pre-failure delamination was most evident in the post-fracture appearance of the compression specimens. Delaminated plies were free to buckle and, therefore, did not fracture as readily as the more constrained, undelaminated plies.

The double-edge notched specimens under the high load level behaved similarly to the center-notched specimens (Table 8, Table 9, and Figure 69). Except for the middle-life tensile strength — which was slightly higher in DEN specimens — all strength measurements were nearly equivalent in the CN and DEN notch configurations. Fracture appearances of DEN specimens were analogous to those in CN specimens. High-load DEN specimens on the "high-load" side of the damage mode transition had less delamination than those on the "low-load" side of the transition, though no differences as clear as those seen in the post-fatigue-failure radiographs (Figure 44 on page 110) were seen among the residual strength specimens. As evidenced by the merging of residual compressive strengths and the maximum compressive fatigue load at the end of life, the DEN specimens failed in compression.

## **6.2 AS4/1808, Orthotropic Laminate**

Table 9. Normalized residual stiffness and strength of double-edge-notched, AS4/1808, (0,45,90,-45)<sub>s4</sub> specimens

Spcmn. I.D.	Load Level	No. Cycles	Est. % Life	$E_f/E_o^o$	$E_c/E_o^o$	$S_f/S_o^o$	$S_c/S_o^o$
3-7	high	800	5-10	.981	.970	1.02	—
4-4	high	904	5-10	.986*	.977*	1.14	—
4-13	high	904	5-10	.980*	.977*	1.08	—
3-1	high	960	5-10	.992	.969	—	.821
4-2	high	703	5-10	.986*	.984*	—	.891
4-1	high	904	5-10	.984*	.985*	—	.942
3-5	high	8600	40-60	.940	.940	1.29	—
4-8	high	9000	40-60	.950*	.943*	1.25	—
4-11	high	10000	40-60	.927*	.922*	1.20	—
3-3	high	8300	40-60	.951	.921	—	.820
4-7	high	4750	40-60	.942*	.946*	—	.846
4-14	high	3100	40-60	.928*	.932*	—	.799
2-12	high	5824	≥90	.643	.447	1.09	—
4-6	high	8070	≥90	.825*	.835*	.946	—
4-5	high	13960	≥90	.758*	.804*	.958	—
4-3	high	32630	≥90	.751	.584	—	.730
4-12	high	83860	≥90	.742*	.683*	—	.626

\* Average stiffness, computed by averaging strains from front and back extensometers.

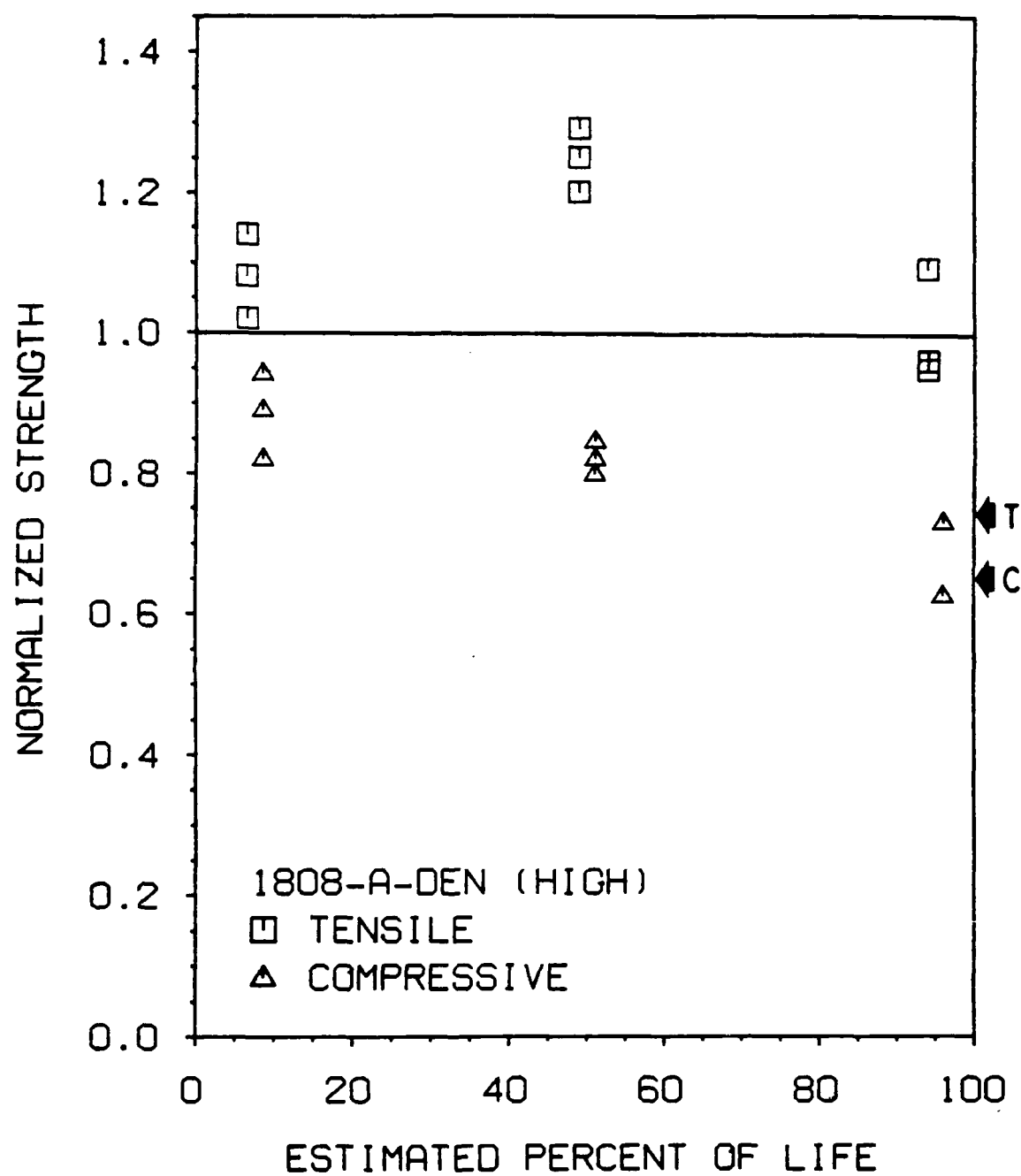


Figure 69. Normalized residual strength of double-edge-notched, AS4/1808, (0,45,90,-45)<sub>s4</sub> specimens during high-load fatigue

Table 10. Normalized residual stiffness and strength of center-notched, AS4/1808, (0,45,0,-45)<sub>s4</sub> specimens

Spcmn. I.D.	Load Level	No. Cycles	Est. % Life	$E_r/E_o^o$	$E_c/E_o^o$	$S_r/S_o^o$	$S_c/S_o^o$
3-3	high	250	5-10	.935	.923	1.16	—
6-8	high	616	5-10	.941	.946	1.14	—
6-14	high	200	5-10	.953	.993	1.07	—
3-5	high	350	5-10	.938	.941	—	1.04
6-2	high	690	5-10	.944	.959	—	1.11
6-10	high	200	5-10	.948	.966	—	1.12
3-7	high	3708	40-60	.793	.770	1.42	—
6-6	high	3360	40-60	.799	.857	1.13	—
4-8	high	4340	40-60	.748	.759	1.25	—
3-9	high	6570	40-60	.790	.871	—	1.02
6-12	high	3450	40-60	.845	.941	—	.879
4-2	high	3930	40-60	.805	.866	—	.904
2-18	high	10460	≥90	.673	.755	1.10	—
5-6	high	6880	≥90	.700	.610	1.27	—
4-14	high	8410	≥90	.657	.586	1.29	—
4-7	high	5760	≥90	.663	.730	—	.884
4-12	high	6900	≥90	.594	.570	—	.880
5-9	low	25860	5-10	.899	.894	1.16	—
4-11	low	10500	5-10	.898	.901	1.10	—
4-9	low	22000	5-10	.901	.906	1.17	—
5-13	low	60000	5-10	.890	.887	—	1.13
4-1	low	25000	5-10	.898	.901	—	1.06
4-3	low	31400	5-10	.902	.910	—	1.15
5-2	low	100000	40-60	.875	.893	1.26	—
5-1	low	230500	40-60	.801	.781	1.21	—
4-6	low	166000	40-60	.801	.809	1.22	—
5-4	low	188450	40-60	.798	.722	—	1.03
4-10	low	100010	40-60	.810	.838	—	1.03
5-10	low	100000	40-60	.706	.711	—	.933
3-1	low	291000	≥90	.524	.460	1.10	—
5-14	low	234900	≥90	.652	.624	1.06	—
4-5	low	524000	≥90	.530	.465	1.22	—
5-5	low	782910	≥90	.684	1.09	—	.960
6-4	low	255210	≥90	.582	.492	—	.679



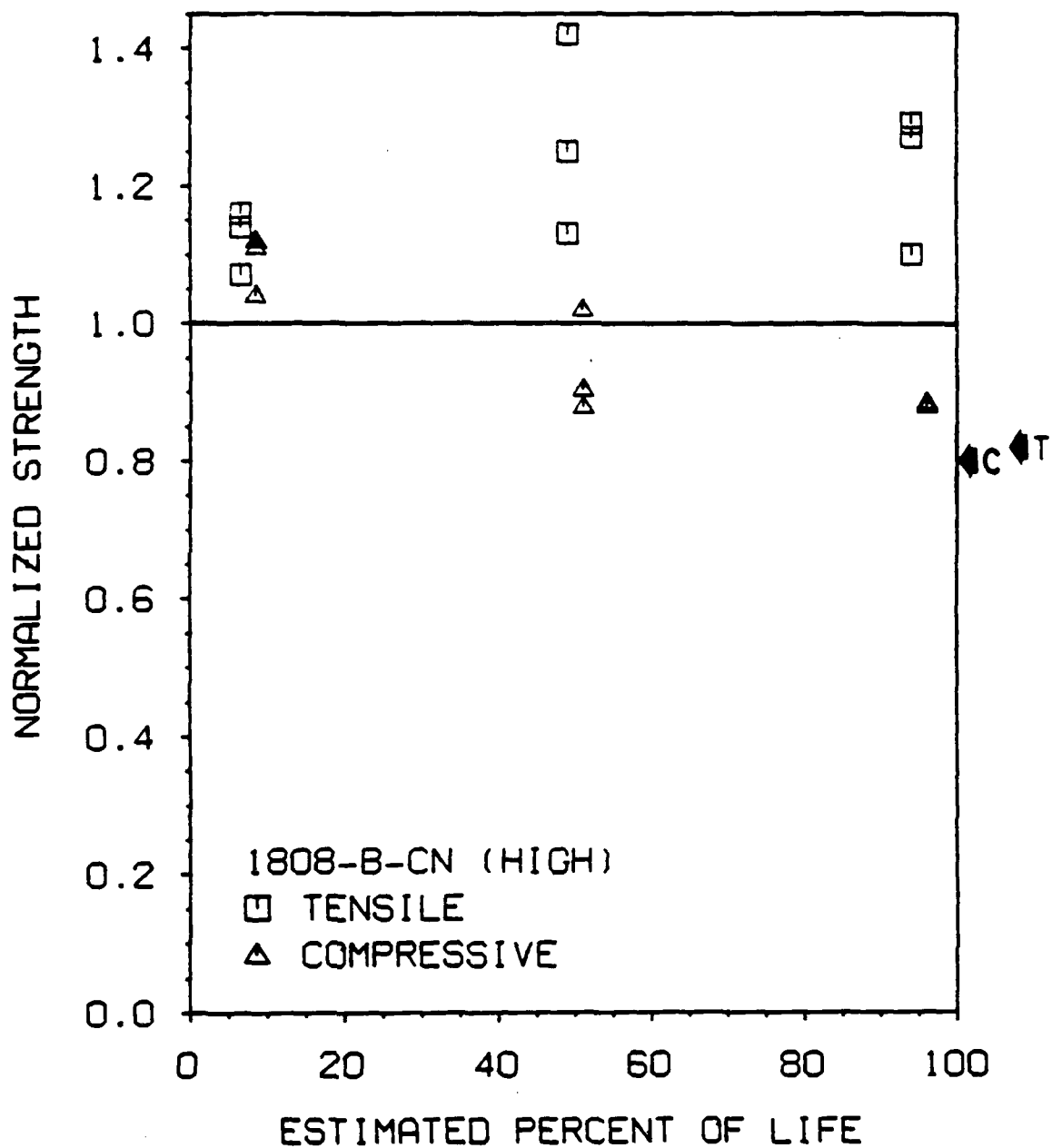


Figure 70. Normalized residual strength of center-notched, AS4/1808, (0,45,0,-45)<sub>s4</sub> specimens during high-load fatigue

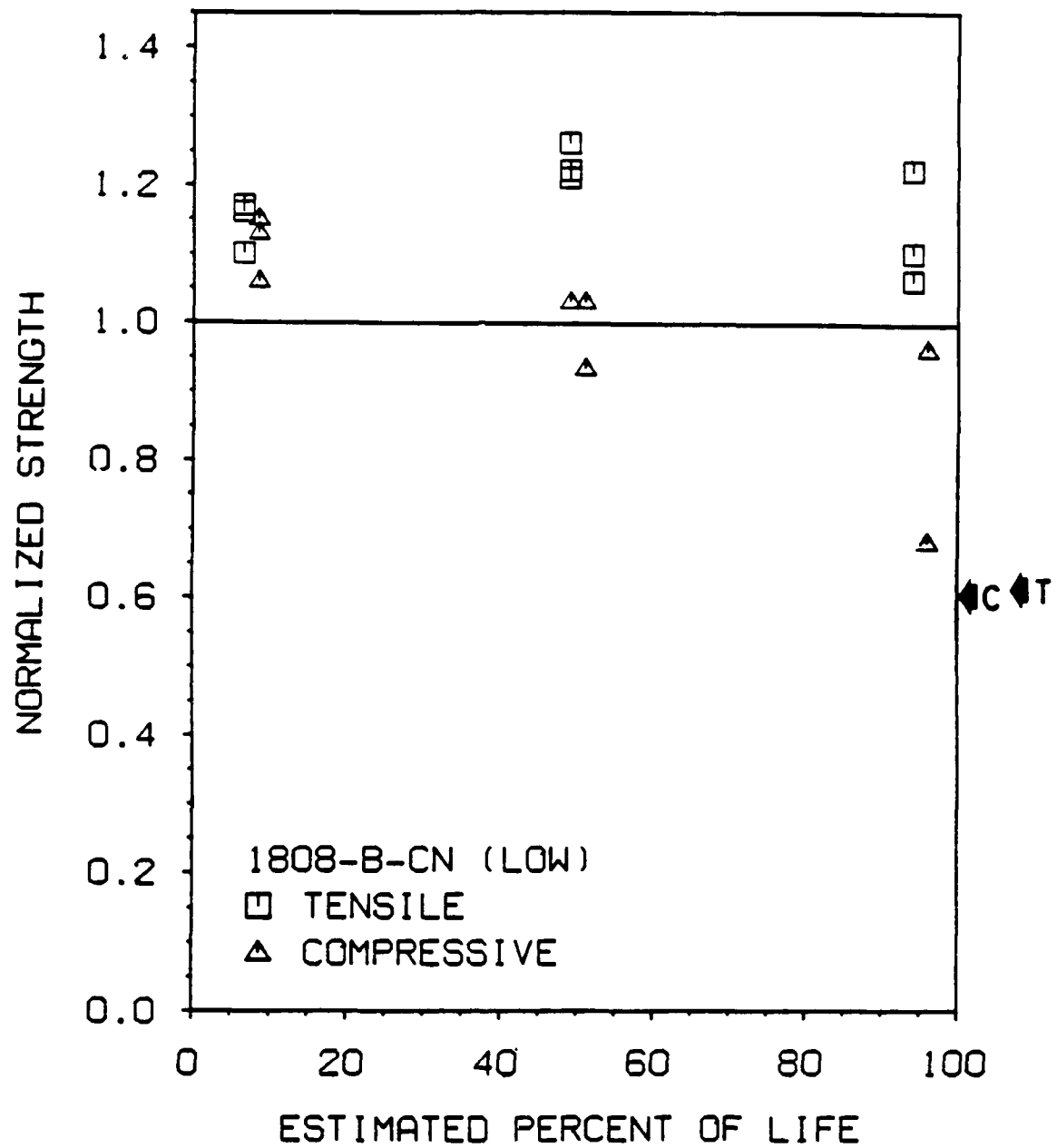


Figure 71. Normalized residual strength of center-notched, AS4/1808, (0,45,0,-45)<sub>s4</sub> specimens during low-load fatigue

Normalized stiffness and strength data for center-notched, AS4/1808, (0,45,0,-45)<sub>s4</sub> specimens are listed in Table 10. The averaged, normalized strengths are listed in Table 8. Figure 70 and Figure 71 illustrate the strength data graphically for the high and low load levels, respectively.

The tensile strengths of high- and low-load specimens increased approximately the same amount at the early- and middle-life measurement points. By the end of high- and low-load fatigue lifetimes, tensile strengths decreased, but remained above 1.0. The averaged tensile strengths of middle- and late-life specimens were higher during high-load fatigue than during low-load fatigue, though the data overlapped significantly. Due to the greater localization of damage in variable locations in high-load specimens, there was more scatter in the high-load residual strength data.

The compressive strengths of high- and low-load specimens both increased at the early-life measurement point, and decreased somewhat linearly with respect to cycles after that time. During the period when the normalized compressive strength was greater than 1.0, damage around the notch was comprised primarily of matrix cracks. Only after the appearance of delaminations did the compressive strength decrease. Compressive strengths were slightly higher in low-load specimens than in high-load specimens at the early- and middle-life measurement points, though the differences were not very significant. Reduced compressive strengths in the second half of life caused compressive fatigue failures under both loading regimes. The lower compressive strength of low-load specimens near fatigue failure could be related to the greater extent of delaminations in those specimens.

Much can be learned about the effect of fatigue damage on the failure mode in residual strength tests by examining the fracture surfaces after failure. The appearance of internal 0-deg. plies was particularly interesting since it is these plies that apparently controlled fracture (the exterior plies were usually replete with through-the-thickness fiber fractures and delaminations, and were difficult to characterize because of their highly variable appearance).

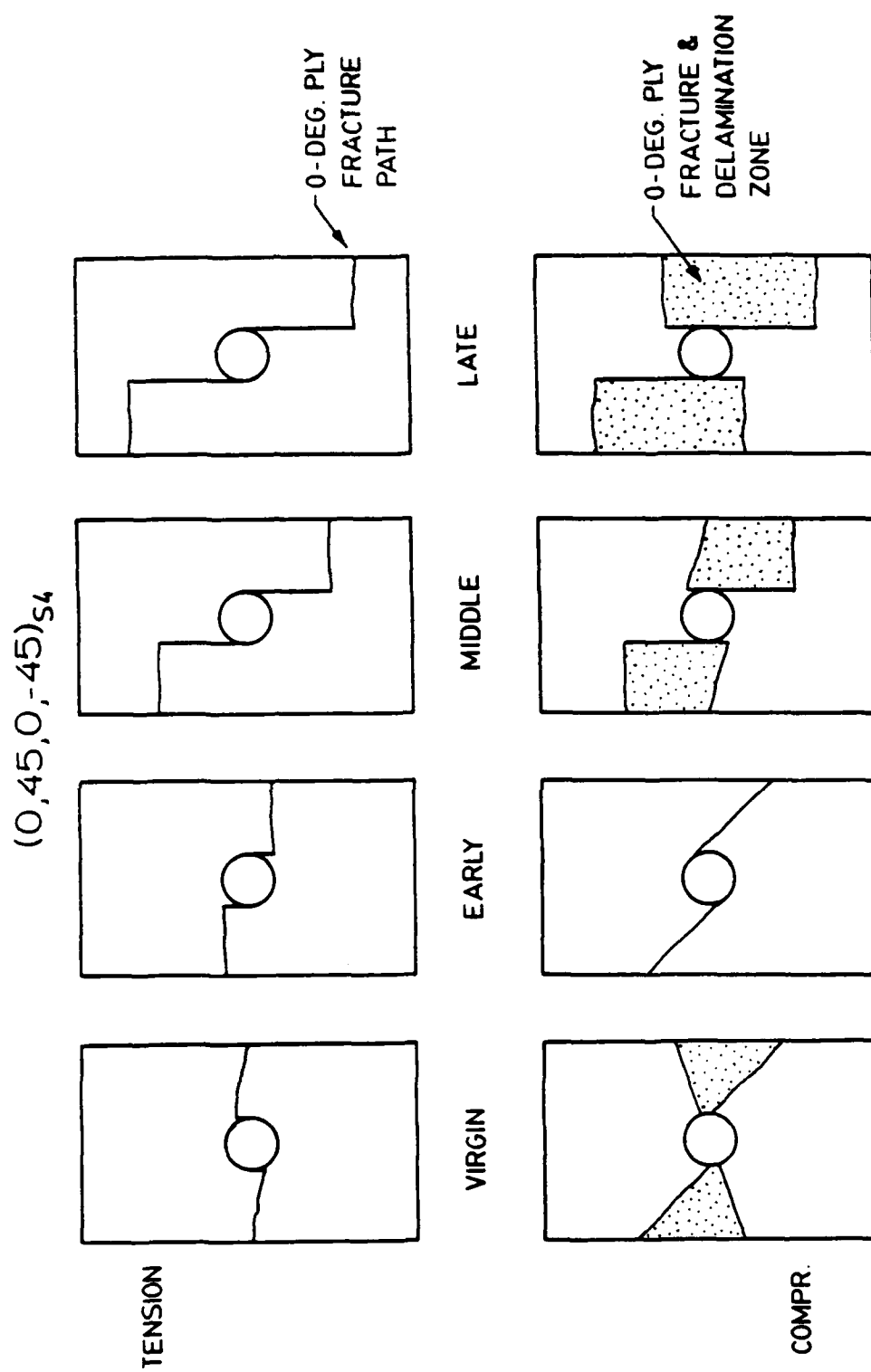


Figure 72. Schematic illustration of 0-deg. ply fracture and delamination in AS4/1808,  $(0,45,0,-45)_s$  specimens after residual strength tests

Schematic illustrations of the location of fracture and delamination of the internal 0-deg. plies in center-notched, AS4/1808, (0,45,0,-45)<sub>s4</sub> laminates after tensile and compressive strength measurements are shown (to scale) in Figure 72. As fatigue damage increased, the tensile fracture path of the internal 0-deg. plies shifted farther from the transverse centerline. Apparently, the tensile fracture process began near the tips of the 0-deg. cracks tangent to the hole in the even quadrants, near the highly-stressed areas seen in the SPATE patterns. In terms of the fracture mode, the damage pattern in these fatigue-damaged specimens could effectively be replaced by a slanted slit with the two ends of the slit located at the tips of the 0-deg. tangent cracks. Since the growth of the 0-deg. tangent cracks slowed in the second half of the lifetime, the location of fracture also remained nearly the same. Therefore, near the end of life, local stress redistribution mechanisms must have played a more active role in strength reduction than global stress redistribution mechanisms.

In residual compressive strength specimens, there were some radical failure mode changes that may explain the unusual residual compressive strength characteristics of this laminate. In virgin specimens, there was a mixed mode of failure in compression. One mode consisted of buckling and delamination of all 0-deg. plies along the transverse centerline. The other failure mode consisted of shear-kinking with little delamination along a -45-deg. path tangent to the notch. The early-life specimens, which were the strongest of all in compression, almost always failed in the shear mode. The middle- and late-life specimens underwent delaminations and 0-deg. ply fractures in the two longitudinal ligaments of material adjacent to the notch. The longitudinal shift of the fracture locus in compression tests was less extreme than in tension tests.

### **6.3 AS4/3501-6, Orthotropic Laminate**

Table 11. Normalized residual stiffness and strength of center-notched, AS4/3501-6, (0,45,0,-45)<sub>s4</sub> specimens

Spcmn. I.D.	Load Level	No. Cycles	Est. % Life	$E_f/E_f^o$	$E_c/E_c^o$	$S_f/S_f^o$	$S_c/S_c^o$
4-18	high	114	5-10	.952	.949	1.04	—
9-9	high	2000	5-10	.945	.935	1.07	—
9-5	high	600	5-10	.890	.902	1.12	—
6-11	high	907	5-10	.954	.952	—	1.11
9-7	high	470	5-10	.931	.943	—	1.10
9-1	high	770	5-10	.945	.936	—	1.05
4-17	high	5000	40-60	.890	.902	1.18	—
9-8	high	5000	40-60	.804	.842	1.34	—
9-10	high	9640	40-60	.804	.743	1.38	—
6-3	high	2947	40-60	.889	.932	—	.956
9-14	high	3860	40-60	.844	.810	—	1.08
6-9	high	13820	≥90	.600	.497	1.23	—
9-6	high	13000	≥90	.628	.480	1.32	—
3-7	high	13190	≥90	.611	.541	—	.879

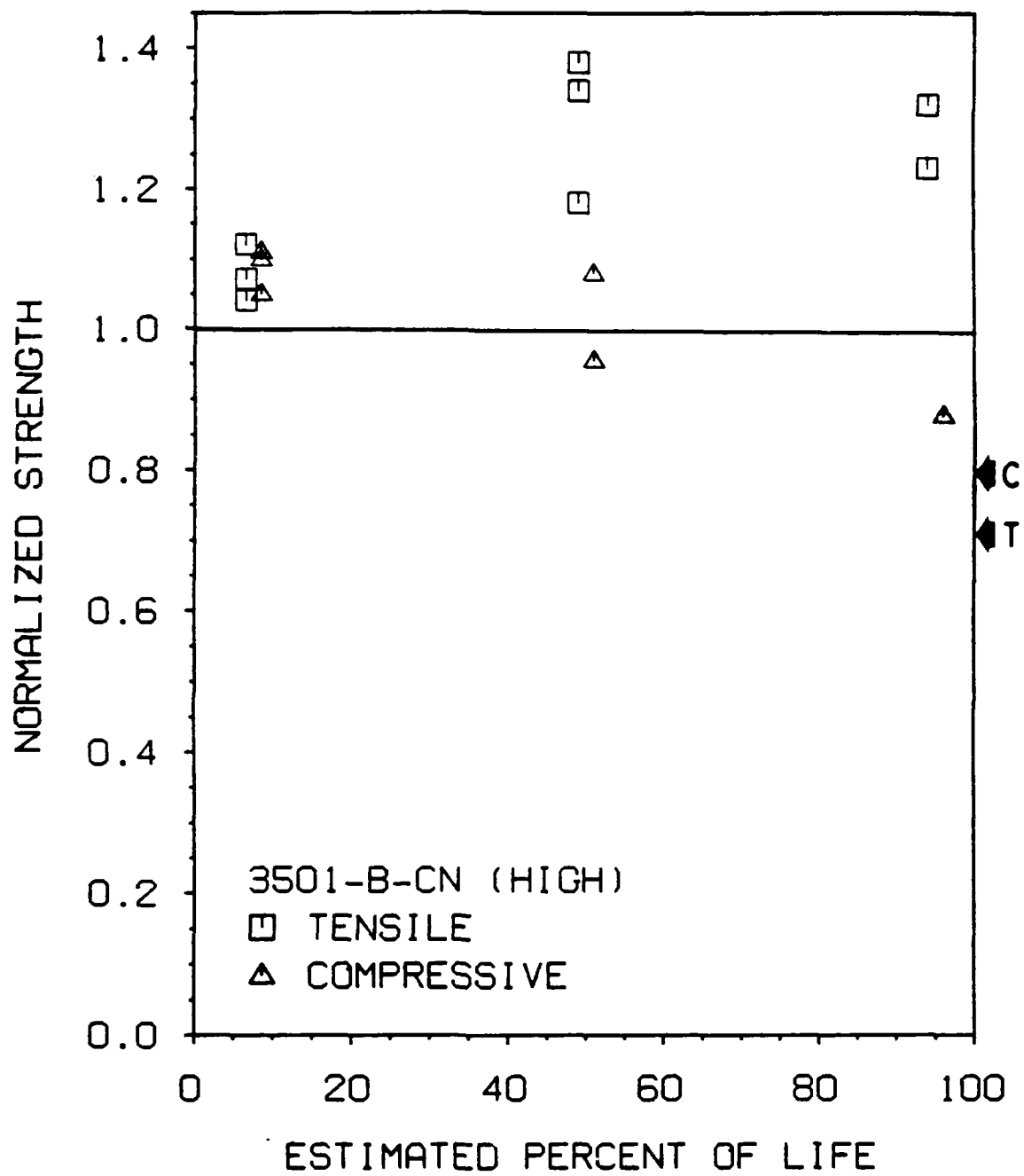


Figure 73. Normalized residual strength of center-notched, AS4/3501-6, (0,45,0,-45)<sub>s4</sub> specimens during high-load fatigue

Normalized residual stiffness and strength data for center-notched, AS4/3501-6, (0,45,0,-45)<sub>s4</sub> specimens under the high load level are listed in Table 8 and Table 11. The strength data are graphically represented in Figure 73. Overall, the residual strength behavior of AS4/3501-6, (0,45,0,-45)<sub>s4</sub>, CN specimens was similar to analogous AS4/1808 specimens at the same load level. Rapid increases in tensile and compressive strengths at the early-life measurement point indicated that strength at this time in life was controlled by the relaxed stress concentration near the notch, and not by delaminations. Later in life, lower compressive strengths and, eventually, fatigue failure were caused by delaminations. The average tensile strength of these specimens were highest at the middle-life measurement point, and dropped slightly by the late-life measurement point. Failure modes of the AS4/3501-6 specimens were similar to those described in Figure 72 except for a relatively slower shifting of the tensile fracture path in the longitudinal direction. This observation was consistent with the shorter 0-deg. cracks tangent to the notch in the AS4/3501-6 specimens compared to the AS4/1808 specimens.

## **6.4 Summary of Residual Strength Data**

In the present investigation, the most important factor affecting the residual strength characteristics of notched carbon epoxy laminates was the lamination arrangement. Fatigue damage accumulation had a stronger effect on failure modes and residual strengths in the (0,45,0,-45)<sub>s4</sub> laminates than in the (0,45,90,-45)<sub>s4</sub> laminates. This difference can be mostly attributed to the more complete notch blunting and the later onset of delamination in the (0,45,0,-45)<sub>s4</sub> laminate. Matrix cracks and delaminations in both laminates improved the tensile strength of the specimens because tensile strength depends highly on the stress concentration near the notch. Only in the (0,45,0,-45)<sub>s4</sub> laminate, however, was the stress con-



RD-A207-623

INVESTIGATION AND MODELING OF DAMAGE GROWTH IN  
COMPOSITE LAMINATES. (U) VIRGINIA POLYTECHNIC INST AND  
STATE UNIV BLACKSBURG MATERIALS.

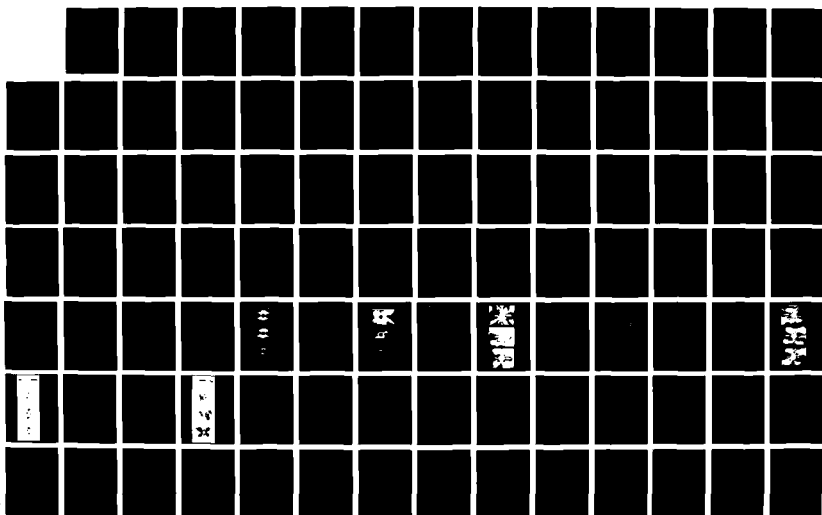
325

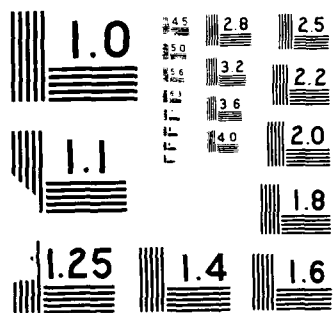
UNCLASSIFIED

K L REIFSNIDER ET AL. 25 SEP 88

F/G 11/4

NL





centration near the notch blunted without the presence of delaminations; thus causing the residual compressive strength to be improved for a short time.

The second most important influence on residual strength was the load level. The effect of load level was more evident in the quasi-isotropic laminate than in the orthotropic laminate because of the greater dependence of damage patterns on load level in the former laminate. High load levels resulted in a ply fracture dominated, transversely directed damage pattern that limited reductions in the notch effect during the lifetime. The delamination dominated, longitudinally directed pattern of damage in low-load specimens was associated with higher tensile strengths throughout the lifetime, but lower compressive strengths at the middle- and late-life measurement points.

Material system in the present investigation was not a strong influence on the residual strength of  $(0,45,0,-45)_{s4}$  laminates during high-load fatigue. The only differences ascertained in the present investigation were the slightly higher middle-life residual compressive strength and late-life tensile strength of the AS4/3501-6 material compared to the AS4/1808 material. This was despite the shorter 0-deg. cracks tangent to the notch in the AS4/3501-6 specimens. Perhaps a stronger material dependence would emerge in the more matrix-sensitive quasi-isotropic laminate. The effect of notch configuration on the residual strength of AS4/1808,  $(0,45,90,-45)_{s4}$  specimens during high-load fatigue was not significant except for the higher middle-life tensile strength in the DEN specimens.

## **VII**

### **Modeling**

#### **7.1 *Model Development***

##### **7.1.1 Approach**

If it is true that the subdiscipline of "fatigue" is a legacy of the insight of Wohler, then it may also be fair to claim that the "classical" approach to the study of that subject has been largely phenomenological. The most common descriptions of "the fatigue effect" are "Wohler curves," or "SN curves" which are simple plots of the number of cycles of life verses the level of loading. These descriptions may include various statistical interpretations, but they are primarily phenomenological correlations of observations used for comparative characterizations and design exercises at the applied level.

However, it is becoming increasingly difficult to find the time and resources necessary to test and evaluate all materials of interest to us. Moreover, the advent of "engineered materials" such as composite materials which can be "designed" to have certain properties and response has presented us with the need to anticipate the fatigue behavior of materials which may not be available for testing, which we cannot fully characterize, or which we have not yet "created". Phenomenological descriptions and correlations will not suffice for this purpose.

Mechanistic models must be developed that allow us to project the long-term behavior of composite materials under cyclic loading, and, ultimately, under the influence of elevated temperature and aggressive environments which cause reductions in the properties and performance of composites over time during service use. However, the development of mechanistic models is very difficult. It requires that the mechanisms of stiffness, strength, and life reduction during service be identified, and accurately represented with mechanics analysis (including constitutive theory) that is appropriate for material states and stress states which are changing with the history of loading. For composite materials, this is a considerable challenge. The complexity of stress states, damage modes, and failure modes that are common to this class of materials makes it very difficult to determine the details of the processes which cause the degradation of such materials.

The present section deals with the use of damage analysis, especially experimental investigative methods, to form a basis of understanding and a foundation for the construction of models which can be used to predict the remaining strength and life of composite laminates under cyclic loading. Special attention will be given to the requirements imposed by modeling efforts for notched materials of typical engineering interest, and to the results of one such modeling approach, the "critical element method" developed by the Materials Response Group at Virginia Tech. The results of the modeling effort for the materials and circumstances associated with the present investigation will be presented in two subsections which discuss "Damage Analysis and Stress Redistribution," and "Modeling Features."

### 7.1.2 Damage Analysis and Stress Redistribution

The previous sections have presented the details of the initiation and propagation of damage in the two material systems investigated extensively in this program. In this subsection we will only highlight the features which are of particular importance to the development of the critical element model. These features are:

- The redistribution of stress, especially in the region of notches, caused by damage development.
- The geometric distribution of damage and the influence of that damage on the properties of the material at the local and global level.

Appendix A contains a discussion of "Damage Initiation and Growth in Notched Laminates Under Reversed Cyclic Loading". We will use the figures and discussion in that paper for the present discussion of stress redistribution. As described in Appendix A, full field measurements of isochromatic photoelastic fringes and thermal emission contours were recorded during cyclic loading of many of the specimens tested in this program. In all cases except the virgin specimens, the photoelastic data were obtained on the same side of the specimen as the thermographic data were taken from.

Figure 6 in Appendix A illustrates the isochromatic fringe patterns in three quasi-isotropic specimens with sequential states of damage. The corresponding damage states are shown in Fig. 2 of that appendix. As the damage state develops, it is clear that two general effects occur. The "butterfly" pattern of shear stress around the hole is sharply disturbed; the "wings" flatten towards the horizontal centerline of the patterns and diminish in size. Second, a region of intense fringes develops along the horizontal direction through the center of the hole, corresponding to the growth of damage along that transverse direction as seen in Fig. 2 of Ap-

pendix A. Figures 7a and 8a quantify this effect along sections A-A' and C-C' as defined in those figures. Along section A-A', the strain contours increase more slowly with distance from the center hole as damage develops, and the stress level away from the hole increases, i.e., the stress concentration associated with the hole decreases and the stress in the remaining "ligament" increases with damage development. Along C-C', the late-life growth along the horizontal direction causes a sharp spike in the stress.

The corresponding data for the orthotropic laminates is shown in Figs. 7b and 8b of Appendix A. The unsymmetry of the corresponding damage pattern (shown in Fig. 4 of the Appendix) causes a corresponding asymmetry of the strain patterns. Damage growth along the vertical lines tangent to the hole (in the loading direction) creates a spike in the stresses along A-A' as shown in Fig. 7b. Stresses along the horizontal axis are greatly relaxed, as shown by the distributions in Fig. 8b and by the photoelastic patterns for that laminate shown in Fig. 9 of Appendix A.

Thermographic measurements of strain distributions, as described elsewhere in this report, were also made for many specimens. As seen in Figs. 10 and 11 of Appendix A, the thermoelastic patterns agree with the photoelastic patterns in general, but there is one significant difference. There is a region around the hole which ceases to emit heat energy as damage develops. This loss of "signal" is caused by the development of delamination which effectively unloads the surface ply observed by the heat camera in those regions. This was a limit on the utility of the thermoelastic method. However, loss of information about the stress distribution quite near the hole was not a serious matter in the sense that the critical regions where damage was occurring, and which initiated failure, did continue to produce very bright thermoelastic images. This is illustrated in Fig. 12 of Appendix A. The effect is most noticeable in the lower-right quadrant of Fig. 12b, and in the upper-left quadrant of Fig. 12c. It is in these two quadrants that much of the middle and late life fatigue damage growth occurs. For both laminate types, the fracture path seen in residual strength tests for tensile loading frequently passed through, or at least near, these hot spots. Moreover, it was found

that the level of temperature measured in these hot spots scaled to the corresponding values of residual strength measured for those specimens.

The redistribution of stress discussed above was, of course, a direct consequence of the geometric distribution of damage. As described in the section on "Fatigue Damage Mechanisms," the geometric distribution of damage was concentrated in two regions, one along lines tangent to the hole in the direction of loading, and the other along lines perpendicular to the load axis. We will call these the "shear region" (S region) and the "damage growth region" (DG region) respectively. The details of damage development in these two regions are the basis of the major components of the model.

The effect of damage development in the S region is to "disconnect" the material on either side of the notch from the regions above and below the hole. This has the result of reducing the constraint associated with the hole, and consequently, of reducing the stress concentration around the hole. The nature of this damage process and the attendant stress relaxation at the local level is very complex. It is not feasible to attempt to represent all of the complexity of the formation, growth, and interaction of individual cracks and flaws in that region. For the purposes of modeling, it is sufficient to find a way to represent the global influence of the damage process on the laminate strain distribution. A method of doing this will be discussed below.

By contrast, the effect of damage development in the DG region reduces strength directly. As we established earlier, the stress concentration associated with the hole may be reduced by damage in the S region, but the concentration associated with damage development in the DG region may be at least as high as the original one associated with geometric constraint. The influence of damage in this region appears in the model in two ways. The damage changes stiffnesses at the local level which causes stress redistribution. And second, the remaining properties (especially properties like ply strength) are degraded by the damage process. Both of these effects tend to cause a strength reduction.



Hence, damage growth in the S region tends to increase remaining strength (at least tensile strength), and growth in the DG regions tends to reduce remaining strength. The manner in which these changes occur must form the basis for a proper model of strength variations during damage development.

### **7.1.3 Modeling Features**

The critical element concept has been discussed in the literature. [110-112] A flow diagram of the approach is shown in Figure 74. The approach is based on a thorough and precise experimental determination of the nature of the failure mode associated with the strength or life reduction to be calculated, and of the attendant damage development process. The model is created for each such failure mode. The controlling reduction mechanism is determined by running the model for all such modes thought to be operable in a given situation, and comparing the predicted remaining strength and life.

Based on this experimental information, a "critical element" is identified as the material element or volume whose failure defines the failure event for the global laminate, component, or material volume. For fiber dominated laminates, for example, the critical element may be the fibers in the ply which has an orientation most nearly aligned with a principle load direction. For compression failure, the critical element may be the undelaminated ligament which finally buckles or crushes, etc. The model consists of a continuous evaluation of the state of stress and state of material in the critical element for a given failure mode, as cyclic loading, variations in temperature, or other influences are applied over the term of expected life of the component in question.

The state of material is represented by updated properties (such as strength and stiffness), i.e., by continuum constitutive relations and quantities. The state of stress is determined by

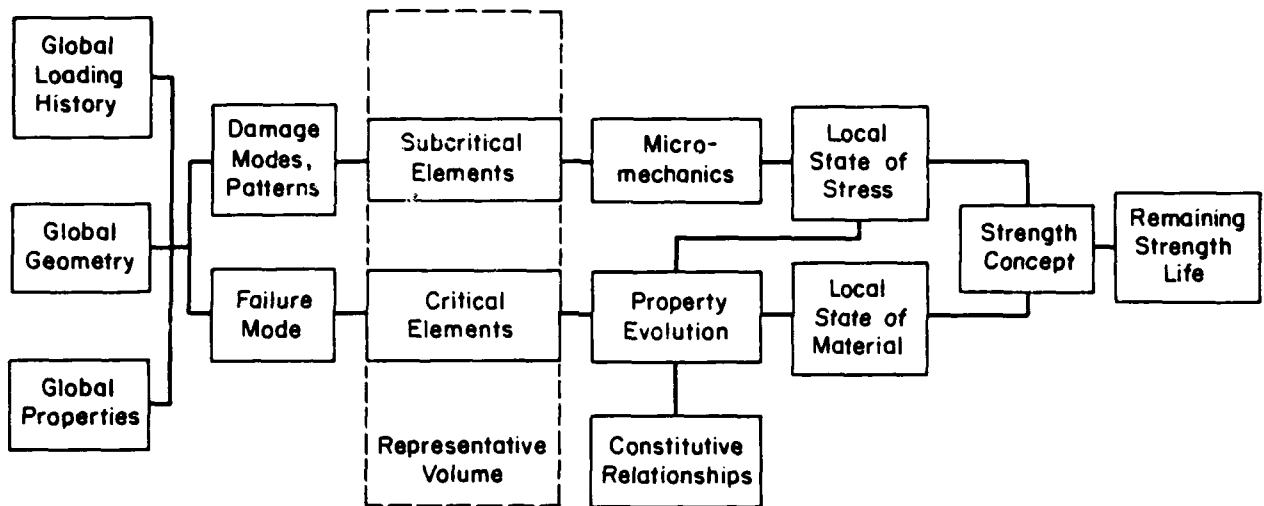


Figure 74. Flow diagram of the critical element approach.

solving the appropriate boundary value problem for the critical element concerned, using macro- or micro-mechanics. The state of stress in the critical element is a function of loading history since the development of damage continuously changes the local geometry and the manner in which the load is distributed among the material elements at the local level.

As we noted above, a major feature of the stress state change is the relaxation of the stress concentration around the notch for specimens or components which have cutouts, such as the center hole or edge notches studied in this program. In order to calculate the stress field around the hole as damage changes the constraint in that region, an effective geometry scheme was used. Lekhnitskii's solution for the stresses around an elliptical hole in an anisotropic plate was used to find the global stresses around the circular hole in the initial condition. As damage developed, the geometry of the hole was made into an ellipse with the long axis in the load direction, to approximate the relaxation of the notch constraint. This approximate computational scheme was calibrated using the photoelastic and thermoelastic measurements of the actual stress states as damage developed. The effective geometry of the hole was made elliptical in proportion to the measured change in the stiffness across the hole as damage developed. The stiffness change calculated was matched to the measured value to determine the proper elliptical axis ratio for a given amount of damage development. Figure 75 shows the results of such a calculation and calibration for the AS4/3501 material. It is interesting to note that the reductions are not dependent on the stacking sequence of the laminate. When the proper ellipticity ratio was determined in this way, the calculated stress state was compared with those observed in the laboratory for the corresponding damaged condition. Of course, the approximate method does not reproduce the complex stresses associated with the details of the damage state, but the general features of the relaxation of the stress concentration are well represented. It should be noted that the consequence of this calculation is an increase in the predicted remaining strength due to the stress concentration relaxation. The amount of this calculated increase is controlled by the calibration just described, i.e., once the calibration is made the calculated strength increase is fixed and cannot

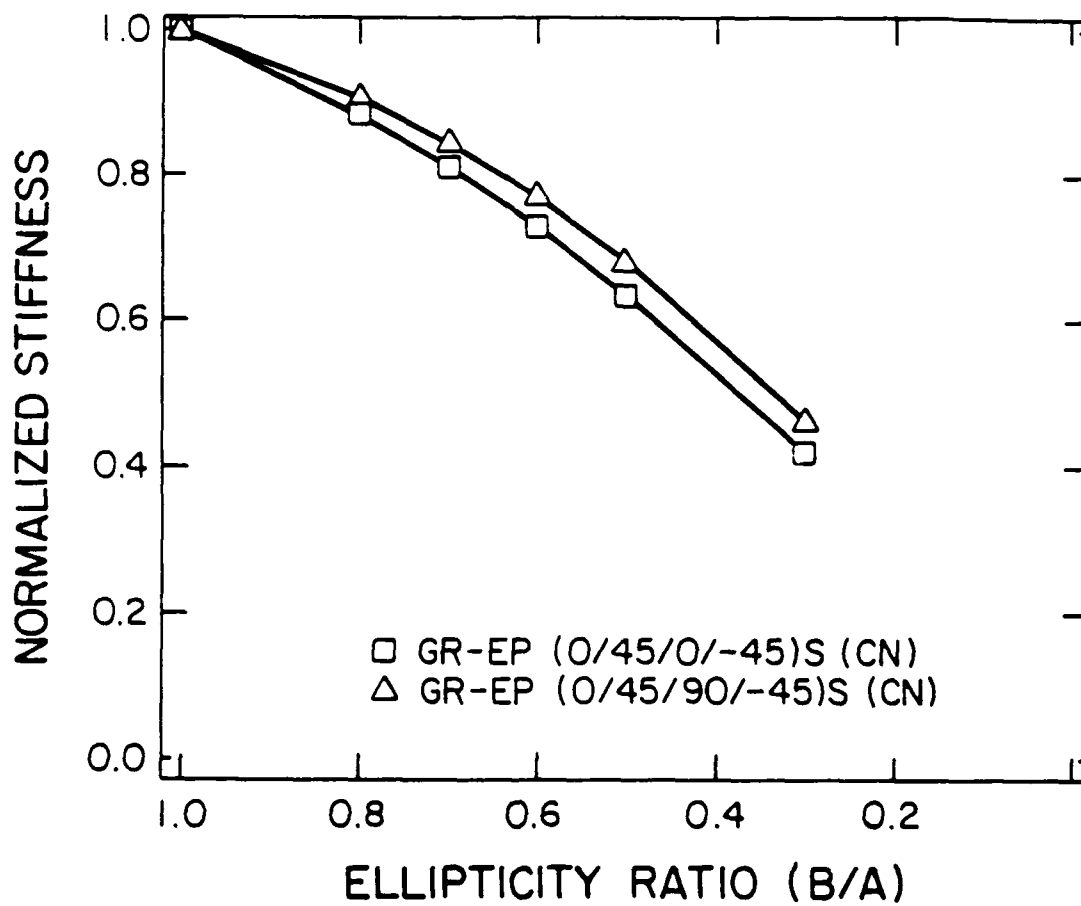


Figure 75. Calibration curves for the ellipticity ratio as a function of stiffness reduction across the hole.

be "adjusted" in any way to "fit" the data. We will see that the agreement with data is generally good, indicating that the approximate scheme is quite acceptable for the calculations required.

Changes in the stress state at the local level are a result of the changes in the stiffness of the off-axis plies that undergo matrix cracking. These changes are also determined from experimental measurement when such data are available. However, these changes can also be estimated by laminate analysis by "discounting" the stiffness of the plies that fail according to an appropriate failure theory such as the Tsai-Hill criterion, and examining the global stiffness change associated with the known applied load level. Figure 76 shows an example of such changes for fully reversed loading of the materials investigated in the present program, at a load level of about 75% of the static strength in compression. This curve and a corresponding one for the 50% load level were used to reduce the modulus transverse to the fibers and the in-plane shear modulus of the sub-critical elements, the off-axis plies in the examples to follow. The stress in the critical element, the zero degree plies in those examples, increases as the load is "shed" by the off-axis plies. This increase increases the rate at which the critical elements degrade and accelerates the reduction of strength.

The strength of the critical element may also be degraded. Elevated temperature or aggressive environments such as chemicals, atomic oxygen, etc. may cause "static fatigue" to occur in the critical elements. This change must be measured independently in the laboratory and a phenomenological representation of the reduction established. The model constructed in the present investigation has the capability to include such relationships. This capability results in the prediction of creep rupture lives, for example, a very valuable feature.

Once the state of stress and state of strength has been set for a given point in the loading history, as described above, the remaining strength is calculated. For the notched geometry, this calculation is made using the average stress concept of Whitney, et. al. Figure 77 illustrates the geometry used for that calculation. A radial direction is chosen at some angle,  $\alpha$ ,

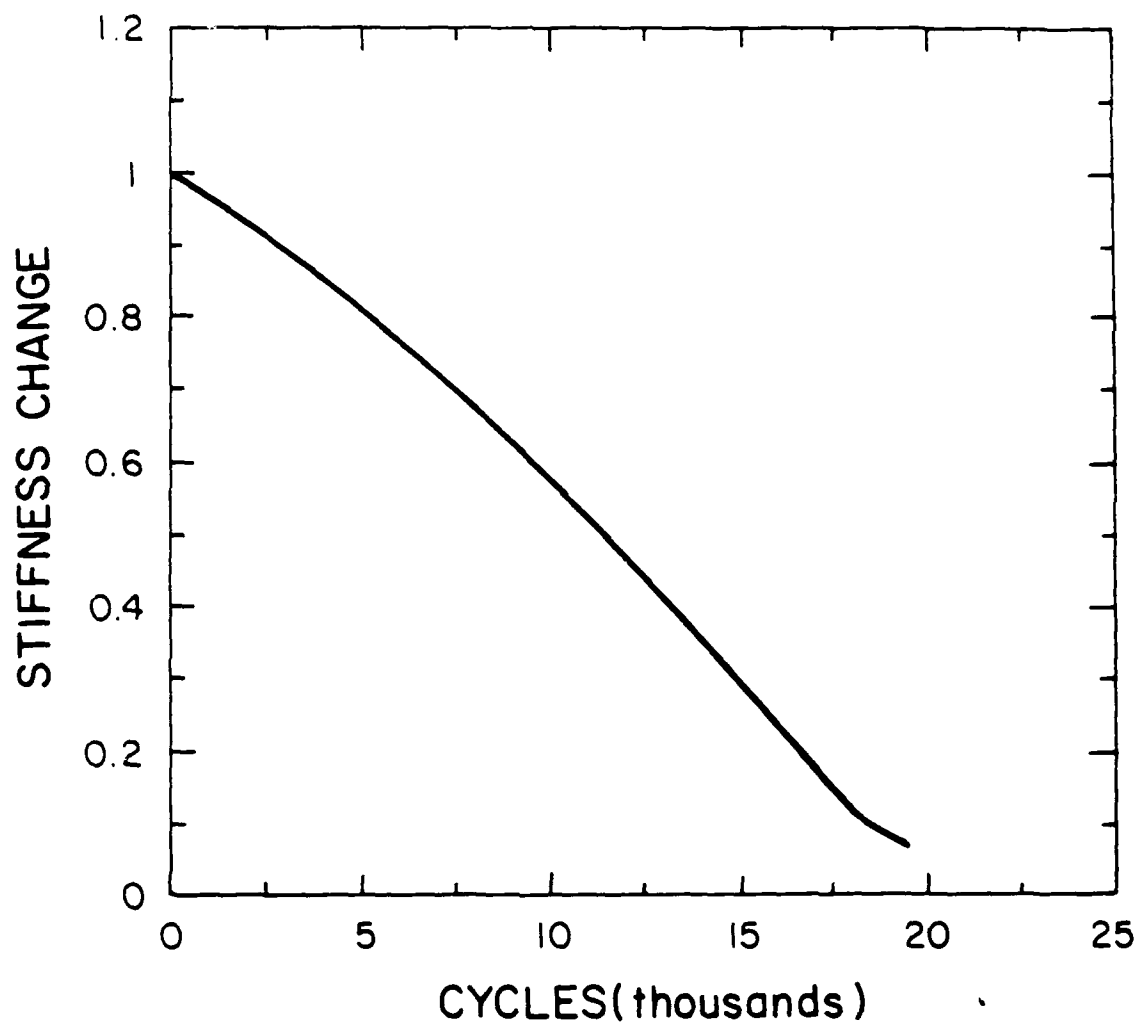


Figure 76. Stiffness reduction of off-axis plies for two loading levels.

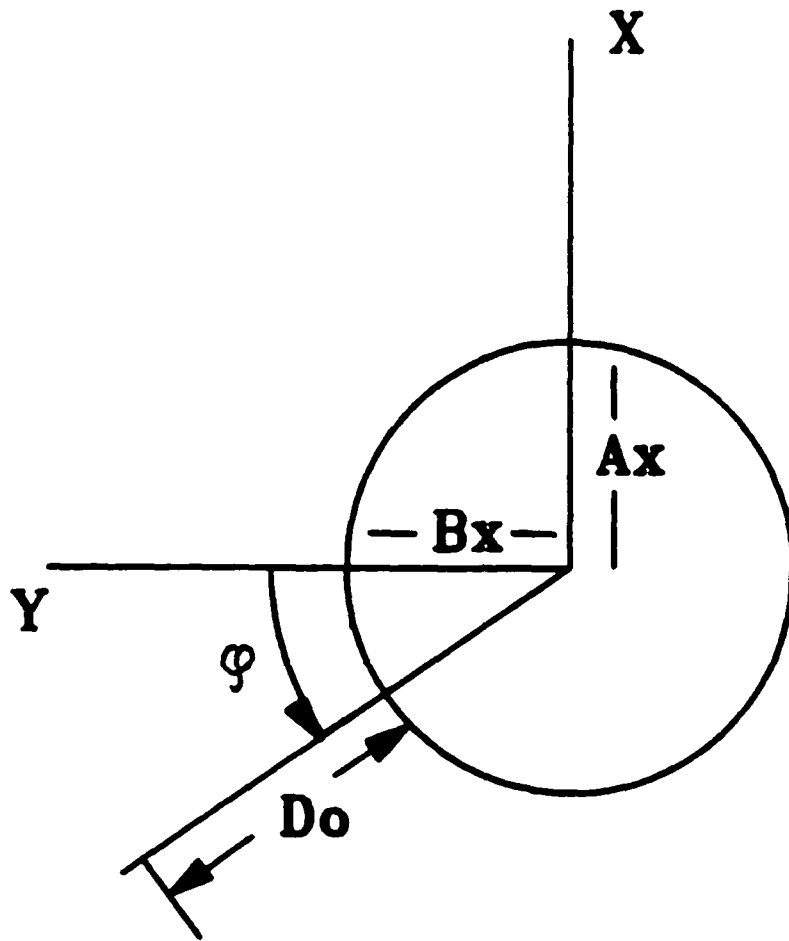


Figure 77. Geometry used for remaining strength calculation.

to the axis transverse to the loading direction. The choice of this direction is dictated by the failure mode. If the failure event occurs along a direction transverse to the load axis (which is typical for tensile failure under primarily tensile cyclic loading, for example), then a choice of  $\alpha = 0$  is appropriate. If a shear failure passes through the 45 degree direction, then a value of  $\alpha = 45$  degrees is appropriate, etc. The stresses in the critical element (the zero degree ply for this example) are calculated along the chosen line, over a distance, D, and the average value of an appropriate failure theory over the distance D is then determined. The proper value of D is determined by comparing the average value of the failure function with the quasi-static strength of the ply (or critical element) in the unnotched condition, when the notched member is loaded with the known (initial) notched strength load level. This value of D is then used for all subsequent calculations of the failure function during damage development.

Strength reduction is actually calculated by the relationship illustrated in Figure 78. The failure functions indicated are the average values of the failure criteria calculated over the distance D as mentioned above. Their values change as a function of the number of cycles due to the changes in stiffness at the global and local level, and the changes in material strengths. The parameter,  $i$ , is an adjustable quantity which has been held constant with a value of 1.2 since the model was introduced in 1980. The code associated with the model calculates the remaining strength by numerical integration of the integral shown in Figure 78. Since the remaining strength is calculated from an integral, variations in the applied load as a function of time (spectrum loading) are easily handled.

Figure 79 and Figure 80 show examples of predicted and observed residual strength and life curves for a quasi-isotropic and (0,45,0,-45)s laminate, respectively. The short life (high load) data were recovered from specimens loaded to about 75% of their static compression strength with  $R=-1$ , and the long life data were recovered from specimens tested at about 50% of the static compression strength. Both data sets were normalized by the total life in order to plot them on a common abscissa.



$$F_r(\tau_1) = F_u - \int_0^{\tau_1/\tau_0} (F_u - F_e(\tau)) i \left(\frac{\tau}{\tau_0}\right)^{i-1} d\left(\frac{\tau}{\tau_0}\right)$$

Parameter
Generalized Time

Residual Strength Function
Initial Strength Function
Applied Strength Function
Critical Element Characterization

**Figure 78.** Summation equation used for the calculation of remaining strength.

Several features of the predictions from the model are significant. First, the model correctly predicts an increase in the tensile strength. In fact, the magnitudes of the predicted increases are consistently conservative but fall within the data scatter bands or along the lower end of the bands in all but one case. It should be noted that these levels of strength increase are, in fact, predictions; they cannot be "adjusted" in any way with a parameter. They are a direct result of the model, and provide evidence of the validity of the modeling approach.

The compressive strength predictions are monotonic decreasing. The data shown in Figure 79 and Figure 80 show initial increases before the monotonic decrease occurs. As we noted earlier in this report, this particular specimen type was the only case to show initial compressive strength increases. The model does not predict compressive strength increases, but does predict the correct compressive strength decreases as damage develops.

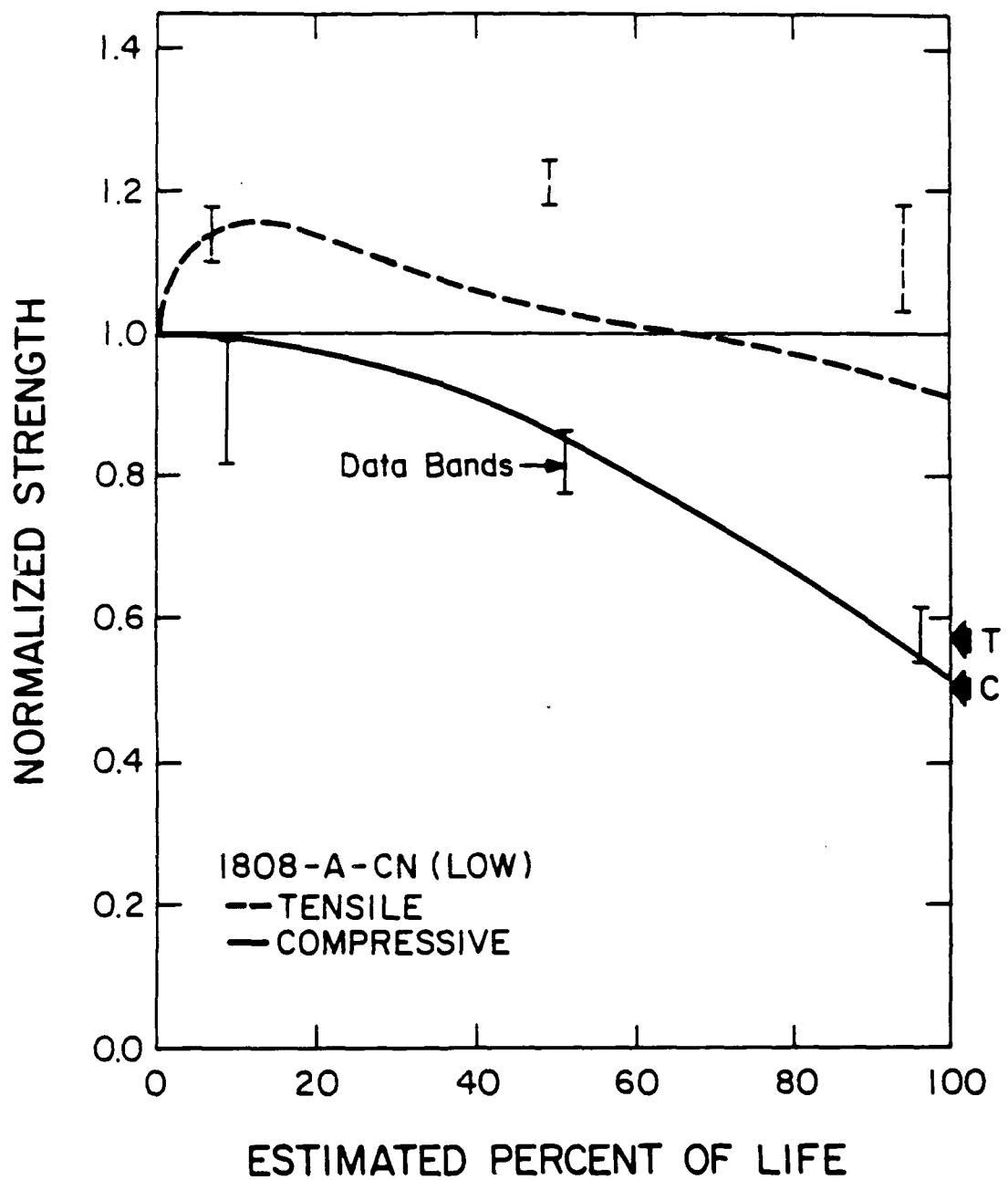


Figure 79. Predicted and observed residual strength for a quasi-isotropic laminate.

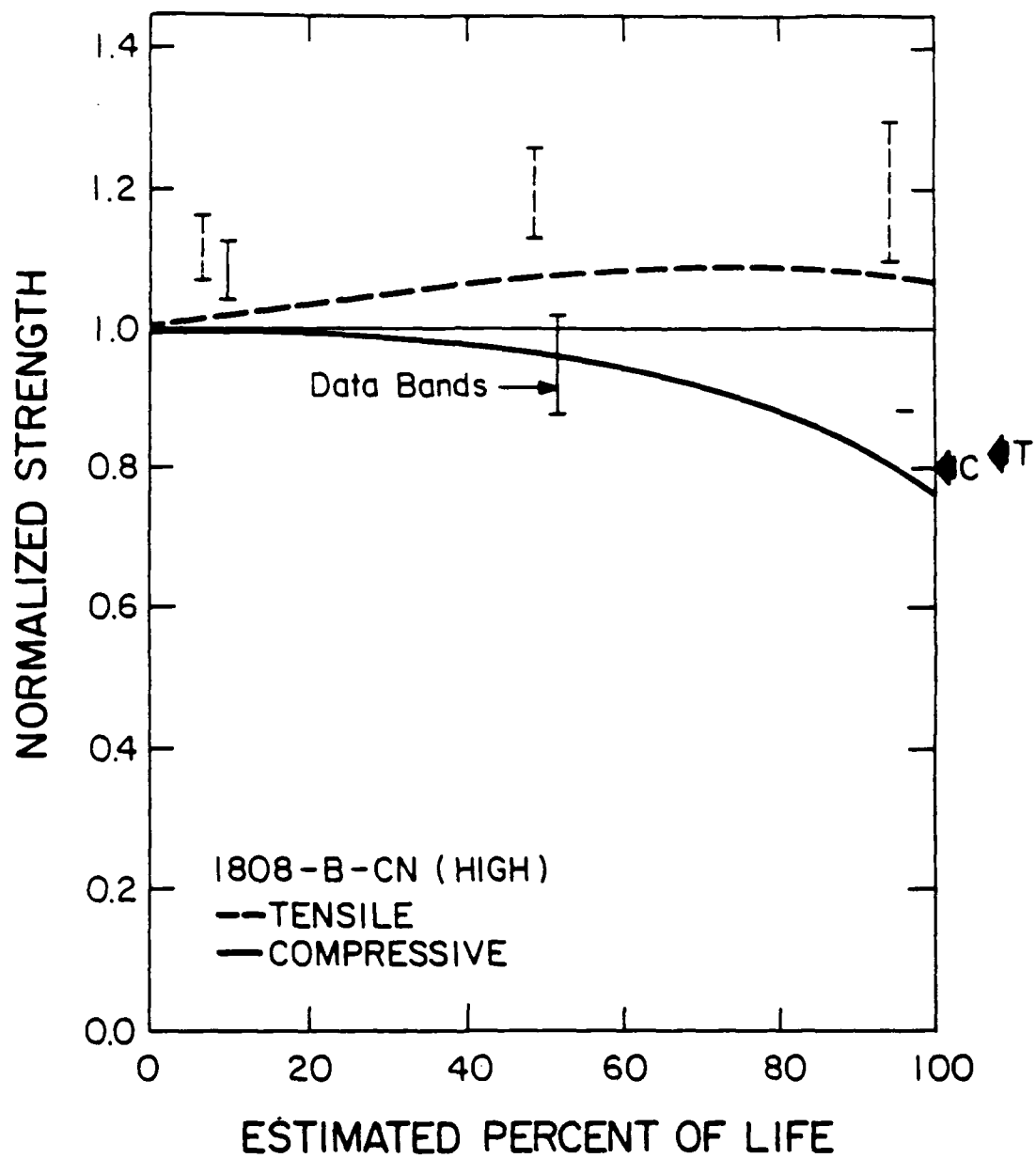


Figure 80. Predicted and observed residual strength for a (0,45,0,-45)s laminate.

Of special interest is the comparison of tensile strength and compressive strength behavior for the same loading. This situation amounts to a comparison of remaining tensile and compression strength for the same specimen during fully reversed testing. This comparison can identify, for example, the failure mode. If the compression strength drops to a lower level relative to the initial static compressive strength than does the tensile strength (compared to that initial value) at the point in life when failure occurs, then compressive failure is predicted. This situation was predicted for all simulations shown here. The laboratory observations support these predictions without exception; all fatigue failures were in compression.

An even more subtle prediction also emerged. The model predicted that the residual tensile strength of the 1808 material system would be reduced to lower levels than those of the 3501 material. In fact, for the high cyclic load levels, the model predicted that one might see a fracture mode transition from compression to tension failure. We were surprised to find that tensile strength reductions were, in fact, greater in the 1808 system. Although no fracture mode transition was observed in the present program, such a transition to tensile failure (for fully reversed loading) was observed for a similar "tough resin" composite system under quite similar conditions. This capability to predict failure modes in such subtle conditions was unexpected; if it proves to be a general capability, it will be of great value to the applications community.

Another feature highlighted by the model has to do with the volume of material involved in the failure process. The general size of that volume is proportional to the distance,  $D$ , that is used in the model, over which stresses are averaged in the critical element. The value of  $D$  is fixed by matching the applied load (in tension or compression) with the known fraction of quasi-static notched strength measured in the laboratory and predicted by the model before cyclic loading and damage development begins. Table 12 shows some of these values for the cases investigated in this program. The volumes for tensile failure are noticeably smaller than those that control compressive failure, suggesting that the physics of the two failure processes is quite different.

Table 12. Calibration values for critical element model.

Case	Laminate Type <sup>1</sup>	Tension/Compression	A <sub>n</sub>	B <sub>n</sub>	P <sub>n</sub>	D <sub>o</sub>
<u>Short Life</u> <u>3501</u>	QI	compression	1	-0.0725	1	0.0585
	QI	tension	1	-0.0725	1	0.079
	Q0	compression	1	-0.055	1	0.03
	Q0	tension	1	-0.055	1	0.071
<u>Short Life</u> <u>1808</u>	QI	compression	1	-0.0875	0.9	0.53
	QI	tension	1	-0.0875	0.9	0.015
	Q0	compression	1	-0.0575	1	0.205
	Q0	tension	1	-0.0575	1	0.019
<u>Long Life</u> <u>3501</u>	QI	compression	1	-0.0725	1	0.0585
	QI	tension	1	-0.0725	1	0.079
	Q0	compression	1	-0.055	1	0.03
	Q0	tension	1	-0.055	1	0.071
<u>Long Life</u> <u>1808</u>	QI	compression	1	-0.0875	0.9	0.53
	QI	tension	1	-0.0875	0.9	0.015
	Q0	compression	1	-0.0575	1	0.205
	Q0	tension	1	-0.0575	1	0.019

<sup>1</sup> QI = (0,45,90<sub>S</sub>,-45)<sub>S</sub>; Q0 = (0,45,0,-45)<sub>S</sub>

## VIII

### Conclusions

#### 8.1 *Investigative Methods*

The complementary data provided by stiffness monitoring and X-ray radiography were essential to estimate the fatigue "age" of specimens slated for destructive testing prior to fatigue failure. Counting cycles to estimate the "age" of specimens would not have been satisfactory, given the large amount of scatter in fatigue lifetimes.

The inability to accurately resolve stress or strain components from SPATE measurements was a severe handicap. The importance of knowing such components in materials with anisotropic strength properties cannot be understated. A means of directly measuring full-field strains in the 0-deg. fiber direction would have been more useful in understanding the effects of stress redistribution on residual strength. The interrogation of surface 0-deg. plies for stress redistribution data had limited utility since the interior plies apparently controlled residual tensile and compressive strength. Peak temperature change measurements in highly

stressed areas of the laminate needed to be normalized by the temperature change in a remote, undamaged portion of the specimen to facilitate comparisons among different specimens.

## **8.2 *Fatigue Response***

Relationships between the fully-reversed, cyclic loading history, damage development, stress redistribution, residual tensile and compressive strengths, and failure modes have been identified for the two material systems, two laminate configurations, two load levels, and two notch configurations included in the present test program. Conclusions concerning damage development, stress redistribution, and residual strength are presented next.

### **8.2.1 *Damage Development***

The direction and form of damage growth in notched laminates were determined principally by the lamination arrangement and load level. Damage growth favored the transverse direction in the laminate with a higher percentage of off-axis plies and in specimens under high-amplitude cyclic load histories. The transverse mode of damage growth consisted of relatively more 0-deg. ply fracture and less delamination than the longitudinal mode of damage growth. Low load specimens and quasi-isotropic specimens had more delaminations and matrix cracks than high-load and orthotropic specimens. Matrix cracks were more extensive in AS4/3501-6 specimens than in AS4/1808 specimens. Delaminations, however, were similar in form and extent in both material systems, despite the improved toughness of the 1808 matrix.

Incremental fractures of principal load-bearing plies were precipitated by matrix cracks in adjacent plies. The interaction of these damage modes was therefore highly dependent on the stacking sequence. In the AS4/1808 material, incremental fractures of 0-deg. plies were always followed by delaminations of the broken 0-deg. plies. However, if a 0-deg. ply delaminated first, fiber fractures did not occur in the delaminated portion of the ply, perhaps because the delamination buffered the 0-deg. ply from the stress concentration caused by the matrix crack. Similarly, delaminations on the outermost 0/45 interfaces prevented fractures of the 45-deg. plies along the 0-deg. matrix cracks tangent to the notch in the orthotropic laminate. This behavior is in contrast to the large number of broken 0-deg. fibers scattered within delaminated areas in center-notched, T300/5208, (0,45,90,-45)<sub>s4</sub> laminates in Ref. [76].

Damage, especially delamination, was usually more extensive closer to the surface of the specimens, causing a transfer of load into the interior plies. This surface effect was less obvious in specimens under high load levels.

## 8.2.2 Stress Redistribution

During fatigue, zones of high stress concentration observed with the SPATE apparatus were always located in areas of the specimen soon to be invaded by matrix and fiber damage. Depending on the peculiar mode of damage growth, highly stressed areas shifted either transversely from the notch (as in the quasi-isotropic specimens) or longitudinally from the notch (as in the orthotropic specimens). The highly stressed areas were located at or near the locus of tensile fracture in residual strength tests. Comparing specimens at various points in their fatigue lifetimes, the magnitude of the highly stressed area was lower in specimens having a higher residual tensile strength. In several instances, there was no correlation of the residual tensile strength and the stress concentration in the surface ply. In some of those cases, particularly those involving late-life specimens with extensive surface ply damage,



failure was assumed to be initiated by the failure of highly stressed fibers in some location not visible to the SPATE apparatus (perhaps in the interior of the laminate). In other cases, inordinately high, but extremely localized, stress concentrations did not correspond to proportionally lower tensile strengths, perhaps because of the occurrence of additional stress relaxation mechanisms during the course of the residual strength test.

The tendency for delaminations to grow unstably under compressive loads could not be ascertained with the SPATE technique. Hence, there was no correlation between stress patterns and residual compressive strengths except in the few situations where there were no appreciable delaminations. In the absence of extensive delaminations, the stress concentration near the notch controlled the compressive strength of the specimens.

### **8.2.3 Residual Strength**

Matrix cracks and delaminations blunted the original stress concentration near the notch, but caused new stress concentrations to appear immediately ahead of the damage zone. Up to and including the last strength measurement point just prior to fatigue failure, residual tensile strengths remained greater than the tensile strengths of virgin specimens except when extensive 0-deg. ply fractures emanated from the notch in several plies through the thickness. Compressive strengths decreased in the presence of 0-deg. ply fractures or delaminations transverse to the notch. Therefore, residual compressive strengths decreased monotonically throughout the fatigue lifetime in all cases except those involving orthotropic specimens prior to the onset of 0-deg. ply fractures or delaminations immediately adjacent to the notch.

Since 0-deg. fibers controlled the tensile strength of the laminates used in the present investigation, specimens with a larger amount of 0-deg. ply fractures had higher stress concentrations throughout their fatigue lifetimes and failed at lower tensile loads than specimens

with less 0-deg. ply fractures. Hence, tensile strengths were lower in quasi-isotropic specimens and in high-load fatigue tests. Residual compressive strengths were found to depend more on the extent and location of damage (particularly delamination) and less on the magnitude of stress concentrations than did residual tensile strengths.

## **8.2.4 Modeling of Remaining Strength**

The manner in which experimental damage analysis was used to construct a mechanistic model that predicts remaining strength - and from that prediction, predicts remaining life - has been discussed. It was seen that for continuous fiber reinforced notched laminates, two distinct damage zones were identified under fully reversed cyclic loading. Back-reflection photoelastic and thermoelastic stress analysis techniques established that damage development in the shear zone had the effect of reducing the stress concentration caused by the notch, causing increases in tensile residual strength. Micro-analysis of the damage in the damage growth zone established that tensile and compressive strength reduction was caused by that damage development.

Careful damage analysis identified the nature of matrix cracking and delamination in the damage zones. These details were used to identify "critical elements" which were described by constitutive equations to define the "state of material," and to set proper local boundary value problems to solve for the local "state of stress" in those critical elements. The changes in these material and stress states as a function of loading history were followed by recording global stiffness changes. These state changes were represented in an integral equation which summed the reductions in strength to provide a calculation of remaining strength. When the remaining strength reached the level of applied stress, life was predicted.

These modeling concepts have been combined into a performance simulation code which has been successfully applied to the prediction of remaining tensile and compressive strength of laminates constructed from two different composite material systems. Moreover, the model predicts which failure mode will cause specimen failure, and predicts the threshold of a fracture mode transition from compression to tensile failure.

## References

1. Hahn, H. T., Ed., *Composite Materials: Fatigue and Fracture*, STP 907, ASTM, Philadelphia, 1986.
2. Bakis, C. E. and Stinchcomb, W. W., "Response of Thick, Notched Laminates Subjected to Tension-Compression Cyclic Loads," *Composite Materials: Fatigue and Fracture*, STP 907, H. T. Hahn, Ed., ASTM, Philadelphia, 1986, pp. 314-334.
3. Simonds, R. A., Bakis, C. E., and Stinchcomb, W. W., "Effects of Matrix Toughness on Fatigue Response of Graphite Fiber Composite Laminates," *Composite Materials: Fatigue and Fracture (2nd Symp.)*, STP 1012, P. A. Lagace, Ed., ASTM, Philadelphia, 1988 (in press).
4. Kress, G. R. and Stinchcomb, W. W., "Fatigue Response of Notched Graphite/Epoxy Laminates," *Recent Advances in Composites in the United States and Japan*, STP 864, J. R. Vinson and M. Taya, Eds., ASTM, Philadelphia, 1985, pp. 173-196.
5. Wagnecz, L., "Material Properties and Damage Mechanisms of Woven Graphite Polyimide Composite Materials," Masters Thesis, College of Engineering, Virginia Polytechnic Institute and State University, Blacksburg, VA, June 1987.
6. Morton, J., Kellas, S., and Bishop, S. M., "Fatigue Damage Development in a Notched Carbon Fibre Composite," *Comp. Struct.*, **5** (1986), pp. 143-157.

7. Bishop, S. M. and Dorey, G., "The Effect of Damage on the Tensile and Compressive Performance of Carbon Fibre Laminates," *AGARD Conf. Proc. No. 355*, North Atlantic Treaty Organization, 12-14 April 1983, pp. 10.1-10.10.
8. Black, N. F. and Stinchcomb, W. W., "Compression Fatigue Damage in Thick, Notched Graphite/Epoxy Laminates," *Long-Term Behavior of Composites, STP 813*, T. K. O'Brien, Ed., ASTM, Philadelphia, 1983, pp. 95-115.
9. Ramani, S. V. and Williams, D. P., "Notched and Unnotched Fatigue Behavior of Angle-Ply Graphite/Epoxy Composites," *Fatigue of Filamentary Composite Materials, STP 636*, K. L. Reifsnider and K. N. Lauraitis, Eds., ASTM, Philadelphia, 1977, pp. 27-46.
10. Walter, R. W., Johnson, R. W., June, R. R., and McCarty, J. E., "Designing for Integrity in Long-Life Composite Aircraft Structures," *Fatigue of Filamentary Composite Materials, STP 636*, K. L. Reifsnider and K. N. Lauraitis, Eds., ASTM, Philadelphia, 1977, pp. 228-247.
11. Hedgepeth, J. M., "Stress Concentrations in Filamentary Structures," NASA TN-D882, Nat. Aeronautics and Space Admn., May 1961.
12. Hedgepeth, J. M. and Van Dyke, P., "Local Stress Concentrations in Imperfect Filamentary Composite Materials," *J. Comp. Mater.*, **1** (1967), pp. 294-309.
13. Van Dyke, P. and Hedgepeth, J. M., "Stress Concentration From Single Fiber Failures in Composite Materials," *Textile Res. J.*, **39** (1969), pp. 618-626.
14. Rosen, B. W., "Tensile Failure of Fibrous Composites," *AIAA J.*, **2** (1964), pp. 1985-1991.
15. Zweben, C., "Fracture Mechanics and Composite Materials: A Critical Analysis," *Analysis of the Test Methods for High Modulus Fibers and Composites, STP 521*, ASTM, Philadelphia, 1973, pp. 65-97.
16. Goree, J. G. and Gross, R. S., "Stresses in a Three-Dimensional Unidirectional Composite Containing Broken Fibers," *Eng. Fract. Mech.*, **13** (1980), pp. 395-405.
17. Goree, J. G. and Gross, R. S., "Analysis of a Unidirectional Composite Containing Broken Fibers and Matrix Damage," *Eng. Fract. Mech.*, **13** (1980), pp. 563-578.
18. Batdorf, S. B., "Tensile Strength of Unidirectionally Reinforced Composites — I" *J. Reinf. Plast. and Comp.*, **1** (1982), pp. 153-164.

19. Batdorf, S. B. and Ghaffarian, Reza, "Tensile Strength of Unidirectionally Reinforced Composites — II" *J. Reinf. Plast. and Comp.*, **1** (1982), pp. 165-176.
20. Batdorf, S. B. and Ghaffarian, Reza, "Size Effect and Strength Variability of Unidirectional Composites," *Int. J. Fract.*, **26** (1984), pp. 113-123.
21. Waddoups, M. E., Eisenmann, J. R., and Kaminski, B. E., "Macroscopic Fracture Mechanics of Advanced Composite Materials," *J. Comp. Mater.*, **5** (1971), pp. 446-454.
22. Whitney, J. M. and Nuismer, R. J., "Stress Fracture Criteria for Laminated Composites Containing Stress Concentrations," *J. Comp. Mater.*, **8** (1974), pp. 253-265.
23. Karlak, R. G., "Hole Effects in a Related Series of Symmetrical Laminates," *Proc. Failure Modes in Composites, IV*, Metallurgical Soc. AIME, Chicago, 1977, pp. 105-117.
24. Caprino, G., "On the Prediction of Residual Strength for Notched Laminates," *J. Mater. Sci.*, **18** (1983), pp. 2269-2273.
25. Daniel, I. M., Rowlands, R. E., and Whiteside, J. B., "Effects of Material and Stacking Sequence on Behavior of Composite Plates with Holes," *Exp. Mech.*, **14** (1974), pp. 1-9.
26. Whitney, J. M. and Kim, R. Y., "Effect of Stacking Sequence on the Notched Strength of Laminated Composites," *Composite Materials: Testing and Design (4th Conf.)*, STP 617, ASTM, Philadelphia, 1977, pp. 229-242.
27. Pipes, R. B., Wetherhold, R. C., and Gillespie, J. W., Jr., "Notched Strength of Composite Materials," *J. Comp. Mater.*, **12** (1979), pp. 148-160.
28. Garbo, S. P. and Ogonowski, J. M., "Strength Predictions of Composite Laminates with Unloaded Fastener Holes," *AIAA J.*, **18** (1980), pp. 585-589.
29. Tan, S. C., "Notched Strength Prediction and Design of Laminated Composites Under In-Plane Loadings," *J. Comp. Mater.*, **21** (1987), pp. 751-780.
30. Lekhnitskii, S. G., *Anisotropic Plates*, transl. from the 2nd Russian ed. by S. W. Tsai and T. Cheron, Gordon and Breach, New York, 1968.
31. Poe, C. C., Jr. and Sova, K. A., "Fracture Toughness of Boron/Aluminum Laminates With Various Proportions of 0° and  $\pm 45^\circ$  Plies," NASA TP-1707, Nat. Aeronautics and Space Admn., 1980.

32. Morley, J. G., "On the Development of a General Theory for the Mechanics of Tensile Fracture of Fibre Reinforced Materials," *J. Mater. Sci.*, **20** (1985), pp. 1794-1806.
33. Chou, S. C., Orringer, O., and Rainey, J. H., "Post-Failure Behavior of Laminates: II — Stress Concentration," *J. Comp. Mater.*, **11** (1977), pp. 71-78.
34. Witt, W. P. and Palazotto, A. N., "Numerical and Experimental Comparison of the Notch Tip Stresses in a Laminated Plate," *AIAA J.*, **17** (1979), pp. 500-506.
35. Sandhu, R. S., Gallo, R. L., and Sendeckyj, G. P., "Initiation and Accumulation of Damage in Composite Laminates," *Composite Materials: Testing and Design (6th Conf.)*, STP 787, I. M. Daniel, Ed., ASTM, Philadelphia, 1982, pp. 163-182.
36. Lee, J. D., "Three Dimensional Finite Element Analysis of Damage Accumulation in Composite Laminate," *Computers & Structures*, **15** (1982), pp. 335-350.
37. Irvine, T. B. and Ginty, C. A., "Progressive Fracture of Fiber Composites," *J. Comp. Mater.*, **20** (1986), pp. 166-184.
38. Chang, F.-K. and Chang, K.-Y., "A Progressive Damage Model for Laminated Composites Containing Stress Concentrations," *J. Comp. Mater.*, **21**, pp. 834-855.
39. Rhodes, M. D., Mikulas, M. M. Jr., and McGowan, P. E., "Effects of Orthotropy and Width on the Compression Strength of Graphite-Epoxy Panels with Holes," *AIAA J.*, **22** (1984), pp. 1283-1292.
40. Nuismer, R. J. and Labor, J. D., "Application of the Average Stress Failure Criterion: Part II — Compression," *J. Comp. Mater.*, **13** (1979), pp. 49-60.
41. Rosen, B. W., "Mechanics of Composite Strengthening," *Fiber Composite Materials*, ASM, 1965, pp. 37-75.
42. Greszczuk, L. B., "Microbuckling of Lamina-Reinforced Composites," *Composite Materials: Testing and Design (3rd Symp.)*, STP 546, ASTM, Philadelphia, 1974, pp. 5-29.
43. Hahn, H. T. and Williams, J. G., "Compression Failure Mechanisms in Unidirectional Composite," NASA TM 85834, Langley Research Center, Nat. Aeronautics and Space Admn., Hampton, VA, Aug. 1984.

44. Gurdal, Z. and Haftka, R. T., "Compressive Failure Model for Anisotropic Plates with a Cutout" *AIAA J.*, **25** (1987), pp. 1476-1481.
45. Nemeth, M. P., "Buckling Behavior of Orthotropic Composite Plates with Centrally Located Cutouts," Ph.D. Dissertation, College of Engineering, Virginia Polytechnic Institute and State University, Blacksburg, VA, May 1983.
46. Shivakumar, K. N. and Whitcomb, J. D., "Buckling of a Sublaminar in a Quasi-Isotropic Composite Laminate," *J. Comp. Mater.*, **19** (1985), pp. 2-18.
47. Halpin, J. C., Johnson, T. A., and Waddoups, M. R., *Int. J. Fract. Mech.*, **8** (1972), pp. 465-472.
48. Broutman, L. J. and Sahu, S., "A New Theory to Predict Cumulative Fatigue Damage in Fiberglass Reinforced Plastics," *Composite Materials: Testing and Design (2nd Conf.)*, STP 497, ASTM, Philadelphia, 1972, pp. 170-188.
49. Reifsnider, K. L. and Stinchcomb, W. W., "A Critical-Element Model of the Residual Strength and Life of Fatigue-Loaded Composite Coupons," *Composite Materials: Fatigue and Fracture*, STP 907, H. T. Hahn, Ed., ASTM, Philadelphia, 1986, pp. 298-313.
50. Reifsnider, K. L. and Bakis, C. E., "Modeling Damage Growth in Notched Composite Laminates," *Proc. Japan-US Symp. on Composite Materials*, Tokyo, 22-24 June 1986.
51. Highsmith, A. L. and Reifsnider, K. L., "Internal Load Distribution Effects During Fatigue Loading of Composite Laminates," *Composite Materials: Fatigue and Fracture*, STP 907, H. T. Hahn, Ed., ASTM, Philadelphia, 1986, pp. 233-251.
52. Jamison, R. D., "Fiber Fracture in Composite Laminates," *Proc. 6th ICCM and 2nd ECCM*, Vol. 3, F. L. Mathews, N. C. R. Buskell, J. M. Hodgkinson, and J. Morton, Eds., Elsevier, Amsterdam, 1987, pp. 3.185-3.199.
53. Jamison, R. D., "On the Interrelationship Between Fiber Fracture and Ply Cracking in Graphite/Epoxy Laminates," *Composite Materials: Fatigue and Fracture*, STP 907, H. T. Hahn, Ed., ASTM, Philadelphia, 1986, pp. 252-273.



54. Reifsnider, K. L., Stinchcomb, W. W., and Henneke, E. G., II, "Defect-Property Relationships in Composite Laminates," AFML Technical Report 76-81, Part IV, Wright-Patterson AFB, Dayton, OH, April 1979.
55. O'Brien, T. K., "Characterization of Delamination Onset and Growth in a Composite Laminate," *Damage in Composite Materials, STP 775*, K. L. Reifsnider, Ed., ASTM, Philadelphia, 1982, pp. 140-167.
56. Highsmith, A. L. and Reifsnider, K. L., "On Delamination and the Damage Localization Process," *Fracture of Fibrous Composites — AMD Vol. 74*, C. T. Herakovich, Ed., ASME, New York, 1985, pp. 71-87.
57. Sundaresan, M. J. and Henneke, E. G., II, "SEM Observations of Failure Process in Unidirectional Composite Materials," *Composite Materials: Testing and Design (9th Symp.)*, STP xxx, S. P. Garbo, Ed., ASTM, Philadelphia, in press.
58. Bakis, C. E., Yih, H. R., Reifsnider, K. L., and Stinchcomb, W. W., "Damage Initiation and Growth in Notched Laminates Under Reversed Cyclic Loading," *Composite Materials: Fatigue and Fracture (2nd Symp.)*, STP 1012, P. A. Lagace, Ed., ASTM, Philadelphia, 1988 (in press).
59. Simonds, R. A. and Stinchcomb, W. W., "Response of Notched AS4/PEEK Laminates to Tension/Compression Loading," *Advances in Thermoplastic Matrix Composite Materials*, STP xxx, Golam Newaz, Ed., ASTM, Philadelphia, in press.
60. Curtis, P. T., "An Investigation of the Tensile Fatigue Behavior of Improved Carbon Fibre Composite Materials," *Proc. 6th ICCM and 2nd ECCM Conf.*, Vol. 4, F. L. Mathews, N. C. R. Buskell, J. M. Hodgkinson, and J. Morton, Eds., Elsevier, Amsterdam, 1987, pp. 4.54-4.64.
61. Baron, Ch. and Schulte, K. "Fatigue Damage Response of CFRP with Toughened Matrices and Improved Fibers," *Proc. 6th ICCM and 2nd ECCM Conf.*, Vol. 4, F. L. Mathews, N. C. R. Buskell, J. M. Hodgkinson, and J. Morton, Eds., Elsevier, Amsterdam, 1987, pp. 4.65-4.75.

62. Baron, Ch., Schulte, K., and Harig, H., "Influence of Fibre and Matrix Failure Strain on Static and Fatigue Properties of Carbon Fibre-Reinforced Plastics," *Composites Science and Technology*, **29** (1987), pp. 257-272.
63. Daniel, I. M., "Mixed Mode Failure of Composite Laminates," *Exp. Mech.*, **25** (1985), pp. 413-420.
64. Wood, J. D., "Detection of Delamination Onset in a Composite Laminate Using Moiré Interferometry," *J. Comp. Tech. & Res.*, **7** (1985), pp. 121-128.
65. Reifsnider, K. L., Stinchcomb, W. W., and O'Brien, T. K., "Frequency Effects on a Stiffness-Based Fatigue Failure Criterion in Flawed Composite Specimens," *Fatigue of Filamentary Composite Materials*, STP 636, K. L. Reifsnider and K. N. Lauraitis, Eds., ASTM, Philadelphia, 1977, pp. 171-184.
66. Phillips, E. P., "Effects of Truncation of a Predominantly Compression Load Spectrum on the Life of a Notched Graphite/Epoxy Laminate," *Fatigue of Fibrous Composite Materials*, STP 723, ASTM, Philadelphia, 1981, pp. 197-212.
67. Bakis, C. E., Simonds, R. A., and Stinchcomb, W. W., "A Test Method to Measure the Response of Composite Materials Under Reversed Cyclic Loads," *Test Methods and Design Allowables for Fiber Composites (2nd Conf.)*, STP 1003, C. C. Chamis and K. L. Reifsnider, Eds., ASTM, Philadelphia, 1988.
68. Evans, R. E. and Masters, J. E., "A New Generation of Epoxy Composites for Primary Structural Applications: Materials and Mechanics," *Toughened Composites*, STP 937, N. J. Johnston, Ed., ASTM, Philadelphia, 1987, pp. 413-436.
69. Masters, J. E., "Characterization of Impact Damage Development in Graphite/Epoxy Laminates," *Fractography of Modern Engineering Materials: Composites and Metals*, STP 948, J. E. Masters and J. J. Au, Eds., ASTM, Philadelphia, 1987, pp. 238-258.
70. Ratwani, M. M., and Kan, H. P., "Effect of Stacking Sequence on Damage Propagation and Failure Modes in Composite Laminates," *Damage in Composite Materials*, STP 775, K. L. Reifsnider, Ed., ASTM, Philadelphia, 1982, pp. 211-228.

71. Reifsnider, K. L., Stinchcomb, W. W., Bakis, C. E. and Yih, H. R., "Investigation and Modeling of Damage Growth in Composite Laminates," AFOSR Contract No. 85.0087, Bolling AFB, Washington, DC, July 1986.
72. O'Brien, T. K., "Stiffness Change as a Nondestructive Damage Measurement," *Mechanics of Nondestructive Testing*, W. W. Stinchcomb, Ed., Plenum Press, New York, 1980, pp. 101-121.
73. Reifsnider, K. L. and Highsmith, A. L., "The Relationship of Stiffness Changes in Composite Laminates to Fracture-Related Damage Mechanisms," *Proc. 2nd USA-USSR Symp. on Fracture of Composite Materials*, Lehigh Univ., Bethlehem, PA, March 1981, pp. 9-12.
74. Reifsnider, K. L. and Stinchcomb, W. W., "Stiffness Change as a Fatigue Damage Parameter for Composite Laminates," *Advances in Aerospace Structures, Materials and Dynamics — AD-06*, U. Yuceoglu, R. L. Sierakowski and D. A. Glasgow, Eds., ASME, New York, 1983.
75. Owens, G. R., "An Experimental Investigation of the Material Response of Graphite/Polyphenylene Sulfide," Masters Thesis, College of Engineering, Virginia Polytechnic Institute and State University, Blacksburg, VA, Aug., 1986.
76. Bakis, C. E., "Fatigue Response of Notched Laminates Subjected to Tension-Compression Loading," Masters Thesis, College of Engineering, Virginia Polytechnic Institute and State University, Blacksburg, VA, Dec., 1984.
77. Rummel, W. D., Tedrow, T., and Brinkerhoff, H. D., "Enhanced X-Ray Stereoscopic NDE of Composite Materials," AFWAL-TR-80-3053, Final Report, AFWAL, FDL, AFSC, Wright-Patterson AFB, Ohio, June 1980.
78. Sendekyj, G. P., Maddux, G. E., and Porter, E., "Damage Documentation in Composites by Stereo Radiography," *Damage in Composite Materials, STP 775*, K. L. Reifsnider, Ed., ASTM, Philadelphia, 1982, pp. 16-26.
79. Freeman, S. M., "Characterization of Lamina and Interlaminar Damage in Graphite/Epoxy Composites by the Deply Technique," *Composite Materials: Testing and Design (6th Conf.)*, STP 787, I. M. Daniel, Ed., ASTM, Philadelphia, 1982, pp. 50-62.

80. D. E. Oliver, "Stress Pattern Analysis by Thermal Emission," *Handbook on Experimental Mechanics*, A. S. Kobayashi, Ed., SEM, Prentice-Hall (1987), pp. 610-620.
81. R. T. Potter, "Stress Analysis in Laminated Fiber Composites by Thermoelastic Emission," *Proc. 2nd Intl. Conf. on Stress Anal. by Thermoelastic Tech.*, Paper No. 20, 17-18 Feb. 1987, London.
82. P. Stanley and W. K. Chan, "SPATE Stress Studies of Plates and Rings Under In-Plane Loading," *Exp. Mech.*, **26** (1986), pp. 360-370.
83. M. H. Belgen, "Structural Stress Measurements with an Infrared Radiometer," *ISA Trans.*, **6** (1967), pp. 49-53.
84. Bakis, C. E. and Reifsnider, K. L., "Nondestructive Evaluation of Fiber Composite Laminates by Thermoelastic Emission," *Review of Progress in Quantitative NDE*, **7B**, D. O. Thompson and D. E. Chimenti, Eds., Plenum, 1988, pp. 1109-1116.
85. B. N. Cox and D. E. Pettit, "Nondestructive Evaluation of Composite Materials Using the Stress Pattern Analysis by Thermal Emissions Technique," *Proc. SEM Spring Conf. on Exp. Mech.*, 14-19 June 1987, Houston, TX.
86. Lohr, D. T. and Sandor, B. I., "Impact Damage Analysis by Differential Infrared Thermography," *Proc. SEM Fall Conf.*, Savannah, GA, 1987.
87. Lohr, D. T., Enke, N. F., and Sandor, B. I., "Analysis of Fatigue Damage Evolution by Differential Infrared Thermography," *Proc. SEM Fall Conf.*, Savannah, GA, 1987.
88. Neubert, H., Schulte, K., and Harig, H., "Evaluation of the Damage Development in CFRP by Monitoring Load Induced Temperature Changes," *Composite Materials: Testing and Design (9th Symp.)*, STP xxx, S. P. Garbo, Ed., ASTM, Philadelphia, in press.
89. W. Thomson, "On the Dynamical Theory of Heat," *Trans. Roy. Soc. Edinburgh*, **20** (1853), pp. 261-288.
90. W. Thomson, "On the Thermo-Elastic and Thermo-Magnetic Properties of Matter," *Qtlly. J. Math.*, **1** (1857), pp. 57-77.
91. Joule, J. P., "On Some Thermo-dynamic Properties of Solids," *Philos. Trans. Roy. Soc.*, **149** (1859), pp. 91-131.

92. Compton, K. T. and Webster, D. B., "Temperature Changes Accompanying the Adiabatic Compression of Steel," *Phys. Rev., Series 2*, **5** (1915), pp. 159-166.
93. Dillon, O. W. and Tauchert, T. R., "The Experimental Technique for Observing the Temperatures Due to the Coupled Thermoelastic Effect," *Int. J. Solids Str.*, **2** (1966), pp. 385-390.
94. Stanley, P. and Chan, W. K. "Quantitative Stress Analysis by Means of the Thermoelastic Effect," *J. Strain Anal.*, **20** (1985), pp. 129-137.
95. Gilmour, I. W., Trainor, A., and Haward, R. N., "The Thermoelastic Effect in Glassy Polymers," *J. Polym. Sci.: Polym. Phys. Ed.*, **16** (1978), pp. 1277-1290.
96. Haward, R. N. and Trainor, A., "The Thermoelastic Effect in PMMA," *J. Mater. Sci.*, **9** (1974), pp. 1243-1254.
97. Jordan, E. H. and Sandor, B. I., "Stress Analysis from Temperature Data," *J. Testing and Eval., JTEVA*, **6** (1978), pp. 325-331.
98. Enke, N. F. and Sandor, B. I., "Cyclic Plasticity Analysis by Differential Infrared Thermography," *Proc. VI Intl. Congr. Exper. Mech.*, Vol. II, Portland OR, 6-10 June 1988, SEM, Bethel CT, pp. 837-842.
99. Higuchi, M. and Imai, Y., "Rheological Interpretation of Heat Generation Associated with Fatigue of Polycarbonate," *J. Appl. Polym. Sci.*, **14** (1970), pp. 2377-2383.
100. M. A. Biot, "Thermoelasticity and Irreversible Thermodynamics," *J. Appl. Phys.*, **27** (1956), pp. 240-253.
101. W. Nowacki, *Dynamic Problems of Thermoelasticity*, Noordhoff (1975).
102. Huang, Y. M., Hamdi AbdelMohsen, M. H., Lohr, D., Feng, Z., Rowlands, R. E., and Stanley, P., "Determination of Individual Stress Components from SPATE Isopachics Only," *Proc. VI Intl. Congr. Exper. Mech.*, Vol. I, Portland OR, 6-10 June 1988, SEM, Bethel CT, pp. 578-584.
103. Hudson, R. D., Jr., *Infrared System Engineering*, Wiley, New York, 1969.
104. Lesniak, J. R., "Internal Stress Measurements," *Proc. VI Intl. Congr. Exper. Mech.*, Vol. II, Portland OR, 6-10 June 1988, SEM, Bethel CT, pp. 825-829.

105. Jones, R. M., *Mechanics of Composite Materials*, Scripta, 1975, Washington, D.C.
106. C. C. Chamis, "Simplified Composite Micromechanics Equations for Hygral, Thermal, and Mechanical Properties," *SAMPE Qtly.*, **15** (1984), pp. 14-23.
107. Kriz, R. D. and Stinchcomb, W. W., "Effects of Moisture, Residual Thermal Curing Stresses, and Mechanical Load on the Damage Development in Quasi-Isotropic Laminates," *Damage in Composite Materials*, STP 775, K. L. Reifsnider, Ed., ASTM, Philadelphia, 1982, pp. 63-80.
108. Harris, C. E. and Morris, D. H., "An Evaluation of the Effects of Stacking Sequence and Thickness on the Fatigue Life of Quasi-Isotropic Graphite/Epoxy Laminates," NASA CR-172169, Langley Research Center, Hampton, VA, April 1983.
109. J. Morton, S. Kellas, and S. M. Bishop, "The Effect of Environment on the Fatigue Damage Development in Notched Carbon Fibre Composites," *Proc. 6th ICCM and 2nd ECCM*, Vol. 4, F. L. Mathews, N. C. R. Buskell, J. M. Hodgkinson, and J. Morton (Eds.), Elsevier, Amsterdam, 1987.
110. Reifsnider, K.L. and Stinchcomb, W.W., "A Critical-Element Model of the Residual Strength of Life of Fatigue-Loaded Composite Coupons," in *Composite Materials: Fatigue and Fracture*, ASTM STP 907, H.T. Hahn, Ed., American Society for Testing and Materials, Philadelphia, 1986.
111. Reifsnider, K.L., "Critical Element Concepts for Composite Structures," *Proc. of Spacecraft Structures Conf.*, CNES, Dec. 1985 (ESA SP-238, April 1986).
112. Reifsnider, K.L., "The Critical Element Model: A Modeling Philosophy," *Mechanics of Damage and Fatigue*, Pergamon Press, 1986, pp.739-750.

## **APPENDIX A**

# Damage Initiation and Growth in Notched Laminates Under Reversed Cyclic Loading

C. E. Bakis, H. R. Yih, W. W. Stinchcomb, and K. L. Reifsnider<sup>1</sup>

**ABSTRACT:** The initiation and growth of fatigue damage in notched Cycom AS4/1808 graphite/epoxy laminates was investigated experimentally. Two layups,  $(0/45/90/-45)_{s4}$  and  $(0/45/0/-45)_{s4}$ , provided contrasting responses to the fully-reversed fatigue loads. Full-field strains surrounding the circular notch were evaluated at several stages of fatigue life with the photoelastic coating and isentropic thermal emission measurement techniques, and were related to the corresponding damage state and residual properties.

**KEY WORDS:** composite material, graphite/epoxy, notched laminate, fatigue, damage, stiffness, strength, strain redistribution, nondestructive evaluation, photoelasticity, thermography.

With the expanded use of fiber-reinforced composite materials with cutouts as primary load-bearing structural components under long-term cyclic loading comes the need for an understanding of fatigue damage development within stress gradients and its effect on the residual strength, stiffness and life of the components. Recent experimental and analytical advances explicate the significant effects of localized subcritical damage on load transfer (or stress redistribution) in unnotched laminates which, in turn, influences the global fracture event [1,2]. The current understanding of load redistribution in notched laminates is not as complete as that for unnotched laminates, due primarily to the additional complexity of in-plane damage and stress gradients. Attempts to characterize strain or displacement fields near a notch in the presence of damage have successfully utilized photoelasticity and moiré interferometry (for example, Ref 3 for monotonic loads, and Ref 4 for tensile cyclic loads). Recent analytical efforts have used two- or quasi-three-dimensional finite element models to predict incremental (element-wise) damage growth near notches during monotonic loads [5,6], but a unified treatment of the problem that accurately models the changes in stress dis-

---

<sup>1</sup> Graduate project assistant, graduate research assistant, professor, and Reynolds Metals professor, respectively, Materials Response Group, Engineering Science and Mechanics, Virginia Polytechnic Institute and State University, Blacksburg VA, 24061-4899.



tribution and corresponding changes in residual properties during fatigue damage development is still not available. The present paper addresses the problem through an experimental investigation of the interaction of fatigue damage, the global state of deformation, and the residual strength, stiffness and life in two contrasting center-notched graphite/epoxy laminates under fully reversed cyclic loading. Two methods are employed to characterize full-field, in-plane deformations at intermittent points in the fatigue lifetime. The first method involves measurement of surface strains with a photoelastic coating applied to the specimen. The second method employs, for the first time in a laminated composite material, the measurement of the dynamic, isentropic temperature change during cyclic loading of the specimen, which is related to the dilatation of the microconstituents.

## *Mechanical Testing*

The (0/45/90/-45)<sub>s4</sub> and (0/45/0/-45)<sub>s4</sub> graphite/epoxy laminates were fabricated in an autoclave with Cycom AS4/1808 prepreg tape as per the manufacturer's specifications.<sup>2</sup> Fiber volume fraction was nominally 60 percent in both laminates. Specimens measuring 152 mm long and 38.1 mm wide were cut from the cured panels with a diamond-impregnated wheel.<sup>3</sup> Average gross (unnotched) cross-sectional area for both specimen types was 174 mm<sup>2</sup>. A 9.52-mm-diameter hole was drilled through the center of each specimen with a diamond-impregnated core drill.

Mechanical tests were performed on a servo-hydraulic test frame equipped with hydraulically-actuated wedge grips. Using the test method for reversed cyclic loads described in Ref [7], the specimens were designed with 63.5 mm of unsupported length between the grips to allow damage to develop without the influence of anti-buckling supports. Quasi-static strength tests were performed in displacement control with a strain rate of .0004 sec<sup>-1</sup> measured over the gage length. Fully reversed (R = -1) cyclic loading was carried out with a load-controlled 10 Hz sinusoidal form.

---

<sup>2</sup> Positive ply angles are measured clockwise from the longitudinal loading axis.

<sup>3</sup> All original measurements were recorded in U.S. customary units.

Load levels for the two laminates were chosen such that the specimens failed between approximately 5K and 20K cycles.

An effective secant stiffness of the specimen was monitored with a 25.4-mm extensometer centered on the notch, as previously described in Ref [8]. During the fatigue lifetime of several specimens cycled at a given load level, periodic monitoring of stiffness and the examination of penetrant-enhanced X-ray radiographs enables the identification of an approximate relationship between stiffness and damage state (and, thereby, the fraction of life consumed), both of which follow generally reproducible patterns [7,8]. For consistency, radiographs included in this paper are all of the "front side" of the specimens, as per the ply-angle notation described earlier.<sup>2</sup>

The approach taken to document the influence of damage on the strain distribution in and residual strength of notched laminates at a particular load level is: a) cycle four specimens to failure, with periodic interruptions for stiffness measurement and X-ray radiography, to establish typical stiffness response and damage accumulation data throughout life; b) via stiffness measurement and radiography, choose three points in the fatigue lifetime where stress redistribution and residual strength data are desired (these points turned out to be approximately 15, 70 and 90 percent of life for the quasi-isotropic laminate, and 10, 50 and 90 percent of life for the orthotropic laminate); c) cycle two additional specimens to each selected point in the fatigue lifetime, based on stiffness change and radiographs; d) with the photoelastic coating and isentropic thermal emission techniques, record the full-field strain measurements for each specimen described in step c; e) measure residual tensile and compressive strength at each selected point in the fatigue lifetime.

## *Full-Field Strain Measurement Techniques*

### **Photoelastic Coating**

The photoelastic coating technique is well known for its capability of revealing true surface strains of metallic components, and has been used successfully to measure the static and dynamic response of notched composite structures [3,9,10]. Detailed principles and procedures for the

photoelastic coating technique are given in Refs // and /2. Briefly, photoelastic coating materials are optically homogeneous when unstressed, and optically heterogeneous when stressed. That is, the index of refraction of the coating is a function of the strain induced by the external load. When polarized light enters the coating, the light vector splits into two polarized waves, which then proceed in the directions of the principal strains at a particular point. Since the index of refraction is different in the two directions, a relative retardation is formed, which forces the two waves to be out of phase when they emerge from the coating. Therefore, all points having the same amount of principal strain difference will possess an equal relative retardation. A color fringe corresponding to those points can be viewed through a crossed reflection-type polariscope. Corrections on the order of the fringes are required when the mechanical reinforcement from the coating and the Poisson's ratio mismatch between the coating and the specimen are not negligible [//, /2].

A 1-mm-thick coating material with a reflective backing (PS-1, Photolastic Division, Measurement Group, Inc.) was machined to match the specimen width and hole size. To prevent interference with the grips, the coating length of 51 mm was slightly less than the unsupported length of the specimen. The coating was bonded to the specimen with PC-1 adhesive after the introduction of fatigue damage.

In the present investigation, no corrections to the fringe order were attempted. Instead, fringes measured in specimens with damage were compared to fringes in a virgin specimen under the same stress (102 MPa over the unnotched area). At various states of damage, fringe orders measured along sections of the specimen labeled *A-A'* and *C-C'* in Fig. 1 were plotted and compared.

### Isentropic Thermal Emission

Non-contact measurement of the isentropic (adiabatic, reversible) thermoelastic effect in materials as a means of determining the dynamic state of stress or strain during cyclic loading has recently been made feasible with the commercial availability of the SPATE 8000 (Stress Pattern Analysis by measurement of Thermal Emission) instrument by Ometron, Inc. Through infrared optics, a computer-controlled camera measures (with a resolution of .001°C) the minute change in surface temperature occurring at the same frequency as the applied sinusoidal load. The camera scans the

specimen in a raster-like manner, with each measurement point representing an average temperature change in a circle of approximately .5-mm-diameter. The only specimen preparation required is a thin coating of flat black paint for maximum emissivity. Provided adiabatic and reversible deformations are maintained, the measured temperature change can be related to the state of strain in the material.

The theory linking temperature change with isentropic deformations of elastic matter was established by Thomson in 1857 [13]. Biot later expressed the relationship for homogeneous anisotropic materials as (summation implied over repeated indices)

$$T - T_0 = - \frac{T_0}{c_e} \alpha_{kl} C_{ijkl} \epsilon_{ij}$$

where  $T_0$  and  $T$  are the temperatures of the material before and after deformation,  $c_e$  is the specific heat at constant strain,  $\alpha_{kl}$  are components of the thermal expansion tensor,  $C_{ijkl}$  are components of the isothermal elastic modulus tensor, and  $\epsilon_{ij}$  are components of the strain tensor [14]. Thus, a negative temperature change occurs during positive dilatation of an orthotropic material with positive thermal expansion coefficients. A simplified relationship between the plane-stress, isentropic strains in a heterogeneous, orthotropic material, such as a graphite/epoxy lamina, and the attendant temperature change measured in the laboratory is obtained through consideration of the nonhomogeneous strains and temperature changes of the microconstituents (i.e. fibers and matrix). The result can be represented by an equation of the form

$$T - T_0 = K_1 \epsilon_1 + K_2 \epsilon_2 \quad (1)$$

where  $T_0$  and  $T$  are now the average, effective temperatures of the material before and after deformation,  $K_1$  and  $K_2$  are material constants involving the initial temperature, thermomechanical properties, and volume fraction of each microconstituent, and  $\epsilon_1$  and  $\epsilon_2$  are the in-plane strain components derived from the theory of anisotropic plates [15]. Since a typical graphite/epoxy lamina has a very small (or slightly negative) thermal expansion coefficient parallel to the fibers ( $\alpha_{11}$ ), a relatively small temperature change results from uniaxial loads in the fiber direction. On the other hand, a very large temperature decrease results from transverse tension in the lamina due to the large, positive transverse thermal expansion coefficient ( $\alpha_{22}$ ).

The accuracy of strain measurements via infrared thermal emission measurements has been previously verified for isotropic, homogeneous materials [16], but not for anisotropic, laminated, composite materials. Therefore, the technique and related analytical tools are still under development. The advantage of the technique is that it is an entirely non-contact, nondestructive evaluation tool. A limitation is the unknown amount of dissipative versus isentropic temperature change. Furthermore, it is difficult to isolate the separate components of strain from a single measured temperature change when the local deformations are influenced by changing elastic properties and boundary conditions. These factors restrict the thermal emission data to qualitative analyses of strain distributions, at present.

In the series of thermal emission measurements, all specimens of similar stacking sequence were cycled at the same, reduced stress limits, which were selected such that negligible damage development occurs during the scanning process. The stress limits for the quasi-isotropic and orthotropic specimens were 2.6 to 104.7 MPa and 2.6 to 130.2 MPa, respectively. The entire gage length of the specimen was scanned on both the front and back sides. Full-field color contour maps of the temperature change were photographed on the system monitor screen. In the included illustrations, the color scale is uncalibrated, but is directly proportional (including sign) to the difference  $T_0 - T$ , where  $T_0$  and  $T$  are the instantaneous surface temperatures at the minimum and maximum loads, respectively.

## *Results and Discussion*

### **Quasi-Static Properties and Fatigue Life**

Tensile and compressive quasi-static strengths and secant (zero to maximum cyclic load excursions) stiffnesses for the notched specimens are given in Tables 1 and 2, where stress has been computed over the gross (unnotched) cross-sectional area, and strain has been measured across the notch. Both laminates are stiffer and weaker in tension than in compression.

To achieve fatigue lives on the order of 5K to 20K cycles, stress levels of  $\pm 203$  MPa and  $\pm 305$  MPa were chosen for the quasi-isotropic and orthotropic laminates, respectively. All specimens tested at these load levels failed in a compressive mode due to unstable delamination growth in the ligament of material between the notch and straight edge.

## Fatigue Damage Initiation and Growth

Fatigue damage in the  $(0/45/90/-45)_{s4}$  laminate initiates at the notch with matrix cracking in all plies by the first or second load cycle, followed shortly by delaminations of the 0/45, 45/90 and 90/-45 interfaces in regions of dense matrix cracks (Fig. 2a). Delaminations form earliest and grow fastest at interfaces closest to the surface. In situations where delaminations have not yet formed between the surface 0-deg. ply and the underlying +45-deg. ply near the notch, short (up to 2 mm long), piecewise-linear ply fractures in the 0-deg. ply form sequentially in a stepwise manner along the direction of an underlying +45-deg. matrix crack (Fig. 3a). The 0-deg. ply fractures serve as a catalyst for cracking in the 0-deg. ply and for delamination of the associated 0/45 interface. This mode of damage is primarily a surface effect, although it occasionally develops in interior plies near the end of life. The damage growth rate is slowest between the tenth and ninetieth percentiles of life. Figure 2b illustrates the characteristic X-shaped pattern of damaged material at an estimated 70 percent of fatigue life. The damage condition in Specimen 2-3 near the end of life (Fig. 2c) is atypical in that it closely resembles the earlier damage state in Specimen 3-2. More frequently, delaminations will extend across the entire width of the specimen at the end of life. In Specimen 2-3, however, local fracture of the surface 0-deg. plies near the notch, as in Fig. 3a, was sufficient to cause the precipitous loss of compressive stiffness that precedes specimen failure.

Fatigue damage initiation in the  $(0/45/0/-45)_{s4}$  laminate is dominated by 0-deg. matrix cracks tangent to the notch (Fig. 4a). The cracks initiate symmetrically in all four quadrants, but grow fastest in the upper-left and lower-right quadrants. This behavior is attributed to an interaction of the 0-deg. matrix cracks and adjacent paths of ply fractures in the +45-deg. plies following those cracks only in the upper-left and lower-right quadrants (Fig. 3b). The -45<sub>2</sub> ply groups do not display this mode of damage. Staircase-type fractures of the 0-deg. plies, as in Fig. 3a, always grow away from the notch along the +45-deg. direction. As in the quasi-isotropic laminate, this is primarily

a surface effect, although large 0-deg. ply breaks have been noted to pass through the adjacent 45-deg. ply and into the next 0-deg. ply. Matrix cracks in the off-axis plies are concentrated along the length of the 0-deg. cracks during the early stages of damage accumulation. At approximately half of fatigue life, delaminations at interfaces involving the -45<sub>2</sub> ply groups have grown away from the notch and along the 0-deg. matrix cracks tangent to the notch (Fig. 4b). Much of the new damage growth after this point in fatigue life is associated with the tips of the large 0-deg. matrix cracks. At impending laminate failure, delaminations typically extend across the width of the specimen, resulting in a large stiffness loss and a compressive mode of failure (Fig. 4c). Much of the delaminated area visible in Fig. 4c is due to the 0/45 interface delaminations associated with several fracture paths in the surface plies.

## Residual Stiffness and Strength

Residual properties for six quasi-isotropic specimens at various stages of fatigue life are given in Table 3. X-ray radiographs of specimens used in the residual tension tests were seen previously in Fig. 2. A typical plot of tensile and compressive stiffnesses during the fatigue lifetime, normalized to their respective values on the first load cycle, is given in Fig. 5a. There is an initial loss of tensile and compressive stiffness during the first 10 percent of life, corresponding to a rapid increase in the tensile strength and a rapid decrease in the compressive strength. During the middle 80 percent of fatigue life, the rate of stiffness change slows markedly. Neither tensile nor compressive strength change appreciably during this period. At impending laminate failure, tensile and compressive stiffnesses decline sharply, as do both components of strength. Residual tensile strength at impending failure is noted to be below the average tensile strength of virgin specimens. As evidenced by the residual compressive strength data and post-failure fractography, fatigue failure of the specimen occurs during the compressive portion of the load cycle. The relatively high stiffness values indicated for Specimen 2-2 reflect the nonsymmetrical distribution of damage through the thickness. In this case, the side of specimen where the extensometer was attached experienced much less strain than the opposite side, due to out-of-plane deflection in the gage length. Although in Table 3 the stiffness degradation in tension generally exceeds that in compression, results from other fatigue

tests at the same load level indicate that this is not always true. The rates of change of stiffness and strength were noted to correlate with the damage growth rate.

Residual properties for orthotropic specimens at three stages of fatigue life are given in Table 4, and a typical normalized stiffness response during the fatigue lifetime is shown graphically in Fig. 5b. X-ray radiographs of residual tension test specimens were seen previously in Fig. 3. Stiffness response of this laminate differs from that of the quasi-isotropic laminate in that there is a more uniform degradation throughout fatigue life, and a slightly greater cumulative change at failure. Tensile stiffness change generally exceeds compressive stiffness change throughout fatigue life. Up to approximately 50 percent of life, tensile strength is noted to increase more than in the quasi-isotropic laminate, while compressive strength remains nearly equal to virgin specimen values. During the last 10 percent of fatigue life, when surface 0-deg. ply fractures and delaminations are the primary modes of damage growth, both components of strength decrease until the compressive strength reaches the applied cyclic load amplitude. The residual tensile strength near the end of life is still greater than that of virgin specimens. With increasing amounts of fatigue damage, the tensile fracture path frequently was offset from the transverse centerline through the hole.

## Strain Redistribution

Full field measurements of isochromatic fringes and thermal emission in all of the specimens of Tables 3 and 4 were recorded, in many cases on both front and back surfaces. For brevity, only three images will be included here: a virgin specimen; a middle-life specimen; and a late-life specimen. In all cases except the virgin specimens, the photoelastic data were obtained on the same side of the specimen as the thermographic data. Hence, the sensitivity of the two techniques to damage can be evaluated directly.

### *Isochromatic Fringe Measurements*

Figure 6 illustrates the isochromatic fringe patterns in three quasi-isotropic specimens with sequential states of fatigue damage. The middle- and late-life radiographs were seen previously in Fig. 2. Due to increased compliance in the region of intense matrix cracks and delamination adja-



cent to the notch, higher fringe orders appear on the photoelastic coating directly over the damage zone. The existence of increased fringe orders in the region surrounding the damage zone indicates that a larger proportion of the load is being carried by the undamaged material. As damage grows away from the notch in the transverse direction, regions of high fringe order move toward the straight edges of the specimen. This phenomenon is most prominent at the tips of the 0-deg matrix cracks bounding the near-surface 0/45 delamination. Figures 7a and 8a quantify this effect along sections *A-A'* and *C-C'* of the specimen, respectively. Along section *A-A'*, the increase in remote strain near the straight edges is most evident in the late-life specimen. Fringe orders along section *A-A'* are affected by the growing areas of lightly loaded material directly above and below the notch. The slight asymmetry in Fig. 6c is the result of a short fracture path in the back-surface 0-deg. ply directly under the coating, on the left side of the illustration.

In the orthotropic laminate, the fringe patterns become antisymmetric about the load axis after the appearance of damage (Fig. 9). This response is attributed to the antisymmetric distribution of damage seen previously in the X-ray radiographs of Fig. 3. High fringe orders are induced across the 0-deg. matrix cracks extending tangentially from the notch in the upper-left and lower-right quadrants due to high shear deformation across the crack. A more uniform distribution of fringes evolves in the load-bearing ligaments of material isolated by the 0-deg. cracks. The regions of uniform fringe distribution directly above and below the notch have a larger area than the corresponding regions in the quasi-isotropic laminate. Plotting fringe orders along section *A-A'* reveals the quantitative strain distribution (Fig. 7b). In the mid-life specimen, a short line of 0-deg. ply fracture to the left of the notch causes a strong, local concentration of strain in the coating (Fig. 9b). At the late state of damage, fringes along section *C-C'* are relatively uniform due to the absence of 0-deg. ply fracture on the front surface (Fig. 8b). A delamination between the surface 0-deg. ply and the underlying 45-deg. ply caused by 0-deg. ply fracture in the lower-right quadrant near the end of life results in greatly reduced fringe order in the unloaded area (Fig. 9c).

### ***Thermal Emission Measurements***

Thermographs of (0/45/90/-45)<sub>s4</sub> specimens with sequential states of damage development are shown in Fig. 10. The outstanding feature of the series is the growth of a region of near-zero ther-

mal emission around the notch. Considering the thermoelastic relation of Eq 1, the decreased temperature change can be caused by strain or stress relaxation in the surface ply via 0-deg. ply fracture and delamination, as in Fig. 3a. In the corresponding radiographs of Fig. 2, it is apparent that the low thermal emission region encompasses the delaminated area under the surface ply. As surface ply delaminations grow in the transverse direction, the "hot spots" originally located adjacent to the notch shift immediately ahead of the delaminations (Fig. 11a), reflecting the redistribution of strain around the damage zones. The highest magnitude of temperature change in each thermograph, normalized to the remote value, varied from 2.8 in the undamaged specimen to 2.1 and 2.5 in the middle- and late-life specimens, respectively. In an inverse manner, the trend in maximum temperature change agrees with the trend of increasing then decreasing residual tensile strength during fatigue life. Furthermore, the specimens shown in Figs. 2 and 10 failed in tension along the transverse section of the laminate that includes the notch and the hot spots. Hence, the region of high temperature change coincides with the region that is involved in the tensile fracture event, and the magnitude of the temperature change in those regions correlates well with the fracture load. In conjunction with radiographs, thermographs provide an understanding of the effects of damage on the stress distribution that was heretofore unavailable with radiographs alone. For example, 0-deg. ply fractures near the notch on the back side of specimen 2-3 are visible to the discerning eye in Fig. 2c, but, given the overall similarity of Figs. 2b and 2c, it is not obvious that there would be a significant difference in residual strength. However, one may suspect such a strength change by noticing the differences in the corresponding thermographs of Figs. 10b and 10c.

Due to the high Poisson's ratio of the (0/45/0/-45)<sub>s4</sub> laminate, the far-field temperature change is very close to zero. Thermographs of virgin, middle-life, and late-life orthotropic specimens indicate the severity of stress redistribution in the gage length (Fig. 12). In this laminate, the hot spots initially adjacent to the notch generally shift in the load direction, close behind the tips of the 0-deg. matrix cracks tangent to the notch. Figure 11b illustrates the movement of the hot spot away from the notch along profile C-C'. The effect is most noticeable in the lower-right quadrant of Fig. 12b, and in the upper-left quadrant of Fig. 12c. It is in these two quadrants that much of the middle and late life fatigue damage growth occurs. As in the quasi-isotropic laminate, the fracture path seen in residual tension tests frequently passes through, or at least near, these hot spots. The maximum, unscaled temperature changes seen in the virgin, middle-life, and late-life specimens of Fig. 12 were

500, 430, and 475, respectively, which correlate in an inverse manner to the corresponding values of residual tensile strength.

## *Summary and Conclusions*

### **Damage**

In both laminates, there exist matrix cracks parallel to the fibers in all plies, delamination between plies of differing orientation, and macroscopic concentrations of fiber fracture extending through the thickness of a lamina (local ply fracture). Damage in both cases initiates along the hole boundary in the form of matrix cracking, followed by delamination. Short, 0-deg. ply fractures served as sites for delamination initiation away from the hole boundary. The different patterns of matrix cracking and delamination in the two laminates can be attributed to the directional nature of damage growth caused by the interaction of damage in adjacent plies. For example, the lack of 90-deg. plies and the abundance of 0-deg. plies in the orthotropic laminate resulted in a routing of damage longitudinally along paths tangent to the notch, rather than along the transverse centerline, as in the quasi-isotropic laminate.

### **Residual Stiffness and Strength**

Tensile and compressive stiffness degradation rates in the orthotropic material were more uniform over the fatigue lifetime than in the quasi-isotropic material, where the rates were highest at the beginning and end of life. Tensile stiffness degraded faster than compressive stiffness in the orthotropic laminate. Residual compressive strength of the quasi-isotropic laminate degraded quickly early in life, and again at the end of life, causing a compressive mode of failure under the reversed cyclic loads. The orthotropic laminate also failed in compression, but the compressive residual strength did not degrade significantly until near the end of life. Until late in the fatigue lifetime of both laminates, residual tensile strengths increased to values above those for virgin specimens. At impending failure, residual tensile strength degraded in both laminates, but not sufficiently to induce a tensile failure mode.

## Photoelastic Coating

The isochromatic fringe patterns measured with the photoelastic coating technique at various points in the fatigue lifetime provide an understanding of strain redistribution in the presence of damage. In the quasi-isotropic laminate, damage zones near the notch were indicated by extremely high fringe orders. Zones of high fringe order in the undamaged material shifted toward the straight edge of the specimen as delaminations grew away from the notch, reflecting the damage-induced redistribution of load. In the orthotropic laminate, the long 0-deg. matrix cracks tangent to the hole resulted in a line of concentrated fringes along the cracks and a more uniform strain field in undamaged ligaments of material adjacent to the notch. This result is attributable to the lack of shear load transfer capability across the 0-deg. matrix cracks tangent to the hole. In situations where fractures in the surface ply grew transversely to the notch (accompanied by delamination of the surface ply), high fringe orders resulted over the fracture path, and low fringe orders resulted over the unloaded lamina. In both laminates, fringe orders increased in the remaining load-bearing material after the formation of fatigue damage near the notch. Fringe orders decreased in the regions above and below the notch, reflecting the relaxation of strain there. Overall, more strain redistribution was seen in the orthotropic laminate than in the quasi-isotropic laminate due to the more complete reduction of the notch effect by the damage. The greater increase in residual tensile strength of the orthotropic laminate supports this observation.

## Thermal Emission

Full-field strain distribution data near the notch measured with the isentropic thermal emission technique provides valuable insight into the nature of load redistribution in the presence of damage, especially when used in conjunction with X-ray radiography. The damage mechanisms that cause increased strains and, hence, increased thermal emission in some region of the laminate are likely to cause that same region to be involved in damage growth, and, eventually, the tensile fracture process. Measurements indicated that regions of high thermal emission shifted to remain in front of growing damage zones. In the quasi-isotropic laminate, the critical zones of high thermal emission shifted away from the notch along a transverse direction, just ahead of the 0/45-interface de-

laminations under the surface ply. In the orthotropic laminate, the critical zones shifted along the 0-deg. matrix cracks tangent to the hole. The increase and decrease of temperature change measured in the critical zones corresponded well with the increase and decrease of residual tensile strength of the specimens. Regions of high thermal emission were frequently part of the tensile fracture surface. In both laminates, there is no correlation between the amplitude of thermal emission and the residual compressive strength, which can be attributed to a dependence of residual compressive strength on the size and distribution of delaminations, and their effect on the stability of the notched laminates, rather than on the notch effect itself. The thermographs, however, do indicate delamination growth, and therefore can be used to indicate a potential loss of compressive strength. In contrast with the photoelastic data, the thermographic measurements indicated little deformation near fracture paths in the surface plies. This is due to the sensitivity of thermal emission to actual surface material deformation, rather than to a coating deformation.

## General

Significant relations between fatigue damage and the concomitant changes in residual stiffness, residual strength and strain distribution in two notched laminates have been presented. In particular, the associations existing between the residual tensile strength and the distribution and magnitude of strains measured with the photoelastic coating and isentropic thermography techniques were quite encouraging, and should be investigated further.

**Acknowledgement:** The authors wish to acknowledge the support of the Air Force Office of Scientific Research through contract No. 85.0087.

## References

1. Highsmith, A. L. and Reifsnider, K. L. in *Composite Materials: Fatigue and Fracture*, ASTM STP 907, H. T. Hahn, Ed., American Society for Testing and Materials, Philadelphia, 1986, pp. 233-251.

2. Highsmith, A. L. and Reifsnider, K. L. in *Fracture of Fibrous Composites*, AMD Vol. 74, C. T. Herakovich, Ed., American Society of Mechanical Engineers, New York, 1985, pp. 71-87.
3. Daniel, I. M., *Experimental Mechanics*, **25**, No. 12 (Dec. 1985), pp. 413-420.
4. Kress, G. R. and Stinchcomb, W. W. in *Recent Advances in Composites in the United States and Japan*, ASTM STP 864, J. R. Vinson and M. Taya Eds., American Society for Testing and Materials, Philadelphia, 1985, pp.173-196.
5. Sandhu, R. S., Gallo, R. L., and Sendekyj, G. P. in *Composite Materials: Testing and Design (Sixth Conference)*, ASTM STP 787, I. M. Daniel, Ed., American Society for Testing and Materials, Philadelphia, 1982, pp. 163-182.
6. Irvine, T. B. and Ginty, C. A., *J. Composite Materials*, **20** (March 1986), pp. 166-184.
7. Bakis, C. E., Simonds, R. A., and Stinchcomb, W. W., "A Test Method to Measure the Response of Composite Materials Under Reversed Cyclic Loads," presented at the Second ASTM Symposium on Test Methods and Design Allowables for Fiber Composites, Phoenix AZ, November 3-4, 1986.
8. Bakis, C. E. and Stinchcomb, W. W. in *Composite Materials: Fatigue and Fracture*, ASTM STP 907, H. T. Hahn, Ed., American Society for Testing and Materials, Philadelphia, 1986, pp. 314-334.
9. Kawata, K., Takeda, N. and Hashimoto, S., *Experimental Mechanics*, **24**, No. 12 (Dec. 1984), pp. 316-327.
10. Daniel, I. M., Rowlands, R. E. and Whiteside, J. B. in *Analysis of the Test Methods for High Modulus Fibers and Composites*, ASTM STP 521, American Society for Testing and Materials, Philadelphia, 1973, pp. 143-164.
11. Zandman, F., Render, S. and Dalley, J. W., *Photoelastic Coatings*, SESA Monograph 3, Society for Experimental Stress Analysis, Westport CT, 1977.

12. *Experimental Mechanics of Fiber Reinforced Composite Materials*, SESA Monograph 4, Society for Experimental Stress Analysis, Brookfield Center CT, 1982.
13. Thomson, Sir William, "On the Thermo-elastic and Thermo-magnetic Properties of Matter," *Q'tly. J. Mathematics*, 1 (Cambridge, 1857), pp. 57-77.
14. Biot, M. A., *J. Applied Physics*, 27, No. 3 (1956), pp. 240-253.
15. Bakis, C. E., Ph.D. Dissertation, Dept. of Engineering Science and Mechanics, VPI & SU, Blacksburg VA, 1987.
16. Stanley, P. and Chan, W. K., *J. Strain Analysis*, 20, No. 3 (1985), pp. 129-137.

### List of Figures

1. Schematic of notched specimen coordinate notation and identification of sections over which full-field data are plotted.
2. Front view radiographs of fatigue damage in quasi-isotropic specimens: *a)* Specimen 3-12 at 15% of life; *b)* Specimen 3-2 at 70% of life; *c)* Specimen 2-3 at 90% of life.
3. Schematic of typical ply fracture patterns and associated matrix cracks: *a)* 0-deg. ply fracture seen in the quasi-isotropic and orthotropic laminates; *b)* 45-deg. ply fracture seen in the orthotropic laminate.
4. Front view radiographs of fatigue damage in orthotropic specimens: *a)* Specimen 3-3 at 10% of life; *b)* Specimen 3-7 at 50% of life; *c)* Specimen 2-18 at 90% of life.
5. Typical normalized tensile and compressive stiffnesses during fatigue lifetime: *a)* quasi-isotropic specimen; *b)* orthotropic specimen.
6. Isochromatic fringe patterns in the photoelastic coating of quasi-isotropic specimens: *a)* Specimen 3-10 with no damage (front); *b)* Specimen 3-2 at 70% of life (front); *c)* Specimen 2-3 at 90% of life (rear).
7. Birefringence distributions along Section *A-A'*: *a)* quasi-isotropic specimens; *b)* orthotropic specimens.  $R_0$  = hole radius.
8. Birefringence distributions along Section *C-C'*: *a)* quasi-isotropic specimens; *b)* orthotropic specimens.  $R_0$  = hole radius.
9. Isochromatic fringe patterns in the photoelastic coating of orthotropic specimens: *a)* Specimen 2-11 with no damage (front); *b)* Specimen 3-7 at 50% of life (front); *c)* Specimen 2-18 at 90% of life (front).



10. Isentropic thermal emission patterns in quasi-isotropic specimens: *a)* Specimen 3-10 with no damage (rear); *b)* Specimen 3-2 at 70% of life (front); *c)* Specimen 2-3 at 90% of life (rear).
11. Isentropic thermal emission profiles: *a)* Section *B-B'* in quasi-isotropic specimens; *b)* Section *C-C'* in orthotropic specimens.  $R_0$  = hole radius.
12. Isentropic thermal emission patterns in orthotropic specimens: *a)* Specimen 2-11 with no damage (rear); *b)* Specimen 3-7 at 50% of life (front); *c)* Specimen 2-18 at 90% of life (front).

Table 1 — Effective secant stiffness of virgin center-notched AS4/1808 laminates measured during the first fatigue cycle.

Stacking Sequence	Tensile Stiffness, GPa				Compressive Stiffness, GPa			
	qty.	min.	max.	mean	qty.	min.	max.	mean
(0/45/90/-45) <sub>s4</sub>	9	30.4	32.3	31.0	9	27.1	29.9	28.4
(0/45/0/-45) <sub>s4</sub>	12	41.3	44.8	42.8	12	36.1	39.1	37.6

Table 2 — Strength of virgin center-notched AS4/1808 laminates.

Stacking Sequence	Tensile Strength, MPa				Compressive Strength, MPa			
	qty.	min.	max.	mean	qty.	min.	max.	mean
(0/45/90/-45) <sub>s4</sub>	3	265	275	272	3	-304	-318	-312
(0/45/0/-45) <sub>s4</sub>	3	354	392	373	3	-373	-394	-381

Table 3 — Center-notched (0/45/90/-45)<sub>ss</sub> AS4/1808 laminate residual properties under fully-reversed fatigue at 203 MPa.

Specimen I.D.	Approx. % of Life	No. Cycles	Stiffness*		Strength*	
			$E_t$	$E_c$	$S_t$	$S_c$
3-12	15	1305	.93	.96	1.11	—
2-1	15	904	.94	.92	—	.839
3-2	70	9240	.85	.92	1.19	—
3-14	70	9400	.85	.89	—	.896
2-3	90	11024	.67	.73	.883	—
2-2	90	8800	.82	1.14	—	.628

\* Normalized to values for virgin specimens.

Table 4 — Center-notched (0/45/0/-45)<sub>ss</sub> AS4/1808 laminate residual properties under fully-reversed fatigue at 305 MPa.

Specimen I.D.	Approx. % of Life	No. Cycles	Stiffness*		Strength*	
			$E_t$	$E_c$	$S_t$	$S_c$
3-3	10	250	.94	.92	1.16	—
3-5	10	350	.94	.94	—	1.04
3-7	50	3708	.79	.77	1.42	—
3-9	50	6570	.79	.87	—	1.02
2-18	90	10460	.67	.76	1.10	—
4-7	90	5760	.66	.73	—	.884

\* Normalized to values for virgin specimens.

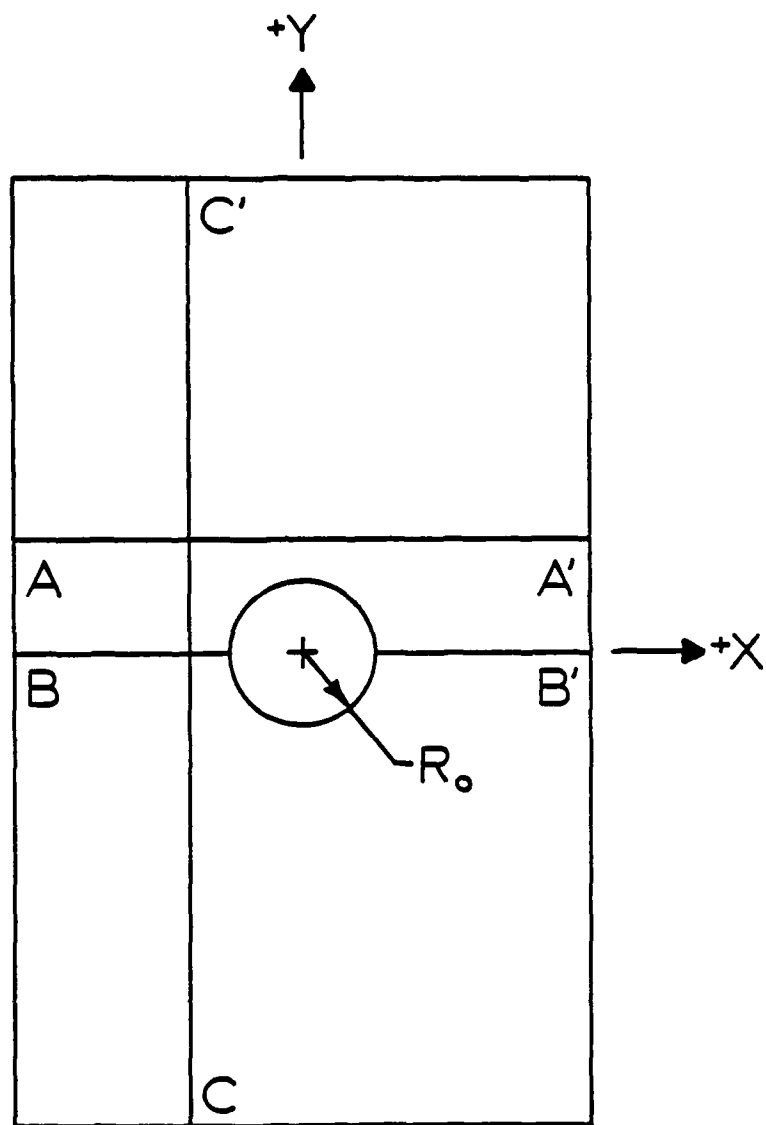
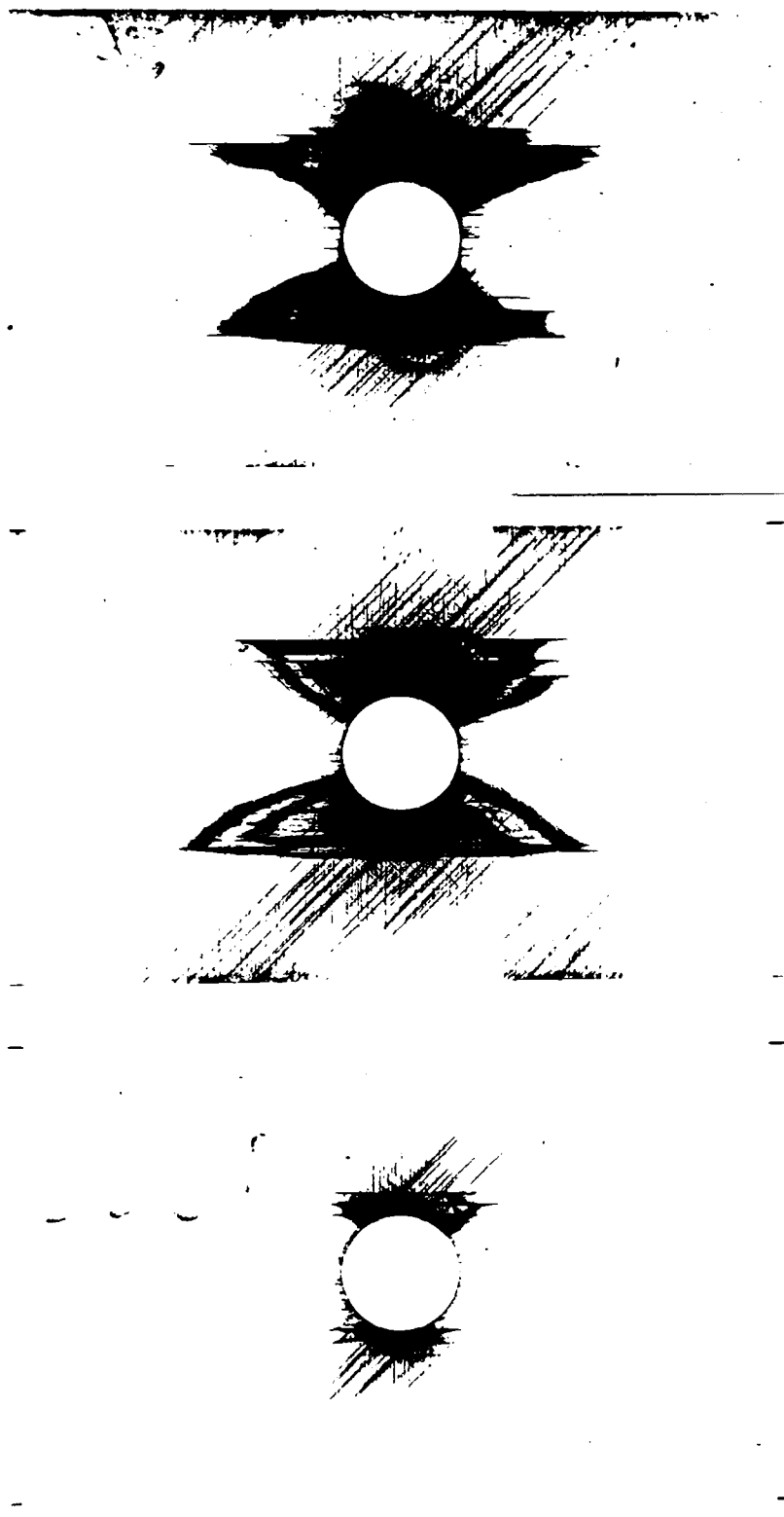


Fig. 1

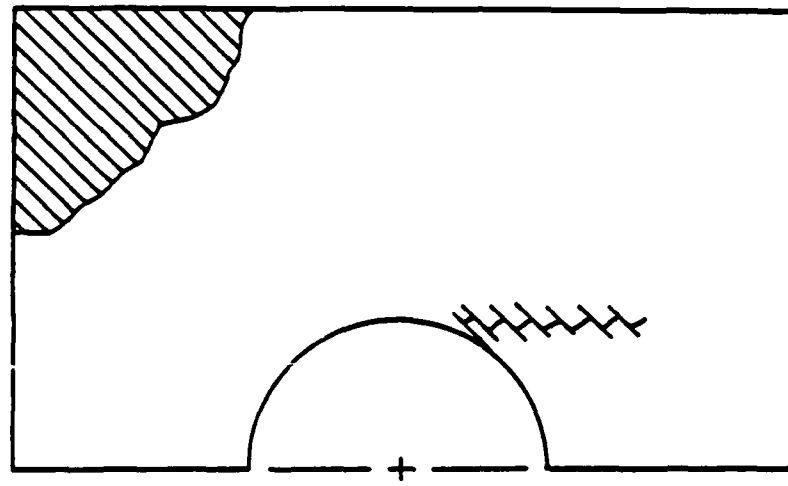


(c)

(b)

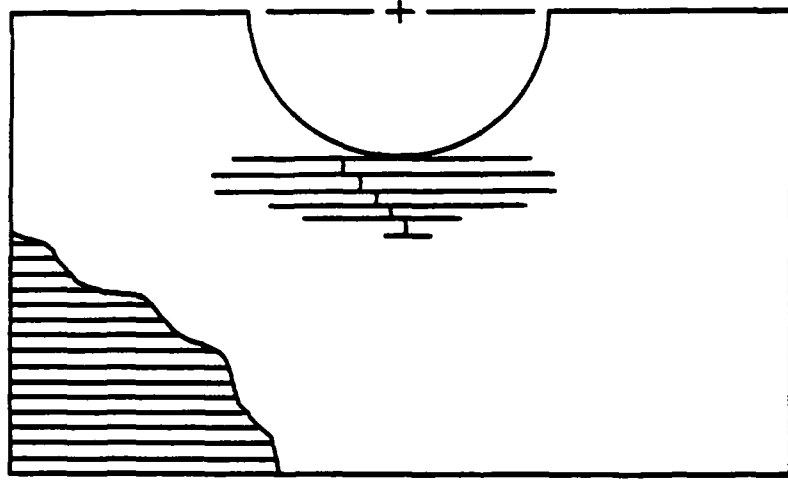
(a)

Fig. 2



(b)

←  
LOAD  
→

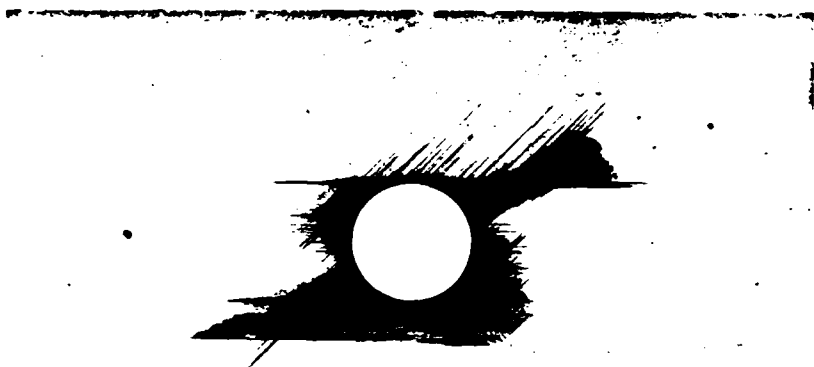


(a)

Fig. 3



(c)



(b)



(a)

Fig. 4

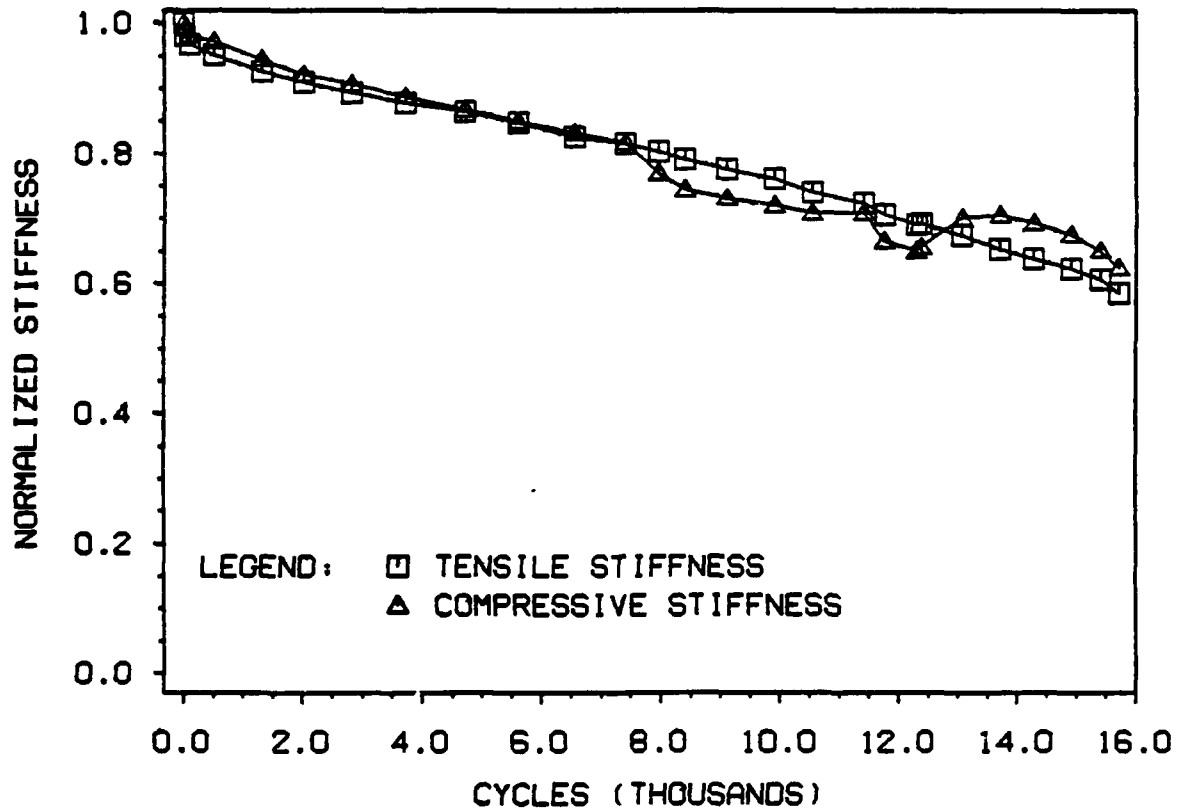
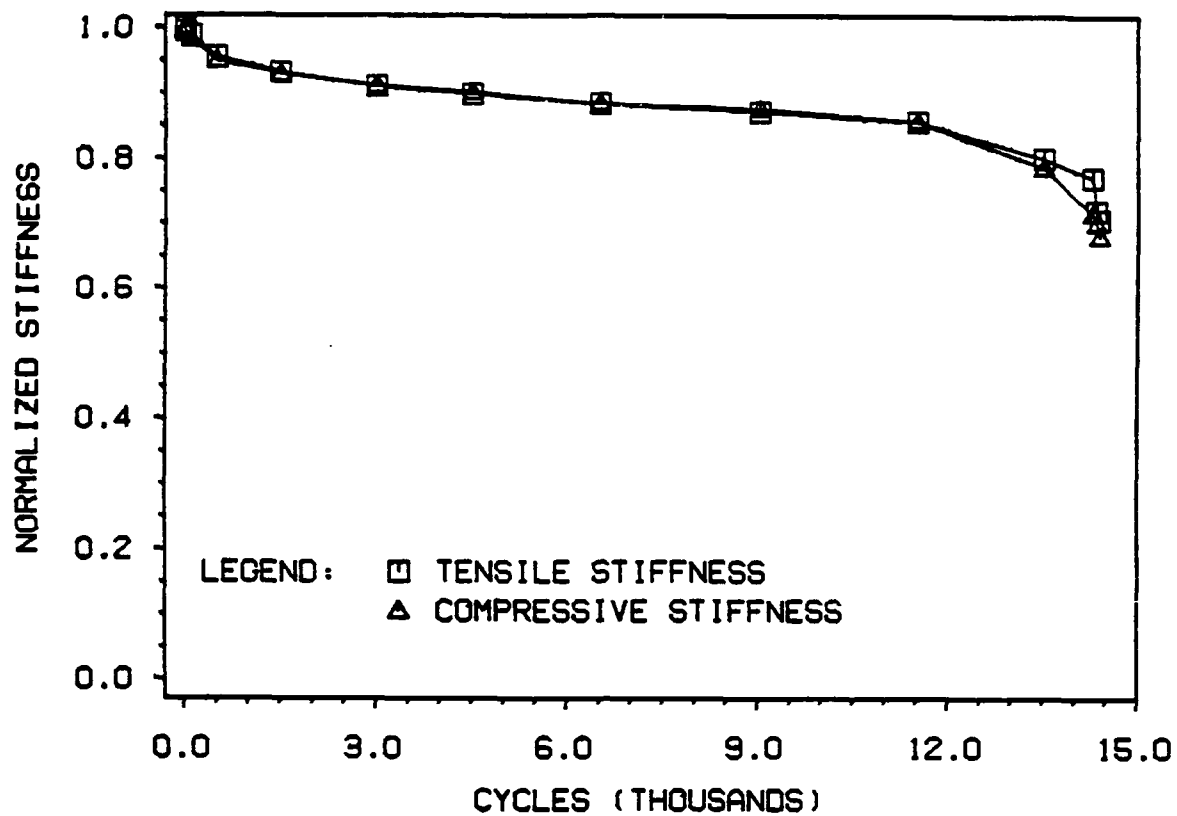
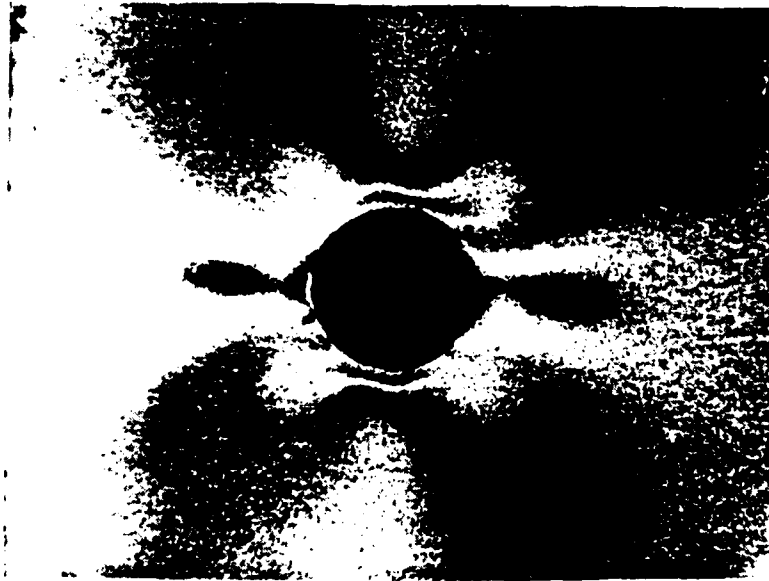


Fig. 5

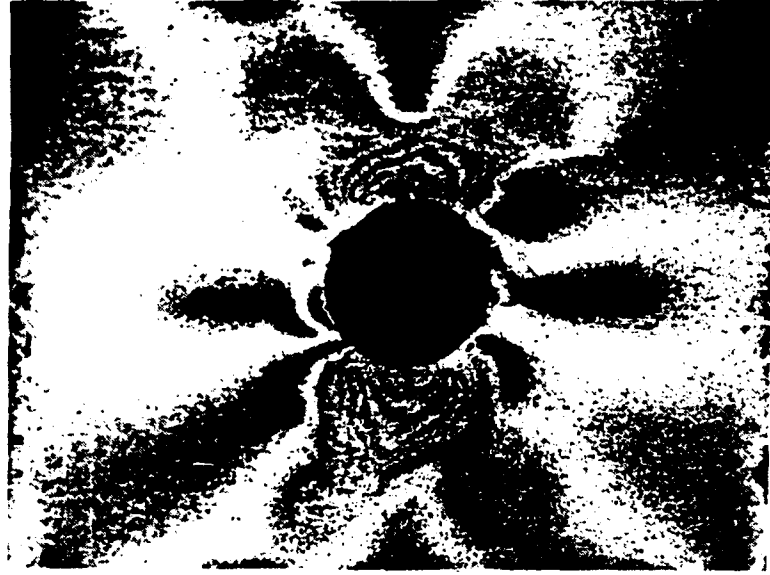




(a)



(b)



(c)

Fig. 6

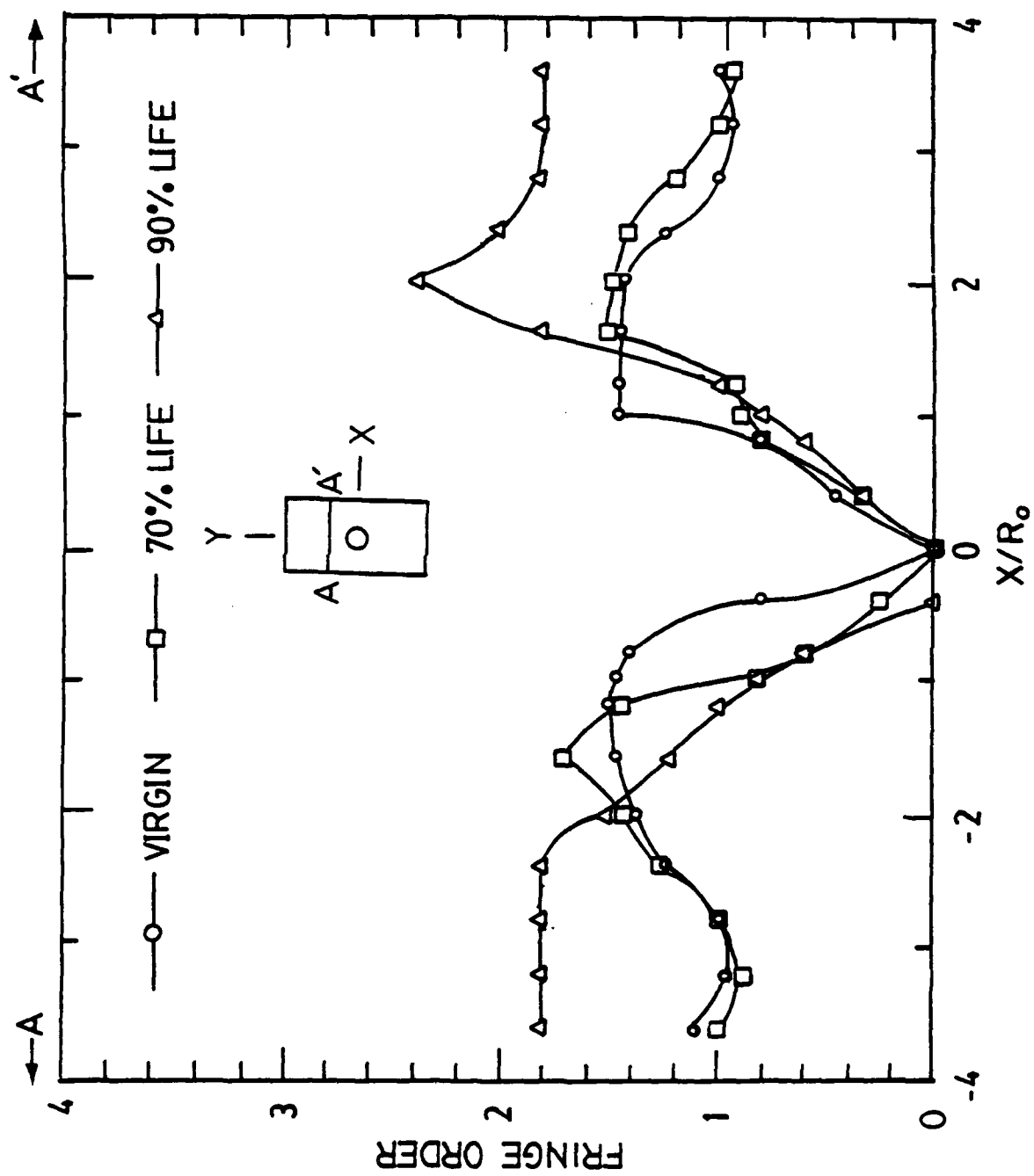


Fig. 7 (a)

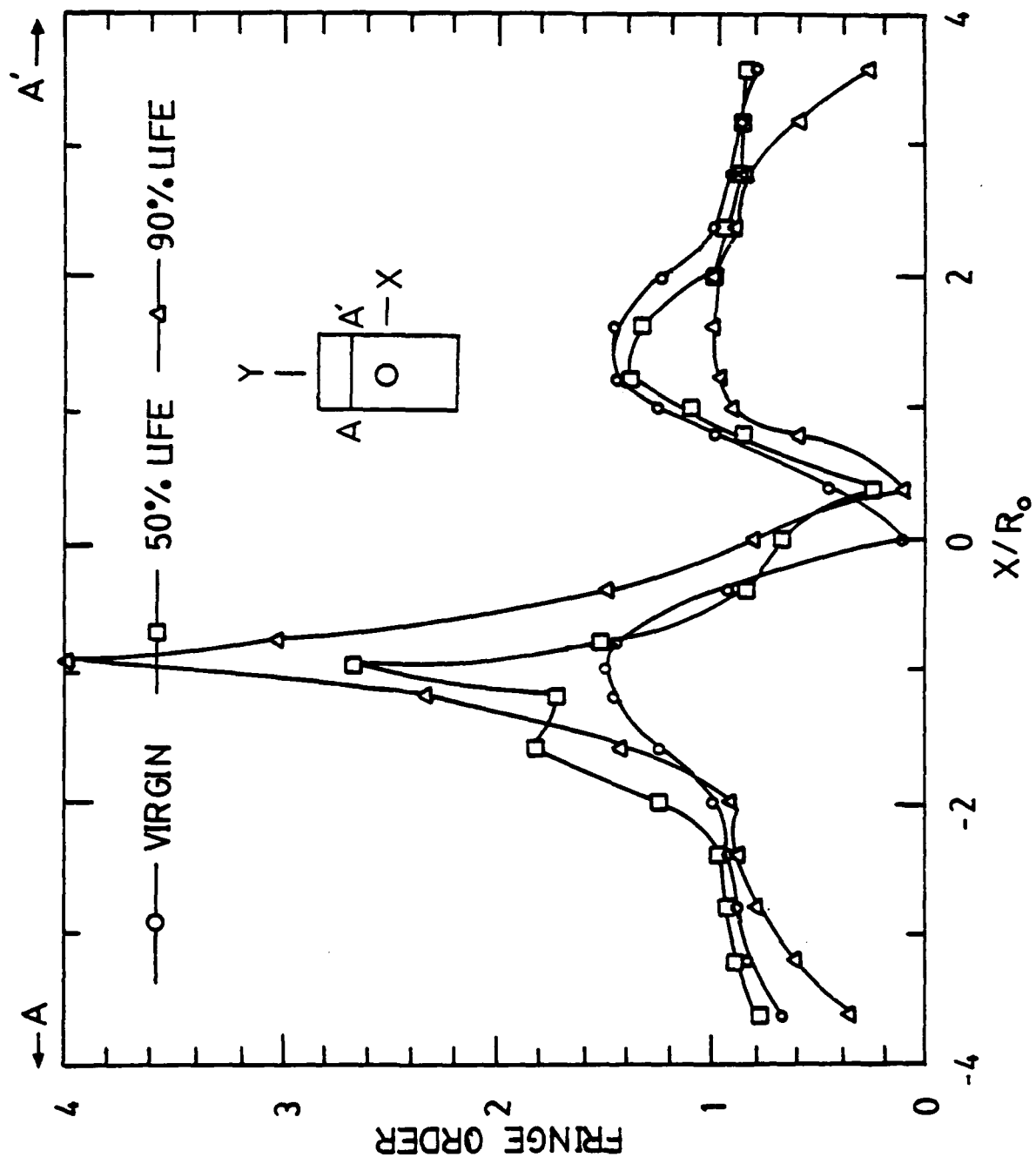


Fig. 7 (b)

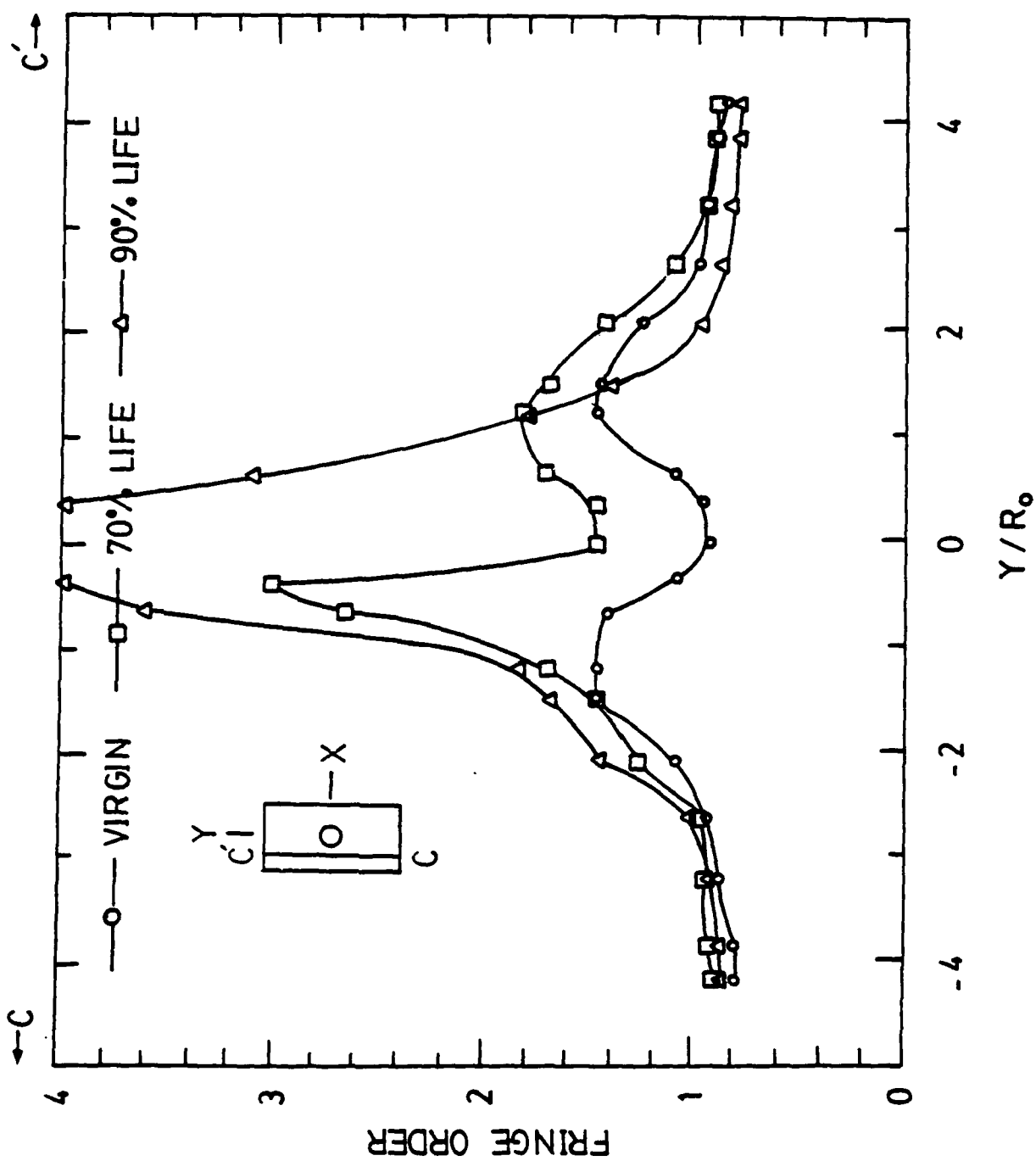


Fig. 8(a)

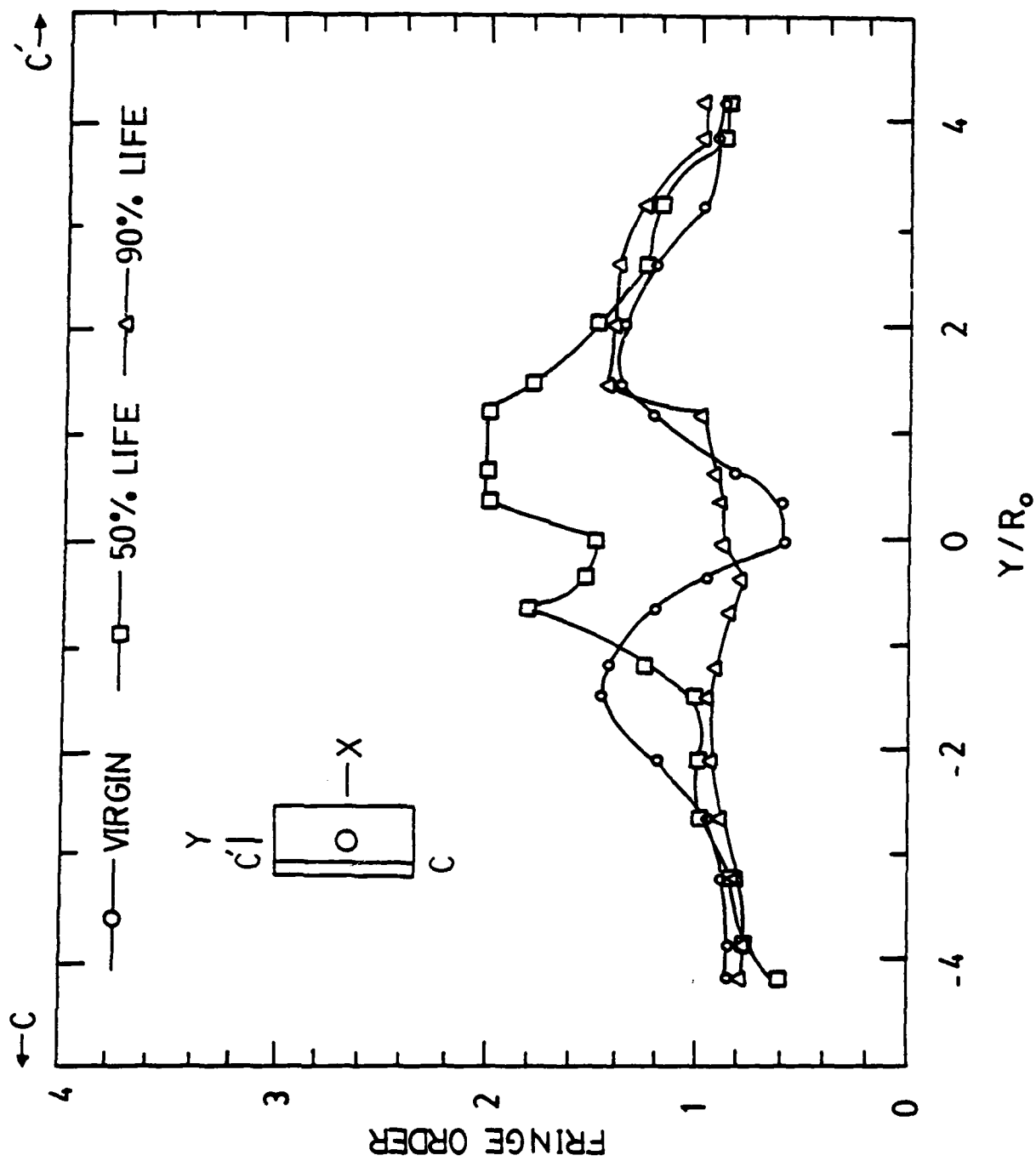
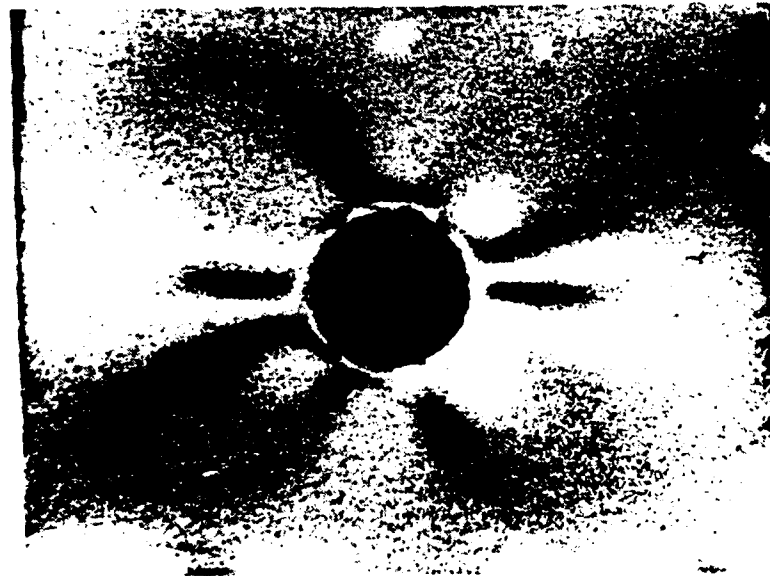


Fig. 8(b)



(a)

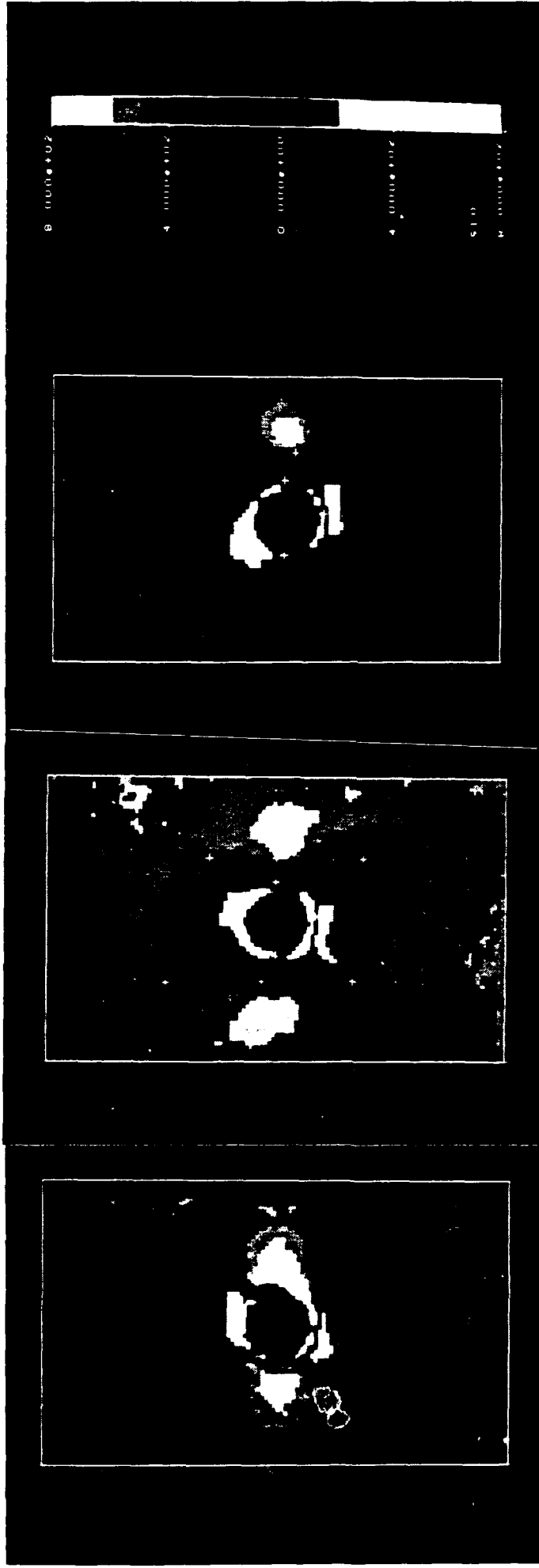


(b)



(c)

Fig. 9



(a)

(b)

(c)

Fig. 10

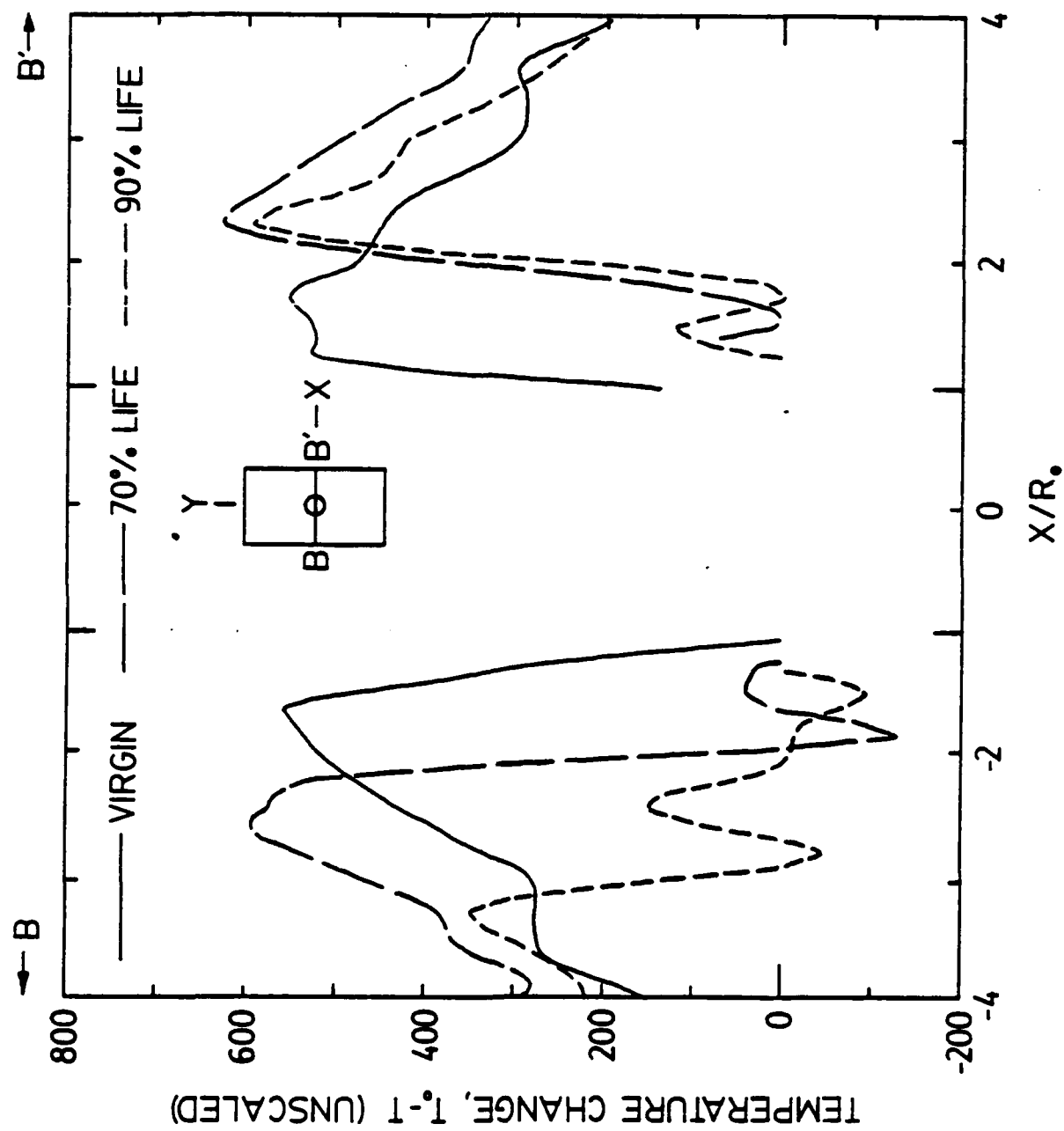


Fig. 11(a)



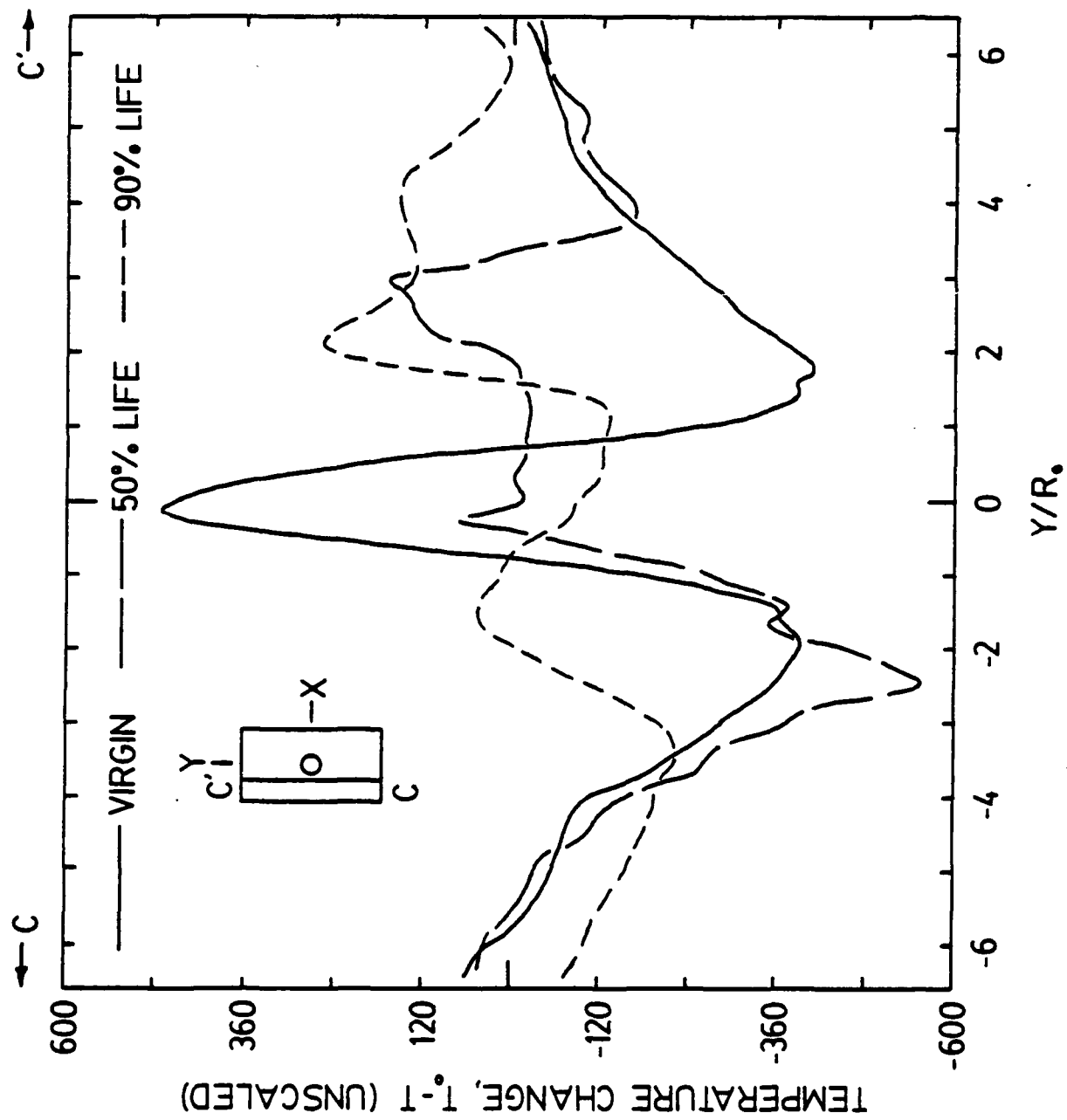
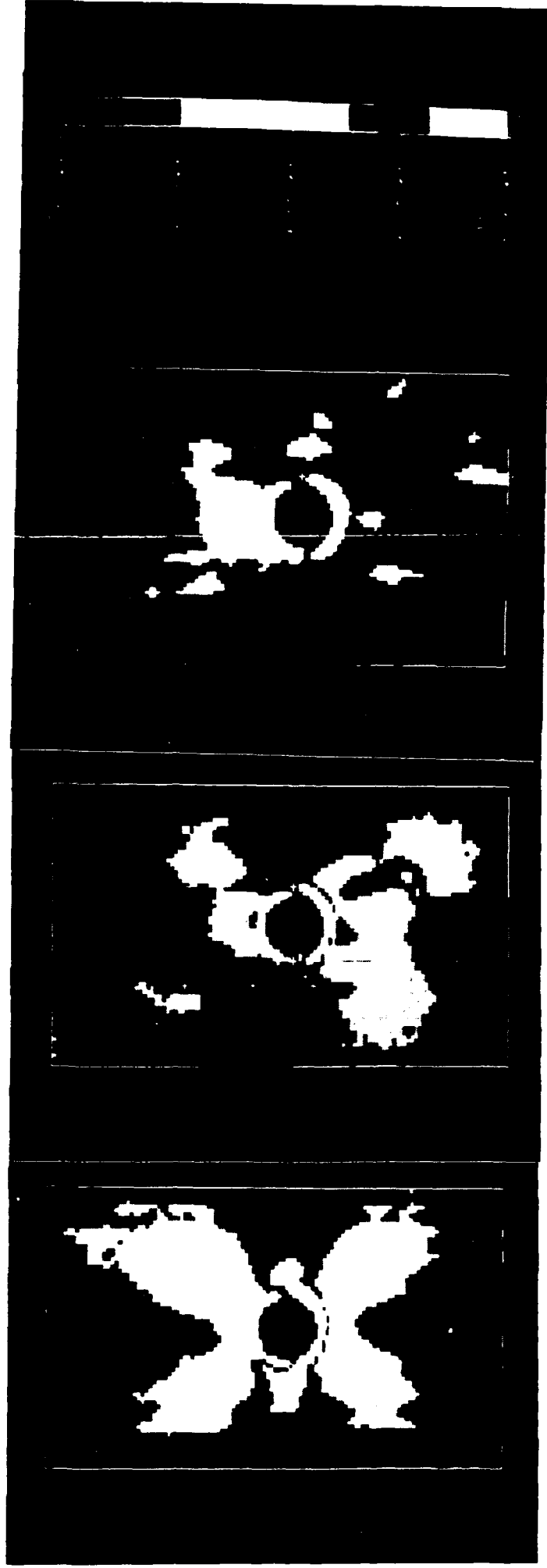


Fig 11(b)



(a)

(b)

(c)

Fig. 12

## **APPENDIX B**

PREDICTION MODEL FOR THE ONSET OF EDGE-EFFECT DELAMINATION  
AT HOLES IN COMPOSITE LAMINATES

by

Doron Shalev

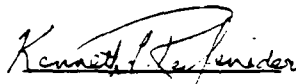
Dissertation submitted to the Faculty of the  
Virginia Polytechnic Institute and State University  
in partial fulfillment of the requirements for the degree of


DOCTOR OF PHILOSOPHY

in

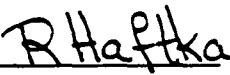
Engineering Science and Mechanics

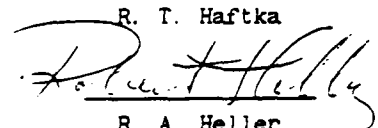
APPROVED:

  
K. L. Reifsnider

  
C. W. Smith

  
R. M. Jones

  
R. T. Haftka

  
R. A. Heller

July, 1988

Blacksburg, Virginia

PREDICTION MODEL FOR THE ONSET OF EDGE-EFFECT DELAMINATION  
AT HOLES IN COMPOSITE LAMINATES

by

Doron Shalev

Committee Chairman: K. L. Reifsnider

Engineering Science and Mechanics

(ABSTRACT)

Composite laminates are prone to delamination at free edges, straight edges or at holes, due to the mismatch at interfaces where two adjacent plies have different fiber orientations and/or different material properties. The linear analysis of the mismatch at the edge results in a mathematical singularity. That phenomenon occurs in a boundary layer and has to be treated mathematically and physically as such. In the literature it is called the "Boundary Layer Effect" or simply the "Edge Effect". It is of great importance to recognize and be able to predict delamination locations at edges prone to such events. The goal of this research was to create a model capable of providing such a prediction. In an effort to generalize the model, the more complicated case of a free edge at holes in the composite laminate was chosen rather than the case of a straight free edge.

A sequel of three major efforts was completed: 1) Development of the analysis of the free-edge effect at a hole in a composite laminate, 2) Performance of an extensive experimental program to provide data for the creation of the prediction model, and 3) On the basis of the analysis,

establishment of the model, and comparison with the experimental results.

The prediction model consists of two major products of the analysis, the order of the singularity and the strain energy release rate. Both are useful in locating the interface most prone to delaminate and the point along the hole circumference where it initiates.

Two material systems (AS4/3501-6 and AS4/1808) and two stacking sequences  $[(0/45/0/-45)_s]_4$  and  $[(0/45/90/-45)_s]_4$ , quasi-orthotropic and quasi-isotropic respectively, were quasi-statically tested under tension and compression. The specimens were X-rayed after each loading stage in order to locate the initiation of delaminations. The fact that both materials consisted of the same type of fibers, was an excellent opportunity to examine the performance of the matrix and its influence on the process of delamination. Matrix dependent behavior was successfully examined and studied through the experiments and the prediction model. Results showed good correlation and high sensitivity to the type of matrix material involved.

## ACKNOWLEDGEMENTS

This study was supported in part by the United States Air Force Office of Scientific Research under grant no. 85.0087. Acknowledgment is expressed and appreciated. Large support, fruitful guidance and interesting discussions are acknowledged to the chairman of my committee Prof. Reifsnider. Thanks to C. R. Bakis who guided me through the fascinating world of experiments. Special thanks to Dr. A. Unger of Israel Aircraft Industry who navigated me toward that turning point in my life. Finally, I thank my wife *Eti* and "my three sons" (not the TV show), *Naftaly*, *Eilon* and *Gad* for major support and I take the opportunity to apologize for being too committed to that work rather than to them.

Thanks Joe Kennedy, for making me a happy person during the last year

## TABLE OF CONTENTS

	Page
ABSTRACT.....	ii
ACKNOWLEDGEMENTS.....	iv
LIST OF ILLUSTRATIONS.....	vii
LIST OF TABLES.....	viii
CHAPTER	
1. INTRODUCTION.....	1
1.1 Survey of the state of the art.....	2
1.1.1 Edge effect in composite laminate.....	2
1.1.2 Models of delamination prediction.....	3
1.2 Scope of investigation.....	5
2. ANALYSIS OF THE EDGE EFFECT AT HOLES IN COMPOSITE PLATE.....	8
2.1 Basic formulation.....	9
2.1.1 Solution methodology.....	9
2.1.2 Boundary conditions.....	14
2.1.2.1 Traction free boundary conditions.....	15
2.1.2.2 End conditions.....	15
2.1.2.3 The cavity boundary conditions.....	16
2.1.3 Interfacial continuity.....	16
2.2 Solution of the governing equations.....	17
2.2.1 The homogeneous solution.....	17
2.2.2 The particular solution.....	24
2.3 Convergence of the solution and example.....	34
3. PREDICTION MODEL OF THE DELAMINATION ONSET BASED ON THE BOUNDARY LAYER EFFECT.....	39



4. EXPERIMENTAL PROCEDURE.....	46
4.1 Specimens - materials and geometry.....	46
4.1.1 How specimens were made.....	47
4.1.2 Notched and unnotched properties.....	48
4.2 Testing procedure.....	52
4.2.1 Testing machines.....	52
4.2.2 Loading fixture and measurements during test.....	53
4.2.3 Detection techniques, X-Ray.....	53
4.3 Observations and results.....	54
5. ANALYSIS OF TEST SPECIMENS.....	74
5.1 Order of singularity around the hole at all interfaces.....	74
5.2 Stress Fields at locations of dominant singularities.....	87
5.3 Application of analytical results to the prediction model...	90
6. COMPARISON OF ANALYTICAL AND EXPERIMENTAL RESULTS.....	91
7. SUMMARY AND CONCLUSIONS.....	93
NOMENCLATURE.....	96
REFERENCES.....	100
APPENDICES	
A. INTEGRATION OF END CONDITION EQUATIONS.....	102
B. PROGRAM "SINGULAR".....	107
B1 Interactive input process.....	107
B2 Output file - example.....	112
C. PROGRAM "EDGSTR".....	113
C1 Input file.....	113
C2 Output file.....	121
VITA.....	122

# LIST OF ILLUSTRATIONS

	page
1. Research methodology, flow-chart.....	6
2. Geometry and coordinates of composite laminate with hole.....	10
3. Convergence of $\sigma_{22}$ , examine eig. val. and integ. pts.....	35
4. Stress distributions at different scanning azimuth.....	37
5a. Explanation of figs. 5 - 20, 29.....	56
5. Delamination process in Y-B 3-4, tension.....	57
6. X-ray of Y-B 3-4, 90% critical tension load.....	58
7. Delamination process in Y-B 3-8, compression.....	59
8. X-ray of Y-B 3-8, 80% critical compression load.....	60
9. Delamination process in Z-B 7-2, tension.....	61
10. X-ray of Z-B 7-2, 90% critical tension load.....	62
11. Delamination process in Z-B 7-3, compression.....	63
12. X-ray of Z-B 7-3, 80% critical compression load.....	64
13. Delamination process in Z-A 7-7, tension.....	65
14. X-ray of Z-A 7-7, 90% critical tension load.....	66
15. Delamination process in Z-A 7-8, compression.....	67
16. X-ray of Z-A 7-8, 80% critical compression load.....	68
17. Delamination process in Y-A 6-9, tension.....	69
18. X-ray of Y-A 6-9, 85% critical tension load.....	70
19. Delamination process in Y-A 6-13, compression.....	71
20. X-ray of Y-A 6-13, 80% critical tension load.....	72
21. Interface [0/45], scan at 20, 40, 60, 80, 90 deg.....	75
22. Interface [45/90], scan at 20, 40, 60, 80, 90 deg.....	76
23. Interface [90/-45], scan at 20, 40, 60, 80, 90 deg.....	77

	page
24. Interface [0/-45], scan at 20, 40, 60, 80, 90 deg.....	78
25. Dominant singularities at $[(0/45/90/-45)]_4$ - AS4/3501-6.....	83
26. Dominant singularities at $[(0/45/0/-45)]_4$ - AS4/3501-6.....	84
27. Dominant singularities at $[(0/45/90/-45)]_4$ - AS4/1808.....	85
28. Dominant singularities at $[(0/45/0/-45)]_4$ - AS4/1808.....	86
29. Locations of onset of delamination, analysis Vs. tests.....	92
B1. Program "SINGULAR" - opening logo.....	108
B2. Chose input form for "SINGULAR".....	109
B3. Input/output file names for "SINGULAR".....	110
B4. On screen input process for "SINGULAR".....	111

#### LIST OF TABLES

	page
1. Material properties.....	49
2. Laminate properties.....	50
3. Test specimens - dimensions and strength.....	51
4. Final interfaces to compute order of singularity.....	81
5. Dominant singularities, $-\text{Re}[\delta]$ , at examined interfaces.....	82
6. Locations predicted by order of singularity.....	88
7. Near-field parameters at all examined locations.....	89

## Chapter 1

### INTRODUCTION

It is known that a wide range of properties and performance can be achieved through the utilization of composite laminates in structures, since it is possible to adjust the ply orientations, stacking sequence, and thickness. At the edge of the laminate, however, high values of stresses are often obtained due to ply deformation mismatching, which may lead to delamination. That delamination can be controlled by artificial means such as stitching, tufting, or constraining the edge by caps.

A more natural procedure is available through optimization of fiber orientation, weaving, and layer sequencing in the vicinity of the edge in order to reduce edge effects, or even by reversing the situation by changing tension conditions to compression. In order to utilize the above mentioned improvements, a tool is needed to provide the means to locate and qualify locations prone to delaminate, so that we can make the necessary changes. This tool should consist of a prediction model and the supporting analysis.

In the search for such a criterion, some parameters involved in the analysis are investigated as major factors which control the phenomenon. These parameters are the order of stress singularity, the free edge stress intensity factors, and energy considerations associated with the energy release rate.

Even though a singularity is the result of a mathematical procedure within a boundary layer, and not a physical parameter, its order

reflects a local trend and rate. Thus, comparing the order of the singularity at different locations results in the method of rating the vulnerability to delamination in those positions.

There are three major steps in the investigation of the problem of delaminations at free edges. First, a proper way to analyze the phenomenon of the edge effect at holes should be developed. Then, a prediction model should be built upon that analysis. Finally, it is essential to compare the analysis-based model with the result of appropriate experiments. The next few sections will examine the present situation in conjunction with the above-mentioned steps, and then preview the scope of the current investigation.

### 1.1 Survey of the state of the art

As mentioned above, two major aspects of the current research are surveyed in the literature. (1) the analysis of edge effects at composite laminates at free edges and at holes, and (2) the development and utilization of a prediction model for the onset of delamination.

#### 1.1.1 The edge effect in composite laminates

The behavior of the stress field at edges of composite laminates due to the deformation mismatching has been the subject of extensive investigation during the last two decades. Pipes and Pagano (1970) used a finite difference method to solve the relevant elasticity equations, whereas Wang and Crossman (1977) employed a finite element approach to

investigate this phenomenon. Recently, an approximate method was presented by Lagace (1987) using the force balance method in conjunction with minimization of energy. Due to the approximate nature of the approaches involved in the previous studies, it was not possible to determine the order of singularity of the stresses at the free edges. Wang and Choi (1982) derived an analytical solution, following a Lekhnitskii (1963) formulation, and obtained the exact order of singularity at the edge of the laminate. Their derivation involves a special form of Lekhnitskii's stress potentials which explicitly includes a parameter identified as the order of the singularity. However, their solution for the stresses is approximate, and due to mathematical difficulties the method was only applied to the analysis of special types of laminates at the straight free edge, as was done by the previously mentioned researchers.

#### 1.1.2 Models for delamination prediction

The significance of the ability to predict the onset of delaminations in composites, as discussed above, drove many investigators to postulate methods and models to provide such a tool.

The simple idea of looking at high values of stresses or strains at the region of influence of the phenomenon was applied by various investigators. Klang and Hyer (1985) used the finite element method to calculate the distribution of strains looking for the maximum as a criterion for initiation of delamination. Kim and Soni (1984) looked at the distribution of the out-of-plane interlaminar stress, then averaged

that stress along a fixed distance called the critical length taken as one ply thickness, assuming failure to occur when the average value reached some interlaminar tensile strength. That critical stress is very difficult to determine and so was taken as the transverse strength of the composite material.

Pagano and Pipes (1972) searched for a fast and simple way to look for initiation, provides an engineering tool, easy apply. In doing so, they looked at the transverse planner stresses resulting from classical lamination theory, and the moments these stresses apply on the interfaces. Then stresses were calculated utilizing these moments, and the most vulnerable interface was predicted simply by comparison of those stresses.

O'Brien (1982) looked at the energy release rate at the interfaces at free edges of the laminate. The calculation of the energy release rate was based on the stiffness loss due to delamination, calculated by means of classical lamination theory. The expression for the energy release rate is as follows,

$$G = \frac{\epsilon^2 t}{2} (E_{lam} - E^*)$$

where,  $\epsilon$  is the nominal axial strain at the undelaminated laminate,  $t$  is the laminate thickness,  $E_{lam}$  is the axial laminate stiffness calculated from classical lamination theory.  $E^*$  is axial stiffness of the laminate when completely delaminated along one or more interfaces, calculated by the stiffnesses of the separated, delaminated parts weighted by the number of plies in each sublaminde.

## 1.2 Scope of investigation

The overall process of the current research is presented in fig. 1 which shows the logical flow-chart to be followed. The two main branches, as reflected in the flow-chart, are the analytical path and the experimental one. The following is a brief discussion of the intentions and methods employed in both.

As previously described, none of the analyses of the free edge effect except the one done by Wang and Choi (1982) included the mathematical singularity as it appears at the free edge. Indeed, comparison of the results of the different approaches shows discrepancies, sometimes resulting in an opposite stress sign indicating tension instead of compression as it should be. None of the analyses deals with the problem of the free edge at a hole. In the present work, the approach of Wang and Choi (1982) is followed for the analysis of a laminated plate with an elliptical hole. The proposed method is general and can be applied to any type of composite laminate with an elliptical hole. For the special case when the effect of the hole is disregarded, the general method is applicable to the special types of laminates treated by Wang and Choi (1982). The analysis leads to an over-determined system of equations which shows ill-conditioned behavior. This mathematical obstacle is overcome by adopting the Singular Value Decomposition Method, Stewart (1973), to determine the real rank of the matrix when it is less than full rank.

Since the mathematical singularity plays an important role in the analysis, it has to find its way to the prediction model, too. That is, in the formulation of the strain energy release rate, and the order of



# PREDICTION MODEL FOR DELAMINATION ONSET AT HOLES IN COMPOSITE LAMINATES

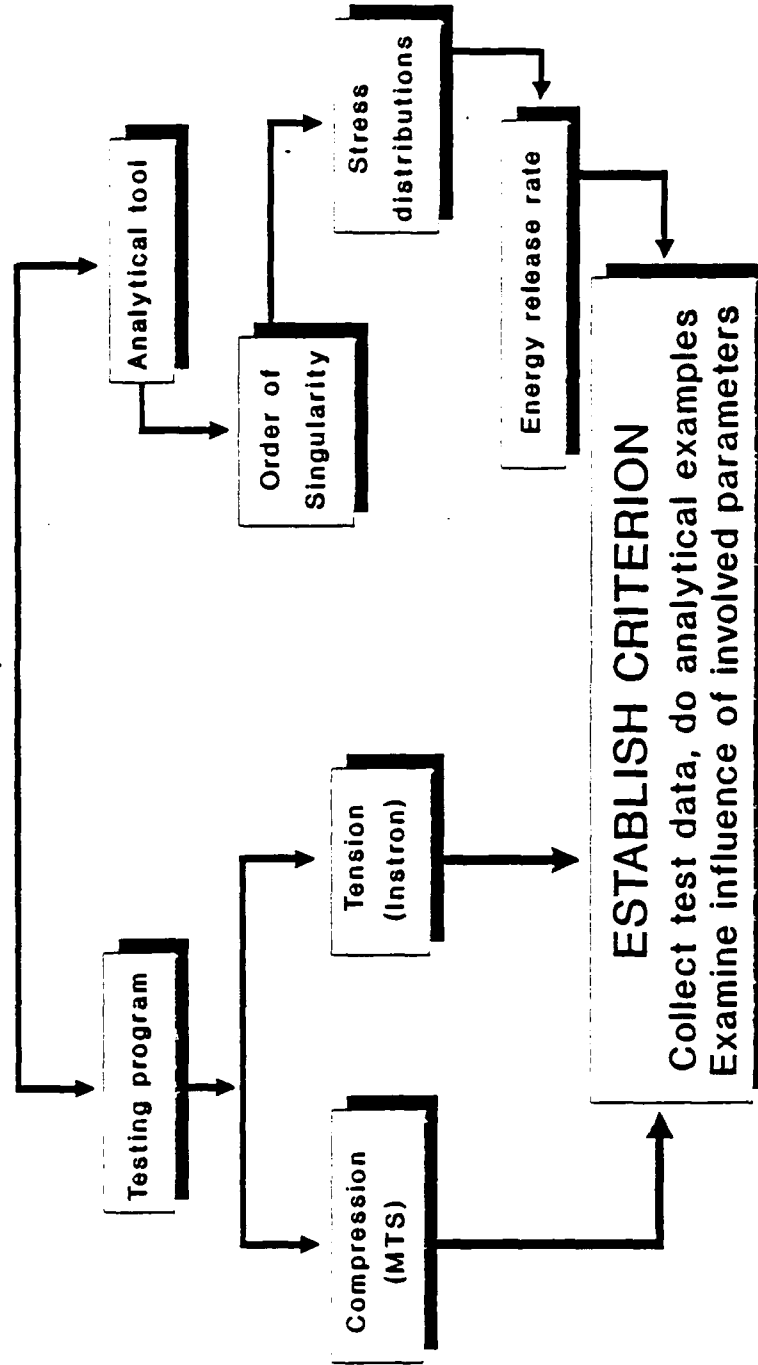


Figure No. 1.: Research methodology; flow-chart

the singularity as a stand-alone parameter as well. The importance of the order of singularity as a physical parameter rather than merely as a mathematical one will be discussed and explained within the context of the boundary layer effect.

Finally, a series of experiments is to be presented, analyzed, and examined in conjunction with the prediction model. In order to meet as many objectives as possible, the testing program consists of various types of materials with different matrix systems and different stacking sequences, as well as different loading (tension and compression).

## Chapter 2

## ANALYSIS OF THE EDGE EFFECT AT ELLIPTICAL HOLES IN COMPOSITE PLATE

The development of a solution for the free edge effect at holes in a composite plate is described in this chapter. The governing equations consist of differential equations and therefore are decomposed into homogeneous and particular parts. The derivation of the homogeneous solution is identical to the method of Wang and Choi (1982). The particular solution satisfies the governing equations, free edge conditions, the interfacial continuity relations, and the upper and lower traction-free surface requirements and represents the influence of the hole. The effect of an elliptical hole is incorporated by adopting Lekhnitskii's solution for anisotropic plates containing an elliptical cavity. By conversion of the composite laminate into an anisotropic plate via classical lamination theory (Jones (1975)), the strains were evaluated from Lekhnitskii's solution. The corresponding stresses in the different plies can thus be determined. As the analysis is based on a set of eigenvalues and includes some numerical integration, the accuracy of the results was assessed and demonstrated by selecting various numbers of eigenvalues and points of integration. Results are given which exhibit the effect of the hole's edge on the behavior of stresses within the boundary layer and, for special cases, throughout the laminate.

## 2.1 Basic formulation

### 2.1.1 Solution methodology

Consider a composite laminate containing an elliptical cutout as shown in fig. 2. A system of Cartesian coordinates is introduced whose origin is located at the bore edge at the examined interface and its orientation follows the scanning azimuth in a way that  $x_1$  axis is always radially oriented away from the center of the hole. Every lamina is assumed to be elastic and anisotropic, obeying the generalized Hooke's law:

$$\{\epsilon\} = [S]\{\sigma\} \quad (1)$$

in which  $\{\epsilon\}$  are the strain components of the  $m^{\text{th}}$  ply,

$$\{\epsilon\} = [\epsilon_{11}, \epsilon_{22}, \epsilon_{33}, 2\epsilon_{23}, 2\epsilon_{13}, 2\epsilon_{12}]^T$$

The solution methodology follows Lekhnitskii's (1963) approach for anisotropic plates as used by Wang and Choi (1982). The problem is treated as a boundary layer problem. It is somewhat similar to the aerodynamic problem of viscous flow around an airfoil. In the aerodynamic problem, we consider a streaming flow past a slender body. The fluid viscosity is taken to be relatively small and the shearing stresses developed are very small. It is known that except for a thin layer adjacent to the solid body, the transverse velocity gradients are negligibly small throughout the flow field. However, within that thin

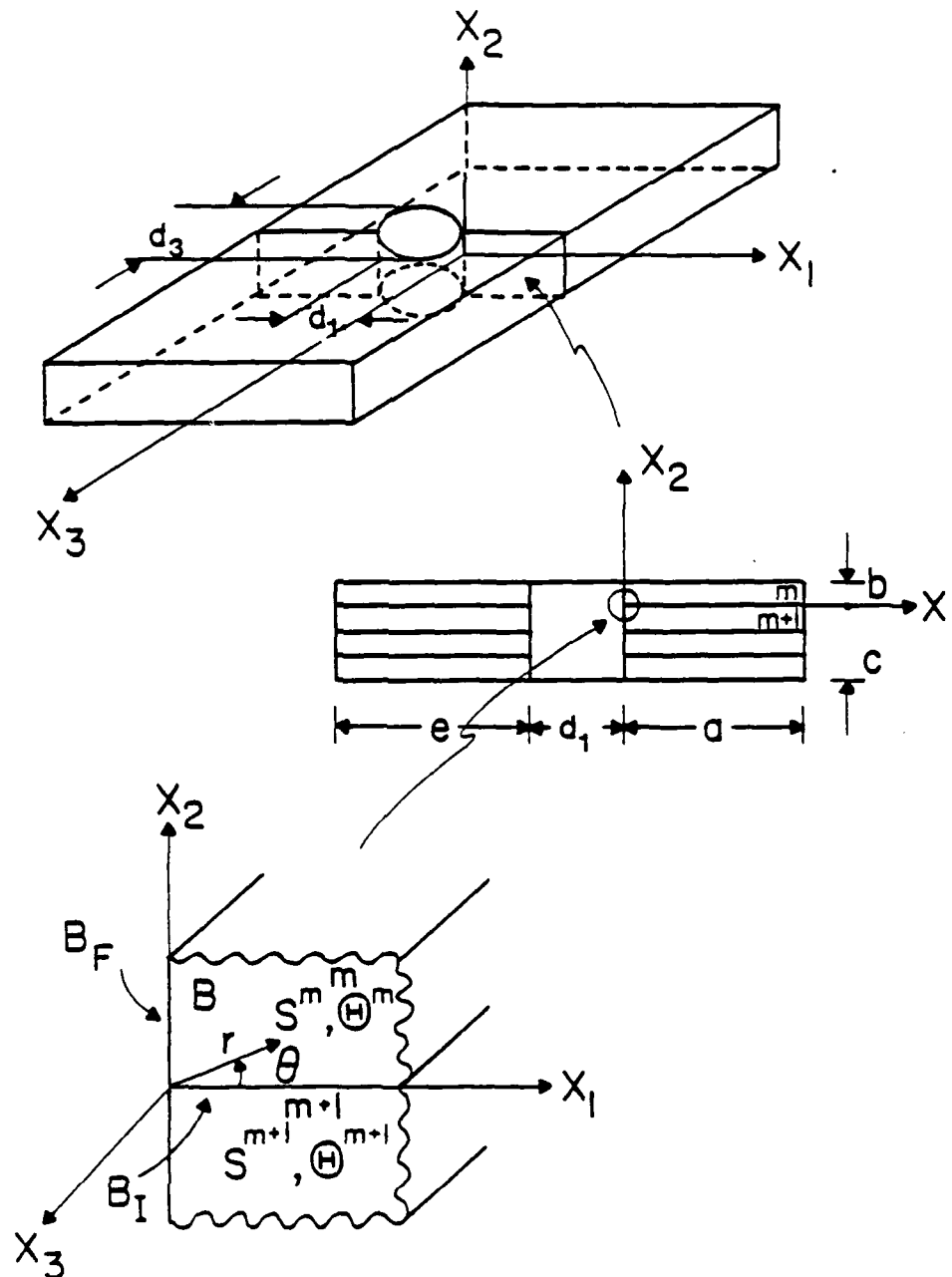


Figure No. 2: Geometry and coordinates of composite laminate with embedded elliptical hole

boundary layer, large shearing velocities are produced resulting in large shear stresses. The importance of this concept is that it allows us to apply the more complicated equations related to the boundary only within that thin layer, and some appreciable simplifying assumptions can reasonably be made. In the aerodynamics case, these are the viscous motion equations. In our case, the boundary layer is a relatively thin region at the vicinity of the edge. At the free edge the stress field is singular and thus its values are infinite. Within the boundary layer stresses change rapidly from the edge to the other side of the region where they agree with results from classical lamination theory, Jones (1975), and anisotropic plates, Lekhnitskii (1963). Within the boundary layer, changes with respect to  $x_1$  and  $x_2$  are considered to be larger than changes with respect to  $x_3$ . Thus, within that region we may simplify the problem and neglect variations with respect to  $x_3$  requiring compatibility with the above mentioned solutions which take changes with respect to  $x_3$  into account such as the solution of an anisotropic plate with cavity, Lekhnitskii (1963). Several assumptions should be noted:

1. The composite laminate is of finite width.
2. The laminate is long enough such that end effects can be neglected.
3. Due to the neglect of variations with respect to  $x_3$  we may assume a state of generalized plane deformation within the boundary layer.

The equilibrium equations, in the absence of body forces, are given by

$$\sigma_{ij,j} = 0 \qquad i, j = 1, 2, 3 \qquad (2)$$

Due to assumption 3, derivatives with respect to  $x_3$  are omitted, reducing (2) to

$$\sigma_{11,1} + \sigma_{12,2} = 0 \quad (a)$$

$$\sigma_{21,1} + \sigma_{22,2} = 0 \quad (b) \quad (3)$$

$$\sigma_{31,1} + \sigma_{32,2} = 0 \quad (c)$$

The small strain tensor is given in terms of the displacements  $u_i$  by

$$\epsilon_{ij} = \frac{1}{2}(u_{i,j} + u_{j,i}) \quad (4)$$

Using (4) in (1) and integrating provides

$$u_1 = -\frac{1}{2} A_1 S_{33} x_3^2 - A_4 x_2 x_3 + U_1(x_1, x_2) + \omega_2 x_3 - \omega_3 x_2 + u_{10} \quad (a)$$

$$u_2 = -\frac{1}{2} A_2 S_{33} x_3^2 + A_4 x_1 x_3 + U_2(x_1, x_2) + \omega_3 x_1 - \omega_1 x_3 + u_{20} \quad (b) \quad (5)$$

$$u_3 = (A_1 x_1 + A_2 x_2 + A_3) S_{33} x_3 + U_3(x_1, x_2) + \omega_1 x_2 - \omega_2 x_1 + u_{30} \quad (c)$$

where  $u_{10}$  and  $\omega_i$  are rigid-body translations and rotations, respectively.

The stress in the longitudinal direction,  $\sigma_{33}$  is given by,

$$\sigma_{33} = A_1 x_1 + A_2 x_2 + A_3 - \frac{S_{3j} \sigma_j}{S_{33}} \quad (6)$$

where  $j=1,2,4,5,6$  using the contracted Greek notation for stresses.

The derivatives of functions  $U_1(x_1, x_2), U_2(x_1, x_2), U_3(x_1, x_2)$  are expressed in the form

$$U_{1,1} = \tilde{S}_{1j} \sigma_j + S_{13}(A_1 x_1 + A_2 x_2 + A_3) \quad (a)$$

$$U_{2,2} = \tilde{S}_{2j} \sigma_j + S_{23}(A_1 x_1 + A_2 x_2 + A_3) \quad (b)$$

$$U_{3,1} = \tilde{S}_{5j} \sigma_j + S_{53}(A_1 x_1 + A_2 x_2 + A_3) + A_4 x_2 \quad (c) \quad (7)$$

$$U_{3,2} = \tilde{S}_{4j} \sigma_j + S_{43}(A_1 x_1 + A_2 x_2 + A_3) - A_4 x_1 \quad (d)$$

$$U_{1,2} + U_{2,2} = \tilde{S}_{6j} \sigma_j + S_{63}(A_1 x_1 + A_2 x_2 + A_3) \quad (e)$$

where  $\tilde{S}$  is the reduced form of  $S$  given by:

$$\tilde{S}_{ij} = S_{ij} - \frac{S_{13} S_{j3}}{S_{33}} \quad i, j=1,2,4,5,6 \quad (8)$$

Following Wang (1982), we adopt Lekhnitskii's stress potentials  $F, \Psi$  defined by

$$\begin{aligned} \sigma_1 = \sigma_{11} = F_{,22}; & \quad \sigma_2 = \sigma_{22} = F_{,11}; & \quad \sigma_4 = \sigma_{23} = -\Psi_{,1}; \\ \sigma_5 = \sigma_{13} = \Psi_{,2}; & \quad \sigma_6 = \sigma_{12} = -F_{,12} \end{aligned} \quad (9)$$



Equation (9) satisfies (3) and when used in conjunction with (5) & (7) it creates a system of governing equations that can be expressed in terms of partial differential operators which have the form:

$$\begin{cases} L_3 F + L_2 \Psi = -2A_4 + A_1 S_{34} - A_2 S_{35} \\ L_4 F + L_3 \Psi = 0 \end{cases} \quad (10)$$

where

$$L_2 = \tilde{S}_{44} \frac{\partial^2}{\partial x_1^2} - \tilde{S}_{45} \frac{\partial^2}{\partial x_1 \partial x_2} - \tilde{S}_{55} \frac{\partial^2}{\partial x_2^2} \quad (a)$$

$$\begin{aligned} L_3 = & -\tilde{S}_{24} \frac{\partial^3}{\partial x_1^3} + (\tilde{S}_{25} + \tilde{S}_{46}) \frac{\partial^3}{\partial x_1^2 \partial x_2} + (\tilde{S}_{14} + \tilde{S}_{56}) \frac{\partial^3}{\partial x_1 \partial x_2^2} \\ & + \tilde{S}_{15} \frac{\partial^3}{\partial x_2^3} \end{aligned} \quad (b) \quad (11)$$

$$\begin{aligned} L_4 = & \tilde{S}_{22} \frac{\partial^4}{\partial x_1^4} - 2\tilde{S}_{26} \frac{\partial^4}{\partial x_1^3 \partial x_2} + (2\tilde{S}_{12} + \tilde{S}_{66}) \frac{\partial^4}{\partial x_1^2 \partial x_2^2} \\ & - 2\tilde{S}_{16} \frac{\partial^4}{\partial x_1 \partial x_2^3} + \tilde{S}_{11} \frac{\partial^4}{\partial x_2^4} \end{aligned} \quad (c)$$

### 2.1.2 Boundary conditions

We consider three types of boundary conditions, as follows in the next sections.

### 2.1.2.1 Traction-free edge boundary conditions

Assuming that the edges of the laminate and the hole are traction-free, it follows that

$$\sigma_{11} = \sigma_{13} = \sigma_{12} = 0 \quad x_1 = 0, \quad x_2 = 0, \quad x_3 = 0 \quad (12)$$

### 2.1.2.2 End conditions

We require static equilibrium with the remote loading by forming the following integrals over the cross-sectional area B as shown in fig. 2 (Lekhnitskii, 1963)

$$\iint_B \sigma_{13} dx_1 dx_2 = 0 \quad (a)$$

$$\iint_B \sigma_{23} dx_1 dx_2 = 0 \quad (b)$$

$$\iint_B \sigma_{33} dx_1 dx_2 = P_{33} \quad (c) \quad (13)$$

$$\iint_B \sigma_{33} x_2 dx_1 dx_2 = M_{11} \quad (d)$$

$$\iint_B \sigma_{33} x_1 dx_1 dx_2 = M_{22} \quad (e)$$

$$\iint_B (\sigma_{23} x_1 - \sigma_{13} x_2) dx_1 dx_2 = M_{12} \quad (f)$$

AD-A207 623

INVESTIGATION AND MODELING OF DAMAGE GROWTH IN  
COMPOSITE LAMINATES. (U) VIRGINIA POLYTECHNIC INST AND  
STATE UNIV BLACKSBURG MATERIALS.

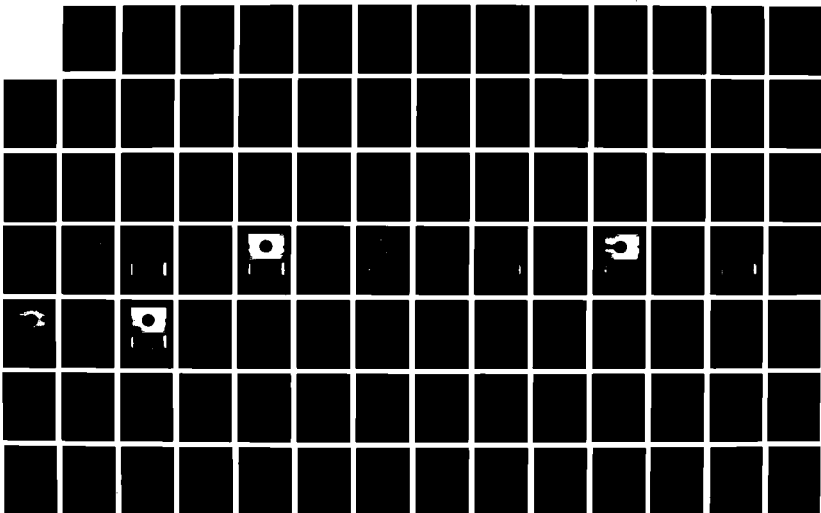
4/5

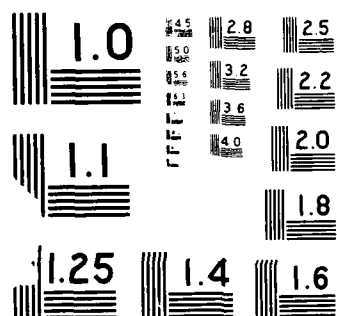
UNCLASSIFIED

K L REIFSNIDER ET AL 25 SEP 88

F/G 11/4

NL





For cases where analysis is done at an azimuthal angle  $\alpha$  different than  $0^\circ$ , the coordinate system is rotated such that the  $x_3$  axis is tangent to the hole surface and creates an angle  $\alpha$  with respect to the longitudinal axis of the plate. The domain in which integration is carried out is cross-sectional area  $B/\cos(\alpha)$ .

#### 2.1.2.3 The cavity boundary conditions

Special treatment is required in the vicinity of the hole. This is achieved by conversion of the laminate plate cross section into an anisotropic plate via its effective elastic constants ( $E_x, E_y, G_{xy}, \nu_{xy}$ ) calculated by classical lamination theory, Jones (1975). Analysis of such a plate with cavity subjected to various loads, is done following Lekhnitskii (1963). The resulting strains, when multiplied by the stiffness components of the relevant ply, provide the planar stress distribution in that ply. These stress distributions are applicable away from the hole where the edge effects are negligible.

#### 2.1.3 Interfacial continuity

Continuity of tractions must be satisfied at the interface between the  $m$  and  $m+1$  plies:

$$\sigma_{21}^{(m)} = \sigma_{21}^{(m+1)} \quad i = 1, 2, 3; \quad x_2 = 0 \quad (14)$$

and the displacements must be continuous:

$$u_1^{(m)} = u_1^{(m+1)} \quad i = 1, 2, 3; \quad x_2 = 0 \quad (15)$$

## 2.2 Solution of the governing equations

The solution consists of two parts, homogeneous and particular solutions. The homogeneous part can be exactly derived and provides the stress singularities at the edges. On the other hand, the particular solution can not be exactly obtained, and an approximate method is applied.

### 2.2.1 The homogeneous solution

Following Lekhnitskii (1963), the general forms of his stress potential are taken in the form

$$F(x_1, x_2) = \sum_{k=1}^6 F_k(Z_k) \quad (a) \quad (16)$$

$$\Psi(x_1, x_2) = \sum_{k=1}^6 \eta_k F'_k(Z_k) \quad (b)$$

where  $Z_k = x_1 + \mu_k x_2$ ,  $\mu_k$  are the roots of the characteristic equation as shown below,  $\eta_k$  are ratios of components of the characteristic equation, and  $F'_k(Z_k)$  is the derivative w.r.t. the argument  $Z_k$ .

Regarding the homogeneous form of Eqn. (10), we consider the

potentials  $F$  and  $\Psi$  to consist of two parts denoted by indices 1 and 0 designating the homogeneous and the particular solutions, respectively. The characteristic equation of the homogeneous solution is defined by the LHS of (10). Eliminating one of the functions, say  $\Psi_1$ , we obtain a 6<sup>th</sup> order equation for the remaining  $F_1$ ,

$$(L_4 L_2 - L_3^2) F_1 = 0 \quad (a)$$

which can be decomposed into (17)

$$D_6 D_5 D_4 D_3 D_2 D_1 F_1 = 0 \quad (b)$$

where

$$D_k = \frac{\partial}{\partial x_2} - \mu_k \frac{\partial}{\partial x_1}$$

Consequently, new sets of operators are obtained from (11):

$$l_2 = \tilde{S}_{55} \mu^2 - 2\tilde{S}_{45} \mu + \tilde{S}_{44} \quad (a)$$

$$l_3 = \tilde{S}_{15} \mu^3 - (\tilde{S}_{14} + \tilde{S}_{56}) \mu^2 + (\tilde{S}_{25} + \tilde{S}_{46}) - \tilde{S}_{24} \quad (b) \quad (18)$$

$$l_4 = \tilde{S}_{11} \mu^4 - 2\tilde{S}_{16} \mu^3 + (2\tilde{S}_{12} + \tilde{S}_{66}) \mu^2 - 2\tilde{S}_{26} \mu + \tilde{S}_{22} \quad (c)$$

The resulting characteristic equation is

$$l_4(\mu)l_2(\mu)-l_3^2(\mu) = 0 \quad (a)$$

also (19)

$$\eta_k = - \frac{l_3(\mu_k)}{l_2(\mu_k)} = - \frac{l_4(\mu_k)}{l_3(\mu_k)} \quad (b)$$

It has been shown by Lekhnitskii (1963) that the  $\mu_k$  are complex conjugates where the real part vanishes for orthotropic materials. Solving the polynomial (19), and substituting for the stresses and displacements (9) and (7), respectively, yields the following results designated by (h) for the homogeneous part of the solution,

$$\sigma_{11}^{(h)} = \sum_{k=1}^6 \mu_k^2 F''(Z_k) \quad (a)$$

$$\sigma_{22}^{(h)} = \sum_{k=1}^6 F''(Z_k) \quad (b)$$

$$\sigma_{23}^{(h)} = - \sum_{k=1}^6 \eta_k F''(Z_k) \quad (c)$$

$$\sigma_{13}^{(h)} = \sum_{k=1}^6 \eta_k \mu_k F''(Z_k) \quad (d) \quad (20)$$

$$\sigma_{12}^{(h)} = - \sum_{k=1}^6 \mu_k F''(Z_k) \quad (e)$$



$$u_1^{(h)} = \sum_{k=1}^6 p_k F'_k(Z_k) \quad (f)$$

$$u_2^{(h)} = \sum_{k=1}^6 q_k F'_k(Z_k) \quad (g)$$

$$u_3^{(h)} = \sum_{k=1}^6 t_k F'_k(Z_k) \quad (h)$$

where

$$p_k = \tilde{S}_{11}\mu_k^2 + \tilde{S}_{12} - \tilde{S}_{14}\eta_k + \tilde{S}_{15}\eta_k\mu_k - \tilde{S}_{16}\mu_k \quad (a)$$

$$q_k = \tilde{S}_{12}\mu_k + \frac{\tilde{S}_{22}}{\mu_k} - \frac{\tilde{S}_{24}\eta_k}{\mu_k} + \tilde{S}_{25}\eta_k - \tilde{S}_{26} \quad (b) \quad (21)$$

$$t_k = \tilde{S}_{14}\mu_k + \frac{\tilde{S}_{24}}{\mu_k} - \frac{\tilde{S}_{44}\eta_k}{\mu_k} + \tilde{S}_{45}\eta_k - \tilde{S}_{46} \quad (c)$$

Following the idea of Wang and Choi (1982), the functions  $F_k(Z_k)$  are expressed in the form

$$F_k(Z_k) = c_k \frac{Z_k^{\delta+2}}{(\delta+1)(\delta+2)} \quad (22)$$

By choosing this particular expression, it can be readily shown (by performing second-order derivatives) that the general form of the stresses can be represented in the form

$$\sigma = Kr^\delta \quad (23)$$

It is obvious that, by solving for  $\delta$ , we obtain the exact order of the singularity as  $r$  approaches zero. Equation (22) followed by (23) have to satisfy all boundary conditions and governing equations for the homogeneous and particular parts of the solution. Substituting (22) into (20) provides the following:

$$\sigma_{11}^{(h)} = \sum_{k=1}^3 [c_k \mu_k^2 Z_k^\delta + c_{k+3} \bar{\mu}_k^2 \bar{Z}_k^\delta] \quad (a)$$

$$\sigma_{22}^{(h)} = \sum_{k=1}^3 [c_k Z_k^\delta + c_{k+3} \bar{Z}_k^\delta] \quad (b)$$

$$\sigma_{23}^{(h)} = - \sum_{k=1}^3 [c_k \eta_k Z_k^\delta + c_{k+3} \bar{\eta}_k \bar{Z}_k^\delta] \quad (c)$$

$$\sigma_{13}^{(h)} = \sum_{k=1}^3 [c_k \eta_k \mu_k Z_k^\delta + c_{k+3} \bar{\eta}_k \bar{\mu}_k \bar{Z}_k^\delta] \quad (d) \quad (24)$$

$$\sigma_{12}^{(h)} = - \sum_{k=1}^3 [c_k \mu_k Z_k^\delta + c_{k+3} \bar{\mu}_k \bar{Z}_k^\delta] \quad (e)$$

$$u_1^{(h)} = \sum_{k=1}^3 [c_k p_k Z_k^{\delta+1} + c_{k+3} \bar{p}_k \bar{Z}_k^{\delta+1}] / (\delta + 1) \quad (f)$$

$$u_2^{(h)} = \sum_{k=1}^3 [c_k q_k Z_k^{\delta+1} + c_{k+3} \bar{q}_k \bar{Z}_k^{\delta+1}] / (\delta + 1) \quad (g)$$

$$u_3^{(h)} = \sum_{k=1}^3 [c_k t_k Z_k^{\delta+1} + c_{k+3} \bar{t}_k \bar{Z}_k^{\delta+1}] / (\delta + 1) \quad (h)$$

It should be noted that the present contribution (23) from the homogeneous solution involves the parameter  $\delta$ . This parameter depends on the specific geometry in the close vicinity of the edge as well as on the elastic constants of the two adjacent plies. Thus, (23) is valid at the hole as well as at the plate edge, and refers to the relevant ply pair in which  $\delta$  was calculated.

Substituting (22) into the free edge boundary conditions (12), yields three equations for each of the two adjacent plies, resulting in a total of six equations. Similarly, substitution into the interfacial conditions, (15), contributes an additional six equations. There are six unknown coefficients  $c_k$ ,  $k = 1-6$ , for each layer and the additional unknown power  $\delta$ . This system of 12 algebraic equations can be presented in a matrix form:

$$[A]\{C\} = 0 \quad (25)$$

where  $[A]$  is a  $12 \times 12$  matrix whose elements involve  $\delta$  as a power. In addition,

$$\{c\} = [c_k^{(m)}, c_k^{(m+1)}]^T \quad k = 1, 2, 3, 4, 5, 6$$

This system establishes a nonlinear eigenvalue problem for which  $\{C\}$  are the eigenvectors and  $\delta_1$  are the corresponding eigenvalues determined from the requirement that  $[A]$  must vanish for a non-trivial solution:

$$\det[A] = 0 \quad (26)$$

The solution of Eqn. (26) is performed by a deflation technique as presented by Muller (1956). Since (26) is a transcendental equation, an infinite set of solutions for  $\delta$  is obtained. The algebraically smallest eigenvalue is a real number in  $[-1,0]$  and is the order of the singularity as explained by Wang and Choi (1982). For the case of an angle-ply laminate, the higher eigenvalues are either integers or pairs of conjugate complex numbers. The properly truncated set of eigenvalues is used in the particular solution to ensure convergence. Once (25) is solved, the stresses and displacements are obtained from (24) using the expressions:

$$\sigma_{\alpha}^{(h)} = \sum_n d_n^{(h)} f_{\alpha n}(x_1, x_2; \delta_n) \quad \alpha = 1, 2, 4, 5, 6 \quad (a)$$

$$u_{\beta}^{(h)} = \sum_n d_n^{(h)} g_{\beta n}(x_1, x_2; \delta_n) \quad \beta = 1, 2, 3 \quad (b) \quad (27)$$

$$\sigma_3^{(h)} = - \frac{S_{3j} \sigma_j^{(h)}}{S_{33}} \quad (c)$$

where  $f_{\alpha n}$  and  $g_{\beta n}$  are the eigenfunctions which coincide with the right-hand side of Eqn. (24) and include the infinite set of  $\delta_n$ . The infinite set of coefficients  $\{d_n^{(h)}\}$  is to be determined in conjunction with the particular solution. A computer program, called "SINGULAR", was developed on a personal computer to provide the list of eigenvalues and the order of singularity. See Appendix B for a description and explanations of that code.

### 2.2.2 The particular solution

A particular solution (denoted by superscript p) to Eqn. (10) is expressed in the form :

$$F^{(p)} = a_1 x_1^3 + a_2 x_1^2 x_2 + a_3 x_1 x_2^2 + a_4 x_2^3 + a_5 x_1^2 + a_6 x_1 x_2 + a_7 x_2^2 \quad (28)$$

$$\Psi^{(p)} = a_8 x_1^2 + a_9 x_1 x_2 + a_{10} x_2^2 + a_{11} x_1 + a_{12} x_2$$

Substitution of Eqn. (28) into Eqn. (9) yields

$$\sigma_{11}^{(p)} = 2a_3 x_1 + 6a_4 x_2 + 2a_7 \quad (a)$$

$$\sigma_{22}^{(p)} = 6a_1 x_1 + 2a_2 x_2 + 2a_5 \quad (b)$$

$$\sigma_{23}^{(p)} = -2a_8 x_1 - a_9 x_2 - a_{11} \quad (c) \quad (29)$$

$$\sigma_{13}^{(p)} = a_9 x_1 + 2a_{10} x_2 + a_{12} \quad (d)$$

$$\sigma_{12}^{(p)} = -2a_2 x_1 - 2a_3 x_2 - a_6 \quad (e)$$

and

$$\sigma_{33}^{(p)} = (A_1 x_1 + A_2 x_2 + A_3) - \frac{S_{3j} \sigma_j^{(p)}}{S_{33}} \quad (30)$$

The expression of the particular part of the displacements,  $u_i^{(p)}$ , follows exactly the form of Eqns. (5a-c), in which

$$U_1^{(p)} = \frac{1}{2} G_{11} x_1^2 + G_{12} x_1 x_2 + G_{13} x_1 + \frac{1}{2} (G_{62} - G_{21}) x_2^2 + \frac{1}{2} G_{63} x_2 \quad (a)$$

$$U_2^{(p)} = G_{12} x_1 x_2 + \frac{1}{2} G_{22} x_2^2 + G_{23} x_2 + \frac{1}{2} (G_{61} - G_{12}) x_1^2 + \frac{1}{2} G_{63} x_1 \quad (b) \quad (31)$$

$$U_3^{(p)} = \frac{1}{2} G_{51} x_1^2 + (G_{52} + A_4) x_1 x_2 + G_{53} x_1 + \frac{1}{2} G_{42} x_2^2 + G_{43} x_2 \quad (c)$$

and

$$G_{j1} = 2\tilde{S}_{j1} a_3 + 6\tilde{S}_{j2} a_1 - 2\tilde{S}_{j4} a_8 + \tilde{S}_{j5} a_9 - \tilde{S}_{j6} a_2 + S_{j3} A_1 \quad (a)$$

$$G_{j2} = 6\tilde{S}_{j1} a_4 + 2\tilde{S}_{j2} a_2 - \tilde{S}_{j4} a_9 + 2\tilde{S}_{j5} a_{10} - 2\tilde{S}_{j6} a_3 + S_{j3} A_2 \quad (b) \quad (32)$$

$$G_{j3} = 2\tilde{S}_{j1} a_7 + 2\tilde{S}_{j2} a_5 - \tilde{S}_{j4} a_{11} + \tilde{S}_{j5} a_{12} - \tilde{S}_{j6} a_6 + S_{j3} A_3 \quad (c)$$

$$j = 1, 2, 4, 5, 6$$

The coefficients in Eqn. (28) are determined by satisfaction of the governing equations (10), the traction-free boundary conditions Eqn. (12), and the interfacial conditions (14,15). To this end, a system of 34 linear algebraic equations is obtained for the 44 unknown coefficients in Eqns. (29)-(32). Equation (10) yields:

$$\begin{aligned}
& -6\tilde{S}_{24}a_1 + 2(\tilde{S}_{25} + \tilde{S}_{46})a_2 - 2(\tilde{S}_{14} + \tilde{S}_{56})a_3 + 6\tilde{S}_{15}a_4 + \tilde{S}_{44}a_8 \\
& - 2\tilde{S}_{45}a_9 + 2\tilde{S}_{55}a_{10} = -2A_4 + A_1S_{34} - A_2S_{35} \quad (a) \\
& a_i^{(m), (m+1)} = 0 \quad i = 3, 4, 6, 7, 10, 12 \quad (b)
\end{aligned} \tag{33}$$

and the following quantities are identical for the  $m$  and the  $m+1$  plies:

$$\begin{aligned}
& a_j, \quad j = 1, 2, 5, 8, 11; \quad A_jS_{33}, \quad i = 1, 2, 3; \quad A_4; \\
& G_{11}; \quad G_{13}; \quad G_{61} - G_{12}; \quad \frac{1}{2}G_{63} + \omega_3; \quad G_{51}; \quad G_{53}; \quad (c) - (m) \\
& u_{10}, \quad i = 1, 2, 3; \quad \omega_k, \quad k = 1, 2;
\end{aligned}$$

Using Eqn. (33 b,c), we can rewrite (33a) in the form

$$(\tilde{S}_{25}^{(k)} + \tilde{S}_{16}^{(k)})a_2 + \tilde{S}_{44}^{(k)}a_8 + 2A_4 = 0 \quad k = m, m+1 \tag{34}$$

Similar elimination will provide

$$G_{11} = 6\tilde{S}_{12}a_1 + \tilde{S}_{15}a_9 + S_{13}A_1 \tag{a}$$

$$G_{13} = 2\tilde{S}_{12}a_5 + S_{13}A_3 \tag{b}$$

$$G_{61} = -2\tilde{S}_{64}a_8 - 2\tilde{S}_{66}a_2 \tag{c}$$

$$G_{12} = 2\tilde{S}_{12}a_2 + S_{13}A_2 \quad (d) \quad (35)$$

$$G_{63} = -\tilde{S}_{64}a_{11} \quad (e)$$

$$G_{51} = 6\tilde{S}_{52}a_1 + \tilde{S}_{55}a_9 \quad (f)$$

$$G_{53} = 2\tilde{S}_{52}a_5 \quad (g)$$

The use of Eqn. (35) in (33 d-k) assuming no rigid body translations and rotations, results in

$$\begin{aligned} a_1 [\delta(\tilde{S}_{12}^{(m)} - \tilde{S}_{12}^{(m+1)})] + a_9 [\tilde{S}_{15}^{(m)}] - a_9' [\tilde{S}_{15}^{(m+1)}] \\ + A_1 [S_{13}^{(m)} - S_{13}^{(m+1)} S_{33}^{(m)} / S_{33}^{(m+1)}] = 0 \end{aligned} \quad (36)$$

$$a_5 [2(\tilde{S}_{12}^{(m)} - \tilde{S}_{12}^{(m+1)})] + A_3 [S_{13}^{(m)} - S_{13}^{(m+1)} S_{33}^{(m)} / S_{33}^{(m+1)}] = 0 \quad (37)$$

$$\begin{aligned} a_8 [2(\tilde{S}_{64}^{(m)} - \tilde{S}_{64}^{(m+1)})] + a_2 [2(\tilde{S}_{66}^{(m)} + \tilde{S}_{12}^{(m)} - \tilde{S}_{66}^{(m+1)} - \tilde{S}_{12}^{(m+1)})] \\ + A_2 [S_{13}^{(m)} - S_{13}^{(m+1)} S_{33}^{(m)} / S_{33}^{(m+1)}] = 0 \end{aligned} \quad (38)$$

$$a_{11} [\tilde{S}_{64}^{(m)} - \tilde{S}_{64}^{(m+1)}] = 0 \quad (39)$$

$$a_1 [6(\tilde{S}_{52}^{(m)} - \tilde{S}_{52}^{(m+1)})] + a_9 [\tilde{S}_{55}^{(m)}] - a_9' [\tilde{S}_{55}^{(m+1)}] = 0 \quad (40)$$

$$a_5 [2(\tilde{S}_{52}^{(m)} - \tilde{S}_{52}^{(m+1)})] = 0 \quad (41)$$



At this stage, we are left with 11 unknowns:  $a_1, a_2, a_5, a_8, a_9, a_9', a_{11}, A_1, A_2, A_3, A_4$  where  $a_9$  and  $a_9'$  are for the  $m^{th}$  and  $m^{th}+1$  plies respectively, and the rest of the coefficients are identical for both layers. These unknowns appear in the 8 equations; (34), (36)-(41). In order to impose the far-end conditions (13), the full expressions for the stresses (i.e., the sum of the homogeneous and particular parts) are needed. This adds the infinite number of unknowns  $d_n^{(h)}$  (Eqn. (27)). It should be noted that although in practical computation this set of unknowns,  $d_n^{(h)}$ , is truncated, the system of equations is still over determined since some of the unknowns were eliminated by the additional equations. Next, the double integrals in (13) are exactly evaluated. The results are in App. A. Equations (A1 - A6) together with (34), (36)-(41), form a system of 14 equations in the above 11 unknowns and the additional unknowns  $\{d_n\}$ .

In order to incorporate the effect of the hole, the approach mentioned in (3.1.2.3) is applied. It should be noted that the calculated stresses using Lekhnitskii's theory for anisotropic plate with elliptical cavity are  $\sigma_{13cal}^{(m)}$  and  $\sigma_{33cal}^{(m)}$ . Thus,

$$\sigma_{33}^{(m)}(x_1, x_2) = \sigma_{33cal}^{(m)}(x_1, x_2)$$

$$m = 1, 2, \dots \text{no. of plies} \quad (42)$$

$$\sigma_{13}^{(m)}(x_1, x_2) = \sigma_{13cal}^{(m)}(x_1, x_2)$$

The traction-free boundary conditions at the upper and lower surfaces of

the laminate are:

$$\sigma_{22}^{(k)}(x_1, x_2) = 0$$

$$\sigma_{23}^{(k)}(x_1, x_2) = 0 \quad (43)$$

$$\sigma_{12}^{(k)}(x_1, x_2) = 0 \quad k = 1, 2; \quad x_2 = b, -c, \text{ respectively}$$

At the exterior free edge

$$\sigma_{11}^{(k)}(x_1, x_2) = 0$$

$$\sigma_{13}^{(k)}(x_1, x_2) = 0 \quad (44)$$

$$\sigma_{12}^{(k)}(x_1, x_2) = 0 \quad k = 1, 2; \quad x_1 = a$$

For the symmetric laminate, the following relations are required at the plane of symmetry

$$u_{1,2}(x_1, x_2) = 0$$

$$u_{2,1}(x_1, x_2) = 0 \quad (45)$$

$$u_{3,2}(x_1, x_2) = 0$$

The above conditions (42)-(45), are satisfied by minimization of the

error of the residuals in the sense of a weighting function technique. The stresses and the relevant derivatives of the displacements (as required in Eqn. (45)) have the general form

$$\mathbb{R} = \sum_n D_n \phi_n - f \quad (46)$$

where  $D_n$  are the coefficients  $a_i$ ,  $A_j$ ,  $d_k^{(h)}$ , and  $\phi_n$  are the trial functions to be identified with the eigenfunctions of the exact solution. The function  $f$  is either zero or consists of the solutions obtained from the hole effect, Eqn. (42). Orthogonalization of  $\mathbb{R}$  with the trial functions, such that the inner product vanishes, is performed in the form

$$(\phi_j, [\sum_{i=1}^n D_i \phi_i - f]) = 0 \quad j = 1, 2, \dots, n \quad (47)$$

The inner product yields  $n$  equations where  $n$  is the number of all unknowns taken into account. Thus

$$\sum_{i=1}^n D_i \int_D (\phi_j \phi_i) dS = \int_D (\phi_j f) dS \quad j = 1, 2, \dots, n \quad (48)$$

where  $D$  is the domain in which the problem is treated and therefore it is where integration is performed. In our case, this domain is changed according to the line where the boundary condition takes place and that is where integration is carried out. The explicit form of Eqn. (48) is given by

$$\begin{aligned}
& D_1 \left[ \int_0^a (F_{21}^{(1)} F_{2j}^{(1)} + F_{41}^{(1)} F_{4j}^{(1)} + F_{61}^{(1)} F_{6j}^{(1)}) dS \right]_{x_2 = b} \\
& + \int_0^b (F_{11}^{(1)} F_{1j}^{(1)} + F_{51}^{(1)} F_{5j}^{(1)} + F_{61}^{(1)} F_{6j}^{(1)}) dS \Big|_{x_2 = a} \\
& + \int_{-c}^0 (F_{11}^{(2)} F_{1j}^{(2)} + F_{51}^{(2)} F_{5j}^{(2)} + F_{61}^{(2)} F_{6j}^{(2)}) dS \Big|_{x_1 = a} \\
& + \int_t^{a-t} (F_{31}^{(1)} F_{3j}^{(1)} + F_{51}^{(1)} F_{5j}^{(1)}) dS \Big|_{x_2 = 0} \\
& + \int_t^{a-t} (F_{31}^{(2)} F_{3j}^{(2)} + F_{51}^{(2)} F_{5j}^{(2)}) dS \Big|_{x_2 = 0} \\
& + \int_0^a (L_{11}^{(2)} L_{1j}^{(2)} + L_{21}^{(2)} L_{2j}^{(2)} + L_{31}^{(2)} L_{3j}^{(2)}) dS \Big|_{x_2 = CL} = \\
& = \int_t^{a-t} (\sigma_{3\alpha 1}^{(1)} F_{3j}^{(1)} + \sigma_{5\alpha 1}^{(1)} F_{5j}^{(1)} + \sigma_{3\alpha 1}^{(2)} F_{3j}^{(2)} + \sigma_{5\alpha 1}^{(2)} F_{5j}^{(2)}) dS \Big|_{x_2 = 0} \quad (49)
\end{aligned}$$

in which  $j=1,2,\dots$  (no. of unknowns) and  $t$  is the laminate thickness. In Eqn. (49),  $F_{\alpha 1}^{(m)}$  is defined by the homogeneous and particular parts of the solution, Eqns. (27) and (29) respectively.

The index  $\alpha = 1,2,3,4,5,6$  denotes the contracted Greek notation for the stresses. The functions  $L_{\beta 1}^{(m)}$  ( $\beta = 1,2,3$ ) are defined by the derivatives (45). The integrals in (49) are performed numerically using Simpson's method. The number of points of integration is of great importance when convergence of the solution is considered. Equations (34), (36)-(41), (49) provide a set of linear algebraic equations

$$AD = B \quad (50)$$

in which  $A$  is the coefficients matrix with order  $(q \times n)$ ,  $q > n$ ;  $q$  is the number of unknowns associated with the 14 equations from the elasticity solution (34), (36)-(41), (49), (A1)-(A6), and  $n$  is the total number of unknowns. In Eqn. (49)  $D$  is a vector  $(n \times 1)$  of the unknowns.

The over determined system may be solved in the least square sense as

$$A^\dagger AD = A^\dagger B \quad (51)$$

in which  $A^\dagger$  is the conjugate transpose of  $A$ . Eqn. (51) turns out to be solvable since  $A^\dagger A$  is of the order  $(n \times n)$  and  $A^\dagger B$  is  $(n \times 1)$ , but due to the nature of the general solution it appears that some rows and/or columns might be zero or show dependency which causes  $A^\dagger A$  to be singular. Even if a mathematical singularity does not occur, due to the use of a computer, the solution of such a system might be strongly ill-conditioned, depending upon the properties of the plies which enter the equations. This ill-conditioned behavior may be treated by adopting the method of singular-value decomposition, Stewart (1973). According to this method, every matrix  $A$   $(q \times n)$ ,  $q > n$ , may be expressed as the multiplication of three matrices as follows

$$A = U \Sigma V^T \quad (52)$$

where  $U$  and  $V$  are  $(q \times q)$  and  $(n \times n)$  unitary matrices whose columns are the

orthonormalized eigenvectors of  $AA^T$  and  $A^TA$ , respectively. The matrix  $\Sigma$  is  $\text{diag}(\sigma, 0)$  which is an  $(q \times n)$  matrix with  $\sigma$  being the square roots of the non-zero eigenvalues of  $A^TA$ . Let  $U'$  be denoted by

$$U' = AV \left[ \begin{array}{c|c} \Sigma_r^{-1} & 0 \\ \hline 0 & 0 \end{array} \right] \quad (53)$$

in which  $\Sigma_r^{-1}$  are the reciprocals of the non-zero components of  $\Sigma$  in a descending order on the diagonal. Let us also define  $w$  by

$$w = U'^T B \quad (54)$$

and

$$v_i = \frac{w_i}{\sigma_i} \quad i = 1, 2, \dots, n \quad (55)$$

The desired solution is determined from

$$\{D\} = [V]\{v\} \quad (56)$$

Having obtained  $\{D\}$ , the displacements and stresses are computed from Eqns. (27), (29) and (30). A description of the program "EDGSTR" is given in appendix C. This program follows the above analysis and calculates the stresses and displacements.

### 2.3. Convergence of the solution and examples

Consider the case of a  $[\pm 45]_5$  laminate which was considered by Wang and Choi (1982), Wang and Crossman (1977), Pipes and Pagano (1970), and Lagace and Kassapoglou (1987). The properties of the unidirectional single ply as given by the above mentioned authors, for the graphite-epoxy system are:

$$E_1 = 20\text{e6 psi}, \quad E_2 = E_3 = 2.1\text{e6 psi}, \quad G_{12} = G_{13} = G_{23} = 0.85\text{e6 psi},$$

and  $\nu_{12} = \nu_{23} = \nu_{13}$ .

As a case study, a circular hole is centrally located, and the laminate is subjected to a unit stress in the  $x_3$  direction as shown in fig. 4a.

Results were obtained in three locations: in the vicinity of the hole and at the free edge of the laminate as well as far from these two locations where classical lamination theory or results of anisotropic plate analysis with a center hole are valid. Convergence of the obtained stresses was studied by examining the effect of the number of eigenvalues and the number of integration points on the results. The study of the effect of the number of eigenvalues was limited to the ability of the computer to provide accurate solutions when using the Muller (1956) deflation method since this method involves calculations of differences between numbers that converge to the point that multiplication by that difference results in computer underflow. Convergence was studied on all stresses. Predicted results for the normal stress  $\sigma_{22}$  are exhibited for three different numbers of eigenvalues and 200 integration points as shown in fig. 3. Observing curves 1-5 in Fig. 3, we conclude that convergence is achieved using 25 eigenvalues with slight changes between the cases of 50, 100, and 200

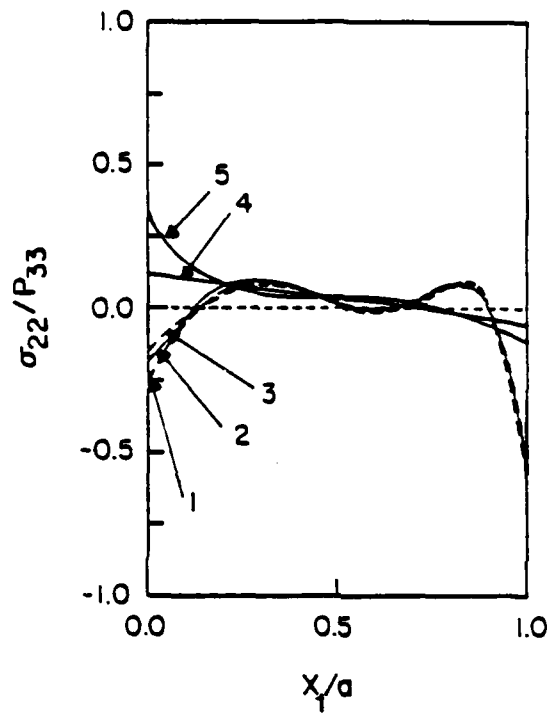


Figure No. 3: Examine convergence of  $\sigma_{22}$  through various numbers of eigenvalues and points of integration

curve #:	1	2	3	4	5
eigenvalues:	25	25	25	15	7
integration pnts:	200	100	50	100	100



integration points. Curves 4 and 5 show results in which low number of eigenvalues are used and therefore result in wrong stress distribution. Curves 1-3 present close results in which the same number of 25 eigenvalues are used and show convergence. The results of curves 1-3 at  $x_1/a = 1$ , match the results presented by Wang and Choi (1982) for the similar case of a straight free edge. In order to investigate the effect of the hole on the stress distribution at various locations along its circumference, we present in fig. 4b all stress distributions along a cut made perpendicular to the laminate straight free edge, and in fig. 4c, the variation of the normal stress  $\sigma_{22}$  along the cross sections which are radial to the hole at  $\alpha = 0^\circ, 10^\circ, 30^\circ, 60^\circ$ , and  $80^\circ$ . This figure exhibits well the fiber orientation dependence which provide various orders of singularities. The values of the orders of singularity are given by

$$\delta_1 = -.025575658 \quad \text{for } \alpha = 0^\circ$$

$$\delta_1 = -.026100409 \quad \text{for } \alpha = 10^\circ$$

$$\delta_1 = -.030274706 \quad \text{for } \alpha = 30^\circ$$

$$\delta_1 = -.030274706 \quad \text{for } \alpha = 60^\circ$$

$$\delta_1 = -.026100409 \quad \text{for } \alpha = 80^\circ$$

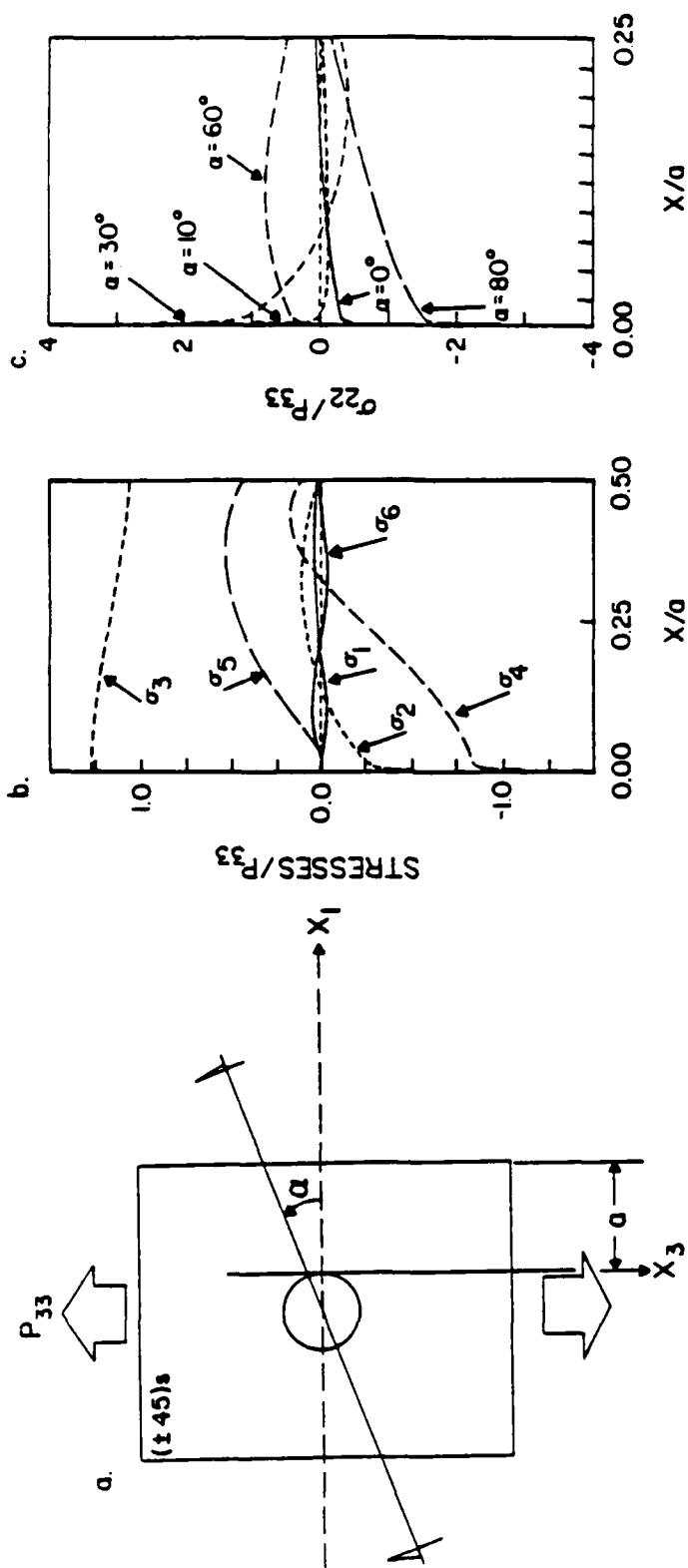


Figure No. 4: a: Geometry and description of cuts  
b: Stress distribution at  $\alpha = 0^\circ$ ; 25 e.v., 200 int. pnts.  
c: Comparison of normal stress  $\sigma_{22}$  at various cuts

where  $\delta_1$  for the cases of  $\alpha = 10^\circ, 30^\circ, 60^\circ$  and  $80^\circ$  is calculated for the direction tangential to the hole edge which provides an interface between  $[35/-55]$ ,  $[15/-75]$ ,  $[-15,75]$  and  $[-35/55]$  orientations, respectively. The latter analysis is done using a coordinate system transformed to match the direction tangential to the hole and to the radial cross section in order to satisfy the basic assumptions introduced in 2.1 and the traction-free boundary conditions at the hole edge as explained in 2.1.2.2. The validity of the results for the transformed configuration are limited to the vicinity of the hole within the region in which the stresses are controlled by the mathematical singularity.

## Chapter 3

PREDICTION MODEL FOR THE ONSET OF DELAMINATION  
BASED ON THE BOUNDARY LAYER EFFECT

The prediction model is established in this chapter, based on the following understandings of the phenomenon of edge delamination.

1. Delaminations are controlled by strain energy and its rate of change during the delamination process which is the strain energy release rate. The latter is a well-defined mathematically quantity and is also experimentally measurable.
2. There is a region of influence of the edge effect within which strain energy should be examined.
3. Since the stress field changes its nature drastically in close vicinity to the edge, the phenomenon is localized and therefore one should consider the rate of changes in that region which is of the order of one laminate thickness.

Near the laminate edge (straight or at the hole), the stress field is completely governed by the singular term  $K_I x^{\delta_1}$  as it appears in Eqn. (23). This expression consists of the coefficient  $K_I$  which is called in the literature "the near-field parameter" or "free-edge stress intensity factor", and by the singularity which appears in the exponent. To compare the stresses at two locations (any of the six components of the stress tensor) while taking the limit as the distance  $r$  goes to zero, we obtain the following:

$$\frac{\sigma^{(1)}}{\sigma^{(2)}} = \frac{K^{(1)} r \delta_1^{(1)}}{K^{(2)} r \delta_1^{(2)}} \quad (57)$$

which is also

$$\frac{\sigma^{(1)}}{\sigma^{(2)}} = \frac{K^{(1)}}{K^{(2)}} r^{\delta_1^{(1)} - \delta_1^{(2)}} \quad (58)$$

in which the indices 1,2 designate two examined and compared interfaces.

We can not actually compare stresses at the edges because they result in infinite values, so we chose to compare the parameters which are a combination of the stress terms. There are three cases to be examined through Eqn. (58). The first occurs when the power  $\delta_1^{(1)} - \delta_1^{(2)}$  is positive, the second when it is negative, and the third when it vanishes. Note that the value of  $\delta$  is always negative and within the region  $[-1,0]$ , and both  $K^{(1)}$  and  $K^{(2)}$  should be positive (negative sign indicates compression which implies no delamination problem). Thus, mathematic manipulation of Eqn. (58) offers the following criterion:

$$\delta_1^{(1)} < \delta_1^{(2)} \Rightarrow \lim_{r \rightarrow 0} \left[ \frac{\sigma^{(1)}}{\sigma^{(2)}} \right] = 0 \Rightarrow \sigma^{(1)} < \sigma^{(2)} \quad (a)$$

$$\delta_1^{(1)} > \delta_1^{(2)} \Rightarrow \lim_{r \rightarrow 0} \left[ \frac{\sigma^{(1)}}{\sigma^{(2)}} \right] = \infty \Rightarrow \sigma^{(1)} < \sigma^{(2)} \quad (b) \quad (59)$$

$$\delta_1^{(1)} = \delta_1^{(2)} \Rightarrow \frac{\sigma^{(1)}}{\sigma^{(2)}} = \frac{K^{(1)}}{K^{(2)}} \quad (c)$$

Let us examine once again the expression for the stress fields as

reflected through Eqns. (24) and (29). We recognize the singular nature at the edge of the laminate. The asymptotic stress field is generally expressed by the combination of the above-mentioned equations as,

$$\sigma_{\alpha} = \sum_{k=1}^3 \left[ C_{\alpha k} Z_k^{\delta_1} + C_{\alpha(k+3)} \bar{Z}_k^{\delta_1} \right] + o(\text{higher order, nonsingular terms})$$

( $\alpha = 1, 2, 3, 4, 5, 6$ ) (60)

in which the coefficients  $C_{\alpha k}$  are related to the homogeneous solution as presented by Eqn. (27) associated with the first eigenvalue,

$$C_{\alpha k} = d_1 f_{\alpha k 1}^* \quad (61)$$

the functions  $f_{\alpha k 1}^*$  are the coefficients of the coordinate  $Z_k$  as they appear in Eqn. (24) and the coefficient  $d_1$  is the relevant component of the vector  $D$  in Eqn. (48), associated with the order of the singularity.

The near-field parameters,  $K_i$ , play the role of amplitudes in the singular edge stresses. These parameters are introduced by

$$K_i = \lim_{x_1 \rightarrow 0} x_1^{-\delta_1} \sigma_i(x_1, 0; \delta_1) \quad i = 1, 2, 3, 4, 5, 6 \quad (62)$$

The coordinate  $x_2$  is zero since the coordinate system is located at the intersection of the interface and the hole edge. Eqn. (62) is the reciprocal form of Eqn. (61). The coordinate  $Z_k$ , as explained in Eqn. (16), is

$$Z_k = x_1 + \mu_k x_2$$

but since  $x_2$  is taken to be zero,

$$Z_k \equiv \bar{Z}_k \equiv x_1$$

Following Eqns. (60) & (61), we conclude

$$K_1 = d_1 \left[ \sum_{k=1}^3 [c_k \mu_k^2 + c_{k+3} \bar{\mu}_k^2] \right] \quad (a)$$

$$K_2 = d_1 \left[ \sum_{k=1}^3 [c_k + c_{k+3}] \right] \quad (b)$$

$$K_4 = - d_1 \left[ \sum_{k=1}^3 [c_k \eta_k + c_{k+3} \bar{\eta}_k] \right] \quad (c) \quad (63)$$

$$K_5 = d_1 \left[ \sum_{k=1}^3 [c_k \eta_k \mu_k + c_{k+3} \bar{\eta}_k \bar{\mu}_k] \right] \quad (d)$$

$$K_6 = - d_1 \left[ \sum_{k=1}^3 [c_k \mu_k + c_{k+3} \bar{\mu}_k] \right] \quad (e)$$

and

$$K_3 = \frac{S_{3j} K_j}{S_{33}} \quad j = 1, 2, 4, 5, 6 \quad (f)$$

In order to solve for the energy release rate quantity, the ideas of fracture mechanics are used. The solution for the problem of delamination crack is similar to the analysis presented in chapter 2.

The calculation of the stress singularity is done with the same tool, taking the angles of the edge faces  $\theta$ , as shown in fig. 2, as  $180^\circ$  and  $-180^\circ$ , respectively. Again, the singularity is the number within the series of eigenvalues which is in the domain  $[-1,0]$ . The similarity to fracture mechanics enables us to denote the near-field parameters as "free-edge stress intensity factors" in equivalent terminology to the crack tip stress intensity factors as it appears in linear elastic fracture mechanics, Broek (1982). For the complete analogy to the field of fracture mechanics, we may present the three modes of stress intensities,  $K_I$ ,  $K_{II}$ , and  $K_{III}$  as presented by Erdogan (1965) and Rice (1965) for the case of cracks in dissimilar media. Here we refer to the interlaminar stresses  $\sigma_2$ ,  $\sigma_4$ , and  $\sigma_6$ ,

$$\begin{aligned}
 K_I &= \lim_{x \rightarrow 0^+} \sum_{n=1}^3 \sqrt{2\pi} x^{-\delta_n} \sigma_{2n}(x, 0; \delta_n) \\
 K_{II} &= \lim_{x \rightarrow 0^+} \sum_{n=1}^3 \sqrt{2\pi} x^{-\delta_n} \sigma_{4n}(x, 0; \delta_n) \\
 K_{III} &= \lim_{x \rightarrow 0^+} \sum_{n=1}^3 \sqrt{2\pi} x^{-\delta_n} \sigma_{6n}(x, 0; \delta_n)
 \end{aligned} \tag{64}$$

As noted by Erdogan (1965), the stress intensities in Eqn. (60) are different than the ones in a homogeneous solid, and therefore its physical interpretation is different as well.

Following the concept of virtual crack extension, Irwin (1957), and adapting that into the problem of delamination cracking, Christensen (1979), we may write the expression for the energy release rate, based



on the displacements  $v, u$ , and  $w$ , and the length of the virtual crack extension,  $\delta\beta$ , as follows,

$$\begin{aligned}
 G_{\text{total}} &= G_I + G_{II} + G_{III} \\
 &= \lim_{\delta\beta \rightarrow 0} \frac{1}{2\delta\beta} \int_0^{\delta\beta} \left\{ \sigma_2(r, 0) [v^{(m)}(\delta\beta - r, \pi) - v^{(m+1)}(\delta\beta - r, -\pi)] \right. \\
 &\quad + \sigma_6(r, 0) [u^{(m)}(\delta\beta - r, \pi) - u^{(m+1)}(\delta\beta - r, -\pi)] \\
 &\quad \left. + \sigma_4(r, 0) [w^{(m)}(\delta\beta - r, \pi) - w^{(m+1)}(\delta\beta - r, -\pi)] \right\} \quad (65)
 \end{aligned}$$

Observing Eqns. (63)-(65), we conclude that all the expressions presented are proportional, respectively. Therefore, for the purpose of comparisons, we may chose the most convenient term out of these three and, rather than using the physical expression of the strain energy release rate, we may use the relatively simple to calculate term of the near-field parameters.

To summarize the procedure of applying the prediction model, we first start with the analysis for the stress singularities at all the interfaces at different azimuthal angles. Next, we calculate the near-field parameters by the completion of the particular solution. The sign of the parameters determines the behavior, minus is compression and plus is tension. We may filter out the cases of negative values of the near-field parameters since obviously it indicates no delamination. For the case in which two similar interfaces are compared, we obtain similar

orders of singularity. Thus, a decision is made based upon comparison of energy release rate or the magnitude of the edge intensity.

## Chapter 4

## EXPERIMENTAL PROCEDURE

Experimental work is essential for the validation of any theory. Postulations and means of investigation may be examined and refined by the results of reality. With these facts in mind, a testing program was setup in an attempt to bring as much reality as possible into the theoretically based prediction model. The testing program with all its aspects is presented in this chapter.

The objective of the tests was to detect and locate the onset of delamination at the edge of a hole in a composite laminate. Two major factors were taken into consideration, the materials and loads. When one considers materials in conjunction with composites, there are two major elements, the combination of fibers/matrix, and the fiber direction as reflected in stacking sequence. The second factor, loading condition, covers the other major aspect of performance of a tested specimen. Therefore, both tension and compression were applied. The following sections give details about these as well as other points of interest, including the description of observations and results.

#### 4.1 Specimens - materials and geometry

Two types of unidirectional systems were chosen. They differ in the type of matrix material but both have used the same fiber. They are the AS4/3501-6 , herein designated by "Z", and the AS4/1808 material designated by "Y". This choice of matrix systems provided an excellent

opportunity to examine the dependency of behavior upon matrix type and its performance sensitivity.

The stacking sequences chosen were  $[(0/45/90/-45)_s]_4$  which is a quasi-isotropic, and  $[(0/45/0/-45)_s]_4$  - an orthotropic layup. The first is designated by "A" and the other by "B".

The geometry of the specimens corresponded to the basis for the analysis and may be viewed in table 3 also referring to fig. 2. All specimens, three each of the Z-A, Z-B, Y-A, and Y-B types (which are the combinations of the two matrix systems and the two types of stacking sequences) for a total of twelve, were center-notched, finite-width coupons 6 inches long.

#### 4.1.1 How specimens were made

All specimens were cut from large plates. The plates were Ultra Sonically scanned in order to detect possible voids and to eliminate extraneous and irrelevant disturbances. A diagram, describing the cutting process, was made. Each specimen was coded by its location within the parent plate. The coding system resulted in the addition of two digits to the two letters from the combination Z, Y, A, and B, and completed the "name" of each specimen. All these procedures were used to assist in isolating peculiar behavior due to irrelevant factors, and to assist in isolating the interpretation of damage.

#### 4.1.2 Notched and unnotched properties

Properties of the unidirectional plates are given in table 1. Table 2 provides unnotched laminate properties for all four combinations of Z-A, Z-B, Y-A, and Y-B, as calculated by means of classical lamination theory, Jones (1975).

Geometrical properties of all specimens may be viewed in table 3. These properties were measured by a digital caliper and averaged over few measurements for each of the dimensions. Table 3 also provides the strength information for critical tensile and compressive stresses of the notched specimens as obtained by testing three specimens of each type. The ungripped length of the specimens was 2.5". For both, tension and compression loadings, a failure in which critical load was determined, was defined when the specimen could not sustain any more load. For the tension case, such failure occurred as the specimen was broken into two pieces. For the compression case, failure occurred when plies started to buckle.

Table No. 1: Material Properties

	AS4/3501-6		AS4/1808	
	compression	tension	compression	tension
$E_1$ [Msi]	21.1	20.7	17.0633	17.2395
$E_2$ [Msi]	2.0	2.0	1.226	1.164
$\nu_{12}$	0.3	0.3	0.2866	0.304
$G_{12}$ [Msi]	0.835		0.6937	
$t$ [in]	0.005		0.0058	

Table No. 2: Laminate Properties

	[(0/45/90/-45) <sub>s</sub> ] <sub>4</sub>		[(0/45/0/-45) <sub>s</sub> ] <sub>4</sub>	
	AS4/3501-6	AS4/1808	AS4/3501-6	AS4/1808
<b>E<sub>1</sub> [Msi]</b>	8.371	6.668	12.19	9.86
<b>E<sub>2</sub> [Msi]</b>	8.371	6.668	3.874	2.096
<b>G<sub>12</sub> [Msi]</b>	3.179	2.558	3.179	2.558
<b>ν<sub>12</sub></b>	0.3169	0.3032	0.6568	0.6661

Table NO. 3: Test specimens - dimensions &amp; strength

type	dimensions [in]				critical stress [ksi]		critical load [kip]	
	e	d <sub>1</sub>	a	t	S <sub>T</sub>	S <sub>C</sub>	tension	compres.
Y-B 3-4	0.366	0.378	0.363	0.18	64.1	-65.2	10.80	11.02
Y-B 3-6	0.364	0.379	0.364	0.1787	64.1	-65.2	10.71	10.93
Y-A 6-9	0.363	0.379	0.364	0.1772	39.4	-45.2	7.74	8.88
Y-A 6-11	0.363	0.38	0.363	0.1773	39.4	-45.2	7.75	8.89
Z-B 7-1	0.558	0.38	0.561	0.1817	59.2	-52.8	16.15	14.4
Z-B 7-2	0.559	0.38	0.56	0.1802	59.2	-52.8	15.99	14.26
Z-A 7-6	0.561	0.378	0.561	0.1817	42.3	-43.8	11.53	11.94
Z-A 7-7	0.565	0.378	0.559	0.1813	42.3	-43.8	11.51	11.92
Y-B 3-8	0.364	0.38	0.367	0.1773	64.1	-55.2	10.65	10.86
Y-A 6-13	0.363	0.379	0.364	0.1728	39.4	-45.2	7.55	8.66
Z-B 7-3	0.557	0.38	0.56	0.18217	59.2	-52.8	16.16	14.41
Z-A 7-8	0.562	0.371	0.559	0.18166	42.3	-43.8	11.52	11.93

note: refer to fig. 2 for dimensions designation



#### 4.2 Testing procedure

To achieve the objectives of the testing program, the procedure consisted of quasi-static loading in both tension and compression. Eight specimens were tested in tension, and the remaining four specimens were tested in compression. A list of the specimens by their codes, divided into the two types of loads, follows:

Tension:

Y-B 3-4, Y-B 3-6, Y-A 6-9, Y-A 6-11, Z-B 7-1, Z-B 7-2, Z-A 7-6, Z-A 7-7

Compression:

Y-B 3-8, Y-A 6-13, Z-B 7-3, Z-A 7-8

The first load condition was chosen as 60% of the given critical load, as found in an early experimental study, for the relevant case. At the critical load level, failure of the specimens was observed. Then, the load was raised in steps of 5% at a time. After each loading step, the specimen was taken out of the testing machine and X-rayed, then put back to the machine to be reloaded. In the following few sections the details of that procedure are described.

##### 4.2.1 Testing machines

For the tension test, an INSTRON screw-driven test machine was chosen. That machine is very convenient due to its simplicity of operation and calibration. The load rate was controlled.

For the compression test, the more complicated MTS servo-hydraulic machine was chosen. This machine is capable of carrying out a reliable compression test without risking the loss of specimens in possible

buckling. The test may be either strain, load, or stroke controlled as required to ensure a successful completion of the experiment.

#### 4.2.2 Loading fixture and measurements during the test

The only measurements taken during the test were of the load level to ensure accuracy of the current load magnitude. In the tension test, two types of load cells were used. A 10-kip load cell was used for load levels under 10 kips. A 20-kip load cell was used for load levels above 10 kips. A Digital Volt Meter was used to measure the load level. For the 10-kip load cell, 1 volt indicated 1 kip loading, while for the 20-kip load cell 1 volt corresponded 2 kips. On the MTS machine, the range of 20 kips was used to provide the range of 1 volt for 2 kips.

#### 4.2.3 X-ray detection technique

As mentioned, the specimens were taken out of the testing machine after each loading step and inspected for delaminations by the X-ray radiographic technique. The following is a full description of the procedure as carried out.

Before the removal of the specimen from the testing machine, the specimen was held under 50% of the testing load and a penetrant material was applied to the edges of the hole and the free edges of the specimen as well as all over the upper and lower surfaces. The type of penetrant used was Zinc Iodine which penetrates delamination areas and cracks of all kinds. When the specimens were X-rayed, the Zinc Iodine blocked the

X-ray beam and, by doing so, it created white spots in the shape of the defects on the film, which become black spots on the positive after being developed. That is the way we detected cracks and delaminations on the resulting pictures.

Once the Zinc Iodine was applied to the specimen, it was left for a couple of hours in order to penetrate as much as possible. Then, the outer surfaces of the specimen were cleaned very carefully with Acetone to prevent any direct contact of Zinc Iodine with the film (to prevent the film destruction).

The next stage was the actual X-ray process. There were two types of radiographs taken for each specimen. The so-called  $0^\circ$ , in which the specimen was X-rayed through its surface while lying on the film, and the  $90^\circ$  in which the specimen was put on its edge resulting in a picture of a longitudinal section. The film used was a Kodak SR-5 single-sided X-ray film. For the  $0^\circ$ , the specimen was exposed for 3 minutes at an intensity of 43 mv. For the  $90^\circ$ , the exposure time was 4 minutes at an intensity of 80 mv. Next, the specimen was removed, and the film was soaked in a developer solution for 4 minutes, then rinsed for less than a minute in pure water and soaked in a fixer for another 4 minutes, then rinsed again and put aside to dry. That process was carried out eight times for the tension test and six time for the compression test, a total of 88 times !

#### 4.3 Observations and results

After being X-rayed, the results were carefully observed in a

microfiche machine under 36X magnification. The purpose, of course, was to inspect for delaminations. Results of selective stages for each specimen are presented in figs. 5 - 20. The first figure of each specimen shows a scheme of the situation throughout the selected stages, while the second figure is a print of the X-ray of the last stage of both the  $0^\circ$  and the  $90^\circ$  exposures. Fig. 5a illustrates the views of specimens shown in figs. 5 - 20.

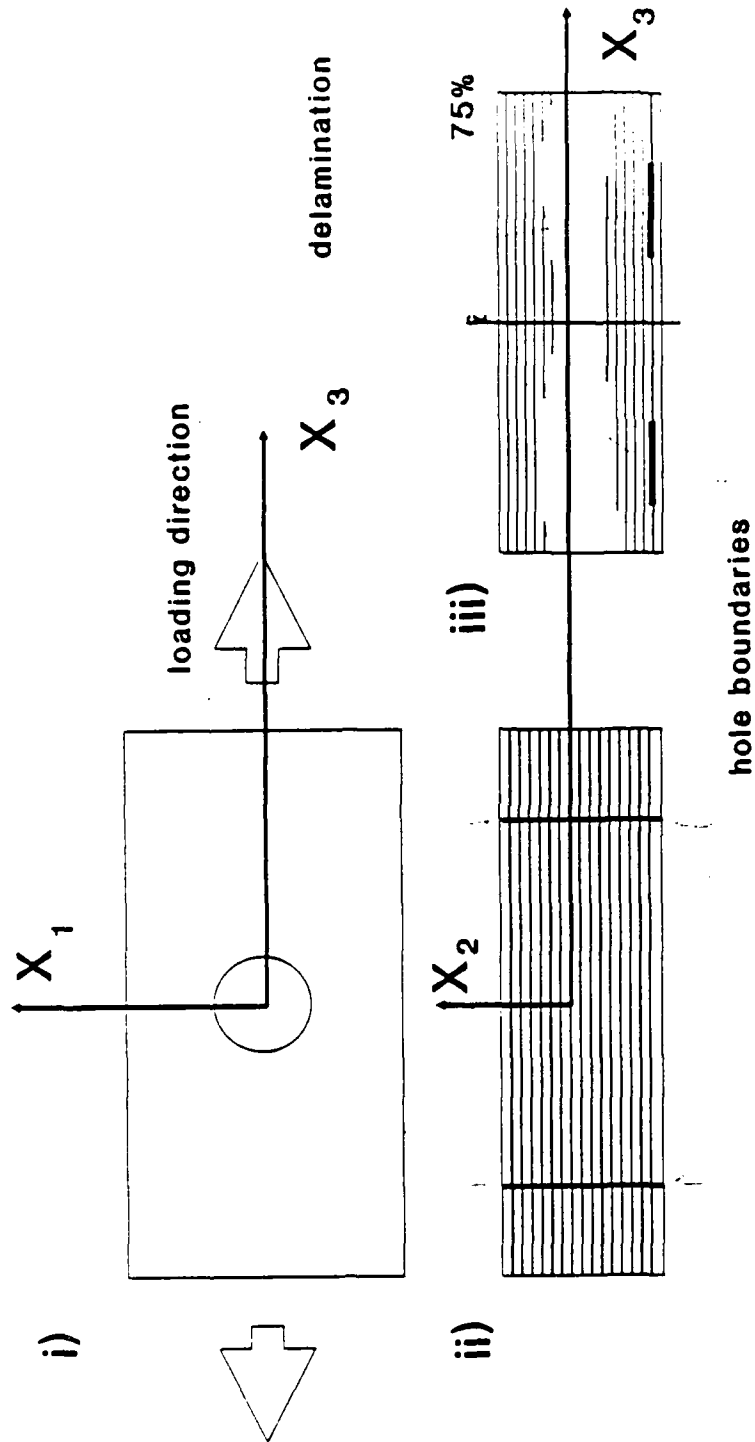


Figure No. 5a: i) top view of specimen, figures 6,8,10,12,14, 16, 18,20  
 ii) edge view, cut at  $x_3$  axis, figures 6,8,10,12,14,16,18,20  
 iii) same view as ii), figures 5,7,9,11,13,15,17,19,29

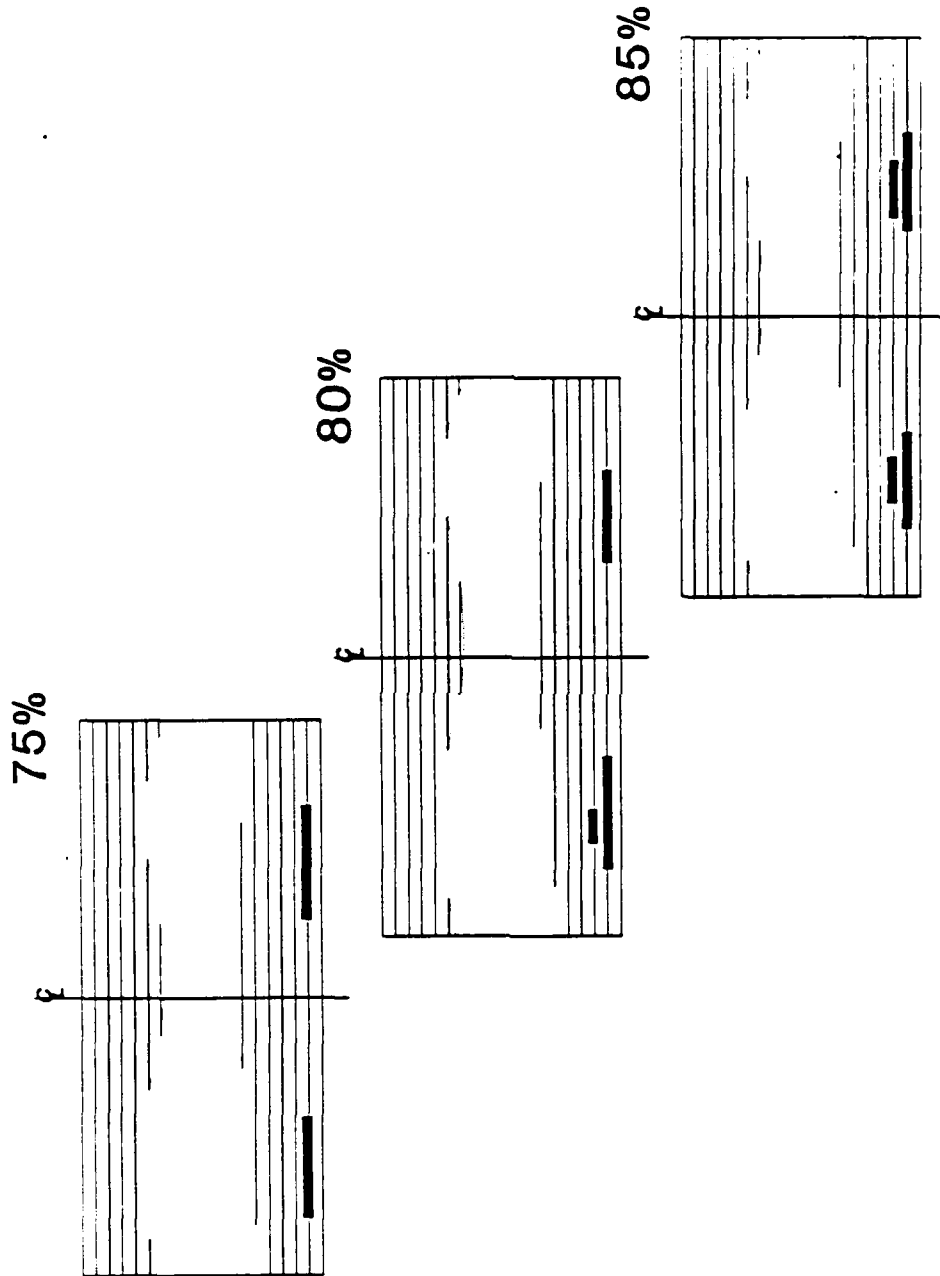
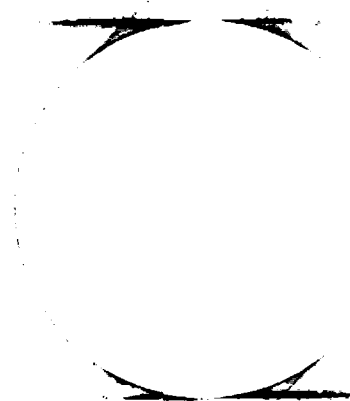


Figure No. 5: delamination process in Y-B 3-4, tension



YB 36 90



YB 36 90

Figure No. 6: X-Ray of Y-B 3-4, 90% critical tensile load  
specimen top view and cut shows hole surface

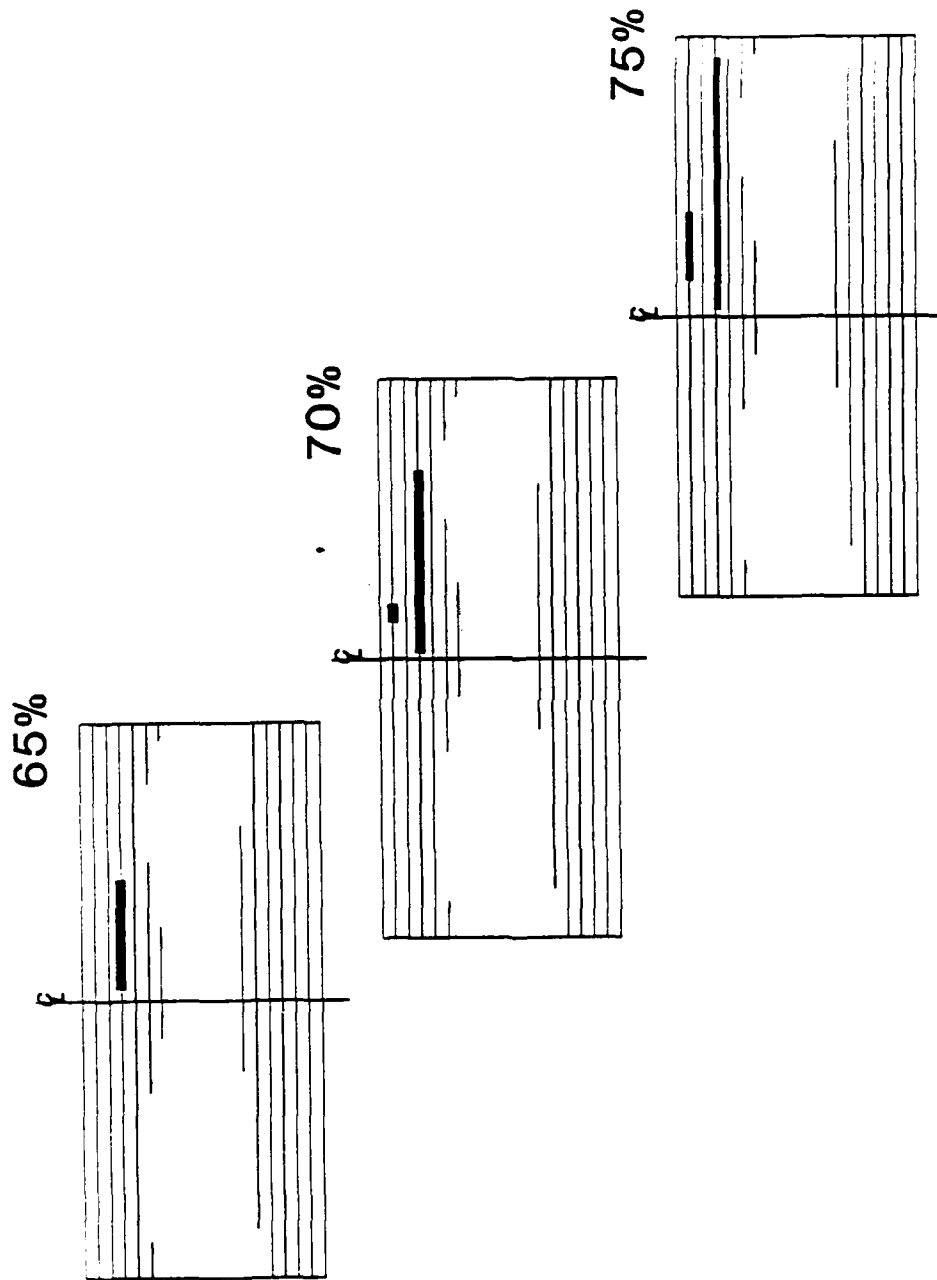
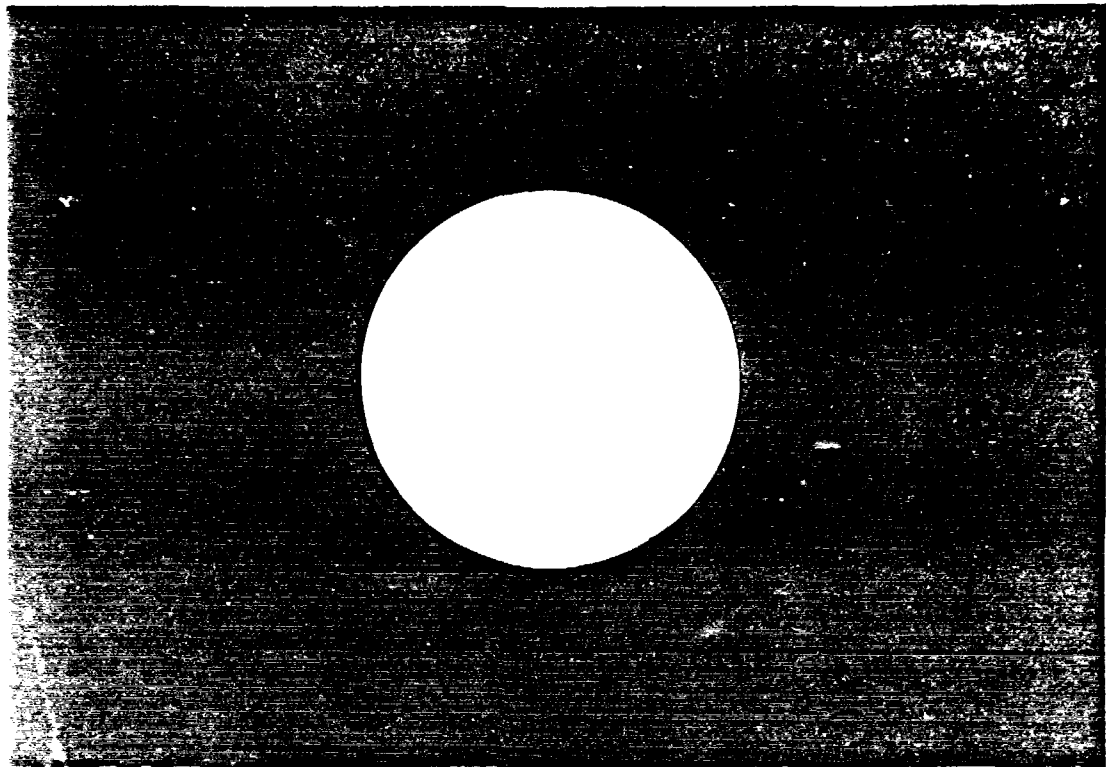


Figure No. 7: delamination process in Y-B 3-8 compression





YB 38 80

YB 38 80

Figure No. 8: X-Ray of Y-B 3-8, 80% critical compress. load  
specimen top view and cut shows hole surface

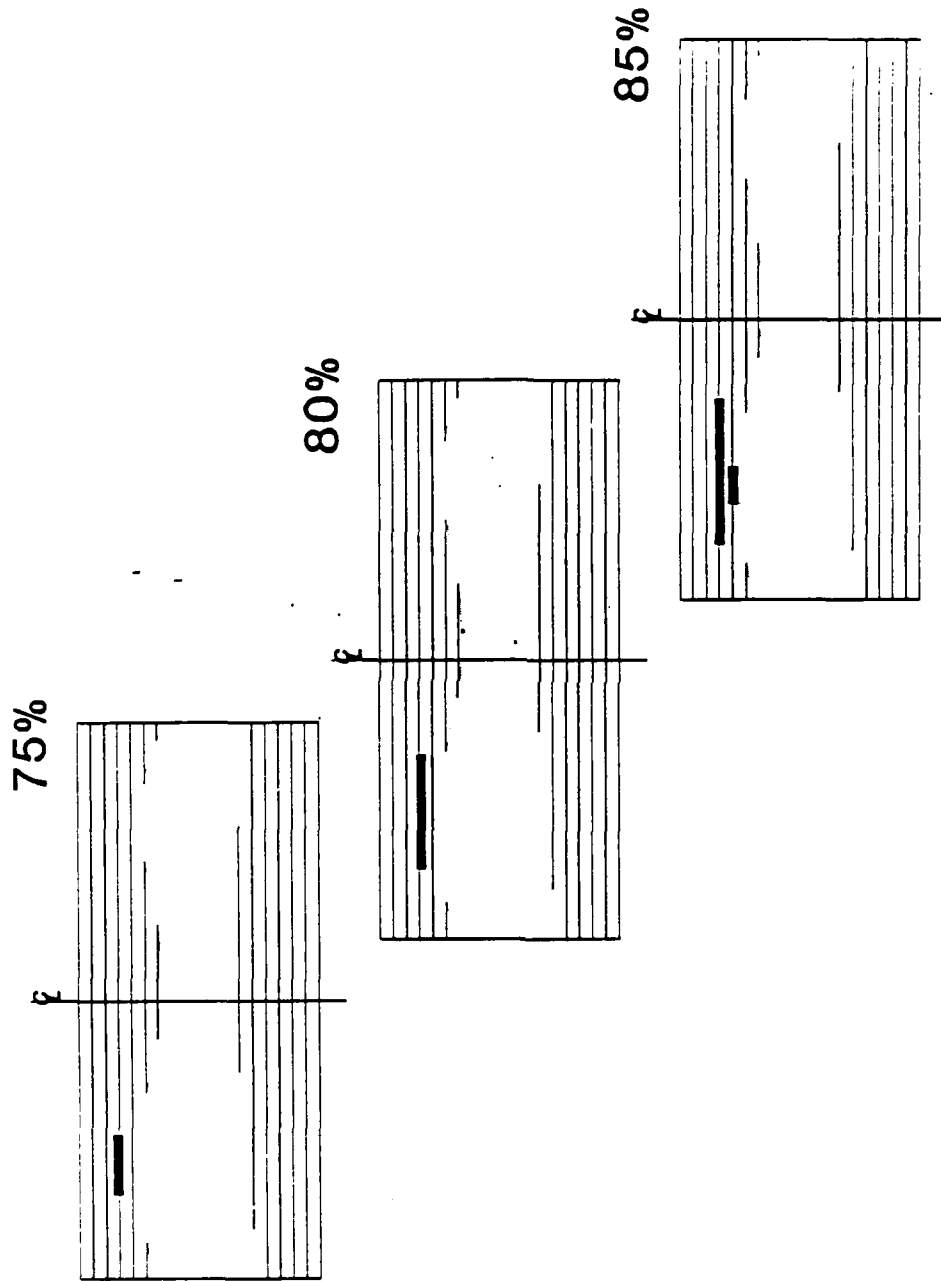
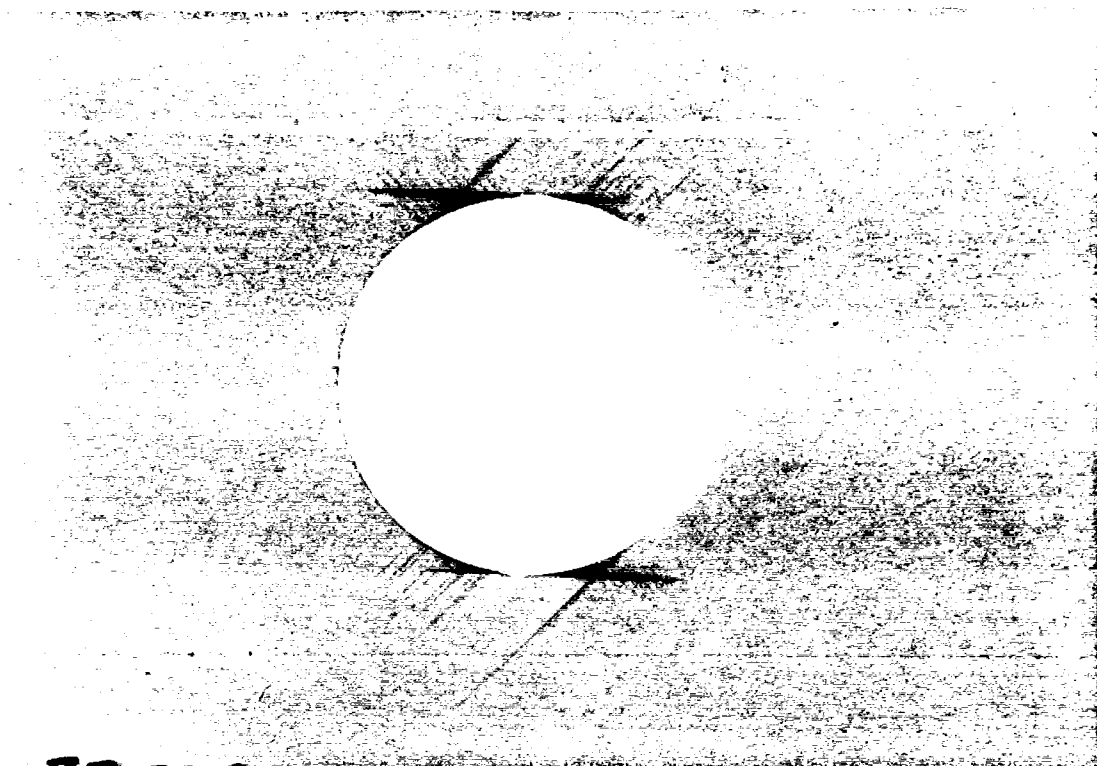


Figure No. 9: delamination process in Z-B 7-2, tension



**ZB 72 90**

**ZB 72 90**

Figure No. 10: X-Ray of Z-B 7-2, 90% critical tensile load  
specimen top view and cut shows hole surface

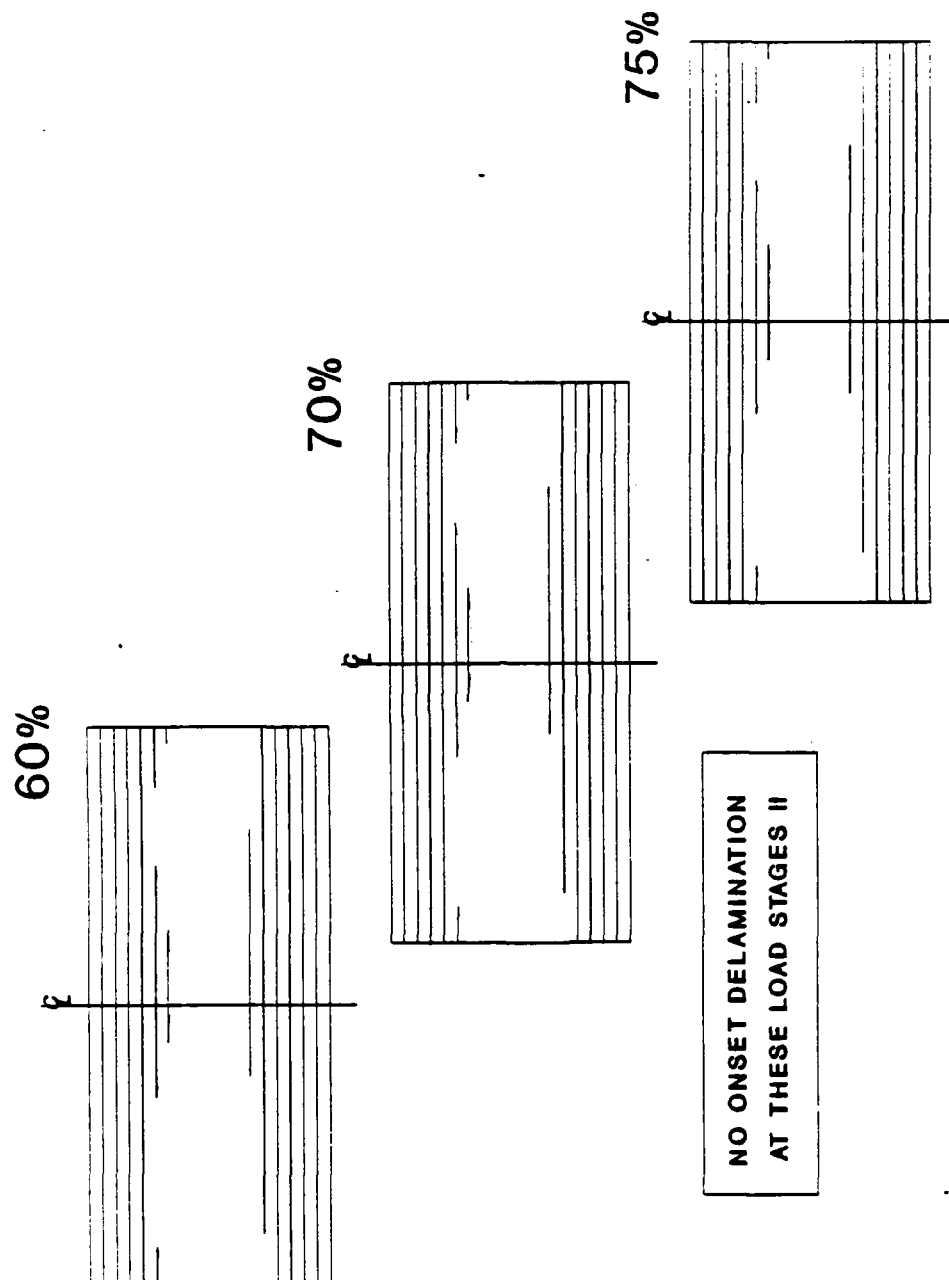
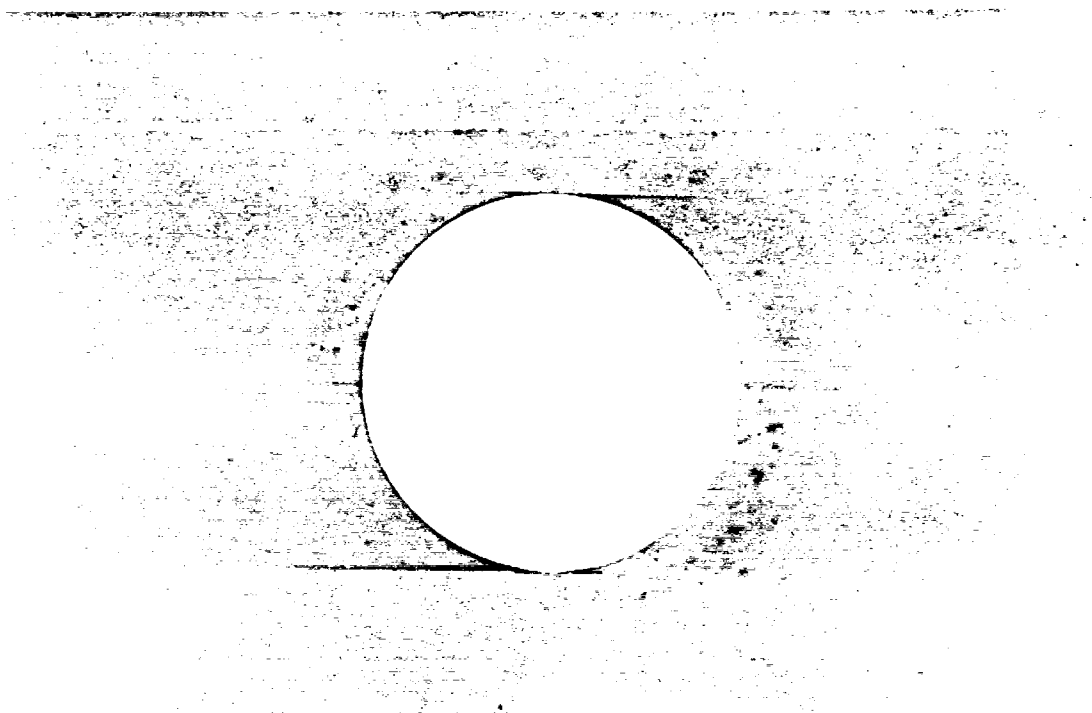


Figure No. 11: delamination process in Z-B 7-3 compression



**ZB 73 80**



**ZB 73 80**

Figure No. 12: X-Ray of Z-B 7-3, 80% critical compress. load  
specimen top view and cut shows hole surface

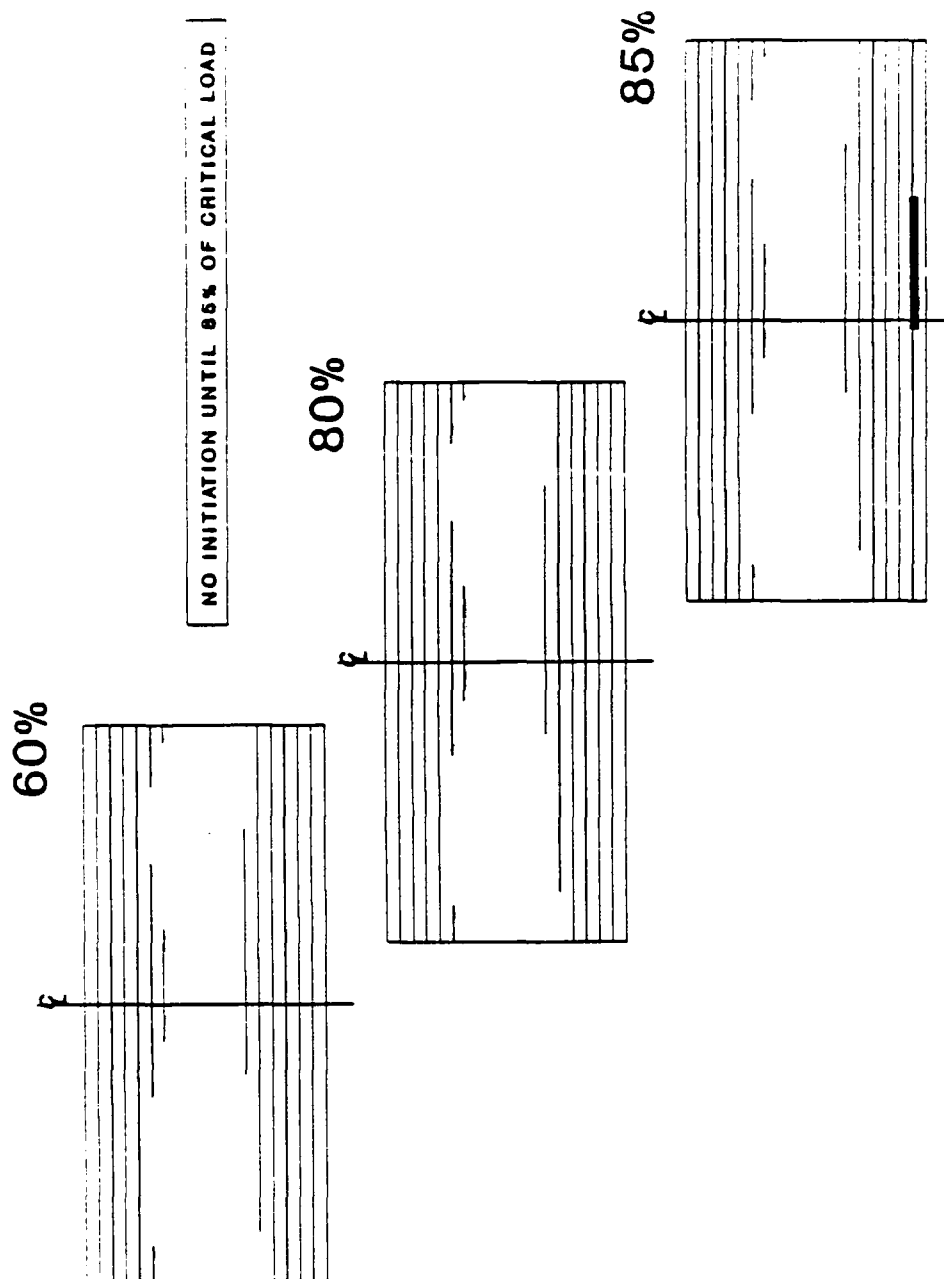
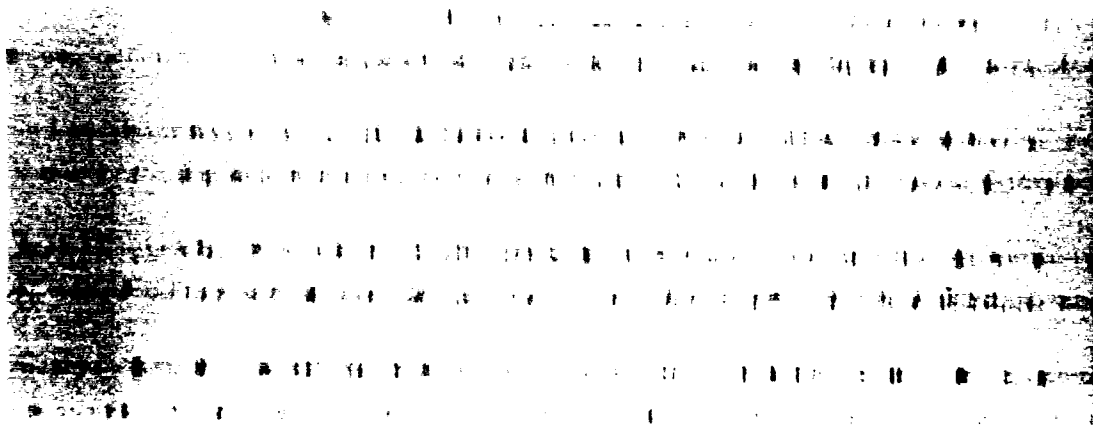
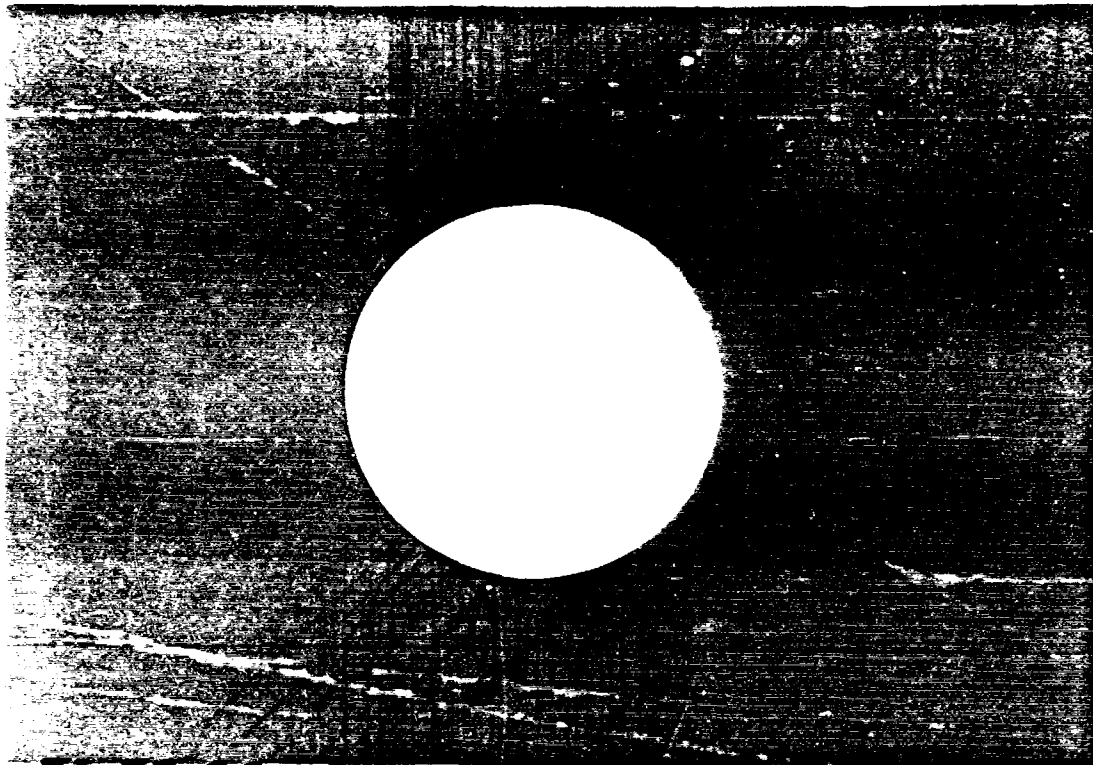


Figure No. 13: delamination process in Z-A 7-7, tension



**ZA 77 90**

Figure No. 14: X-Ray of Z-A 7-7, 90% critical tensile load  
specimen top view and cut shows hole surface

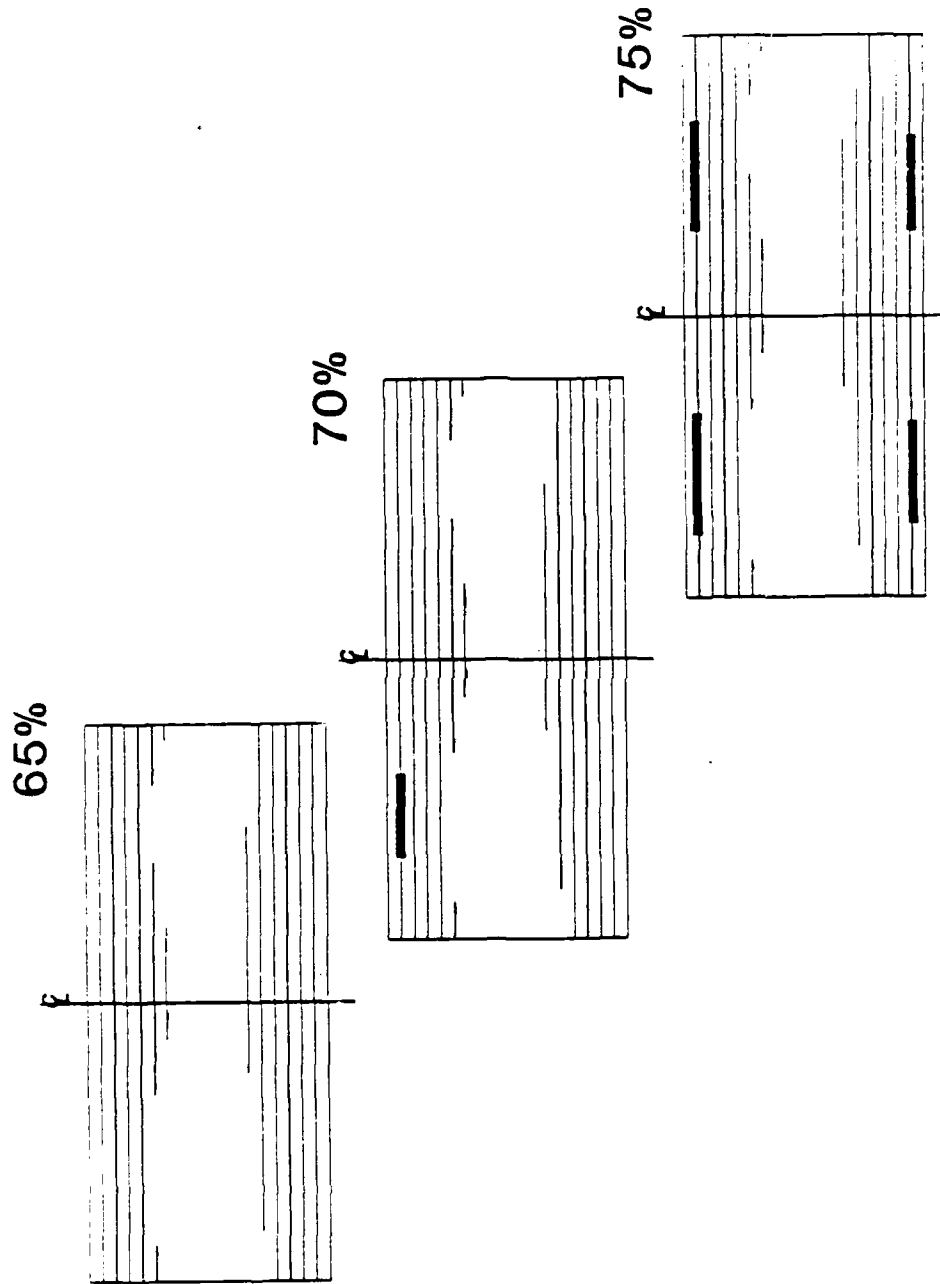
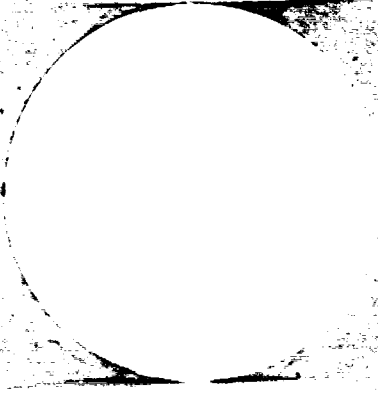



Figure No. 15: delamination process in Z-A 7-8, compression





**ZA 78 80**



**ZA 78 80**

Figure No. 16: X-Ray of Z-A 7-8, 80% critical compress. load  
specimen top view and cut shows hole surface

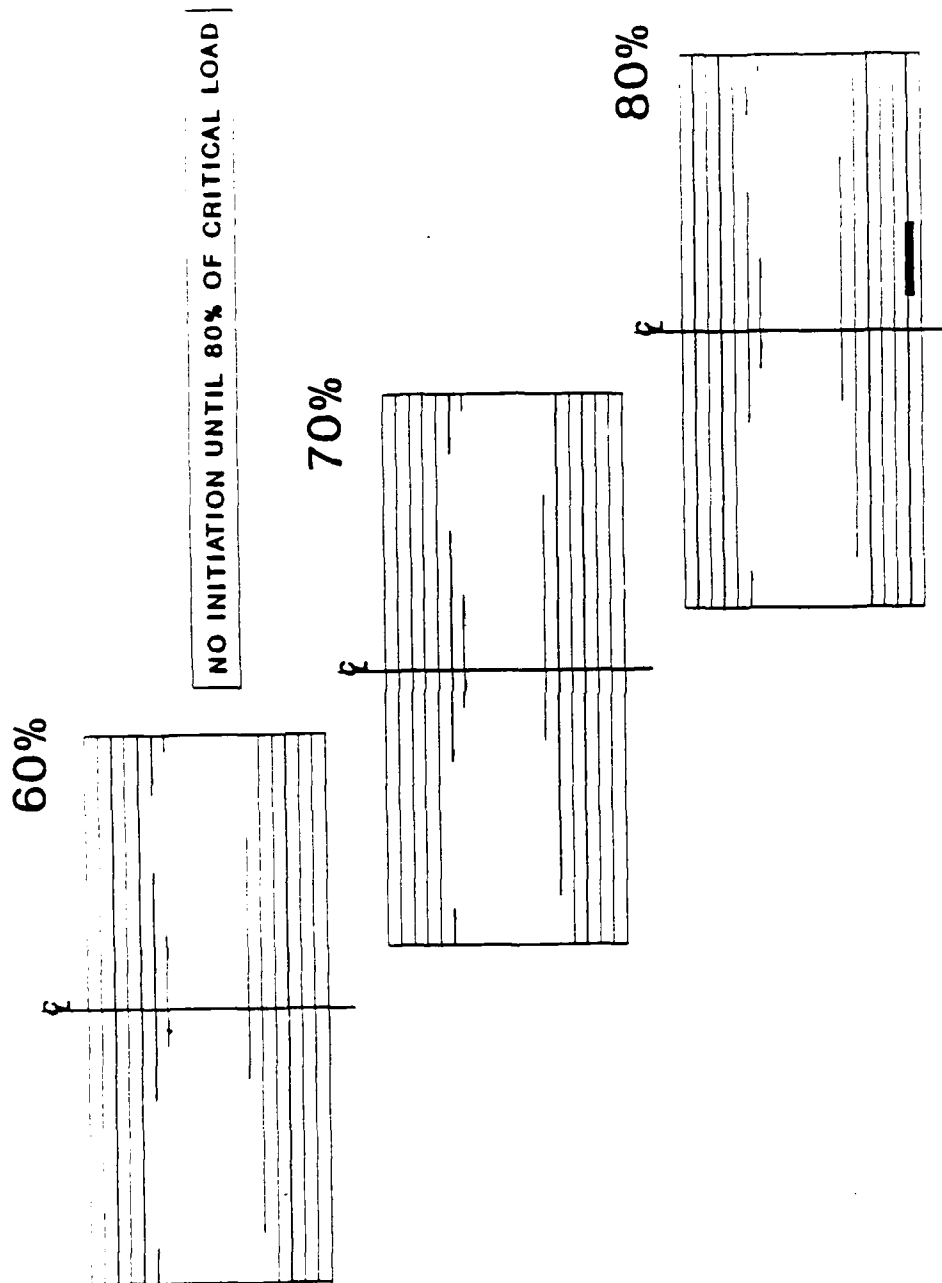
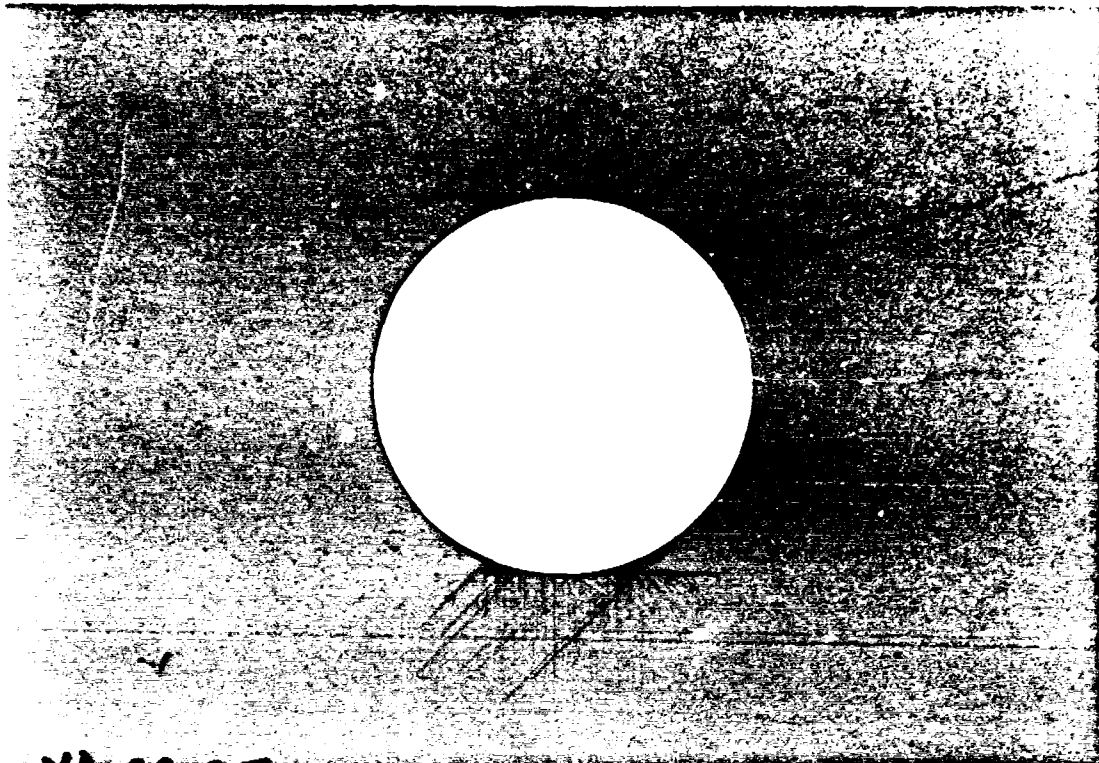
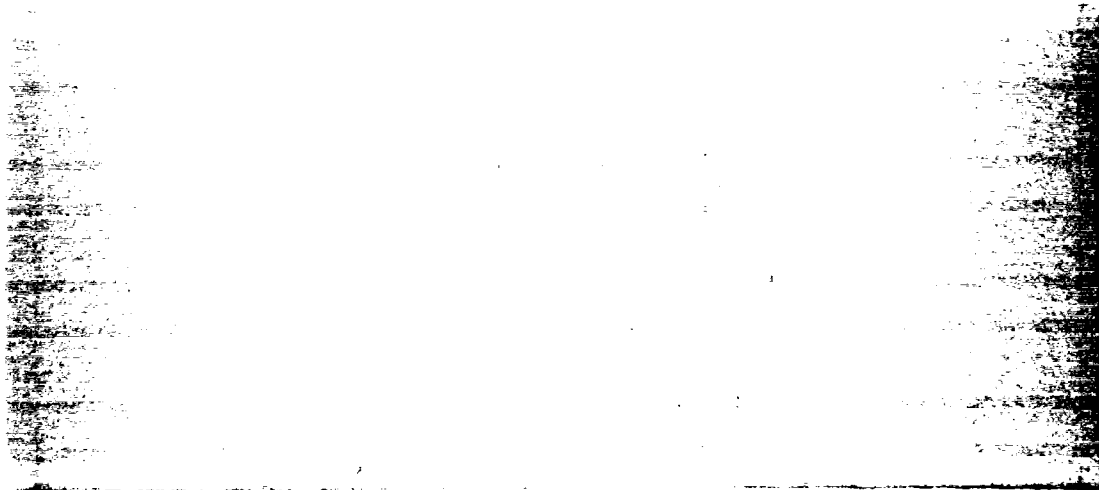


Figure No. 17: delamination process in Y-A 6-9, tension



YA 69 85



YA 69 85

Figure No. 18: X-Ray of Y-A 6-9, 85% critical tensile load  
specimen top view and cut shows hole surface

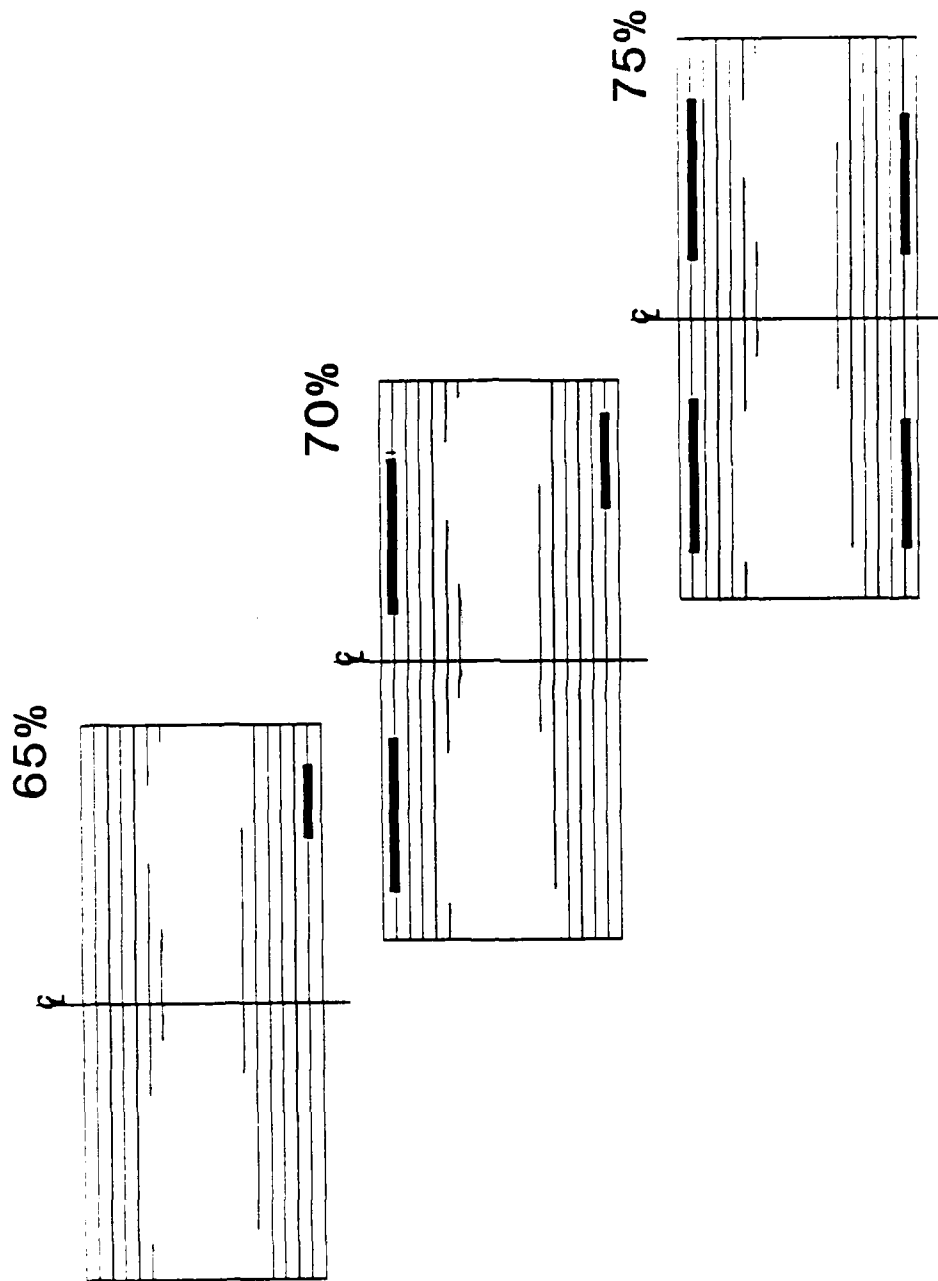
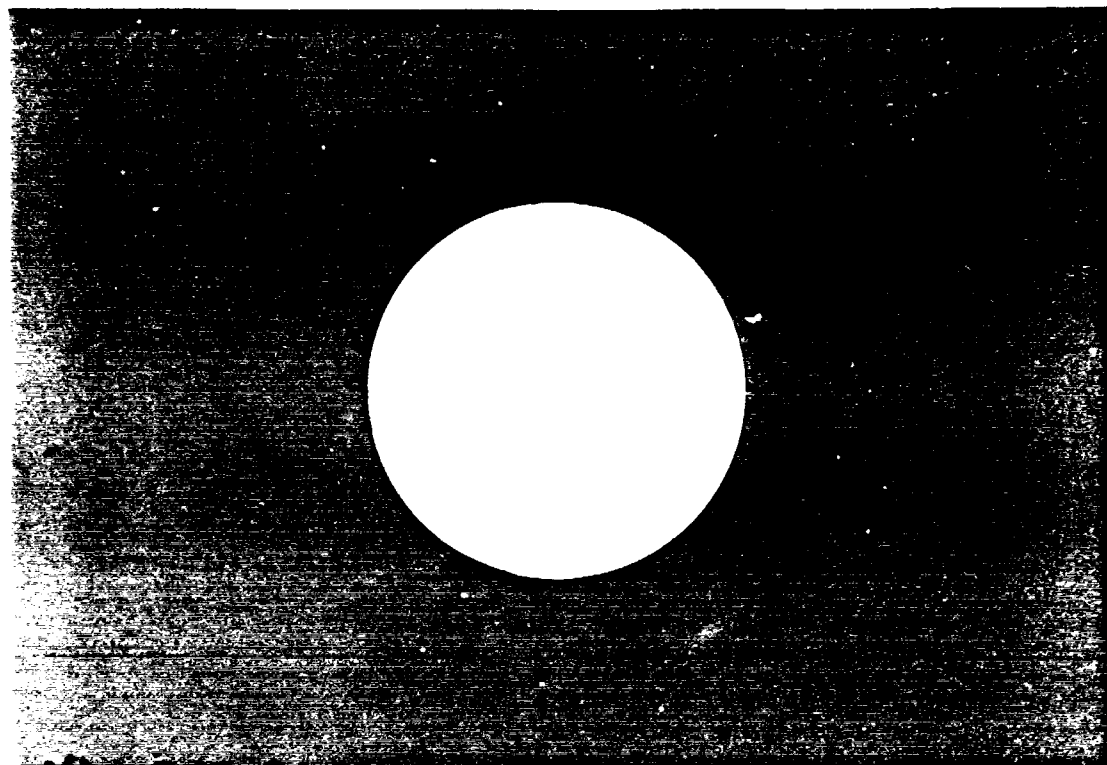


Figure No. 19: delamination process in Y-A 6-13, compression



YA 6 13 80



YA 6 13 80

Figure No. 20: X-Ray of Y-A 6-13, 80% critical compres. load  
specimen top view and cut shows hole surface

The results as reflected in figs. 5 - 20 give rise to the following conclusions about the two types of materials and systems and their performance under tension as well as compression:

1. The 1808 matrix based laminate tended to delaminate more extensively under both tension and compression than did the 3501-6 matrix based laminate.
2. In compression, the 1808 matrix based laminate was more vulnerable to matrix cracking than the 3501-6, while in tension, the opposite was true.
3. All the cases in the above investigation show that delaminations occur always within the external "sub laminate", which is the basic repeating sequence, and are more likely to occur at one, or a combination of the first three interfaces.
4. Matrix cracks occur at low load levels in some cases, (60% and less) but they do not necessarily control delamination.
5. Azimuthal location of delaminations was similar for the cases examined.

## Chapter 5

## ANALYSIS OF TEST SPECIMENS

Following the investigation described in chapter 2, all test specimens were analyzed. Stages of analysis are correlated with the parameters needed for the prediction model. That consists of the calculation of the order of singularity through the homogeneous solution, and the calculation of the stress fields completing the solution with its particular part. In the following sections it will be shown how these analyses were done and provide results.

### 5.1 Order of singularity around the hole at all interfaces

The analysis of the order of singularity was performed with the computer program "SINGULAR". Description of the program and instructions are provided in App. B. Since the order of singularity depends on the two adjacent plies at the examined interface and is independent of the loads or the global geometry, there are several types of interfaces which represent all the cases of the two types of layer sequences. These interfaces are [0/45], [45/90], [90/-45], and [0/-45]. The hole was scanned for all cases at  $0^\circ$ ,  $20^\circ$ ,  $40^\circ$ ,  $60^\circ$ ,  $80^\circ$ , and  $90^\circ$  w.r.t. the longitudinal axis Z. When scanning the hole circumferentially, the coordinate system was reoriented as explained earlier. Therefore the fiber orientations of plies on both sides of the relevant interface, were calculated. Figs. 21 - 24 show the fiber direction and orientation of the sections around the hole for all the cases. Each cut provides a

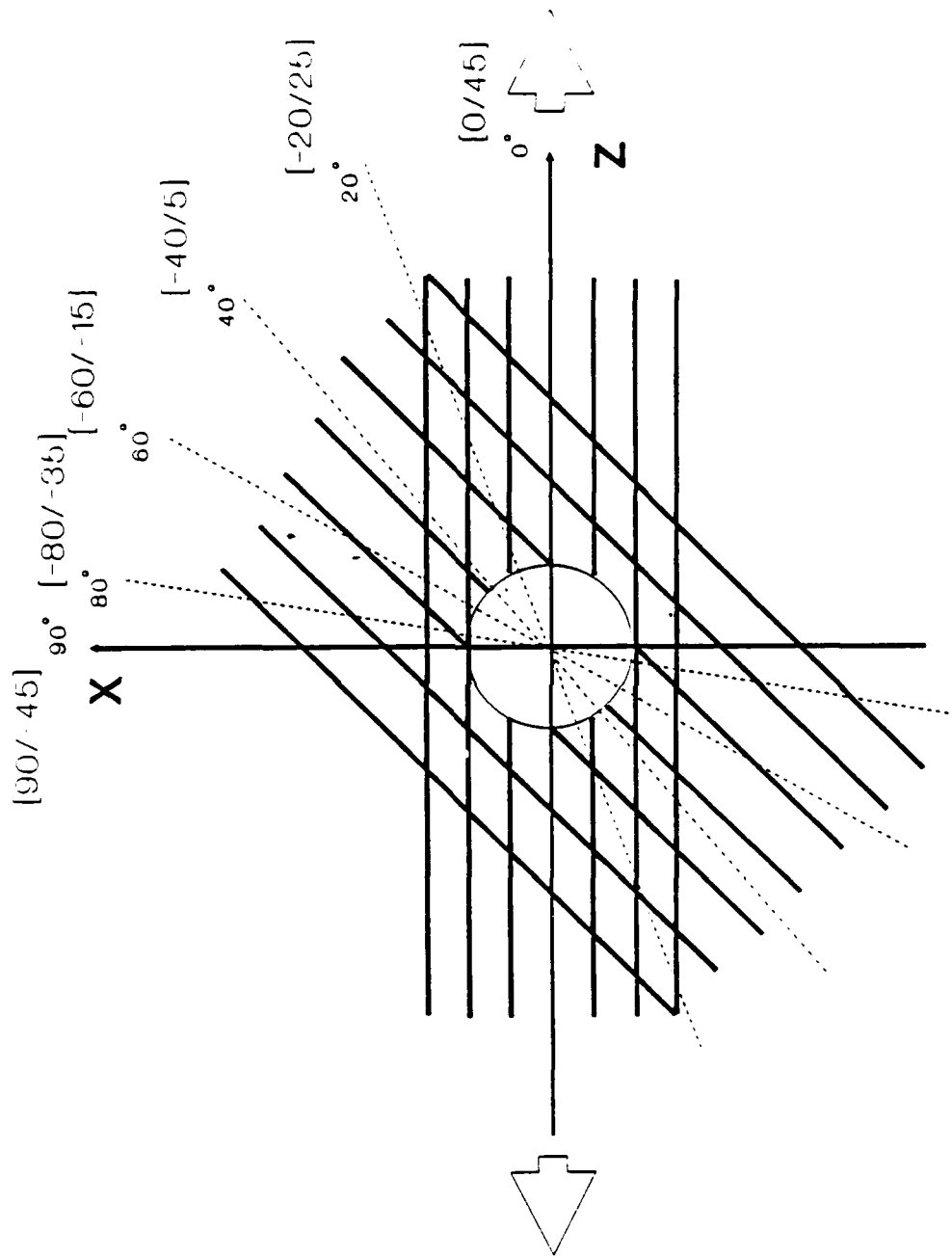


Figure No. 21: Interface  $[0/45]$ , scan at  $20, 40, 60, 80, 90$  deg



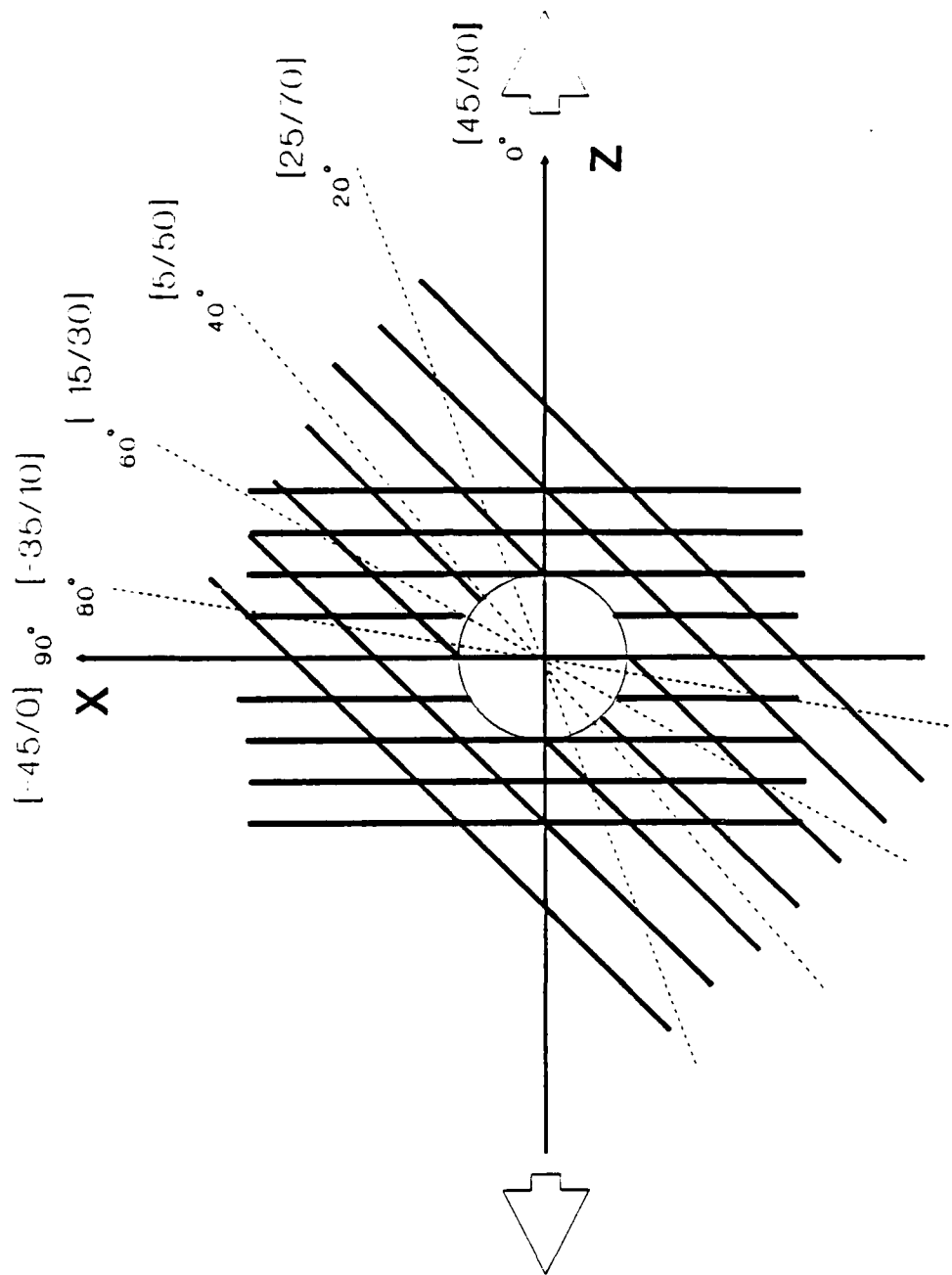


Figure No. 22: Interface [45/90], scan at 20,40,60,80,90 deg

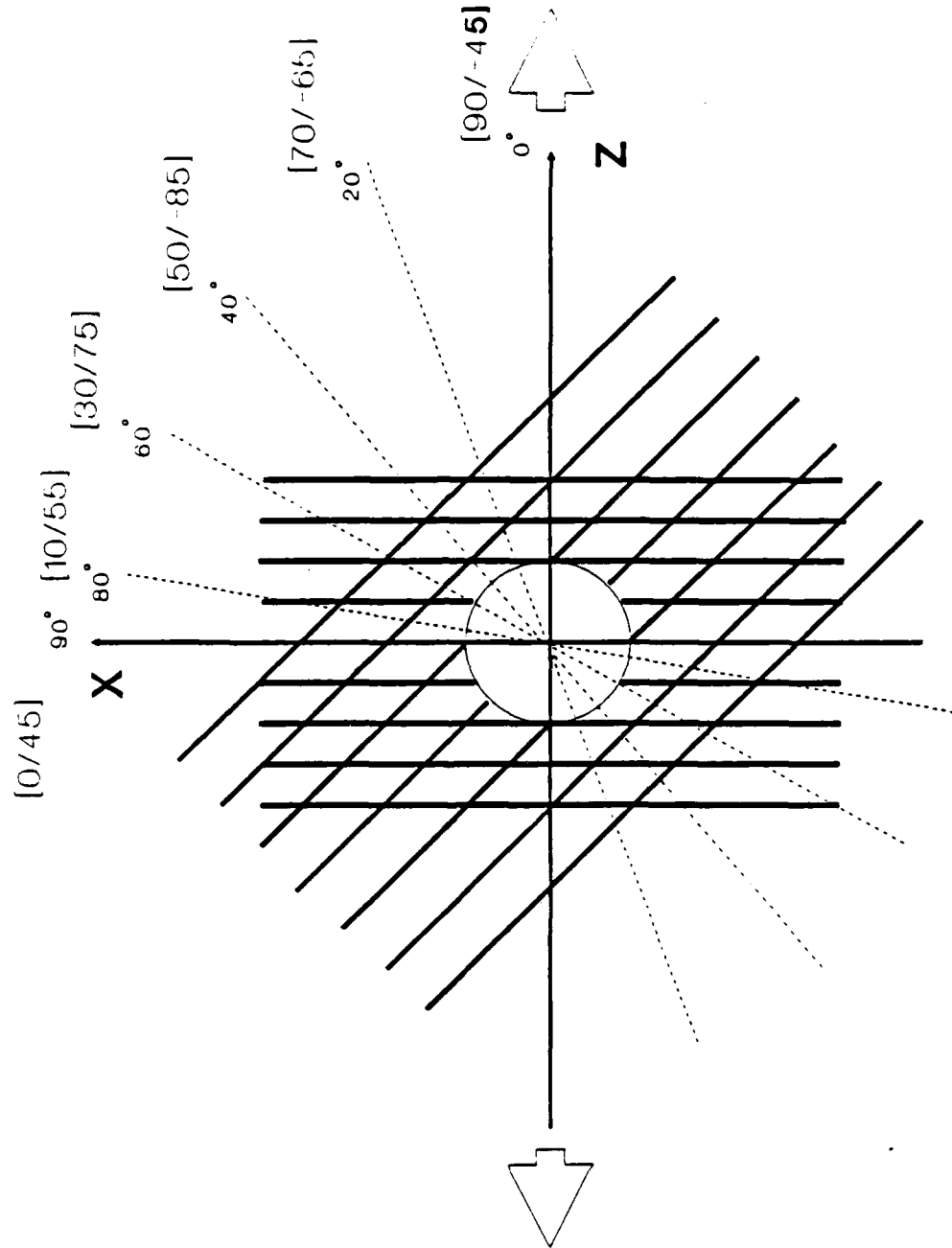


Figure No. 23: Interface [90/-45] scan at 20,40,60,80,90 deg

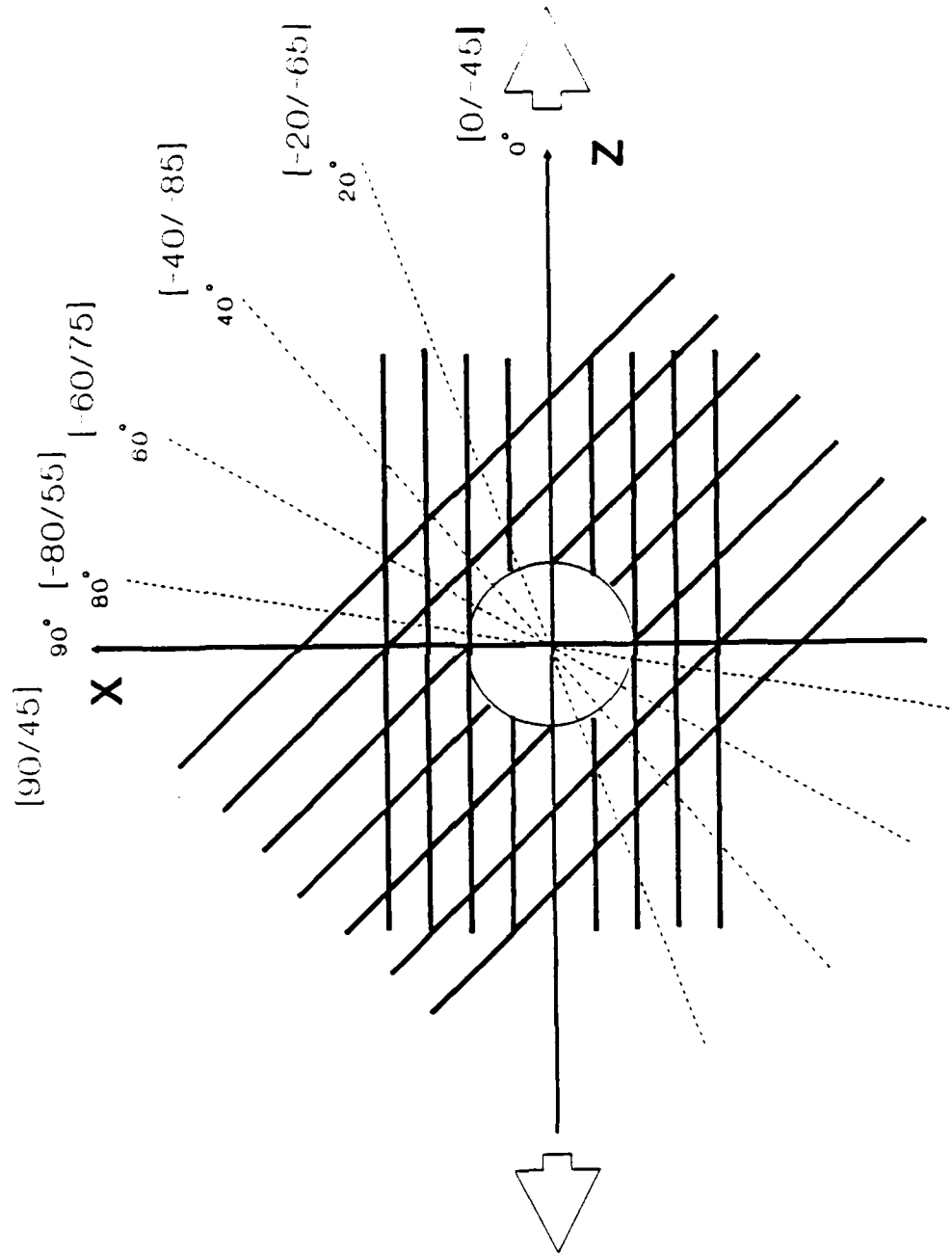


Figure No. 24: Interface [0/-45], scan at 20,40,60,80,90 deg

certain fiber orientation at the relevant interface. Table 4 summarizes all these rotated interfaces which are the subject of the analysis of the order of the singularity. The cases in Table 4 represent all the possibilities of fiber direction relations at all interfaces around the hole. With a proper input procedure, "SINGULAR" provided a series of eigenvalues for each case, and the order of the singularity was recognized by the demand that its real part has to be in the region  $[-1,0]$ . This requirement arises due to the fact that finiteness of displacement components at the origin is ensured only when  $\text{Re}[\delta] > -1$ , positive definiteness of strain energy of an elastic body, dictates the upper zero bound, Wang and Choi (1982). For an angle-ply system, the series of eigenvalues provide one number in that range and its imaginary part is always zero. For the other cases rather than an angle-ply, there might be more than one order of singularity and its imaginary part does not vanish. As mentioned above, for cases of non-angle-ply interfaces, there is more than one order of singularity, i.e., more than one eigenvalue within the region  $[-1,0]$ . For the case of several orders of singularities, Eqn. (60) is modified respectively. For example, for the case of two orders of singularities,

$$\sigma_{\alpha} = \sum_{k=1}^6 \left[ K_{\alpha 1k} Z_k^{\delta_1} + K_{\alpha 2k} Z_k^{\delta_2} \right] + o(\text{higher order, nonsingular terms})$$

( $\alpha = 1, 2, 3, 4, 5, 6$ ) (66)

Results of analysis of all cases are summarized in Table 5. The largest, (algebraically smallest) dominant, order of singularity of each case is plotted in Figs. 25 - 28, as a function of the scanning angle

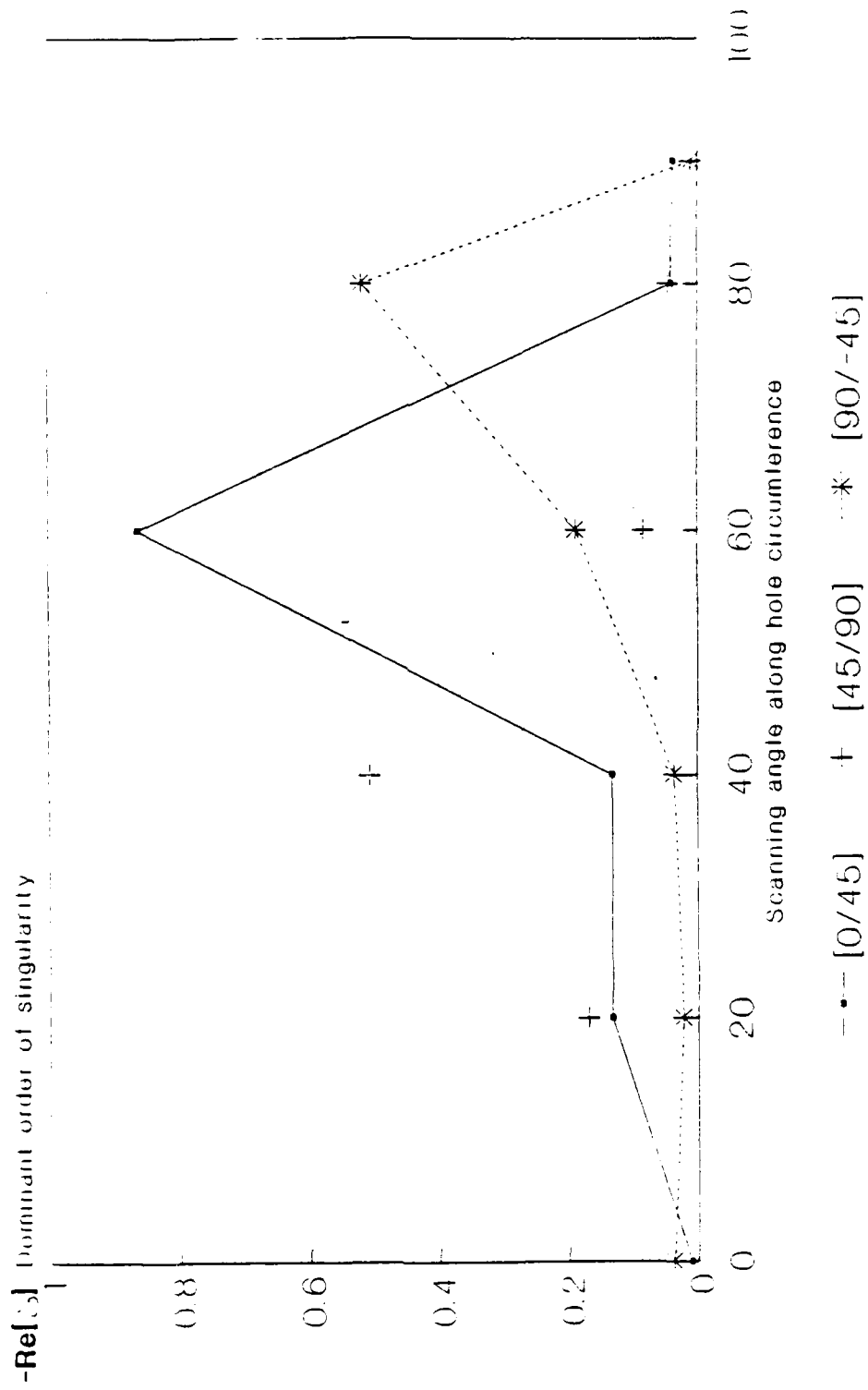
around the hole. These figures exhibit the distributions of the orders of singularity around the hole and assist to decide upon the location of the onset of delamination.

Table No. 4: rotated interfaces within the four types of  
 interfaces in both A & B sequences  
 (in bold - nonrepeating interfaces for analysis)

interface angle	<b>[0/45]</b>	<b>[45/90]</b>	<b>[90/-45]</b>	<b>[0/-45]</b>
0°	<b>0/45</b>	45/90	90/-45	0/-45
20°	<b>-20/25</b>	<b>25/70</b>	<b>70/-65</b>	<b>-20/-65</b>
40°	<b>-40/5</b>	<b>5/50</b>	<b>50/-85</b>	<b>-40/-85</b>
60°	<b>-60/-15</b>	<b>-15/30</b>	<b>30/75</b>	<b>-60/75</b>
80°	<b>-80/-35</b>	<b>35/10</b>	<b>10/55</b>	<b>-80/55</b>
90°	<b>90/-45</b>	<b>-45/0</b>	<b>0/45</b>	<b>90/45</b>

Table No. 5: Dominant singularities,  $-Re\{s\}$ , at examined interfaces for both materials Z & Y

	AS4/3501-6	AS4/1808
[0/45]	0.003644, 0.007254, 0.01088	---
[-20/26]	0.0064, 0.01568, 0.132866	---
[-40/5]	0.00663, 0.013509, 0.131959	0.009961, 0.0161172, 0.482903
[-60/-16]	0.005, 0.0101, 0.64955, 0.86395	---
[-80/-36]	0.007144, 0.01652, 0.04107	0.0126138, 0.0221839, 0.887588
[90/-46]	0.010024, 0.037704	0.008782, 0.012355, 0.05234
[25/70]	0.012296, 0.16937	---
[6/50]	0.00243, 0.012543, 0.50632	---
[-15/30]	0.01037, 0.08328	---
[35/10]	0.01037084, 0.0463	---
[70/-66]	0.0233789	0.010932, 0.05368,
[50/-86]	0.00044, 0.01364, 0.03646	0.001167, 0.010656, 0.223996
[30/75]	0.016546, 0.070888, 0.187593	---
[10/55]	0.0037487, 0.009875, 0.518072	---
[-20/-66]	0.0155814, 0.0789128	---
[-40/-86]	0.01537073, 0.05944	0.005, 0.01, 0.04, 0.14, 0.423, 0.85
[-60/75]	0.02409697	0.012, 0.023, 0.271, 0.43626
[1-80/55]	0.0019114, 0.0180756, 0.23627	0.0095, 0.0104, 0.029, 0.5971



**Figure No. 25: Dominant singularities at interfaces around the hole for  $[(0/45/90/-45)s]_4$  - AS4/3501-6**



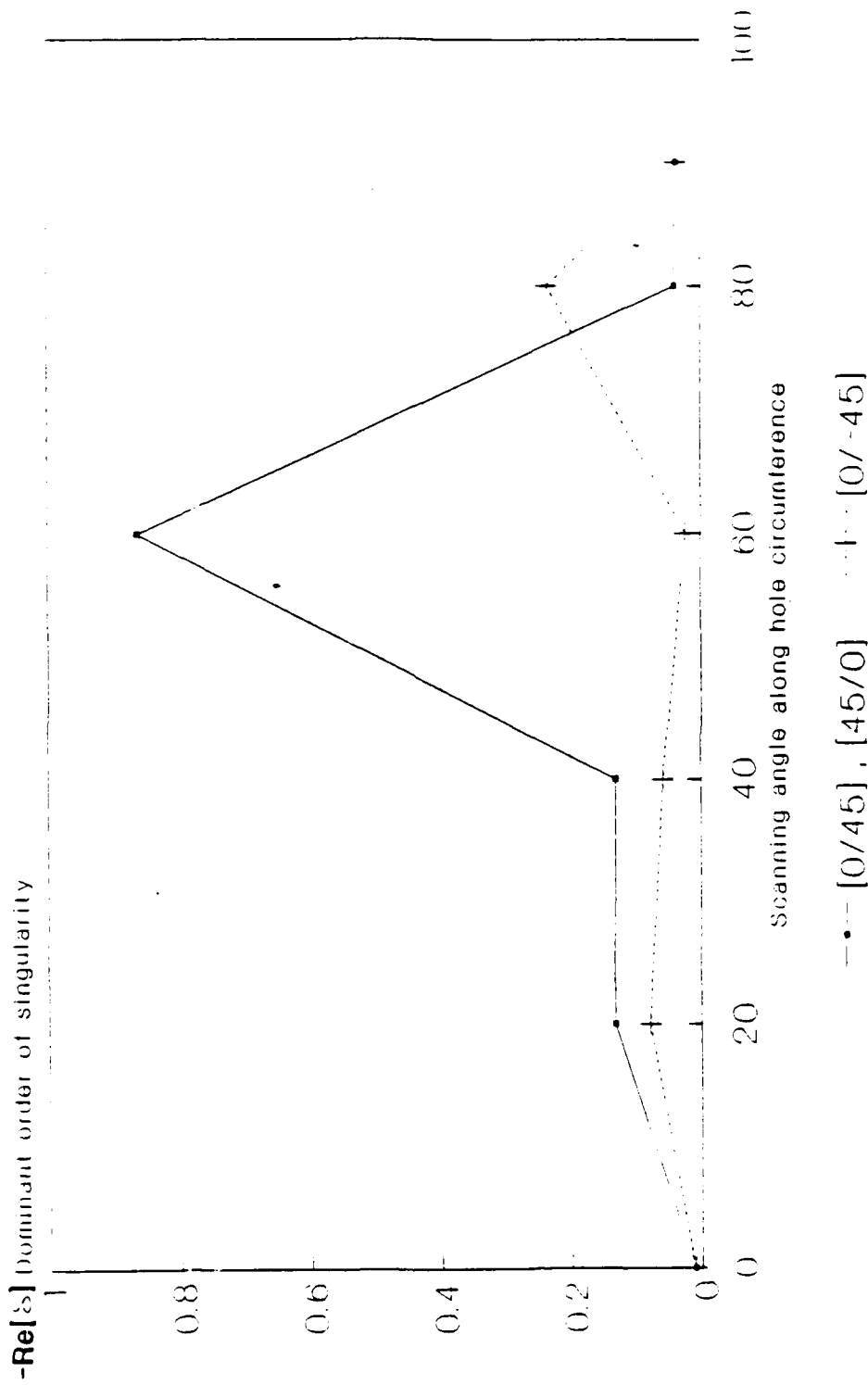


Figure No. 26: Dominant singularities at interfaces around the hole for  $[(0/45/0/-45)_4]_s$  - AS4/3501-6

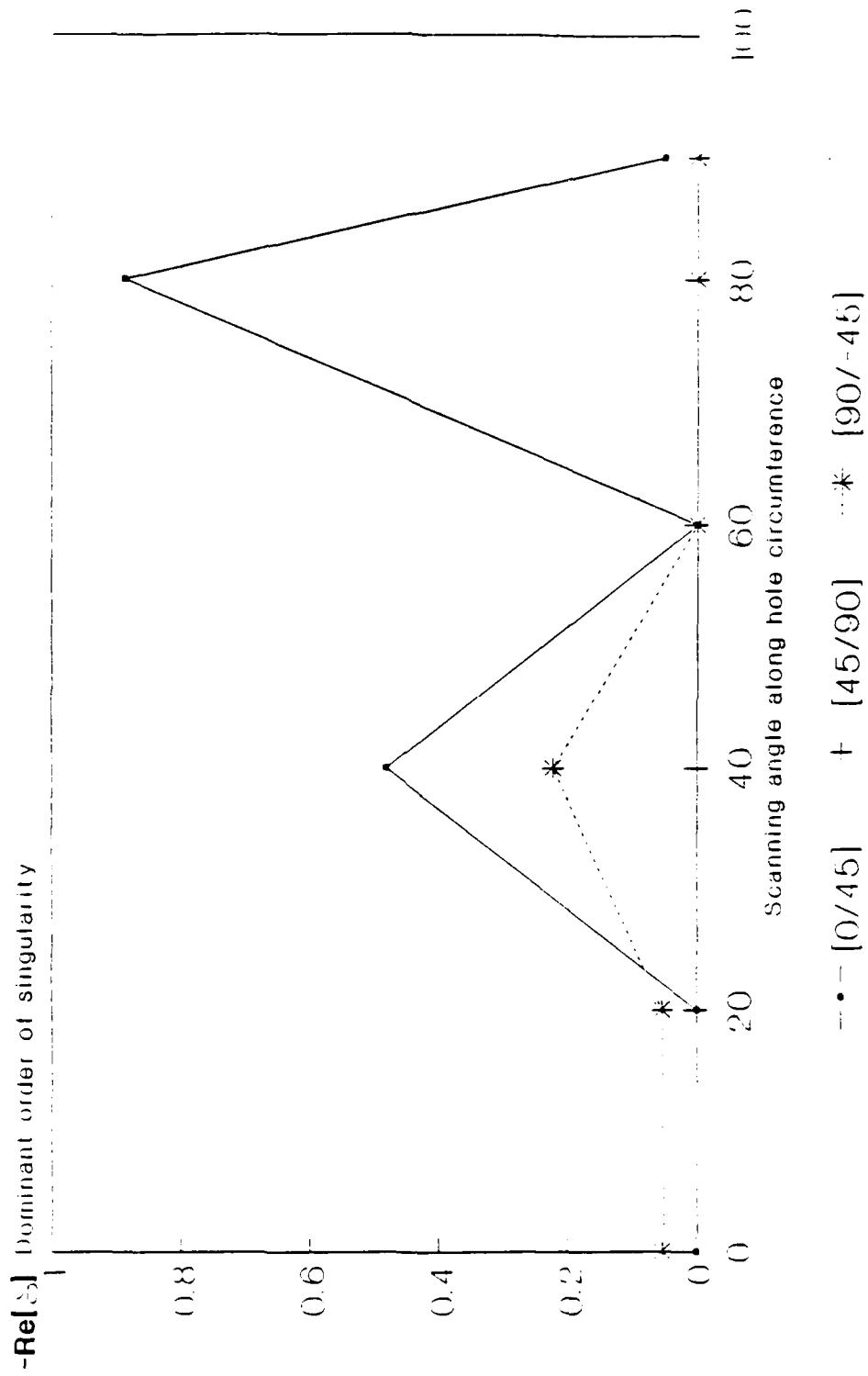


Figure No. 27: Dominant singularities at interfaces around the hole for  $[(0/45/90/-45)s]_4$  - AS4/1808

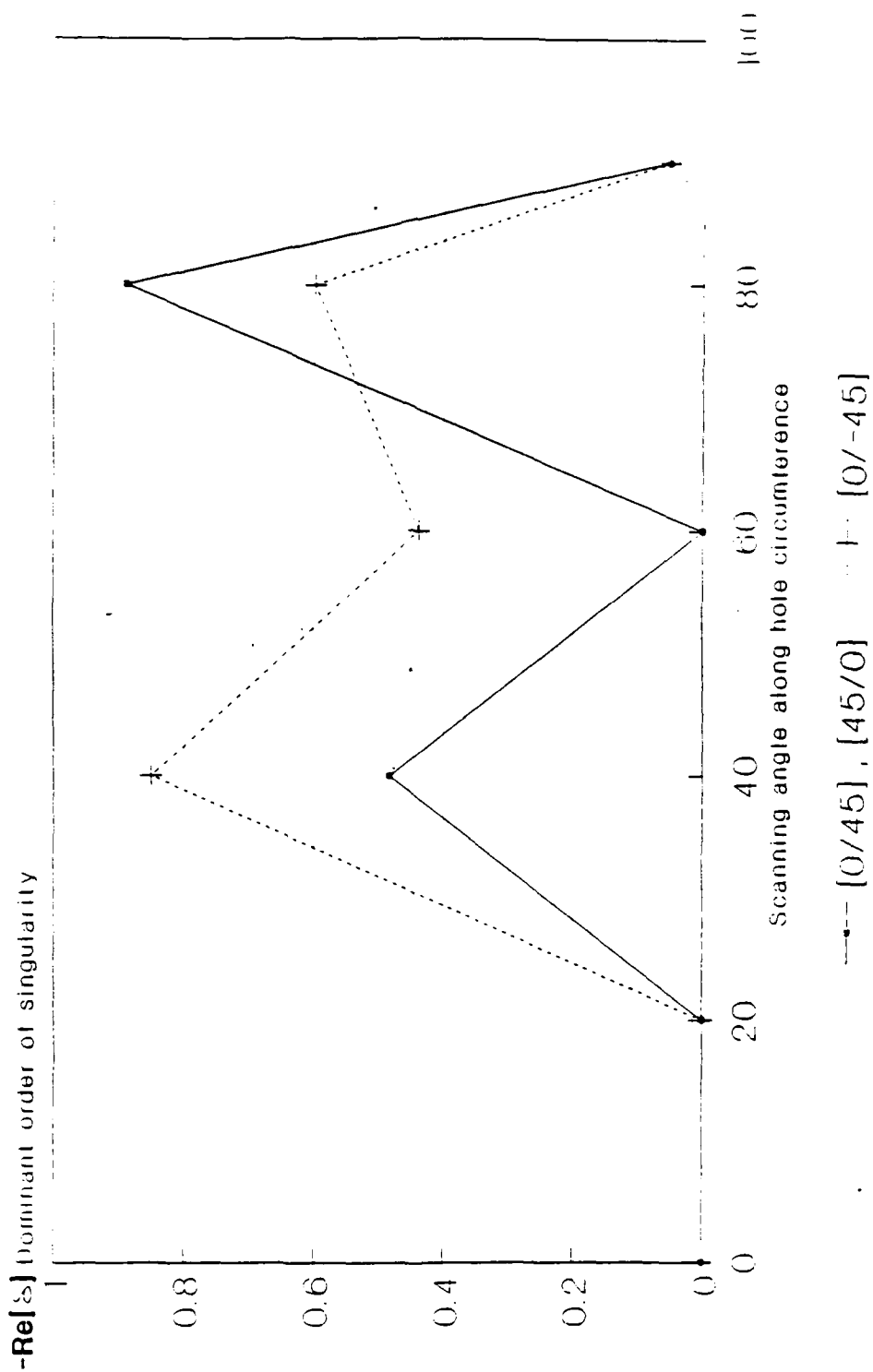


Figure No. 28: Dominant singularities at interfaces around the hole for  $[(0/45/0/-45)s]_4$  - AS4/1808

## 5.2 Stress fields and free edge intensities

Following the ideas drawn in chapter 3, we combine the two major parameters which the prediction model consists of. First, we use the analysis for the order of singularity to determine the interface and locations of interest, and then make final decisions upon the calculation of the energy release rate related parameters, i.e., the near-field parameters  $K_I$ . This process shortens the overall analysis and saves computer time as well. Figs. 25-28 show clearly the variety of locations in which the second choice has to be made, by the peaks of the curves which mean largest values of the plotted orders of singularity along the hole circumference. Analysis of the near-field parameters is made for both tension and compression. The analyzed locations are shown in table 6. The analysis is made using computer program "EDGSTR" which is described in App. C. The results are given in table 7. The analysis was done with positive remote loads which means that positive values indicate tension for the tension case and compression for the compression case, while negative values indicate tension for the case of compression loading, and compression for the case of tension remote load.

Table No. 6: Locations predicted by the order of singularity

type	interface	scanning angle	oriented interface
Z-A	0/45	20	-20/25
	0/45	60	-60/-15
	45/90	40	5/50
	90/-45	80	10/55
Z-B	0/45	60	-60/-15
	45/0	60	-60/-15
Y-A	0/45	80	-80/-35
	0/45	40	-40/5
Y-B	0/-45	40	-40/-85
	0/45	80	-80/-35

Table No. 7: Last stage analysis for selected locations -  
near field parameters

material sequence	AS4/3501-6								AS4/1808			
	A				B				A		B	
	0/45	0/45	45/90	90/-45	0/45	45/0	0/45	45/0	0/45	0/45	0/-45	0/45
scan angle	20	60	40	80	60	60	80	80	80	40	40	80
K <sub>1</sub>	0.783	0.946			2.439	-0.200			0.445	-2.661	-3.438	-4.449
K <sub>2</sub>	0.351	-0.088			-0.227	1.834			-0.480	2.661	-1.548	0.480
K <sub>3</sub>	2.363	-0.298			-0.769	0.511			-0.060	0.881	-6.588	0.060
K <sub>4</sub>	-0.022	0.059			0.153	-0.024			0.307	-0	5.090	-0.306
K <sub>5</sub>	-1.544	0.597			1.54	-0.198			0.529	-0	9.125	-0.529
K <sub>6</sub>	13.29	-0.140			-0.362	-0.333			-0.015	-1.663	-9.115	0.015

### 5.3 Application of the analytical results to the prediction model

Since the locations for the analyses were chosen according to the values of the order of the singularities, final decision upon the location of the onset of delamination was made based on the results of the analysis for the near-field parameters as shown in table 7. The process is very simple. First, we omit the negative magnitudes as they stand for compression which prevents the occurrence of delamination. Then, we look for the largest values which correspond to highest strain energy release rates. A physically related decision has to be made on the subject of which component dominates the phenomenon. Obviously, the out-of-plane component is a good candidate , though, a combination of all components is an option as well. Since there are solid arguments for both, final decision is accepted by observation of the experiments in relation with the analysis. Application of the analytical results to the prediction model will be examined visually in conjunction with the comparison of the analytical and the experimental results in the next chapter.

## Chapter 6

## COMPARISON OF ANALYTICAL AND EXPERIMENTAL RESULTS

As mentioned in a previous section, the prediction process is carried out in two stages. The first stage is to locate vulnerable spots by high singularities, and then the second stage consists of the decision based on the values of the near field parameters which are energy-related coefficients. Once the most vulnerable locations are chosen by values of orders of singularity, final decision is made following the results in table 7. The predicted locations are chosen by the largest values of  $K_2$ , yet a further study might be performed in order to find a more realistic influence by a combination of modes involving shear components, i.e.,  $K_4$ ,  $K_5$ , and  $K_6$ . These locations are compared to the experimental results as shown in Fig. 29. It seems that good agreement is achieved by utilizing the largest values of the out-of-plane component of the near-field parameters. In none of the cases was there a disagreement about the interface. The center of the delaminated area as obtained by the experiments, does not match exactly the analytically based results in every case. In the case of Y-B in tension the location is off by  $40^\circ$ . Nevertheless, it seems that the agreement is generally good, and applicable as a tool upon which engineering decisions can be made, such as making necessary changes to ensure safety of laminate element in its conditions to the examined configuration.



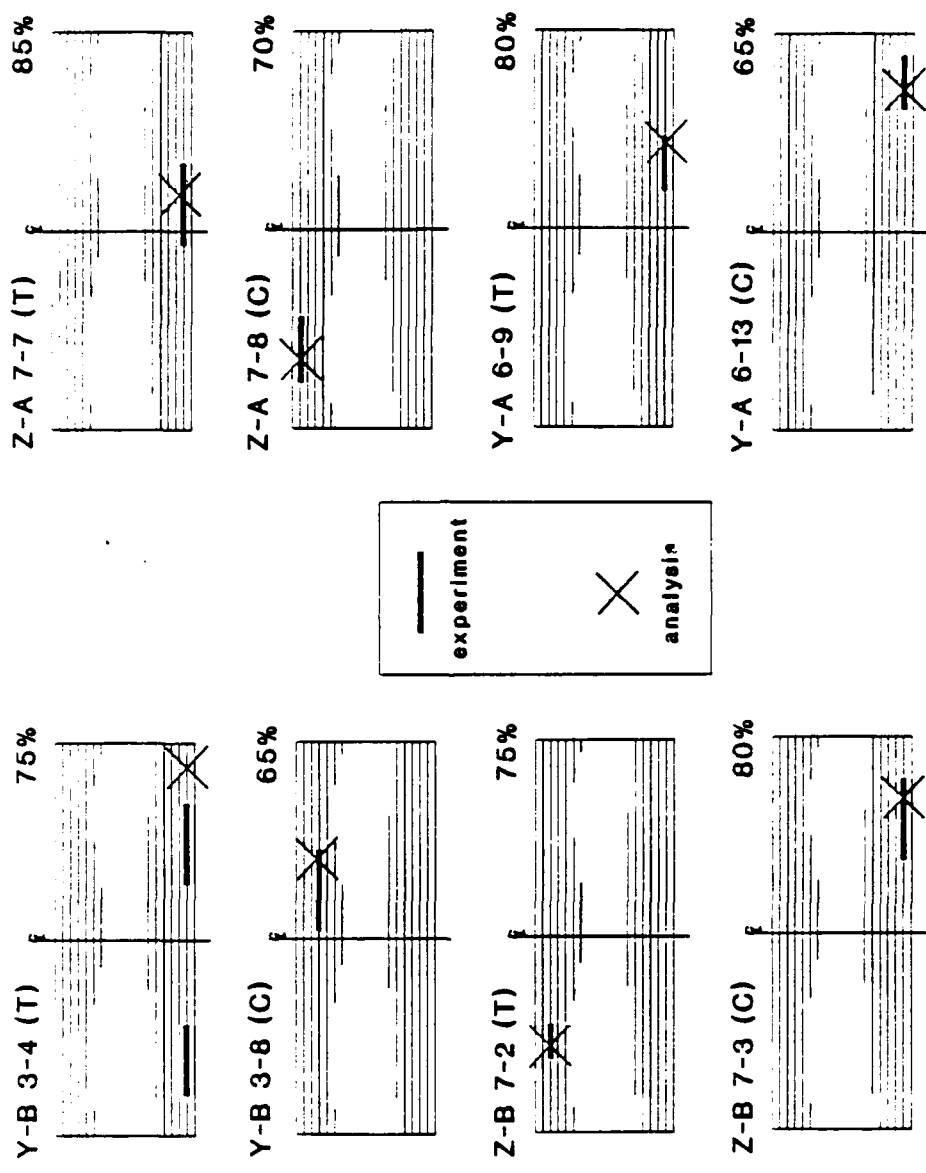


Figure no. 29: locations of the onset of delamination, analysis vs. experimental results

## Chapter 7

## SUMMARY AND CONCLUSIONS

The goal of this study was to investigate the behavior of the onset of delamination in a composite plate, focusing on the case of a hole in a coupon. The investigation was carried out in two parts, analytical and experimental, both combined to create a prediction model for the studied phenomenon.

The mission of establishing a prediction model and validating it by experiments is extremely difficult in this case. This is not a process of matching entities in the sense of curve fitting; here the task is to match the occurrence of a phenomenon at a point, which means that it is either valid or not.

As explained above, the analytically based prediction model consists of two major components. (1) The order of singularity of the stress field at the edge of the laminate, and (2) the near-field parameters which are the major components in the expression of the energy release rate which is linearly dependent upon them. Observation of the analytical results in conjunction with the experimental results, it seems that the nature of the singularity of the solution plays a major role in the mechanism of the delamination. Since that singularity is a result of a mathematical process, it is easy to ignore its physical importance. Indeed, we know that the mathematical singularity leads to infinite values of stresses which are not real, of course. The correct interpretation, however, rather than looking at the point stress values at the edge, is to consider the region of influence of the singular

stress field at a certain distance from the edge. The order of the mathematical singularity indicates the rate of change of stresses, or in its more physical interpretation, the energy release rate if delamination occurs. As in plasticity effects, the stress distribution is prone to a cutoff as dictated by the material performance, but the vicinity of that cutoff behaves in a certain way upon which qualification of the phenomenon is available.

The question of which of the components of the energy plays the major part in the delamination process, or is it the total quantity that should be considered, is partially answered here. It seems that relying on the out-of-plane component is enough to consider for the prediction process, yet this is a possible issue for further investigation in which a massive testing program should be done, probably resulting in statistically based conclusions.

Throughout the experiments, it was found that the type of matrix is a major issue in the subject of delamination, as was reflected through the analytical results as well. In fact, the analysis is capable of emphasizing that point since we obtain results all around the hole and as such we are able to compare and qualify such differences. In our case, we had two types of materials examined through two types of stacking sequences under two types of loads - tension and compression. The two types of materials consisted of the same fiber and differed by the matrix only. That isolated the matrix as an individually investigated parameter. The findings, as reflected throughout different tables and figures in previous chapters, show clearly that a system which consists of a matrix of the type 1808 is more sensitive and

vulnerable to delamination than the type 3501.

The analysis which provides the singularities and the near field parameters as well as stresses and displacements distribution is utilized through the programs "SINGULAR" and "EDGSTR". The first provides the series of eigenvalues which are used later by the second program to utilize the near-field parameters. It is very important to ensure convergence of the solution. Therefore, a series of runs should be performed, using different numbers of eigenvalues, choosing different numbers of integration points, and observing the results until convergence is achieved. The calculation process for the eigenvalues involves a deflation method which may result in division by relatively small numbers. That may lead to computationally ill conditions due to the limitations of the computers. Therefore, a suitable hardware should be selected to carry out the process. The best compiler for the task is the Turbo-Pascal used on PC's. That compiler allows real numbers ranging from  $-10^{-5000}$  to  $10^{5000}$ . That satisfied the needs of the analysis in cases where the IBM main-frame failed to do. The above dictates the usage of micro-computers which are relatively slow. Therefore, the recommended hardware is the new IBM PS/2 model 80 or a similar machine with a CPU that uses the new and revolutionary processor 80386 by INTEL. The architecture of that processor also enables it to carry out multi-tasking jobs, a process which saves significant time.

## NOMENCLATURE

$A$	coefficients matrix
$A_i$	constants of integration
$a_i$	coefficients of polynomials in the particular solution
$a$	distance from hole to laminate edge
$B$	cross sectional area at cut perpendicular to load direction
$B_F$	free edge surface
$B_I$	interface plane
$B$	results vector of set of linear equations
$b$	out-of-plane coordinate of upper surface of laminate
$C$	coefficients vector, final description
$c_i$	coefficients vector of homogeneous solution
$c$	out-of-plane coordinate of lower surface of laminate
$D$	vector of unknowns in the complete formulation
$D$	domain of integration
$d_1, d_3$	elliptical hole axes in $x_1$ and $x_3$ directions respectively
$d_n^{(h)}$	coefficients vector of the homogeneous solution
$ds$	infinitesimal length
$E_1, E_2, E_3$	unidirectional material properties
$E_x, E_y, E_z$	laminate properties
$e$	distance from hole to laminate edge
$F$	Lekhnitskii's stress potentials
$F_k$	Stress function used for the homogeneous solution
$f_{\alpha n}$	stress eigenfunctions of the homogeneous solution
$G_I, G_{II}, G_{III}$	strain energy release rates, mode I, II, and III
$G_{ij}$	functions of the compliance and coeff. of part. solution

$g_{\beta n}$	displacements eigenfunctions of the homogeneous solution
$( )^{(h)}$	magnitude related to the homogeneous solution
$K_I, K_{II}, K_{III}$	stress intensity factors, mode I, II, and III
$K_i$	near-field parameters
$( )_k$	magnitude related to the characteristic equation
$L_i$	differential operator
$l_i$	differential operator
$M_{ij}$	remote loading - moment w.r.t. the indices
$( )^{(m)}$	magnitude related to the $m^{th}$ ply
$n$	no. of unknowns $\equiv$ no. of columns in the coefficients matrix
$p_k$	function related to the homogeneous solution
$( )^{(p)}$	magnitude related to the particular solution
$q_k$	function related to the homogeneous solution
$P_{33}$	uniaxial remote load in the $x_3$ direction
$p$	order of matrix - no. of rows
$R$	residual when utilizing a weighting technique
$r$	polar coordinate starts at the origin of the Cartesian sys
$S_{ij}$	tensorial compliance matrix
$\tilde{S}_{ij}$	reduced tensorial compliance matrix
S.V.D	the method of singular value decomposition
$( )^{(T)}$	transpose
$t$	laminate thickness
$t_k$	function related to the homogeneous solution
$U$	matrix of orthonormalized eigenvectors
$U_i$	function related to the process of governing equations
$u_i$	displacements vector

$u_{i0}$	rigid body displacements
$V$	matrix of orthonormalized eigenvectors
$v$	vector related to the singular value decomposition method
$w$	vector related to the singular value decomposition method
$x_i$	directions
$X$	planner transverse direction of laminate
$Y$	out-of-plane direction of laminate
$Z$	longitudinal direction of laminate
$Z_k$	argument of Lekhnitskii's stress functions
$\alpha$	scanning azimuth at the hole
$( )_\alpha$	Greek notation: 1-6
$\delta_i$	series of eigenvalues
$\delta_i^{(m)}$	series of eigenvalues at interface $m$
$\delta\beta$	virtual delamination length
$\varepsilon$	nominal strain
$\varepsilon_{ij}$	strain tensor
$\eta_k$	coefficients related to the characteristic equation
$\Psi$	Lekhnitskii's stress potential
$\phi$	trial function related to the weighting technique
$\mu_k$	roots of the characteristic equation
$\nu_{ij}$	poisson's ratio
$\theta^{(m)}$	fiber direction at $m^{\text{th}}$ ply
$\theta^{(m)}$	polar coordinate starts from the examined interface
$\Sigma$	diagonal matrix of eigenvalues, related to the S.V.D
$\sigma_i$	stresses in Greek notation
$\sigma_{ij}$	stress tensor

$\sigma_{ijcal}$	stress tensor computed for the anisotropic plate with hole
$\varphi$	angle measured from the interface to $B_F$
$\omega_1$	rigid body rotations
$(\bar{\phantom{x}})$	conjugate of complex number
$(\phantom{x})', (\phantom{x})''$	first and second differentiation
$\partial$	partial differentiation
$\dagger$	transpose of the conjugates
$\det[ \phantom{x} ]$	determinant
$\{ \phantom{x} \}$	vector
$[ \phantom{x} ]$	matrix



## REFERENCES

- Broek, D. (1982). "Elementary engineering fracture mechanics", Martinus Nijhoff
- Christensen, R. M. (1979). "Mechanics of composite materials", John Wiley & Sons, New-York.
- Erdogan, F. (1965). "Stress distributions in bonded dissimilar materials with cracks", J. of Applied mechanics, 32, 403-410.
- Hyer, M. W. and Klang E. C., (1985). "Contact stresses in pin-loaded orthotropic plates", Int. J. Solids Structures Vol. 21, No. 9, pp. 957-975.
- Hyer, M. W. and Klang E. C., (1985). "Damage initiation at curved free edges: Application to uniaxially loaded plates containing holes and notches.", Recent advances in composites in the United States and Japan. ASTM STP 864, J. R. Vinson and M. Taya Eds., pp. 62-90.
- Irwin, G. R. (1957). "Analysis of stresses and strains near the end of a crack transversing a plate. J. of Applied mechanics, 24, 361-364.
- Jones, R. M. (1975). "Mechanics of composite materials", Scripta, Washington D.C.
- Kassapoglou, C., and Lagace, A. P., (1987). "Closed form solutions for the interlaminar stress field in angle-ply and cross-ply laminates", Journal of composite materials, Vol. 21, pp. 292-308.
- Kim, R. Y. and Soni, S. R., (1984). "Experimental and analytical studies on the onset of delamination in laminated composites", Journal of composite materials, Vol. 18.
- Lekhnitskii, S. G., (1981). "Theory of elasticity of an anisotropic body", Mir Publishers, Moscow.

- Muller, D. E., (1956). "A method for solving algebraic equations using an automatic computer", Mathematical tables and computations, Vol. 10, Oct. pp. 208-215.
- O'Brien, T. K., (1982). "Characterization of Delamination Onset and Growth in a Composite Laminate", Damage in composite materials, ASTM STP 775, K. L. Reifsnider, Ed., pp. 140-167.
- Pagano, N. J. and Pipes, B. R., (1973). "Some observations on the interlaminar strength of composite laminates", Int. J. Mech. Sol., Pergamon Press, Vol. 15 pp. 679-688.
- Pipes, R. B., and Pagano, N. J. (1970). "Interlaminar stresses in composite laminates under uniform axial extension", Journal of composite materials, Vol. 4, pp. 538-548.
- Rice, J. R. (1965). "Plane problems of cracks in dissimilar media" J. of Applied mechanics, 32, 418-423.
- Stewart, G. W., (1973). "Introduction to matrix computations", Academic Press, Orlando, pp. 317-325.
- Wang, A. S. D., and Crossman, F. W., (1977). "Some new results on edge effects in symmetric composite laminates", Journal of composite materials, Vol 11, pp. 92-106.
- Wang, S. S. and Choi, I., (1982a). "Boundary-layer effects in composite laminates: Part 1 - Free edge stress singularities", ASME Journal of applied mechanics, Vol. 49, pp. 541-549.
- Wang, S. S. and Choi, I., (1982b). "Boundary-layer effects in composite laminates: Part 2 - Free edge stress solutions and basic characteristics", ASME Journal of applied mechanics, Vol. 49, pp. 549-560.

## Appendix A

## INTEGRATION OF THE FAR END CONDITIONS EQUATIONS

$$\begin{aligned}
 a_9 \left[ \frac{x_1^2 x_2}{2} \right] + \sum_n d_n \left\{ \sum_{k=1}^3 \left[ C_k \eta_k \frac{Z_k^{\delta_n+2}}{(\delta_n+1)(\delta_n+2)} \right. \right. \\
 \left. \left. + C_{k+3} \bar{\eta}_k \frac{\bar{Z}_k^{\delta_n+2}}{(\delta_n+1)(\delta_n+2)} \right] \right\} = 0
 \end{aligned} \tag{A1}$$

$$\begin{aligned}
 a_8 [x_1^2 x_2] + a_9 \left[ \frac{x_1 x_2^2}{2} \right] + a_{11} [x_1 x_2] \\
 + \sum_n d_n \left\{ \sum_{k=1}^3 \left[ C_k \eta_k \frac{Z_k^{\delta_n+2}}{\mu_k (\delta_n+1)(\delta_n+2)} + C_{k+3} \bar{\eta}_k \frac{\bar{Z}_k^{\delta_n+2}}{\bar{\mu}_k (\delta_n+1)(\delta_n+2)} \right] \right\} = 0
 \end{aligned} \tag{A2}$$

$$\begin{aligned}
& A_1 \left[ \frac{x_1^2 x_2}{2} \right] + A_2 \left[ \frac{x_1 x_2^2}{2} \right] + A_3 [x_1 x_2] + a_1 \left[ -\frac{S_{32}}{S_{33}} 3x_1^2 x_2 \right] \\
& + a_2 \left[ -\frac{S_{32}}{S_{33}} x_2^2 x_1 + \frac{S_{36}}{S_{33}} x_1^2 x_2 \right] + a_5 \left[ -\frac{S_{32}}{S_{33}} 2x_1 x_2 \right] + a_8 \left[ \frac{S_{34}}{S_{33}} x_1^2 x_2 \right] \\
& + a_9 \left[ \frac{S_{34}}{S_{33}} \frac{x_2^2 x_1}{2} - \frac{S_{35}}{S_{33}} \frac{x_1^2 x_2}{2} \right] + a_{11} \left[ \frac{S_{34}}{S_{33}} x_1 x_2 \right] \\
& + \sum_n d_n \left\{ -\frac{S_{31}}{S_{33}} \sum_{k=1}^3 \left[ C_k \mu_k \frac{Z_k^{\delta_n+2}}{(\delta_n+1)(\delta_n+2)} + C_{k+3} \bar{\mu}_k \frac{\bar{Z}_k^{\delta_n+2}}{(\delta_n+1)(\delta_n+2)} \right] \right. \\
& \quad - \frac{S_{32}}{S_{33}} \sum_{k=1}^3 \left[ C_k \frac{Z_k^{\delta_n+2}}{\mu_k (\delta_n+1)(\delta_n+2)} + C_{k+3} \frac{\bar{Z}_k^{\delta_n+2}}{\bar{\mu}_k (\delta_n+1)(\delta_n+2)} \right] \\
& \quad + \frac{S_{34}}{S_{33}} \sum_{k=1}^3 \left[ C_k \frac{\eta_k}{\mu_k} \frac{Z_k^{\delta_n+2}}{(\delta_n+1)(\delta_n+2)} + C_{k+3} \frac{\bar{\eta}_k}{\bar{\mu}_k} \frac{\bar{Z}_k^{\delta_n+2}}{(\delta_n+1)(\delta_n+2)} \right] \\
& \quad - \frac{S_{35}}{S_{33}} \sum_{k=1}^3 \left[ C_k \eta_k \frac{Z_k^{\delta_n+2}}{(\delta_n+1)(\delta_n+2)} + C_{k+3} \bar{\eta}_k \frac{\bar{Z}_k^{\delta_n+2}}{(\delta_n+1)(\delta_n+2)} \right] \\
& \quad \left. + \frac{S_{36}}{S_{33}} \sum_{k=1}^3 \left[ C_k \frac{Z_k^{\delta_n+2}}{(\delta_n+1)(\delta_n+2)} + C_{k+3} \frac{\bar{Z}_k^{\delta_n+2}}{(\delta_n+1)(\delta_n+2)} \right] \right\} = P_{33}
\end{aligned}$$

(A3)

$$\begin{aligned}
& A_1 \left[ \frac{x_1^2 x_2^2}{4} \right] + A_2 \left[ \frac{x_1 x_2^3}{3} \right] + A_3 \left[ \frac{x_1 x_2^2}{2} \right] + a_1 \left[ -\frac{S_{32}}{S_{33}} \frac{3x_1 x_2^2}{2} \right] \\
& + a_2 \left[ -\frac{S_{32}}{S_{33}} \frac{2x_1 x_2^2}{3} + \frac{S_{36}}{S_{33}} \frac{x_1 x_2^2}{2} \right] + a_5 \left[ -\frac{S_{32}}{S_{33}} x_1 x_2^2 \right] + a_8 \left[ \frac{S_{34}}{S_{33}} \frac{x_1^2 x_2^2}{2} \right] \\
& + a_9 \left[ \frac{S_{34}}{S_{33}} \frac{x_2^3 x_1}{3} - \frac{S_{35}}{S_{33}} \frac{x_1^2 x_2^2}{4} \right] + a_{11} \left[ \frac{S_{34}}{S_{33}} \frac{x_1 x_2^2}{2} \right] \\
& + \sum_n d_n \left\{ \sum_{k=1}^3 \left[ C_k \left[ \frac{x_2}{\bar{\mu}_k} \frac{\bar{Z}_k^{\delta_n+2}}{(\delta_n+1)(\delta_n+2)} - \frac{1}{\bar{\mu}_k^2} \frac{\bar{Z}_k^{\delta_n+3}}{(\delta_n+1)(\delta_n+2)(\delta_n+3)} \right] \right. \right. \\
& \quad \times \left. \left[ -\frac{S_{31}}{S_{33}} \mu_k^2 - \frac{S_{32}}{S_{33}} + \frac{S_{34}}{S_{33}} \eta_k - \frac{S_{35}}{S_{33}} \eta_k \mu_k + \frac{S_{36}}{S_{33}} \mu_k \right] \right. \\
& \quad \left. \left. C_{k+3} \left[ \frac{x_2}{\bar{\mu}_k} \frac{\bar{Z}_k^{\delta_n+2}}{(\delta_n+1)(\delta_n+2)} - \frac{1}{\bar{\mu}_k^2} \frac{\bar{Z}_k^{\delta_n+3}}{(\delta_n+1)(\delta_n+2)(\delta_n+3)} \right] \right. \right. \\
& \quad \times \left. \left[ -\frac{S_{31}}{S_{33}} \bar{\mu}_k^2 - \frac{S_{32}}{S_{33}} + \frac{S_{34}}{S_{33}} \bar{\eta}_k - \frac{S_{35}}{S_{33}} \bar{\eta}_k \bar{\mu}_k + \frac{S_{36}}{S_{33}} \bar{\mu}_k \right] \right] \Bigg\} \\
& = M_{11} \tag{A4}
\end{aligned}$$

$$\begin{aligned}
& A_1 \left[ \frac{x_1^3 x_2}{3} \right] + A_2 \left[ \frac{x_1^2 x_2^2}{4} \right] + A_3 \left[ \frac{x_1^2 x_2}{2} \right] + a_1 \left[ -\frac{S_{32}}{S_{33}} 2x_1^3 x_2 \right] \\
& + a_2 \left[ -\frac{S_{32}}{S_{33}} \frac{x_1 x_2^2}{2} + \frac{S_{36}}{S_{33}} \frac{2x_1 x_2^2}{3} \right] + a_5 \left[ -\frac{S_{32}}{S_{33}} x_1^2 x_2 \right] + a_8 \left[ \frac{S_{34}}{S_{33}} \frac{2x_1^3 x_2}{3} \right] \\
& + a_9 \left[ \frac{S_{34}}{S_{33}} \frac{x_1^2 x_2^2}{4} - \frac{S_{35}}{S_{33}} \frac{x_1^3 x_2}{3} \right] + a_{11} \left[ \frac{S_{34}}{S_{33}} \frac{x_1^2 x_2}{2} \right] \\
& + \sum_n d_n \left\{ \sum_{k=1}^3 \left[ C_k \left( \frac{x_1}{\mu_k} \frac{Z_k^{\delta_n+2}}{(\delta_n+1)(\delta_n+2)} - \frac{1}{\mu_k} \frac{Z_k^{\delta_n+3}}{(\delta_n+1)(\delta_n+2)(\delta_n+3)} \right) \right. \right. \\
& \quad \times \left. \left[ -\frac{S_{31}}{S_{33}} \mu_k^2 - \frac{S_{32}}{S_{33}} + \frac{S_{34}}{S_{33}} \eta_k - \frac{S_{35}}{S_{33}} \eta_k \mu_k + \frac{S_{36}}{S_{33}} \mu_k \right] \right. \\
& \quad C_{k+3} \left( \frac{x_1}{\bar{\mu}_k} \frac{\bar{Z}_k^{\delta_n+2}}{(\delta_n+1)(\delta_n+2)} - \frac{1}{\bar{\mu}_k} \frac{\bar{Z}_k^{\delta_n+3}}{(\delta_n+1)(\delta_n+2)(\delta_n+3)} \right) \\
& \quad \times \left. \left. \left[ -\frac{S_{31}}{S_{33}} \bar{\mu}_k^2 - \frac{S_{32}}{S_{33}} + \frac{S_{34}}{S_{33}} \bar{\eta}_k - \frac{S_{35}}{S_{33}} \bar{\eta}_k \bar{\mu}_k + \frac{S_{36}}{S_{33}} \bar{\mu}_k \right] \right] \right\} \\
& = M_{22} \tag{A5}
\end{aligned}$$

$$a_8 \left[ \frac{2x_1^3 x_2}{3} \right] + a_9 \left[ \frac{x_1^2 x_2^2}{2} \right] + a_{11} \left[ \frac{x_1^2 x_2}{2} \right]$$

$$+ \sum_n d_n \left\{ \sum_{k=1}^3 \left[ C_k \eta_k \right. \right.$$

$$\times \left[ \left[ \frac{x_1}{\bar{\mu}_k} + x_2 \right] \frac{\bar{z}_k^{\delta_n+2}}{(\delta_n+1)(\delta_n+2)} - \frac{1}{\bar{\mu}_k} \frac{\bar{z}_k^{\delta_n+3}}{(\delta_n+1)(\delta_n+2)(\delta_n+3)} \right]$$

$$+ C_{k+3} \bar{\eta}_k$$

$$\times \left[ \left[ \frac{x_1}{\bar{\mu}_k} + x_2 \right] \frac{\bar{\bar{z}}_k^{\delta_n+2}}{(\delta_n+1)(\delta_n+2)} - \frac{1}{\bar{\mu}_k} \frac{\bar{\bar{z}}_k^{\delta_n+3}}{(\delta_n+1)(\delta_n+2)(\delta_n+3)} \right]$$

$$= - M_{12}$$

(A6)

## Appendix B

## PROGRAM "SINGULAR"

Program "SINGULAR" was developed on a PC using a Turbo Pascal compiler, Ver. 4.0. This compiler enables to use the large range of real numbers  $[1.9 \times 10^{-4951}, 1.1 \times 10^{4932}]$ . This extraordinary range enables the application of the deflation method, Muller (1956), when solving for the eigenvalues of the transcendental form matrix.

B1 Interactive input process

The following figures are the sequence of screens as appear in the process of input data into "SINGULAR". The program is self explanatory, and menu driven. Fig. B1 is the opening logo. Fig. B2 provides the user the choice of using a pre-defined input file or using the interactive on-screen input process. If the choice is a pre-defined file, then fig. B3 is the next screen to appear, asking for the input file name and verifying its existence. Also, this screen gives the exact data needed to be include in the pre-defined file. For the other choice of on-screen input process, fig. B4 views the relevant screen. This screen is self-explanatory and guides the user with a definition of each field shown on a line which is the lower side of the frame. This instruction line changes respectively with the cursor movements from one field to another.



Welcome to:

"singularity\_at\_laminate\_edge"

This program calculates the order of singularity at the free edge of a laminated composite plate. This is the homogeneous part of the solution of the governing equations as presented by S. S. Wang, following Lekhnitzkii's development for the case of anisotropic plates. The solution uses Lekhnitzkii's stress potentials. Once the problem is set in the form of a non-linear eigenvalue problem, the solution is achieved by a deflation method as presented by D. Muller in 1956

Thanks for using "singularity\_at\_laminate\_edge"

Author : D. Shalev

Ver. 1.01  
Feb. 88

NOTE: this is a TurboPascal Ver.4.0 product.  
8087 math co-roc. (or higher) is a MUST.  
mouse is optional

hit <return> to continue

Figure No. B1: program "SINGULAR" - opening logo

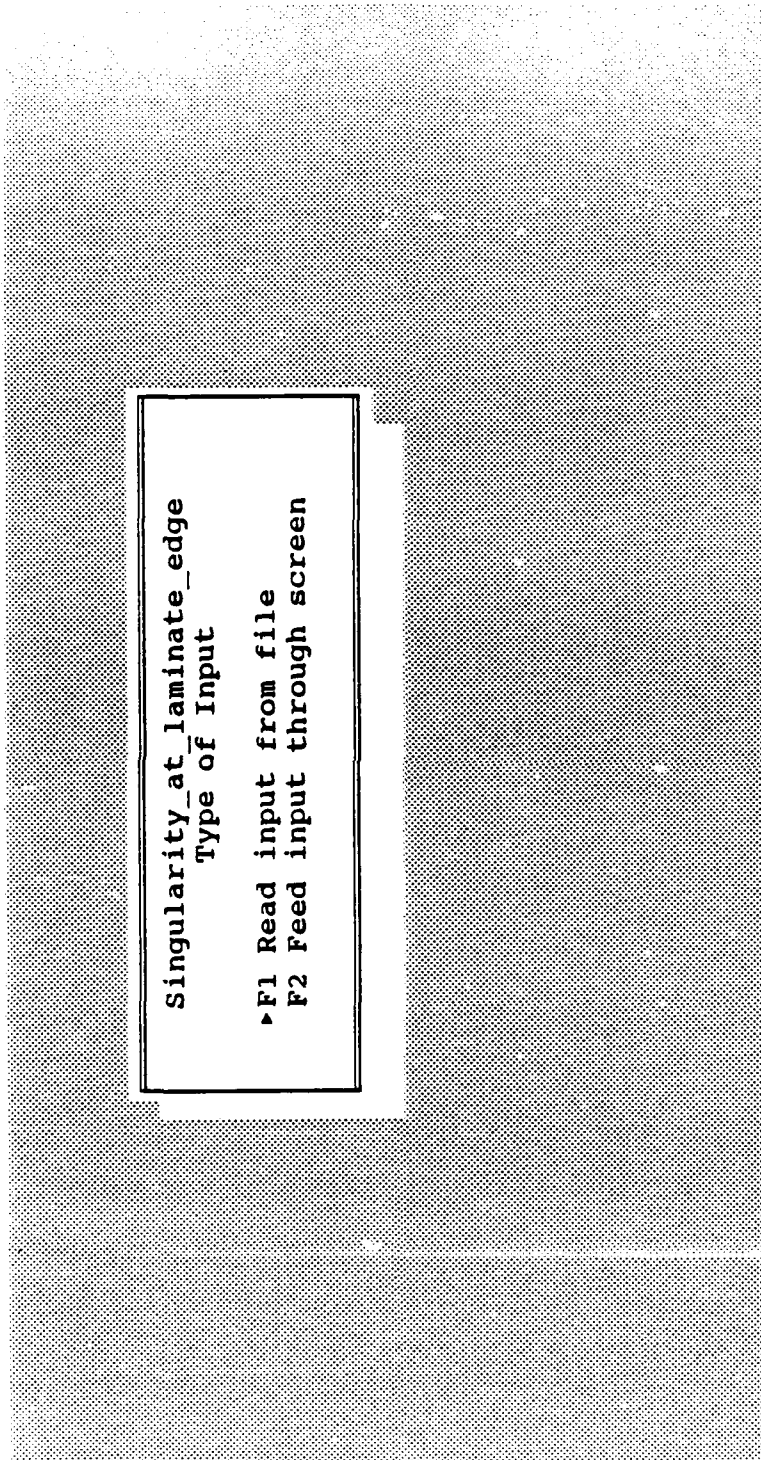


Figure No. B2: Chose input form

give name of input file: \_\_\_\_\_

give name of output file:

NOTE: input should be arranged as follow,

E1[1], E2[1], E3[1], G12[1], G13[1], G23[1], Nu12[1], Nu13[1], Nu23[1], Fi[1], Theta[1]  
 E1[2], E2[2], E3[2], G12[2], G13[2], G23[2], Nu12[2], Nu13[2], Nu23[2], Fi[2], Theta[2]  
 No\_of\_singularities

Figure No. B3: Chose input/output file names

F1 - help with edit keys		ply 2
ply 1		
E1:	_____	E1:
E2:	_____	E2:
E3:	_____	E3:
G12:	_____	G12:
G13:	_____	G13:
G23:	_____	G23:
V12:	_____	V12:
V13:	_____	V13:
V23:	_____	V23:
fi:	_____	fi:
theta:	_____	theta:
	n: _____	
	fn: _____	

elastic modulus in 1 direction for ply no. 1

Figure No. B4: On-screen input process

AD-A207 623

INVESTIGATION AND MODELING OF DAMAGE GROWTH IN  
COMPOSITE LAMINATES. (U) VIRGINIA POLYTECHNIC INST AND  
STATE UNIV BLACKSBURG MATERIALS.

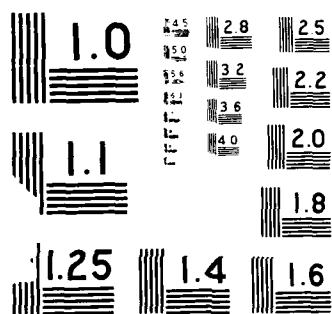
5/5

UNCLASSIFIED K L REIFSNIDER ET AL 25 SEP 88

F/G 11/4

NL





## B2 The output

Program "SINGULAR" results in one output file which contains a list which is the series of eigenvalues. The orders of singularity, following the above-described requirements, are marked for convenience.

## Appendix C

## PROGRAM "EDGSTR"

Program "EDGSTR" was developed on the Virginia Tech main-frame which is an IBM machine, using its vectorized option. The compiler used was a FORTRAN77 2<sup>nd</sup> generation called FORTVS2. This program uses the results of the analysis done by "SINGULAR", in terms of the series of eigenvalues, all the necessary materials and geometrical properties, and certain coefficients in a matrix form as obtained by "SINGULAR".

C1. Input file

The following is the structure of the input file for program "EDGSTR". Most of the input file is obtained automatically as an output file of the main-frame version of "SINGULAR". Few additions are required. The following is the complete structure.

NDEL	INTEG
------	-------

NDEL - Number of eigenvalues to be used

INTEG - Number of integration points

EE1	EE2	GG12	NNI12
-----	-----	------	-------

EE1 - effective modulus of the equivalent anisotropic laminate, dir. 1

EE2 - effective modulus of the equivalent anisotropic laminate, dir. 2

GG12 - effective modulus of the equivalent anisotropic laminate, dir. 12

NNI12 - effective poisson of the equivalent anisotropic laminate, dir. 12



SZ	SX	SXZ	MZ	MX	MT
----	----	-----	----	----	----

SZ - external load in the longitudinal direction

SX - external load in the transverse direction

SXZ - external shear load

MZ - external longitudinal moment

MX - external transverse moment

MT - external torsional moment

X1	X2	Y1	Y2	D	ALFA	XINIT
----	----	----	----	---	------	-------

note: refer to fig. 2 !

X1 - coordinate of  $-(e+2A)$

X2 - coordinate of a

Y1 - Coordinate of b

Y2 - Coordinate of -c

D - hole diameter =  $2A$

ALFA - angle shows location around the hole w.r.t. the Z axis

XINIT - the distance from the edge where first value is to be calculated

The rest of the input is provided automatically as an output of "SINGULAR".

E1	E2	E3	G12	G13	G23	NI12	NI13	NI23	FI	THETA
----	----	----	-----	-----	-----	------	------	------	----	-------

E1, E2, E3, G12, G13, G23, NI12, NI13, NI23 - elastic properties of the

unidirectional material of ply m

FI - fiber direction of ply m

THETA - angle of the free edge

$S(i, j)$

stiffness matrix of ply m

$SBAR(i, j)$

reduced stiffness matrix of ply m

$MIU(i)$

roots of the characteristic equation of ply m

$ETA(i)$

the ratios related to  $MIU(i)$  OF PLY M

$H(i, j)$

coefficients resulting from the analysis - refer to chapter 2

$OMG(i)$

coefficients resulting from the analysis - refer to chapter 2

the above curled parentheses are for ply m = 1,2

$AKS(i, j)$

transformation matrix which turns the problem from order of 12 to order of 6

NDEL(i)
---------

the series of eigenvalues from the homogeneous solution.

The above is the structure of the input file. The next four pages are an example of such a file for the example illustrated in figs. 3 & 4.

```

27      100
.296359D+7 .296359D+7 .532918D+7 .743289
100.DO 0.DO 0.DO 0.DO 0.DO 0.DO
-10.5 9.5 -.015 .005 1. 0.00 1.D-8
  2.0000E+07  2.1000E+06  2.100E+06
  8.5000E+05  8.5000E+05  8.500E+05
  2.1000E-01  2.1000E-01  2.100E-01
  7.8563E-01  1.5707E+00
  0.8408E+01 -0.1105E+01 -0.3356E+01  0.0000E+00  0.4261E+01  0.0000E+00
-0.1105E+01  0.9523E+01 -0.1105E+01  0.0000E+00 -0.1790E+01  0.0000E+00
-0.3356E+01 -0.1105E+01  0.8408E+01  0.0000E+00  0.4261E+01  0.0000E+00
  0.0000E+00  0.0000E+00  0.0000E+00  0.2352E+02  0.0000E+00 -0.4441E-15
  0.4261E+01 -0.1790E+01  0.4261E+01  0.0000E+00  0.1094E+02  0.0000E+00
  0.0000E+00  0.0000E+00  0.0000E+00 -0.4441E-15  0.0000E+00  0.2352E+02
  0.7068E+01 -0.1544E+01  0.0000E+00  0.0000E+00  0.5963E+01  0.0000E+00
-0.1546E+01  0.9378E+01  0.0000E+00  0.0000E+00 -0.1229E+01  0.0000E+00
  0.0000E+00  0.0000E+00  0.0000E+00  0.0000E+00  0.0000E+00  0.0000E+00
  0.0000E+00  0.0000E+00  0.0000E+00  0.2352E+02  0.0000E+00 -0.4440E-15
  0.5963E+01 -0.1229E+01  0.0000E+00  0.0000E+00  0.8783E+01  0.0000E+00
  0.0000E+00  0.0000E+00  0.0000E+00 -0.4440E-15  0.0000E+00  0.2352E+02
  0.0000E+00  0.3444E+01
  0.0000E+00  0.1035E+01
  0.0000E+00  0.8097E+00
  0.0000E+00 -0.3444E+01
  0.0000E+00 -0.1035E+01
  0.0000E+00 -0.8090E+00
  0.0000E+00 -0.3072E+01
  0.0000E+00  0.5584E+00
  0.0000E+00  0.2335E+00
  0.0000E+00  0.3072E+01
  0.0000E+00 -0.5584E+00
  0.0000E+00 -0.2335E+00
-0.1186E+02  0.1201E-14 -0.1058E+02  0.5358E-15  0.2243E-14  0.3444E+01
-0.1071E+01  0.3610E-15  0.5780E+00 -0.9738E-16  0.3612E-15  0.1035E+01
-0.6545E+00  0.2821E-15  0.1881E+00 -0.4073E-16  0.2885E-15  0.8090E+00
-0.1186E+02 -0.1201E-14 -0.1058E+02 -0.5358E-15  0.2243E-14 -0.3444E+01
-0.1071E+01 -0.3610E-15  0.5780E+00  0.9738E-16  0.3612E-15 -0.1035E+01
-0.6545E+00 -0.2821E-15  0.1889E+00  0.4074E-16  0.2885E-15 -0.8090E+00
  0.1743E-15  0.3444E+01
  0.1743E-15  0.1035E+01
  0.1743E-15  0.8090E+00
  0.1743E-15 -0.3444E+01
  0.1743E-15 -0.1035E+01
  0.1743E-15 -0.8090E+00
  2.0000E+07  2.1000E+06  2.1000E+06
  8.5000E+05  8.5000E+05  8.5000E+05
  2.1000E-01  2.1000E-01  2.1000E-01
-7.8539E-01 -1.5707E+00
  0.8408E+01 -0.1105E+01 -0.3356E+01  0.0000E+00 -0.4261E+01  0.0000E+00
-0.1105E+01  0.9523E+01 -0.1105E+01  0.0000E+00  0.1790E+01  0.0000E+00
-0.3356E+01 -0.1105E+01  0.8408E+01  0.0000E+00 -0.4261E+01  0.0000E+00
  0.0000E+00  0.0000E+00  0.0000E+00  0.2352E+02  0.0000E+00  0.4440E-15

```

-0.4261E+01	0.1790E+01	-0.4261E+01	0.0000E+00	0.1094E+02	0.0000E+00
0.0000E+00	0.0000E+00	0.0000E+00	0.4440E-15	0.0000E+00	0.2352E+02
0.7068E+01	-0.1546E+01	0.0000E+00	0.0000E+00	-0.5963E+01	0.0000E+00
-0.1546E+01	0.9378E+01	0.0000E+00	0.0000E+00	0.1229E+01	0.0000E+00
0.0000E+00	0.0000E+00	0.0000E+00	0.0000E+00	0.0000E+00	0.0000E+00
0.0000E+00	0.0000E+00	0.0000E+00	0.2352E+02	0.0000E+00	0.4440E-15
-0.5963E+01	0.1229E+01	0.0000E+00	0.0000E+00	0.8783E+01	0.0000E+00
0.0000E+00	0.0000E+00	0.0000E+00	0.4440E-15	0.0000E+00	0.2352E+02
0.0000E+00	0.3444E+01				
0.0000E+00	0.1035E+01				
0.0000E+00	0.8090E+00				
0.0000E+00	-0.3444E+01				
0.0000E+00	-0.1035E+01				
0.0000E+00	-0.8090E+00				
0.0000E+00	0.3072E+01				
0.0000E+00	-0.5584E+00				
0.0000E+00	-0.2335E+00				
0.0000E+00	-0.3072E+01				
0.0000E+00	0.5584E+00				
0.0000E+00	0.2335E+00				
-0.1186E+02	-0.1201E-14	-0.1058E+02	-0.5358E-15	-0.2243E-14	0.3444E+01
-0.1071E+01	-0.3610E-15	0.5780E+00	0.9738E-16	-0.3612E-15	0.1035E+01
-0.6545E+00	-0.2821E-15	0.1889E+00	0.4073E-16	-0.2885E-15	0.8090E+00
-0.1186E+02	0.1201E-14	-0.1058E+02	0.5358E-15	-0.2243E-14	-0.3444E+01
-0.1071E+01	0.3610E-15	0.5780E+00	-0.9738E-16	-0.3612E-15	-0.1035E+01
-0.6545E+00	0.2821E-15	0.1889E+00	-0.4073E-16	-0.2885E-15	-0.8090E+00
0.1743E-15	-0.3444E+01				
0.1743E-15	-0.1035E+01				
0.1743E-15	-0.8090E+00				
0.1743E-15	0.3444E+01				
0.1743E-15	0.1035E+01				
0.1743E-15	0.8090E+00				
0.5840E-01	0.0000E+00	0.3702E+00	0.0000E+00	0.1881E+00	0.0000E+00
0.2220E-15	0.0000E+00	0.1991E+00	0.0000E+00	0.1165E+00	0.0000E+00
0.5800E+01	0.0000E+00	-0.6210E+00	0.0000E+00	-0.7720E+00	0.0000E+00
-0.3119E+01	0.0000E+00	-0.1221E-14	0.0000E+00	-0.9468E-01	0.0000E+00
-0.4571E+01	0.0000E+00	0.1198E+01	0.0000E+00	0.1562E+01	0.0000E+00
0.2832E+01	0.0000E+00	-0.1468E+00	0.0000E+00	0.5689E-15	0.0000E+00
0.3330E-15	0.0000E+00	0.1991E+00	0.0000E+00	0.1165E+00	0.0000E+00
0.5840E-01	0.0000E+00	0.3702E+00	0.0000E+00	0.1881E+00	0.0000E+00
-0.3119E+01	0.0000E+00	-0.1249E-14	0.0000E+00	-0.9468E-01	0.0000E+00
0.5800E+01	0.0000E+00	-0.6210E+00	0.0000E+00	-0.7720E+00	0.0000E+00
0.2832E+01	0.0000E+00	-0.1468E+00	0.0000E+00	0.1054E-14	0.0000E+00
-0.4571E+01	0.0000E+00	0.1198E+01	0.0000E+00	0.1562E+01	0.0000E+00
-0.02557566		0.00000000			
0.00000000		0.00000000			
0.88147184		-0.23400497			
0.88147184		0.23400497			
1.00000000		0.00000000			
1.51152634		-0.79281732			
1.51152634		0.79281732			
2.00000000		0.00000000			

2.33894332	-1.11584015
2.33894332	1.11584015
3.00000000	0.00000000
3.09135317	1.73604639
3.09135317	-1.73604639
3.95200232	-2.02871459
3.95200232	2.02871459
4.00000000	0.00000000
4.74409286	-2.56838712
4.74409286	2.56838712
5.00000000	0.00000000
5.60214568	-2.85885102
5.60214568	2.85885102
6.00000000	0.00000000
6.39626347	-3.36527066
6.39626347	3.36527066
7.00000000	0.00000000
7.25651744	-3.65759372
7.25651744	3.65759372
8.00000000	0.00000000
8.04972367	-4.14799835
8.04972367	4.14799835
8.91205666	-4.44076090
8.91205666	4.44076090
9.00000000	0.00000000
9.73970143	4.82743595
9.73970143	-4.82743595
10.00000000	0.00000000
10.56741699	5.21487347
10.56741699	-5.21487347
11.00000000	0.00000000
11.35762857	-5.69087082
11.35762857	5.69087082
12.00000000	0.00000000
12.22198471	5.98346243
12.22198471	-5.98346243
13.00000000	0.00000000
13.01073907	-6.45620072
13.01073907	6.45620072
14.00000000	0.00000000
15.00000000	0.00000000
16.00000000	0.00000000
16.31465057	-7.98135589
16.31465057	7.98135589
17.00000000	0.00000000
17.96561409	-8.74253387
17.96561409	8.74253387
18.00000000	0.00000000
19.00000000	0.00000000
20.00000000	-0.00000039
21.00000000	0.00000001
22.00000000	0.00000000

23.00000000	0.00000000
24.00000000	0.00000000
25.00000000	0.00000000
26.00000000	0.00000000
27.00000000	0.00000000
28.00000000	0.00000000
30.00001594	-0.00000364
31.00011385	-0.00028805
31.99647973	0.00133420
33.00003421	-0.00268296
33.99869664	-0.09253746
35.01203137	-0.01801228
35.45796921	1.11312978
35.51097827	0.36380948
35.89506577	-1.61654381

C2 Output file

The output file consists of the following structure. First, there are all the unknown coefficients of the particular and homogeneous parts of the solution. Next are the eigenvectors of the homogeneous solution. Next are the near-field parameters which are the eigenvectors multiplied by the first coefficient of the homogeneous solution. Last listed the stresses. Each line consists of three numbers. The first is an integer indicates the stress following the Greek notation. The second number is the coordinate along the interface going from the hole outward. The third number is the magnitude of the relevant stress.



## VITA

Doron Shalev was born September 12, 1951 in Israel. In 1974 he entered the Technion, Israel Institute of Technology, in Haifa. In July 1977, he graduated with B.Sc. in Civil Engineering. Since then, he was working as a civil engineer, starting as an employee then at his own practice until October 1980. During the academic years 1979-1980 he conducted studies at the Technion in Haifa and received his M.Sc. in structures in January 1981. In October 1980 he joined Israel Aircraft Industry and is employed there until today. Doron is married to **Esti** and has three sons, **Naftaly**, **Eilon** and **Gad**.

END

6-89

DTIC